



Douglas, Rebecca Claire (2016) *Aspects of hydroxide catalysis bonding of sapphire and silicon for use in future gravitational wave detectors*. PhD thesis.

<http://theses.gla.ac.uk/7993/>

Copyright and moral rights for this work are retained by the author

A copy can be downloaded for personal non-commercial research or study, without prior permission or charge

This work cannot be reproduced or quoted extensively from without first obtaining permission in writing from the author

The content must not be changed in any way or sold commercially in any format or medium without the formal permission of the author

When referring to this work, full bibliographic details including the author, title, awarding institution and date of the thesis must be given

Enlighten:Theses
<http://theses.gla.ac.uk/>
theses@ gla.ac.uk

A Thesis submitted for the degree of Doctor of Philosophy

**Aspects of hydroxide catalysis bonding
of sapphire and silicon for use in future
gravitational wave detectors**

Rebecca Claire Douglas

February 4, 2017

School of Physics and Astronomy
College of Science and Engineering
University of Glasgow

Contents

Acknowledgments	xii
Preface	xiv
Summary	xvii
1. Gravitational Wave Detection	1
1.1. Introduction	1
1.2. Nature of gravitational radiation	3
1.3. Sources of gravitational waves	5
1.3.1. Burst sources	6
1.3.2. Continuous sources	8
1.3.3. The stochastic background	9
1.4. Types of gravitational wave detectors	10
1.4.1. Pulsar timing	10
1.4.2. Resonant bar detectors	11
1.5. Ground based interferometric detectors	13
1.5.1. Interferometric techniques	14
1.5.2. Noise limits of interferometric devices	19
1.6. First generation interferometric detectors	25
1.6.1. LIGO	25
1.6.2. Virgo	26

Contents

1.6.3.	GEO600	26
1.6.4.	TAMA	27
1.7.	Current interferometric detectors and upgrades	28
1.7.1.	Advanced LIGO	28
1.7.2.	Advanced Virgo	31
1.7.3.	GEO-HF	31
1.7.4.	KAGRA	31
1.8.	Next generation detectors	32
1.8.1.	The Einstein Telescope	33
1.8.2.	Space-based detectors	34
1.9.	Conclusions	34
2.	Thermal Noise	36
2.1.	Introduction	36
2.1.1.	Brownian motion	37
2.1.2.	The fluctuation dissipation theorem	37
2.2.	Sources of dissipation	40
2.2.1.	External sources of dissipation	40
2.2.2.	Internal sources of dissipation	41
2.3.	Thermal noise associated with a single resonant mode	44
2.3.1.	The loss factor	47
2.4.	Thermal noise in a multi-resonance system	48
2.4.1.	The Arrhenius equation	49
2.4.2.	Debye theory	49
2.5.	Thermal noise in a gravitational wave detector	51
2.5.1.	Coating thermal noise	51
2.5.2.	Bond loss	53
2.5.3.	Conclusion	54

3. Hydroxide catalysis bonding of sapphire	55
3.1. Introduction	55
3.1.1. Use of hydroxide catalysis bonding in fused silica based suspensions	56
3.2. The hydroxide catalysis bonding procedure	58
3.2.1. Surface preparation	60
3.2.2. Considerations in preparation of bonding solution	61
3.2.3. Bond formation	62
3.2.4. Hydration and etching	62
3.2.5. Polymerisation	64
3.2.6. Dehydration	65
3.2.7. Bond formation with sapphire substrates	66
3.3. A comparison of other bonding techniques	67
3.3.1. Indium bonding	67
3.3.2. Adhesives	68
3.4. Hydroxide catalysis bonding for sapphire and silicon in cryogenic suspen- sion systems	69
3.4.1. Sapphire samples for hydroxide catalysis bonding experiments . .	71
3.4.2. Analysis of surface suitability of sapphire samples intended for hy- droxide catalysis bonding experiments	73
3.4.3. Preparation of solutions for bonding sapphire	76
3.5. Bond inspection	77
3.6. Tensile strength testing	79
3.7. Results	80
3.7.1. False breaks	83
3.8. Discussion and summary	84
 4. Further experiments involving the strength of sapphire hydroxide catalysis bonds	 87
4.1. Introduction	87
4.1.1. Crystalline axes of sapphire	88

Contents

4.1.2.	Sapphire test mass suspensions in KAGRA	89
4.1.3.	Strength testing	90
4.2.	Influence of crystalline orientation on bond strength	94
4.2.1.	Shear strength measurements	98
4.2.2.	Results	98
4.2.3.	Conclusions	100
4.3.	Thermal cycling experiments	101
4.3.1.	Bonds for thermal cycling experiments	101
4.3.2.	Strength testing	102
4.3.3.	Results	102
4.3.4.	Conclusions	104
4.4.	Repair of damaged bonds	104
4.4.1.	Re-bonding procedures	106
4.4.2.	Investigating changes in surface conditions	107
4.4.3.	Results and observations	111
4.4.4.	Conclusions	117
4.5.	Bond curing time	119
4.5.1.	Results	120
4.5.2.	Conclusion	124
4.6.	Discussion and summary	125
5.	Loss measurements of hydroxide catalysis bonds between sapphire discs:	
	Theory and modeling	127
5.1.	Introduction	127
5.2.	Mechanical loss of hydroxide catalysis bonds	130
5.3.	Sapphire discs for bond loss experiments	131
5.4.	Finite element modeling of bonded sapphire discs and cylinders	132
5.4.1.	Introduction	132
5.4.2.	Elastic constants of sapphire	137
5.4.3.	Resonant mode shapes and frequencies	138

Contents

5.4.4.	The effect of disc thickness on strain energy ratio	140
5.4.5.	The effect of bond position on strain energy ratio	142
5.4.6.	Summary of FEA modeling calculations	144
6.	Loss measurements of hydroxide catalysis bonds between sapphire discs:	
	Experiment	145
6.1.	Introduction	145
6.2.	Nodal suspension of bonded sapphire discs	146
6.3.	Experimental procedure	147
6.4.	Cooling procedure	148
6.5.	Temperature calibrations	150
6.5.1.	Contact gas	153
6.5.2.	Cooling Rates of the disc and clamp	155
6.6.	Analytical calculations	157
6.7.	Loss measurements of sapphire discs	161
6.7.1.	Disc preparation	161
6.7.2.	Loss of unbonded sapphire discs	161
6.7.3.	Hydroxide catalysis bonding of sapphire discs	162
6.7.4.	Loss measurements of bonded sapphire discs	162
6.8.	Results	164
6.9.	Conclusions	171
7.	Thermal cycling of silicon-silicon hydroxide catalysis bonds	173
7.1.	Introduction	173
7.2.	Silicon samples for hydroxide catalysis bonding experiments	175
7.3.	Oxidation of silicon surfaces	177
7.4.	Bonding of silicon surfaces	179
7.5.	Thermal cycling procedure	180
7.5.1.	Strength testing	182
7.5.2.	Breaking mechanisms	182

Contents

7.6. Results	184
7.6.1. Bond Strength	184
7.6.2. The effect of breaking mechanism on bond strength	185
7.6.3. Conclusions	188
8. Conclusions	190
Appendices	194
A. Temperature calibration runs for low temperature mechanical loss experiments with sapphire discs	195
B. Additional FEA calculations	199
B.1. The effect of Young’s modulus on strain energy ratio	199
B.2. The effect of bond thickness on strain energy ratio	202
C. Oven characterisation for growing oxide layers on silicon samples	204

List of Figures

1.1. Gravitational wave polarisations	4
1.2. Gravitational wave spectrum	5
1.3. Michelson interferometer	13
1.4. Delay line interferometer with input mirror	16
1.5. Delay line interferometer	17
1.6. Interferometer with Fabry-Perot cavities	18
1.7. Power recycling in an interferometer with Fabry-Perot cavities	19
1.8. Signal recycling in an interferometer with Fabry-Perot cavities	20
1.9. Strain Sensitivity for the GEO600 detector	27
1.10. Advanced LIGO sensitivity	29
1.11. Advanced LIGO suspension	29
1.12. GW150914 Signal	30
2.1. Diagram of a mechanical oscillator	42
2.2. Spring-Maxwell unit system	50
2.3. Violin and pendulum modes	52
3.1. Advanced LIGO suspended test mass	58
3.2. Hydroxide catalysis bonding: Hydration	63
3.3. Hydroxide catalysis bonding: Polymerisation	65
3.4. Sapphire fibre with “nail head”	71

List of Figures

3.5. Cuboid sapphire samples	72
3.6. Bonded sapphire samples	72
3.7. Flatness of sapphire samples	74
3.8. An example surface flatness profile	74
3.9. Roughness of sapphire samples	75
3.10. Example surface roughness profile	75
3.11. Four-point strength test	80
3.12. Liquid nitrogen submerged four-point strength test	81
3.13. Strengths of hydroxide catalysis bonds between sapphire samples	82
3.14. Clean break	83
3.15. Break with damage to bulk sapphire	83
4.1. Crystalline axes of sapphire	88
4.2. KAGRA test mass suspensions	90
4.3. Torsional shear strength test apparatus	92
4.4. FEA model of shear stress	93
4.5. Diagram of sapphire sample dimensions	94
4.6. Photograph of sapphire sample	95
4.7. Histogram of the flatnesses of c-plane samples	96
4.8. Histogram of the flatnesses of a-plane samples	96
4.9. Histogram of the flatnesses of m-plane samples	97
4.10. Shear strength of crossed axis bonds between sapphire samples	99
4.11. Tensile strengths of thermally cycled bonds between sapphire samples	103
4.12. Photographs of clean and diagonal breaks	105
4.13. Sapphire surface flatness before and after bonding	108
4.14. Sapphire surface roughness before and after bonding	108
4.15. Tensile strengths of bonds between re-bonded samples: Sodium silicate	114
4.16. Tensile strengths of bonds between re-bonded samples: Sodium aluminate	115
4.17. Tensile strengths of bonds between re-bonded samples: Potassium hydroxide	116
4.18. Diagram of sapphire samples used for bond curing time experiments	119

List of Figures

4.19. Tensile strengths of bonds after various curing times	121
4.20. Combined tensile strengths of bonds after various curing times	121
4.21. Tensile strengths of bonds with heat treatment	123
5.1. Surface flatness profile of a sapphire disc	132
5.2. Resonant modes of a sapphire disc	133
5.3. Convergence plot example	135
5.4. Degrees of freedom for a suspended sapphire disc	136
5.5. Resonant mode shapes	139
5.6. Cylinders for bond loss measurements	140
5.7. Strain energy ratio going from discs to cylinders	141
5.8. Strain energy ratio going from discs to cylinders of unequal thickness . .	142
5.9. Strain energy ratio of bonded discs as bond position changes	143
6.1. Nodal suspension	148
6.2. Cryostat diagram	149
6.3. Temperature calibration data example	151
6.4. Calculated thermoelastic loss	160
6.5. Photographs of bonded sapphire discs	163
6.6. Mechanical loss of an unbonded 0.5 mm thick sapphire disc	165
6.7. Mechanical loss of an unbonded 1.5 mm thick sapphire disc	165
6.8. Mechanical loss of a bonded pair of sapphire discs	166
6.9. Comparison of mechanical loss for bonded and blank discs	167
6.10. Mechanical loss assuming 300 nm thick bond and clamped discs	168
6.11. Mechanical loss assuming 300 nm thick bond and free discs	169
6.12. Difference between mechanical loss for clamped and free discs	170
7.1. Diagram of silicon samples used for bonding experiments	175
7.2. Flatness profile example for a silicon sample	176
7.3. Distribution of flatnesses for silicon samples	176
7.4. Distribution of oxide thickness for silicon samples	179

List of Figures

7.5.	Sample holder used during thermal cycling	181
7.6.	Change of temperature over time during thermal cycles	182
7.7.	Photographs of silicon surfaces after strength testing	183
7.8.	Tensile strengths of thermally cycled silicon bonds	184
7.9.	All tensile strengths of thermally silicon cycled bonds	185
7.10.	Tensile strengths of silicon bonds: Breaking mechanisms	186
7.11.	Tensile strengths of silicon bonds: Diagonal breaks	187
A.1.	First temperature calibration run	196
A.2.	Second temperature calibration run	197
A.3.	Third temperature calibration run	197
A.4.	Fourth temperature calibration run	198
B.1.	Strain energy ratio assuming bond Young's modulus of 7.9 GPa	200
B.2.	Strain energy ratio assuming bond Young's modulus of 25 GPa	200
B.3.	Strain energy ratio assuming bond Young's modulus of 72 GPa	201
B.4.	Strain energy ratio assuming bond Young's modulus of 400 GPa	201
B.5.	Strain energy ratio for bonded silica discs	202
B.6.	Strain energy ratio as the bond thickness increases	203
C.1.	First oven characterisation for silicon oxide thicknesses	205
C.2.	Second oven characterisation for silicon oxide thicknesses	205

List of Tables

3.1. Strengths of hydroxide catalysis bonds between sapphire samples	81
4.1. Shear strength of crossed axis bonds between sapphire samples	99
4.2. Tensile strengths of thermally cycled bonds between sapphire samples . .	103
4.3. Summary of the analysis of roughness surface profile images	109
4.4. Tensile strengths of bonds with pristine samples	111
4.5. Tensile strengths of bonds with once-bonded samples	112
4.6. Tensile strengths of bonds with twice-bonded samples	113
4.7. Tensile strengths of bonds after various curing times	122
5.1. Resonant mode frequencies	139
7.1. Tensile strengths of thermally cycled silicon bonds	185
7.2. Tensile strengths of silicon bonds: Diagonal breaks	188

Acknowledgments

I would like to thank my supervisors, Sheila Rowan and Giles Hammond as well as Jim Hough and Marielle van Veggel, all of whom provided invaluable help, support and wisdom throughout my PhD. Additionally, advice, training and the hours spent with me in labs and at desks by Alan Cumming, Liam Cunningham, Alastair Grant, Karen Haughian, Iain Martin, Peter Murray and Jamie Scott meant that a good deal of my work went more smoothly than it otherwise could have. Endless discussions with my various office mates throughout the years, including Matt Abernathy, Chris Bell, Steven Brampsiepe, Paul Campsie, Kieran Craig, Mark Fletcher, Martin Hart, Hafizah Noor Isa, Rahul Kumar, Sean Leavey, Valentina Mangano, Richard Middlemiss and Raymond Robie, not only helped me solve problems faster but also helped, during challenging times, to remind me that I wasn't alone. Similarly, meetings over coffee with Sheena Barclay, Bryan Barr, Angus Bell, Neil Gordon, Siong Heng, Jan Simon Hennig, Alasdair Houston, Christian Killow, Kyung Ha Lee, John MacArthur, Chris Messenger, Brynley Pearlstone, Margot Phelps, Matt Pitkin, Jade Powell, Mariela Masso Reid, Andrew Spencer, Karl Toland, Zeno Tornasi, Daniel Williams and Jennifer Wright were often surprisingly helpful, not to mention uplifting. The Institute for Gravitational Research is much like a large family, and there isn't a single member within it who hasn't helped me in some way during my PhD, I am thankful for everyone.

Acknowledgments

Additionally, I would like to thank Martin Hendry, as head of the School of Physics and Astronomy, for helping to inspire me to begin my PhD in the first place. I would like to thank Lyndsay Fletcher for involving me in Project Juno and Athena SWAN and Morag Casey for endless hours discussions relating to how we can improve physics for underrepresented groups within it. Not to mention Gail Penny, Kirsty Annand, Lewis MacKenzie, Liam Moore, Graham Kerr, Duncan Stackhouse and countless others within the Kelvin Building who reminded me that there was life outside science. As well as Bhoomi Gor, who understood that sometimes, there isn't.

Of course, I must thank my best friends Jenny Campbell, Hannah Vure and Rhys Smith who showed undeserved patience when all I wanted to talk about was my research and who encouraged me constantly. To my mother, father and sister who always believed in me and in what I was doing, even when I failed to properly explain it, thank you. To my partner, Paul Mullen, I love you, I have no idea where I'd be without you, and I'm pretty sure I owe you pizza.

Finally, I would like to thank the Portuguese and Dutch traders who first brought tea to Britain, the British and Dutch traders who first brought coffee to Britain, the ancient Egyptians for inventing beer, and Tim Berners Lee for inventing the internet. Presumably it was almost impossible to conduct research until the work of all of these people had been completed.

Preface

This thesis is an account of work carried out by the author with support from staff in the Institute for Gravitational Research at the University of Glasgow between October 2012 and October 2016, involving the study of crystalline materials for use in future cryogenic gravitational wave detectors.

The aim of this thesis is to investigate the suitability of hydroxide catalysis bonding for use in sapphire and silicon suspensions in future detectors.

In Chapter 1 the context of the research is introduced: The motivation behind the search for gravitational waves and the first direct evidence of them, as predicted by Einstein.

In Chapter 2 the context of research specifically in this thesis is detailed with a direct focus on thermal noise - one of the important noise sources in gravitational wave detectors. The relationship between thermal noise and mechanical dissipation of energy and the influence this has on detector sensitivity, is discussed.

In Chapter 3 hydroxide catalysis bonding, its role in the construction of suspensions for gravitational wave detectors and its potential for use in cryogenic detectors is investigated. Dr. van Veggel, a research fellow in the IGR and Mr J Davidson of the School of Engineering assisted with the strength testing portion of the cryogenic strength tests

Preface

described in this chapter. The aims of this research were to measure initial strengths for hydroxide catalysis bonds between sapphire pieces at both room temperature and liquid nitrogen temperatures and to draw a comparison between strengths of bonds formed with a variety of different bonding chemicals. The work was supervised by Prof. Rowan, Director of the IGR.

In Chapter 4 further experiments in hydroxide catalysis bonding of sapphire and the strengths of the resulting bonds are discussed. The aim of the first experiment was to investigate the strength of bonds formed between sapphire pieces with different crystalline axes, this was carried out jointly by the author and Dr Haughian, an RA in the IGR. The aim of the second experiment was to investigate the effects of thermally cycling the bonds, the thermal cycling portion of this experiment was carried out jointly with Dr. K. Craig, then a PhD student in the IGR. The aim of the third experiment was to investigate the possibility of re-bonding previously joined and separated pieces and to measure the strengths of bonds where this was done. The aim of the fourth experiment was to investigate the curing time of bonds, the heat treatment portion of this experiment being carried out jointly by the author and Dr. van Veggel.

In Chapter 5 the experimental design and theory are outlined for carrying out an experiment to find the mechanical loss of a hydroxide catalysis bond layer between two sapphire discs. Additionally, finite element analysis models of a pair of hydroxide catalysis bonded sapphire discs is described. These experiments were carried out in order to extract a value of mechanical loss from the results of bond loss experiments described in the following chapter. This was carried out with advice from Dr. Haughian and Dr. Cunningham, a research fellow in the IGR. In particular, initial calculations involving the effect of different Young's moduli were carried out jointly by the author and Dr. Cunningham. The work was supervised by Prof. Rowan and Prof. Hough, Associate Director of the IGR.

Preface

In Chapter 6 experiments carried out by the author are described in which the mechanical loss of a hydroxide catalysis bond layer between two sapphire discs is measured from room temperature down to ~ 10 K. The results of these experiments were combined with results from the FEA calculations described in Chapter 5 to gain a value for the mechanical loss of the bond at several temperature points. The discs were bonded with advice and support from Dr. van Veggel. The loss measurements were carried out using a cryostat set up by Dr. Martin, a research fellow in the IGR, and Dr. K Craig and using LabVIEW software set up by Dr. Nawrodt, a research fellow of the University of Jena, Germany and Dr. Schwarz, then an RA of the University of Jena. The nodal support system was developed by Dr. Cumming, an RA in the IGR. Calculations to find the thermal noise contribution of a bond to that of a suspended system as a whole were carried out by Dr. Cunningham, Dr. Haughian and Dr. van Veggel. Additionally, Dr. van Veggel, Dr. Martin, Dr. K Craig, Dr. Cumming, Dr. Haughian, Prof. Rowan and Prof. Hough provided advice throughout the experiment.

In Chapter 7 the effect of thermally cycling bonds between silicon pieces is investigated in terms of bond strength. The thermal cycles were carried out at the university of Jena using a set up and software designed by Dr. Nawrodt and under Dr. Nawrodt's supervision. The rest of the experimental work was carried out and supervised in a similar manner to that of Chapters 3 and 4.

This thesis concludes by summarising the findings and putting the results into the context of future cryogenic gravitational wave detectors.

Summary

Gravitational waves, predicted by General Relativity, are small, fluctuating strains in space-time that can be detected using interferometric detectors. This was demonstrated for the first time by measurements made using the Advanced LIGO detectors following detector upgrades in 2015.

Ground based long-baseline interferometric gravitational wave detectors, such as the Advanced LIGO detectors, are designed to search for gravitational waves produced by energetic astronomical events such as black hole binary coalescences and supernova explosions. Test masses (mirrors) are suspended using multi-stage pendulum systems at the ends of perpendicular arms up to several kilometers in length. Laser interferometry is used to detect small changes in the relative separation of these masses caused by the passage of gravitational waves.

Several detectors of this form currently exist in addition to the US-based Advanced LIGO detectors, including the UK-German GEO600 detector and the French-Italian Virgo detector. The Japanese KAGRA detector is under construction. Plans for other, future detectors, including the space-based LISA detector, are currently being developed.

In the operational frequency band of between a few Hertz and a few kilohertz, the thermal motion of the test mass and their suspensions limits the design sensitivity of existing

Summary

detectors. The level of thermal noise is related to the mechanical loss of the test masses and suspension materials. This thermal noise could be reduced by operating detectors at cryogenic temperatures although, due to the thermomechanical properties of fused silica (which used for for the mirror and ultimate suspension fibres in all current detectors) this will necessitate a change of material. The most promising candidate materials for cryogenic use are mono-crystalline sapphire and silicon.

In current suspension designs, suspension fibres are welded to interface pieces (or “ears”) which are in turn joined to flat sections on the test masses using hydroxide catalysis bonding. This is a high strength chemical bonding technique and its use for joining similar sapphire and silicon pieces is the focus of this thesis. Both the strength of bonds and the mechanical loss of bonds is explored for use in future cryogenic gravitational wave detectors.

Chapter 1 introduces gravitational waves and their sources as well as the techniques used for detection. In Chapter 2 thermal noise is introduced and how the mechanical losses of suspension elements contribute to thermal noise is discussed. Chapters 3–6 cover the experimental research: the measurements of strength and mechanical loss of hydroxide catalysis bonds formed with sapphire and with silicon between room temperature and cryogenic temperatures.

In Chapters 3 and 4 investigations into the strength of hydroxide catalysis bonds between sapphire blocks at room and cryogenic temperatures are described. Chapter 3 contains a description of the strengths of bonds formed using different chemical bonding agents as well as initial strength measurements at cryogenic temperatures. The tensile strength of bonds formed using sodium silicate solution were found to be the highest of the chemicals tested with an average strength of 74 MPa measured. At 77 K an average strength of 73 MPa was measured for bonds formed in the same way.

Summary

In Chapter 4 experiments investigating further parameters that may affect bond strength are described. These included the effects on strength of bonding different crystal axes of sapphire, the effects on strength of thermally cycling bonds, the possibility of re-bonding previously joined and separated pieces and how different curing times affect bond strength. Although some variation in bond strengths was seen in each case, it was encouraging that all bonds measured would be strong enough for use in typical suspensions with a significant safety factor.

In Chapters 5 and 6 experiments are described investigating the mechanical loss of bonds between sapphire discs at temperatures between ~ 10 K and room temperature. Chapter 5 involves a description of the experimental design and theory, as well as finite element analysis necessary for interpretation of the results presented in the following chapter. Chapter 6 describes the mechanical loss measurements of a bonded system of two sapphire discs and uses the results from the previous chapter to find a value of the mechanical loss of the bond. For the resonant mode measured at ~ 6 kHz at room temperature the mechanical loss of the bond was found to have a value of $\sim 2.6 \times 10^{-2}$. At cryogenic temperatures this decreases down to between $\sim 2.7 \times 10^{-4}$ and $\sim 1.2 \times 10^{-3}$. These values were used to demonstrate that the thermal noise contribution of the bonds to that of the suspensions as a whole would be small enough to meet the thermal noise budget of a detector such as KAGRA.

In Chapter 7 an experiment to study the effect of thermally cycling hydroxide catalysis bonds formed between silicon pieces is described. The bonds were cycled between room temperature and liquid helium temperatures 3, 10 or 20 times and strengths of 19, 16 and 15 MPa were measured after cycling, compared to strengths of 17 MPa for bonds which were not cycled. This suggests that thermal cycles do not lead to a large reduction in strength of hydroxide catalysis bonds between silicon.

1. Gravitational Wave Detection

1.1. Introduction

Gravitational waves were first postulated by Einstein in 1916 as a consequence of the General Theory of Relativity [1, 2]. The waves manifest as ripple-like, propagating deformations of space-time and are created by asymmetric acceleration of massive bodies. The first attempts to directly detect gravitational waves began in the 1960's [3] and the first direct detection was achieved by the LIGO Scientific Collaboration and the Virgo Collaboration using the Advanced LIGO interferometric detectors located in the USA on 14th September 2015 [4].

Attempts to detect gravitational waves through direct means were given an early impetus by a report of findings by Weber in 1969 that featured a signal appearing to be consistent with gravitational waves passing through two resonant bar detectors [5] but attempts to independently reproduce these findings were unsuccessful. Some resonant bar detectors are still in use [6, 7] but due to limitations in both the frequency ranges and the noise floor of such detectors, most of the research efforts of the gravitational wave detection community are now focused on Michelson-type laser interferometers [8]. Such detectors have good sensitivity over a wide frequency range (the detection band for Advanced LIGO is ~ 10 -7000 Hz [9]) and there is now a growing global network of gravitational wave

1. Gravitational Wave Detection

interferometers [10]. Recent upgrades to these detectors improved their sensitivity to the point that the first direct detections of gravitational waves have been possible [4, 11, 12].

The first direct detection of gravitational waves was remarkable not only because it confirmed the predictions of General Relativity [4], but because it was also the first direct detection of black holes [4]. Additionally, it was the first detection of a black hole coalescence and it allowed confirmation of the existence of heavy solar mass black holes, the existence of which had not been expected (the black holes had masses of 36 and 29 solar masses) [4, 13]. This first detection was followed soon after, on 26th December 2015, by a second detection of gravitational waves associated with a slightly smaller pair of coalescing black holes, this time with masses of 14 and 7.5 solar masses [14].

Prior to the direct detection of gravitational waves, strong evidence for their existence was in place, in particular from work by Russell Hulse and Joseph Taylor in 1975, concerning the binary pulsar B1913+16 [15]. Hulse and Taylor received the Nobel Prize for their work studying this system in which they demonstrated that the rate of change of the orbital period of the binary system agreed with that expected from the emission of gravitational radiation as predicted by General Relativity [15]. In 2004 further results were published showing the observations spanning the previous 30 years demonstrating that the behaviour of the binary system agreed with that predicted by general relativity to within 0.2 percent [16].

Further improvements to existing interferometric gravitational wave detectors are planned, alongside which the global network of gravitational wave detectors will be expanded [10]. Currently detectors in the US (Advanced LIGO) and Germany (GEO-HF) are operational and the Italian-French detector, Virgo, is undergoing upgrades to an advanced phase. The TAMA detector was decommissioned in 2004 and efforts moved to the Kamioka mine where the initial stage of the Japanese detector, iKAGRA, has already been completed. An initial Michelson stage of an upgraded cryogenic version, bKAGRA, is expected to be

1. Gravitational Wave Detection

completed in 2018 with further upgrades planned for the following years [17, 18]. Additionally, plans for a third LIGO detector in India, IndIGO, are under way [19]. A global, collaborative network of detectors will allow for a greater range of gravitational wave signals to be detected and will also allow for the location of each source of gravitational waves to be better understood. Gravitational wave astronomy is now a reality.

1.2. Nature of gravitational radiation

Gravitational waves are produced by the non-axisymmetric acceleration of mass [20]. Conservation of mass precludes the existence of monopolar radiation and conservation of momentum precludes the existence of dipolar radiation. As such, the lowest order of gravitational wave radiation is quadrupole in nature [21]. Gravitational waves create a strain, h , in space-time as they propagate through it, transverse to the direction of their propagation. This strain leads distances to be reduced in one direction while they are increased in the orthogonal direction. The waves are made up of a superposition of two independent polarisations, h_+ and h_\times , which are at 45° to each other. The effect that these polarisations would have on a set of free particles positioned in the shape of a ring is shown in figure 1.1.

1. Gravitational Wave Detection

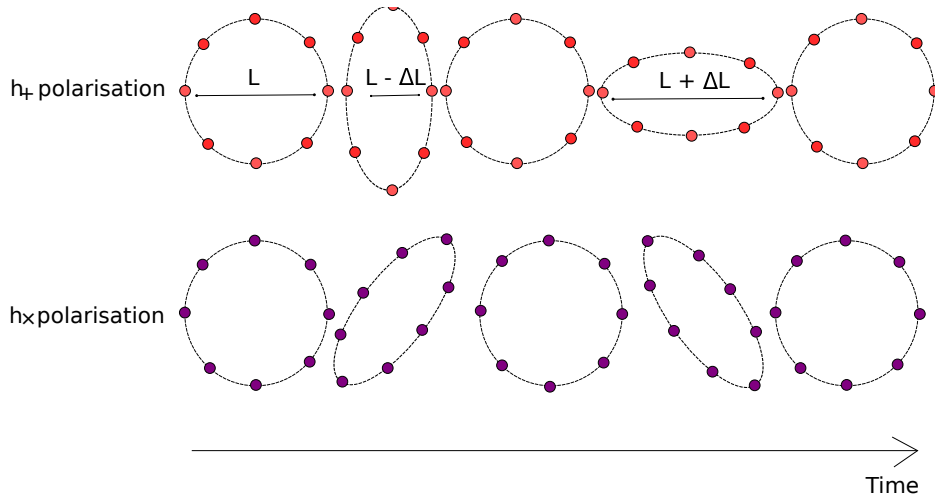


Figure 1.1.: The effect of the passage of h_+ and h_\times polarisations of gravitational waves on a ring of test particles when the incident waves are normal to the page. (Diagram not to scale).

The strain amplitude of a gravitational wave detected by a gravitational wave interferometer is defined as,

$$h = \frac{2\Delta L}{L} \quad (1.1)$$

where L is the distance between two test particles and ΔL is the change in separation due to the passing gravitational wave.

As gravity is by far the weakest of the four fundamental forces it is not practical to attempt generation of measurable gravitational waves in a laboratory; any waves produced would be too small to be measurable [21]. For waves of a measurable amplitude to be produced, astrophysical masses and accelerations are required. Potential sources include supernova explosions and mergers of binary neutron stars and black holes [22]. Even in these cases the strains produced are very small (of the order of $h \sim 10^{-21}$ to $\sim 10^{-23}$ [4, 23]) and therefore direct detection poses significant challenges [24, 25].

1. Gravitational Wave Detection

A major advantage of gravitational wave astronomy is that gravitational waves interact only weakly with matter so this allows for the study of phenomena for which electromagnetic radiation currently only allows limited understanding. Black hole-black hole interactions, the coalescence of binary systems, the rotation of pulsars and supernova explosions are of particular interest, as are other, as yet unpredicted phenomena [26].

1.3. Sources of gravitational waves

A range of astrophysical events are expected to give rise to gravitational waves. These events create waves with frequencies across a very wide frequency band. However, current ground based interferometric detectors are sensitive in the range from a few tens of Hertz to a few thousand Hertz (see figure 1.2). Hence, sources which produce gravitational waves within this frequency range are of interest in the context of this thesis.

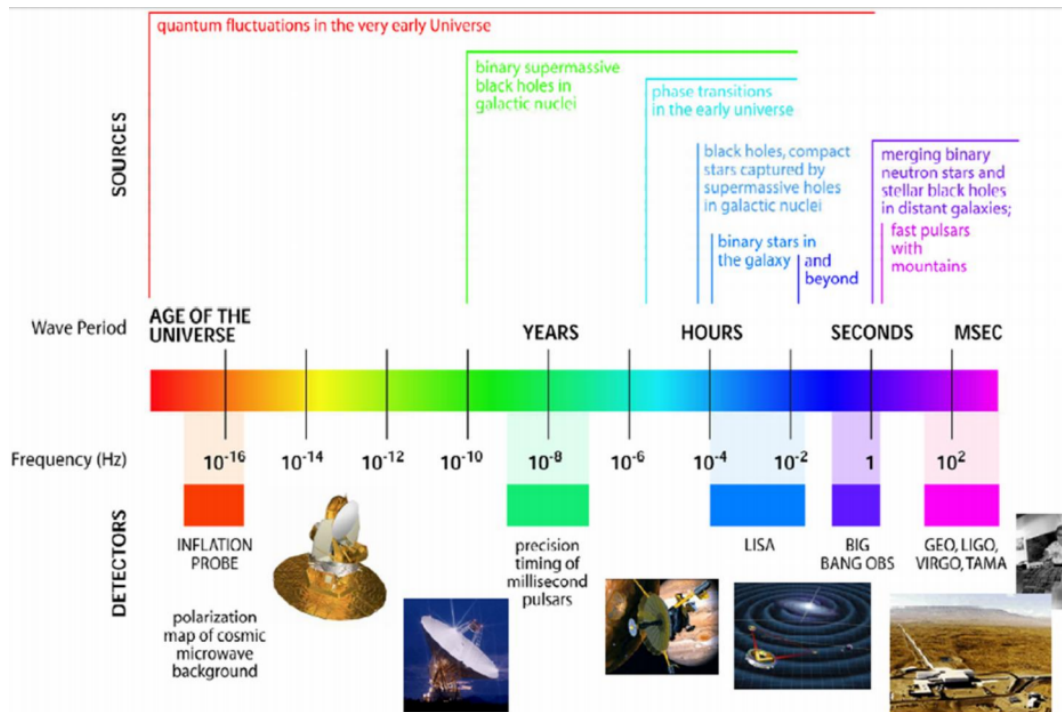


Figure 1.2.: The gravitational wave frequency spectrum with expected sources and detector sensitivities [27].

1.3.1. Burst sources

Brief, rapid outbursts of gravitational radiation (as opposed to continuous signals) are known as burst sources. Examples of burst sources include supernovae, coalescing compact binary systems, magnetars and other, as yet unknown sources.

Coalescing compact binaries

Compact binary systems are astronomical configurations consisting of two extremely dense objects, such as black holes or neutron stars, orbiting a common centre of mass. The orbital radius of the system decreases as the system emits gravitational radiation. As the objects move closer together their orbital frequency increases and this leads to an increase in the frequency of the gravitational waves emitted and, depending on the masses of the binary objects, the frequency may move into the sensitive range of Earth-based gravitational wave detectors. Depending upon the distance of the source, the amplitude of this signal may be great enough to be detectable on Earth while the signal is in these frequency ranges.

The strain, h , produced by such coalescing compact binary systems has been estimated to be [28]

$$h \approx 1 \times 10^{-23} \left(\frac{m_T}{M_\odot}\right)^{\frac{2}{3}} \left(\frac{\mu}{M_\odot}\right) \left(\frac{f}{100 \text{ Hz}}\right)^{\frac{2}{3}} \left(\frac{100 \text{ Mpc}}{r}\right) \quad (1.2)$$

where $m_T = m_1 + m_2$, the total mass of the two objects in the system, $\mu = m_1 m_2 / (m_1 + m_2)$, the reduced mass of the system, f is the frequency of the emitted gravitational wave radiation and r is the distance between the system and the gravitational wave detector.

1. Gravitational Wave Detection

Before the first detection of gravitational waves it was expected that the most commonly occurring sources involving compact binary systems would be those which involved two co-orbiting neutron stars [29]. Now that the first two detections have both been made involving binary black holes [4, 14] these systems are thought to be more common [30], although systems with one black hole and one neutron star are also possible [22]. Binary systems containing black holes are especially important candidates for producing detectable gravitational waves as their high masses and densities leads to the emission of gravitational waves with amplitudes larger than those that would be expected for, for example, neutron star binary systems.

Supernovae

Supernovae are extremely luminous stellar explosions that can occur at the end of the lifetime of certain very massive stars [31]. If at the end of a star's lifetime it approaches the Chandrasekhar limit the star's mass can no longer be supported by electron degeneracy pressure and the core collapses, causing the explosion [31]. The most massive stars will become black holes or neutron stars following this process, while less massive stars will not undergo supernova and will eventually become white dwarfs [32].

In the case of a spherically symmetrical collapse no gravitational waves will be emitted. However, in the case of an asymmetric collapse a burst of gravitational radiation will be produced. The strain, h , of the gravitational waves produced from a core collapse supernova is estimated to be $\sim 1 \times 10^{-21}$ at a distance of 10 kpc from the source but such events are expected to be rare [33].

1.3.2. Continuous sources

A continuous gravitational wave signal is emitted throughout the lifetime of a binary system. However, it is only during the final few seconds before coalescence that the frequency of the waves is sufficiently high that the signal may be within the detection band of a ground-based detector [34].

Some stable rotating systems can produce a continuous gravitational wave signal that should be detectable on Earth. Examples of these include pulsars and low mass x-ray binaries [34]. Additionally, there is thought to be a continuous background of gravitational wave signals caused by a wide range of stochastic sources [34].

Pulsars

Following a supernova a star's core may, depending on the star's mass, become a neutron star or a black hole. Neutron stars emit radio-frequency electromagnetic radiation from their magnetic poles. If a neutron star rotates about an axis that does not pass through these poles the radio waves sweep out a path in space. This path may periodically include the Earth where the radio signals may be detected. Radio pulses of this kind were discovered by Bell in 1967 [35] and this led to the name "pulsar" being given to such neutron stars.

Should a pulsar not rotate axisymmetrically, gravitational radiation will be emitted alongside electromagnetic radiation. At the Earth, such gravitational waves would have a strain amplitude of [36],

$$h_0 = \frac{16\pi^2 G}{c^4} \frac{\epsilon I_{zz} f_{\text{rot}}^2}{r} \quad (1.3)$$

1. Gravitational Wave Detection

Where f_{rot} is the rotational frequency of the neutron star, I_{zz} is its principal moment of inertia, $\epsilon = \frac{I_{xx} - I_{yy}}{I_{zz}}$ is the its equatorial ellipticity and r is the distance from the Earth.

Low mass x-ray binaries

Neutron stars also exist in binary systems with ordinary stars [34]. In such a system the neutron star will have a large enough gravitational field that it will strip matter from its companion, thus gaining mass and increasing its angular momentum [34]. The neutron star will also emit x-rays as a result of this mass accretion [34]. Should the angular momentum increase sufficiently, the Chandrasekhar-Friedman-Schutz (CFS) instability point may be reached [37]. Here, a wave is produced on the surface leading the rotation to become non-axisymmetric and hence gravitational waves can be emitted. Stars existing at this instability point are known as Wagoner stars [38]. The strain amplitude from such a system is directly related to the x-ray flux, L_γ as, [38]

$$h \approx 3 \times 10^{-27} \left(\frac{1 \text{ kHz}}{mf} \right)^{\frac{1}{2}} \left(\frac{L_\gamma}{10^{-8} \text{ ergscm}^{-2} \text{ sec}^{-1}} \right)^{\frac{1}{2}} \quad (1.4)$$

where m is the mode number and f is the frequency and is expected to be ~ 500 Hz.

1.3.3. The stochastic background

Gravitational waves caused by a variety of events across the Universe may be superimposed, creating a stochastic background of gravitational wave signals. Such events could include gravitational waves produced shortly after the Big Bang at the end of the Inflationary Period [21], the gravitational waves produced as the result of a collapse of a

1. *Gravitational Wave Detection*

population of black holes [21], or gravitational waves associated with the production of cosmic strings [39].

This background of stochastic signals is random in its distribution and as such it cannot be detected with just one interferometer. However, cross-correlation of data from multiple gravitational wave detectors could make the detection of the stochastic background of gravitational waves possible [40].

1.4. Types of gravitational wave detectors

Two major detector types for gravitational wave detection are resonant bar detectors [41, 6, 42, 7, 43] and laser interferometers on Earth and in space [44, 45, 46, 47, 48]. Since even those gravitational waves that are detectable on Earth represent very small strains, the detectors used must be extremely sensitive.

Other detection techniques are also being applied in attempts to directly detect gravitational waves. The most notable of these is the radio astronomy technique, pulsar timing [49], although some attempts have also been made to measure the effect of gravitational waves on the cosmic microwave background [50]. So far, however, only ground-based Michelson-type laser interferometric detectors have been successful in directly detecting gravitational waves.

1.4.1. Pulsar timing

Radio signals from pulsars are periodically detected on Earth. The separation between a pulsar and the Earth will be altered by any passing gravitational waves and this will

1. Gravitational Wave Detection

alter the arrival time of radio waves from the pulsar. Pulsar timing involves observing the rate of radio pulses over time and observing any changes in this rate. If this is done for many pulsars, the effect of a passing gravitational wave could be found [51].

This method of detection is sensitive to gravitational waves in the range $\sim 10^{-9} - 10^{-8}$ Hz which is consistent with that expected for a coalescing binary system of two super-massive black holes [49].

Pulsar timing projects currently in operation include EPTA (European Pulsar Timing Array) [52], NANOGrAV (North American Nanohertz Observatory for Gravitational waves) [53] and PPTA (Parkes Pulsar Timing Array) [54] which together form the IPTA (International Pulsar Timing Array) [49].

1.4.2. Resonant bar detectors

Joseph Weber developed the first resonant bar detector in the 1960s, reporting coincident detections in 1969 [5]. Following this, others constructed bar detectors in attempts to confirm Weber's detection. Weber's experiment consisted of two large cylindrical aluminium masses, or "bars," (with masses of the order of a few tonnes). These were separated by a distance of 1000 km and were suspended under vacuum at room temperature [55, 56, 57].

Should a gravitational wave with the appropriate orientation and frequency pass through the mass this would excite the bar's fundamental longitudinal mode, causing a small change in the vibrational movement of the cylinder. This movement would be detected with a set of piezoelectric strain gauges, mounted on the middle of the bar - these would transform the effect of the gravitational wave into an electric signal. In the early configuration for these detectors the electronic noise of the detection system and the thermal noise of the molecules within the bar, were limits to detector sensitivity [58].

1. Gravitational Wave Detection

The minimum gravitational wave strain amplitude that a bar detector of this kind would be capable of measuring was $h \sim 10^{-16}$ [26]; much larger than any predicted strain size for astrophysical sources of gravitational waves [21]. To improve sensitivity by reducing thermal noise, new bar detectors were designed to operate at cryogenic temperatures. Among them were ALLEGRO [59, 43], AURIGA [6, 41], EXPLORER [60, 7] and NAUTILUS [42]. Since moving to cryogenic bar detectors, sensitivities of $h \sim 10^{-20} / \sqrt{\text{Hz}}$ over a band width of ~ 100 Hz have been achieved [61]. Only AURIGA and NAUTILUS are still in operation [26].

One method for further increasing the sensitivity is to increase the mass of the detectors. Altering the bar's geometry allows for an increase in mass without a significant increase in size and also allows for directionality to be achieved [62]. A bar has only one quadrupole mode while a spherical mass has five. Therefore, if a gravitational wave passed through a spherical mass it would be possible to find the direction of the source of the waves by comparing the ratio of excitation of each mode. Two spherical detectors are currently in operation: MiniGRAIL [63] and the Mario Schenberg Detector [64]. These detectors are intended to operate with ~ 60 Hz bandwidth and are designed to measure strains of $h \sim 10^{-21} / \sqrt{\text{Hz}}$ at ~ 3000 Hz.

The main disadvantage in the use of bar detectors and spherical detectors is the narrow sensitive frequency band (~ 100 Hz) as it is only possible to detect a gravitational wave of a frequency close to the resonant frequency of the detector. A possible solution is to construct dual-resonant mass detectors [65]. This involves the construction of two concentric spheres - the outer sphere having a resonant frequency two or three times lower than the inner sphere. If a gravitational wave passed the spheres they would be excited in anti-phase and the signal would be amplified. Such an instrument would potentially achieve strain sensitivities of $h \sim 2 \times 10^{-23} / \sqrt{\text{Hz}}$ over a bandwidth of 2 kHz [65]. Currently the practicality of such a design is uncertain due to the need for a complicated readout system that could add extra loss and reduce the sensitivity levels.

Since the success of Michelson-type interferometric gravitational wave detectors there is very little current research in resonant bar detectors. However, a super-fluid helium resonant mass detector was recently proposed by Singh et al [66].

1.5. Ground based interferometric detectors

Laser interferometric gravitational wave detectors are sensitive across wide frequency bands. The quadrupole moment of gravitational radiation makes Michelson-type laser interferometers particularly suitable as detectors. See figure 1.3 for a schematic of a basic Michelson interferometer.

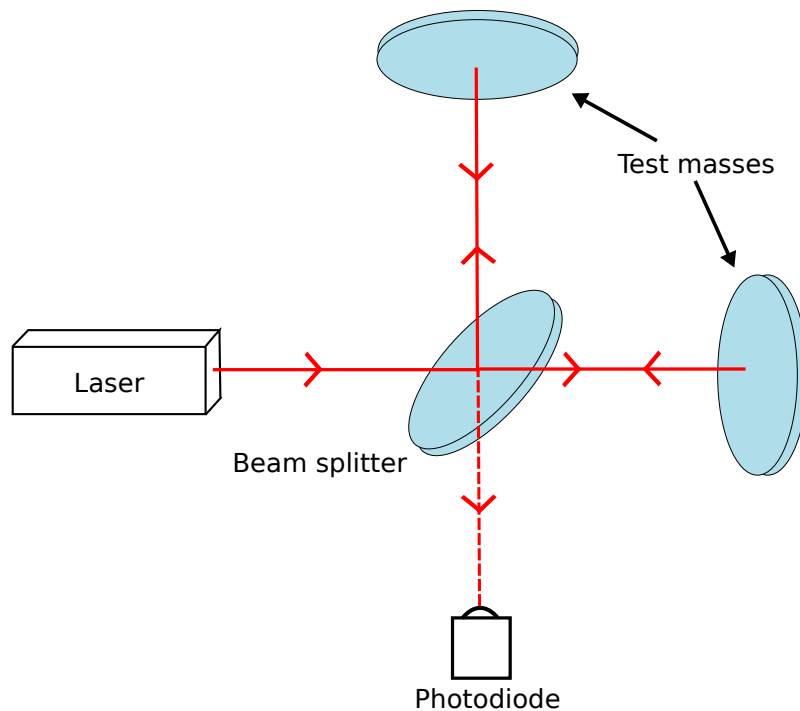


Figure 1.3.: A schematic of a simple Michelson interferometer.

The test masses of an interferometer can be thought of as the test particles at right angles discussed in section 1.2 and shown in figure 1.1. As a gravitational wave passes through the interferometer, the distance between the beam-splitter and one test mass is reduced while the other increases, then vice-versa.

1. Gravitational Wave Detection

The first experimental work into interferometers as gravitational wave detectors was carried out by Forward [67]. In these instruments the laser light is split using a beam-splitter; half the light is transmitted while half is reflected. The two beams travel the length of the interferometer arms to the end test masses (mirrors) where they are reflected back towards the beam splitter where they recombine and the combined light is detected by the photodetector.

The test masses are suspended in a vacuum to reduce excess noise from scattering and gas damping in the system [21]. Without noise or gravitational waves the difference in length of the interferometer arms, and hence the difference in length of the two beam paths, is constant. A change in the difference in arm lengths, such as that caused by a passing gravitational wave, will alter the interference pattern. This change will be detected by the photodiode as a change in light intensity.

For a gravitational wave of amplitude h a longer arm length of the detector will lead to an greater change of length caused by the gravitational wave (see equation 1.1) allowing the wave to be detected more easily. However, due to the availability of land and the curvature of the Earth, detectors on the surface of the Earth are generally limited to ~ 4 km in arm length [21]. This constrained arm length has necessitated the development of advanced interferometric techniques to enhance the sensitivity of these detectors. Longer detector arm-lengths will be possible if the detectors are constructed underground [68] or in space [69].

1.5.1. Interferometric techniques

The maximum sensitivity of an interferometric gravitational wave detector occurs when the time for which the laser light is stored within the interferometer arms is equal to half the period of the gravitational wave [21]. In this case, the light must take a quarter of the

1. Gravitational Wave Detection

period of the gravitational wave to travel from the beam splitter to the end test masses. Hence the light would reach the end test masses as they were maximally displaced by the passing gravitational waves.

For a gravitational wave of frequency ~ 100 Hz to be detectable, the arms of the detector would need to be 750 km in length [70]. As this is impractical on Earth new interferometric techniques were developed to artificially increase the total optical path length without physically increasing the arm lengths, thus allowing increased sensitivity across a desirable range of frequencies.

Delay-line interferometry

Delay-lines in gravitational wave interferometers were first proposed by Weiss in 1972, [71]. The aim of the delay line is to improve sensitivity by increasing the optical path length. This is achieved by reflecting the laser light multiple times between additional mirrors placed within the interferometer arms.

There are two possible configurations for such an interferometer. The first is to insert the secondary mirror close to the beam splitter, facing the end test mass. This method was developed at the Max-Planck-Institut für Quantenoptik in Garching, Germany by Shoemaker *et al* in 1988 [72]. Through the use of curved mirrors, the laser light would enter through a hole in the mirror, be reflected multiple times between the two mirrors, without any beams overlapping, and would then exit back through the hole (see figure 1.4 for a schematic).

1. Gravitational Wave Detection

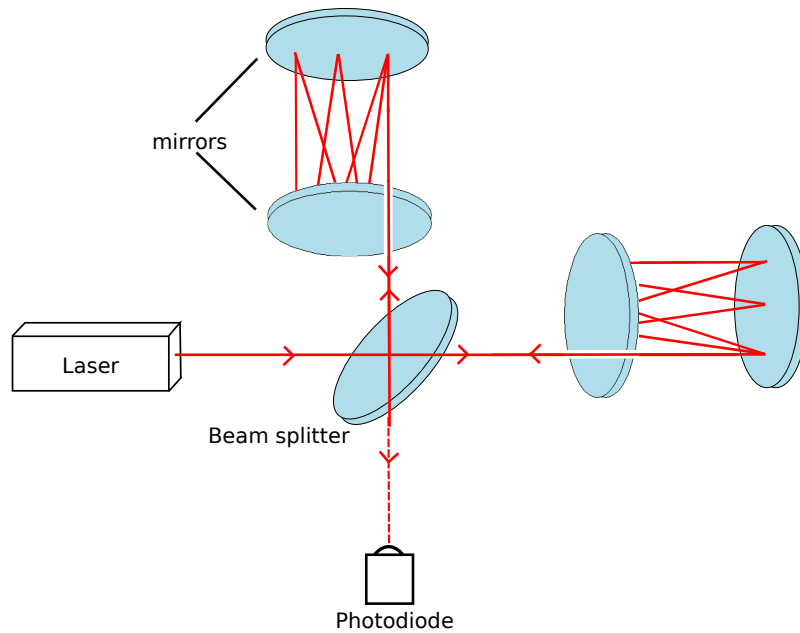


Figure 1.4.: A schematic diagram of an interferometer in a delay line, input mirror, configuration. Here the optical path is extended through reflection against an input mirror.

A second method of increasing the arm lengths of the detector is by folding the arms such that the laser light reflects off a secondary mirror which is positioned at an angle to the end test mass, close to the beam splitter (see figure 1.5 for a schematic). The folded arm design was implemented in the GEO600 detector [46].

Fabry-Perot arm cavities

Detector sensitivity can also be improved through the use of Fabry-Perot cavities, a technique developed in Glasgow in the 1980's [73]. This technique was used in the LIGO [44] and Virgo [45] detectors and was also used by the TAMA detector [47].

In a Fabry-Perot cavity the interferometer arms contain partially transmissive mirrors placed close to the beam splitter which are oriented to face the highly reflective end test masses. The laser light enters the interferometer cavity through a partially transmissive mirror and is reflected back and forth between this and the end test mass. The beams

1. Gravitational Wave Detection

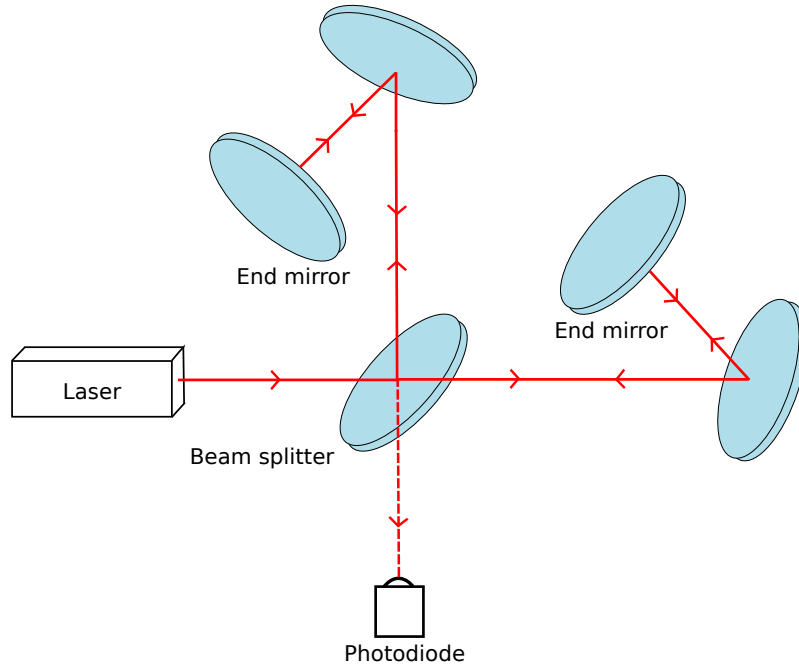


Figure 1.5.: A diagram of an interferometer in a delay line, folded arm, configuration. Here the optical path is extended by additional mirrors at an angle.

in this configuration overlap, allowing for the use of smaller diameter mirrors than those needed in the delay line interferometer configuration.

One cavity is held at resonance by altering the frequency of the input laser light. The other cavity is held at resonance by appropriately amplifying and filtering a portion of the photodiode output and feeding this back to an actuator at the end test mass (see figure 1.6 for a schematic). This process extends the effective arm lengths of the interferometer and hence amplifies the phase change of the laser light caused by any passing gravitational wave. Sophisticated control systems are required in this configuration in order to align, with precision, the mirror orientations and cavity lengths.

Power recycling

Power recycling is a technique used to increase the input laser power from an interferometric gravitational wave detector [74, 75]. A power recycled interferometer is operated

1. Gravitational Wave Detection

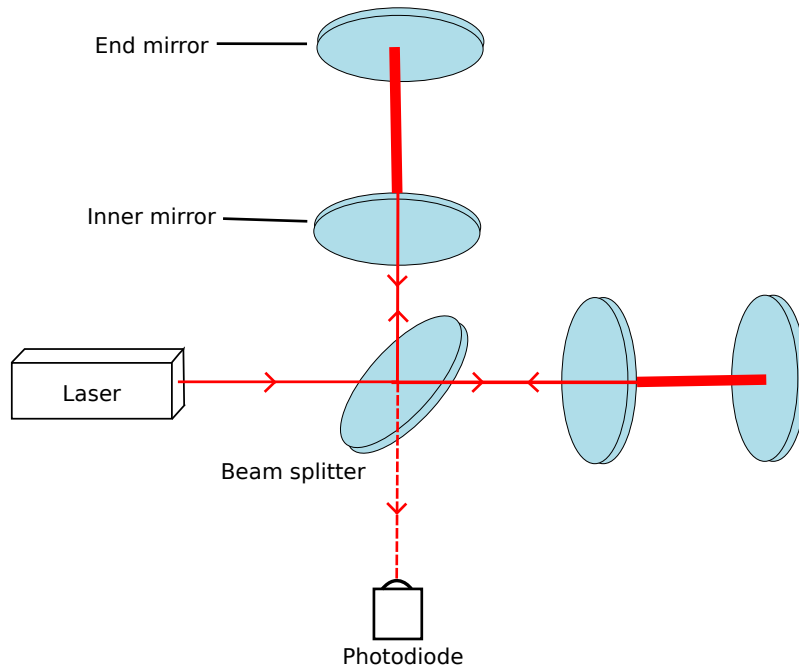


Figure 1.6.: A schematic diagram of an interferometer with Fabry-Perot cavities. Here the optical path is extended through repeated reflections between an intermediate, partially reflective mirror and the highly reflective end test mass.

on a dark fringe, i.e. with the mirrors oriented such that most of the light is directed back towards the laser. A partially transmissive mirror is then placed between the laser and the beam splitter (see figure 1.7 for a schematic). This mirror leads to a cavity forming with the interferometer. The light which is transmitted through the beam-splitter, when traveling back towards the laser, is reflected and is “recycled”. This increases the stored laser power within the interferometer and this in turn increases the sensitivity (see section 1.5.2). Power recycling is used by GEO600, aLIGO and Virgo.

Signal recycling

Signal recycling is a similar technique, in concept, to power recycling. A partially transmissive mirror is placed between the beam splitter and the photodiode to recycle the signal light (see figure 1.8 for a diagram) [76]. To get best sensitivity, gravitational wave interferometers are operated at a dark fringe with a gravitational wave altering the arm lengths such that a small amount of light is directed towards the photodiode. The signal

1. Gravitational Wave Detection

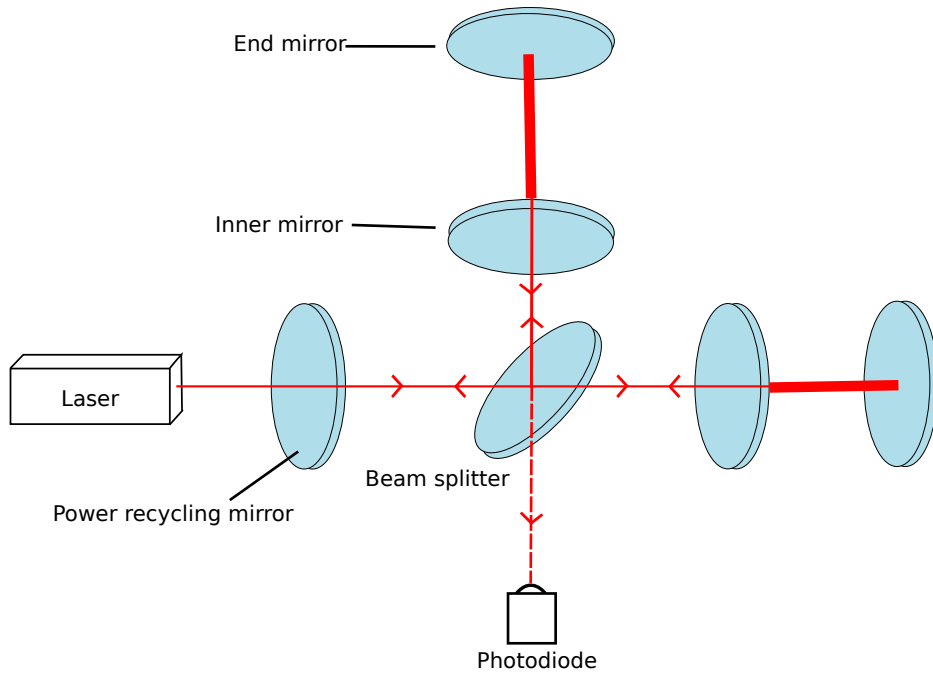


Figure 1.7.: A schematic diagram of a Michelson interferometer with Fabry-Perot cavities and a power recycling mirror.

recycling mirror forms a cavity with the interferometer, amplifying the signal light. This has the added advantage of allowing the peak frequency sensitivity of the detector to be altered by careful placement of the signal recycling mirror. Hence, the detector can be altered to be more sensitive to detecting gravitational waves from specific sources.

1.5.2. Noise limits of interferometric devices

There are a variety of noise sources that can limit the sensitivity of an interferometric gravitational wave detector. These include seismic noise, thermal noise, shot noise and radiation pressure noise and gravitational gradient noise, among others [77, 78]. Reduction of the effect of these noise sources is necessary to increase detector sensitivity.

1. Gravitational Wave Detection

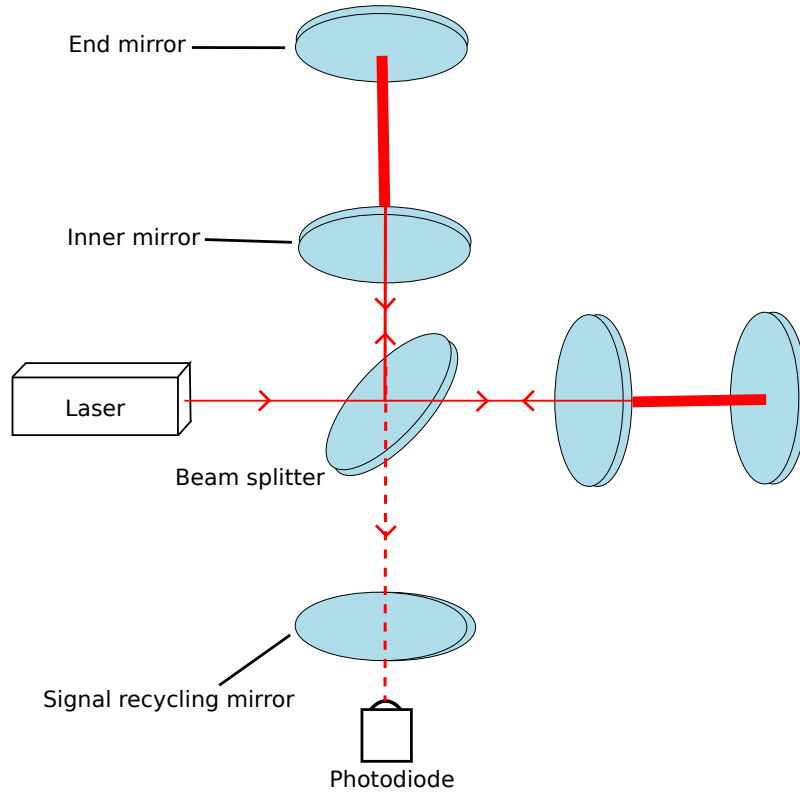


Figure 1.8.: A schematic diagram of a Michelson interferometer with Fabry-Perot cavities and a signal recycling mirror.

Seismic noise

Vibrations of the Earth's surface form a source of seismic noise. These vibrations stem from a range of phenomena, from traffic movements to ocean waves breaking on the shore. The source of the noise and hence its frequency dependence vary according to the time of day. Some areas on the Earth are more susceptible to certain kinds of seismic noise than others. For relatively quiet locations, the seismic noise is $\sim 10^{-7} \times f^{-2} \text{ m}/\sqrt{\text{Hz}}$ [79]. For a gravitational wave to be detected the maximum displacement of each test mass must be $< 3 \times 10^{-20} \text{ m}/\sqrt{\text{Hz}}$ in all three directions for a frequency of 30 Hz [79]. If this requirement is to be met seismic noise in the horizontal direction must be reduced by a factor of 10^9 [79]. Since noise in the vertical directions can couple to the horizontal axis (due the Earth's curvature) seismic isolation must be applied in all three directions.

1. Gravitational Wave Detection

Horizontal seismic noise can be limited by suspending the test masses as pendulums. This has the effect of attenuating the ground motion above the resonant frequency, f_0 , of the pendulum by $\sim f_0^2/f^2$ for a single stage pendulum [21]. The degree of ground motion attenuation increases with increasing pendulum stages. Vertical motion of the test masses can be limited through the use of cantilever springs [80].

Thermal noise

Thermal noise arises from the thermal motion of the atoms in the interferometer suspensions and test masses. As each atom has some thermal energy it also has some associated thermally driven motion. According to the equipartition theorem, the average energy of an atom is $\frac{1}{2}k_B T$ per degree of freedom, where k_B is Boltzmann's constant and T is the temperature of the system [21].

Brownian noise is a consequence of the random motion of atoms resulting in energy dissipation within the bulk of the material [81]. The effect of this noise type can be reduced by choosing low mechanical loss materials with which to construct the detector's suspensions and test masses. The detector sensitivity increases with reduced friction as this leads to reduced noise.

Thermoelastic noise is driven by statistical temperature fluctuations in the test masses and suspension elements on the small, local scale. These fluctuations cause the elements to expand or contract depending on the materials' thermal expansion coefficient.

Thermorefractive noise is caused by small local fluctuations in refractive index of the mirrors which is caused by local temperature fluctuations. These changes in refractive index alter the phase of the laser light passing through them. When light is involved, thermoelastic and thermorefractive noise together are called "thermo-optic" noise. [82].

1. Gravitational Wave Detection

The focus of this thesis has been to reduce thermal noise and to characterise the thermal noise performance of parts of the suspension systems. This is of particular interest for future detectors in which the suspensions and test masses will be manufactured out of silicon or sapphire. Detectors making use of these materials will be operated at cryogenic temperatures. Thermal noise is discussed in more detail in Chapter 2.

Photon shot noise

Photon shot noise (also called photoelectron shot noise) is the result of the distribution of photons being detected by the photodiode following Poisson statistics [83]. Additionally, photodiodes are not 100% efficient [84] so that some photons are not detected - this also leads to a Poisson effect in the photocurrent. Finally, vacuum fluctuations between the beam splitter and the photodiode cause an additional random effect which also contributes to this noise source [85]. This noise type is dominant at higher frequencies (on the order of a few hundred Hertz).

The light intensity reaching the photodetector is dependent on the gravitational wave amplitude. Shot noise is therefore a limiting factor to detector sensitivity. The limit set by shot noise in a Michelson-type interferometer is [21],

$$h_{\text{shot}}(f) = \left(\frac{1}{L}\right)\left(\frac{\hbar c \lambda}{2\pi P_{\text{in}}}\right)^{\frac{1}{2}} \quad (1.5)$$

where L is the interferometer arm length, \hbar is the reduced Planck's constant, c is the speed of light, λ is the laser wavelength and P_{in} is the laser power. From equation 1.5 it can be shown that photon shot noise can be reduced by increasing laser power.

1. Gravitational Wave Detection

One possible method of reducing the effect of shot noise is through “squeezing,” as proposed by Caves [86]. This technique involves operating the interferometer close to a dark fringe and improving certainty in one quadrature at the expense of the other, so for example the uncertainty in the amplitude quadrature may be reduced at the expense of increased uncertainty in the phase quadrature [86]. Squeezed states of light can be used to reduce the total quantum noise in the detector, hence beating the “standard quantum limit” - the minimum level of quantum noise that may be obtained without the use of squeezed states. This technique was first used on a long-baseline gravitational wave detector in the GEO600 instrument [87].

Radiation pressure noise

Radiation pressure is caused by photons interacting with the suspended test masses and transferring momentum to the masses as they are reflected, hence applying a force to the mirror. As discussed above, there are fluctuations in the number of photons being emitted by the laser over a given time period. This leads to a fluctuation in the force applied to the mirror and hence the position of the mirror varies. This in turn leads to a phase change when the beams are recombined. The radiation pressure noise in a Michelson-type interferometer is given by [21],

$$h_{\text{rad}}(f) = \left(\frac{1}{mf^2L}\right)\left(\frac{\hbar P_{\text{in}}}{2\pi^3c\lambda}\right)^{\frac{1}{2}} \quad (1.6)$$

where m is the mass of the test mass, f is the gravitational wave frequency, L is the interferometer arm length, \hbar is the reduced Planck’s constant, P_{in} is the input laser power, c is the speed of light and λ is the laser wavelength. From equation 1.6 it can be seen that radiation pressure noise has the greatest effect at the lowest frequencies and that its effect increases with increasing laser power.

The standard quantum limit

Photon shot noise and radiation pressure noise can be combined in quadrature giving total optical readout noise. In a standard Michelson-type interferometer the noise types are not correlated. Since photon shot noise can be reduced by increasing laser power and radiation pressure noise can be reduced by reducing laser power an optimal power level exists such that noise is at a minimum. This occurs where $h_{\text{shot}}(f) = h_{\text{rad}}(f)$. This sensitivity limit is known as the standard quantum limit and is consistent with the Heisenberg Uncertainty Principle [83, 84].

Some interferometer configurations, such as Sagnac interferometers, introduce correlations between photon shot noise and radiation pressure noise. In such configurations it should be possible to achieve better sensitivities at specific frequencies than are found in simple Michelson interferometers [88].

Gravitational gradient noise

Gravitational gradient noise (also known as Newtonian noise or directly coupled seismic noise) results from the mirrors directly coupling to local fluctuations in the gravitational field caused by local motions of massive objects. This noise source typically affects detector performance at frequencies below 10 Hz [79]. The effects of this noise source can be reduced by building the detector underground, as is being done for KAGRA (previously known as the LCGT) [89] and is planned for the third generation detector, the Einstein Telescope (ET) [90]. An alternative option for significantly reducing gravitational gradient noise is to build a space-based detector. This is planned for the Laser Interferometric Space Antenna, LISA [69].

1.6. First generation interferometric detectors

A global network of ground-based laser interferometric gravitational wave detectors completed initial data runs in 2010. The Advanced LIGO systems then came back online in 2015 following upgrades. Shortly after, the Advanced LIGO detectors were successful in detecting gravitational waves. Advanced Virgo is still undergoing upgrades but is due to come online soon. In many cases the initial detectors were themselves based on the lessons learned through the building and operation of smaller, prototype detectors, sometimes with arm lengths of just a few meters. The initial detectors included the US LIGO detectors [40], the French-Italian Virgo detector [91], the UK-German GEO600 detector [92] and the Japanese TAMA detector [47].

1.6.1. LIGO

LIGO (the Laser Interferometric Gravitational-wave Observatory) was a set of US-based facilities initially consisting of three detectors, two of which were contained within the same vacuum system in Hanford, Washington State and the third at a separate site in Livingston, Louisiana. The two Hanford detectors had 2 km and 4 km arm lengths whilst the Livingston detector had 4 km arms. The first generation of these detectors utilised Fabry-Perot arm cavities and 10.7 kg fused silica test masses suspended on single loops of metal wire [40].

The fifth science run of these measurements (S5) was completed in 2007. During this a sensitivity of $2.5 \times 10^{-23} / \sqrt{\text{Hz}}$ at 150 Hz was achieved. Following this LIGO was upgraded to Enhanced LIGO with improvements including enhanced laser power, modified read out, an output mode cleaner and in-vacuum readout hardware [75].

1. Gravitational Wave Detection

In October 2010 the sixth science run (S6) was completed in conjunction with the Virgo+ detector. Following S6 the detectors were disassembled for installation and commissioning of the Advanced LIGO (aLIGO) detectors (see section 1.7.1).

1.6.2. Virgo

Virgo is a collaborative European project led by Italy and France. The Virgo interferometer has 3 km arms with Fabry-Perot cavities, located near Cascina, Italy. The Virgo mirrors are fused quartz and are suspended via a multi-stage pendulum system designed to reduce seismic noise. This allows improved sensitivities at lower frequencies (down to ~ 10 Hz). Virgo was completed in 2007 and took data for five months during LIGO's S5 science run - this period was Virgo's first science data taking period, known as VSR1.

Following VSR1 the Virgo hardware was upgraded and Virgo+ was built. This included an upgrade to the suspension systems to include a quasi-monolithic system as already featured in the GEO600 detector. This was later decommissioned for further upgrades that are needed for the Advanced Virgo detector.

1.6.3. GEO600

GEO600 is a UK-German detector based near Hannover, Germany. It has 600 m arm lengths and with a delay-line configuration. The use of advanced interferometric techniques such as power and signal recycling and a low mechanical loss, quasi-monolithic fused silica mirror suspension allow for high sensitivity in spite of the arm lengths being shorter than those used by the LIGO and Virgo detectors[46]. As such GEO600 has operated alongside LIGO and Virgo and, since 2002, has participated in four science

1. Gravitational Wave Detection

runs. Between science runs various upgrades and improvements have been made to the detector, resulting in the GEO-HF system (see figure 1.9 for a sensitivity curve).

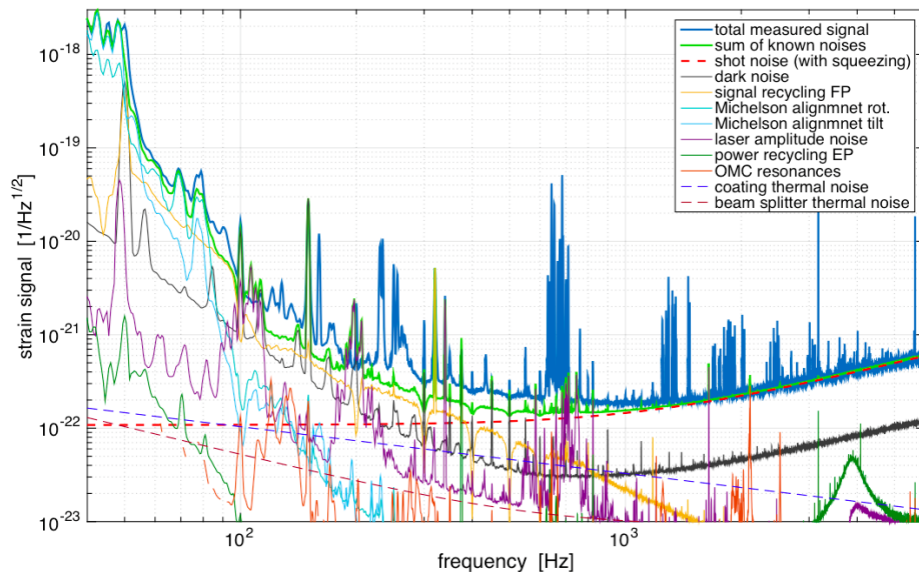


Figure 1.9.: The GEO noise budget and various noise contributions [93].

One of the technologies that was implemented in GEO600 is the use of squeezed light, originally proposed by Caves in 1981 [87, 86] (see section 1.5.2).

1.6.4. TAMA

TAMA was a detector based in Tokyo, Japan at the National Astronomical Observatory. It had 300 m arm lengths with Fabry-Perot cavities and power recycling as well as a multi-stage pendulum suspension system similar to that used in LIGO and Virgo. The pendulum system was developed in collaboration with LIGO and allowed improved sensitivities at lower frequency ranges (down to ~ 10 Hz) [94].

1.7. Current interferometric detectors and upgrades

To improve detector sensitivity a variety of hardware upgrades have been implemented in the LIGO detectors. Similar upgrades are also being carried out at the Virgo site.

In the case of Advanced LIGO sensitivity the design strain sensitivity is a factor of 10 better than Initial LIGO [9] and Advanced Virgo is likely to have a similar improvement in sensitivity. This increase in sensitivity, alongside the initial detections, has led to an increase the expected rate of detection from ~ 0.02 events per year for Initial LIGO, with a plausible range between 0.0002 and 0.2 per year, to up to ~ 40 events per year, with a plausible range between 0.4 and 400 per year [95, 30]. Most of these events are expected to be from coalescing compact binaries [30].

1.7.1. Advanced LIGO

Advanced LIGO (also called aLIGO) is the upgrade to the initial and enhanced LIGO detectors [96]. It consists of two 4 km detectors. The design strain sensitivity is a factor of 10 better than Initial LIGO at mid-frequencies [9] and the detection band has been extended down to close to ~ 10 Hz (see figure 1.10 for a sensitivity curve). The improvements made to achieve this involve the implementation of increased laser power, signal recycling mirrors, multistage pendulums and quasi-monolithic fused silica suspensions, as tested in GEO 600 [96].

The upgrades to the suspension systems featured heavier test masses, 40 kg rather than 10.7 kg [99, 100]. These test masses have flat sections to which fused silica attachment pieces, or “ears”, are joined using the hydroxide catalysis bonding technique (see Chapter 3, sections 3.1 and 3.1.1 for more details on this). The ears feature weld horns for

1. Gravitational Wave Detection

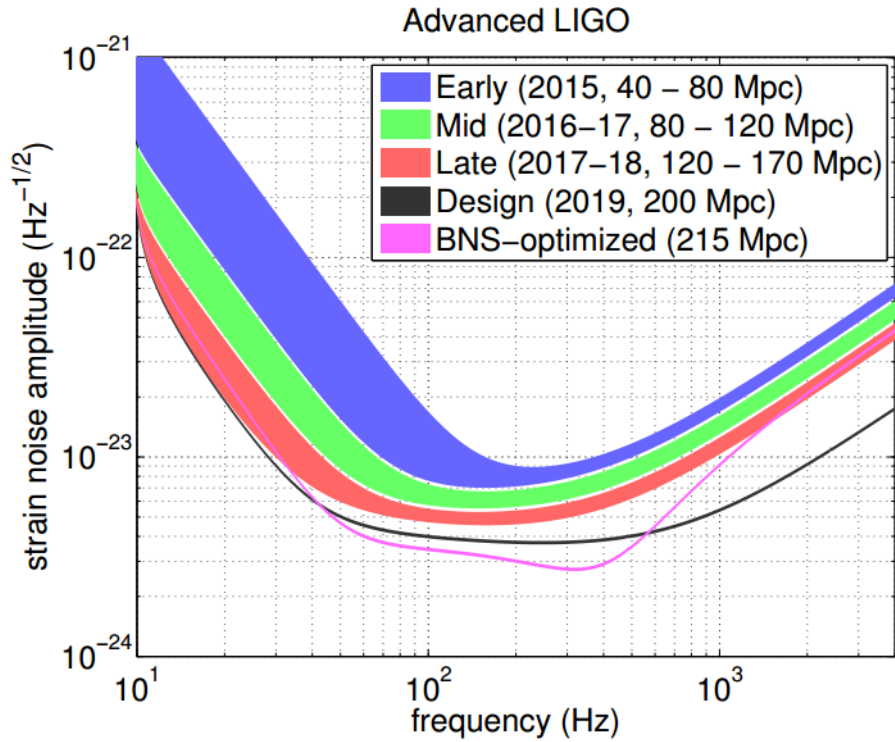


Figure 1.10.: Advanced LIGO design strain sensitivity as a function of frequency. The current strain sensitivity is shown alongside expected improvements in sensitivity over time [97].

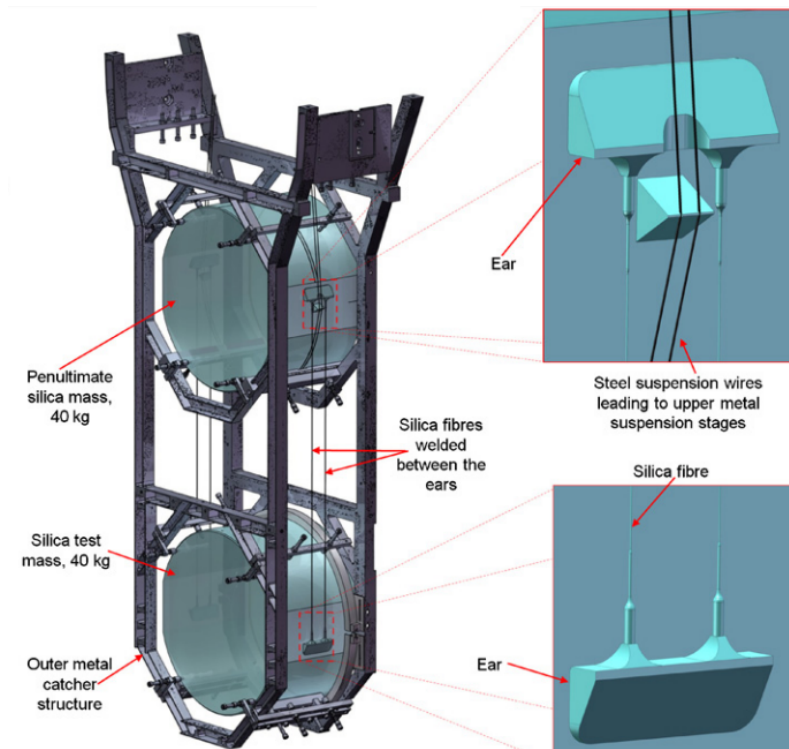


Figure 1.11.: A diagram of the Advanced LIGO quasi-monolithic fused silica suspension design [98].

1. Gravitational Wave Detection

connecting to the fused silica fibres [101, 98], which allowed more control over the location of the weld points. Figure 1.11 shows a diagram of the aLIGO suspension design.

Shortly after the upgrades for aLIGO were completed, the first direct detection of gravitational waves was achieved on 14th September 2015. The event, GW150914, was caused by a black hole binary merger and was detected by both the Hanford and Louisiana detectors. Figure 1.12 shows the coincident signal as observed by the aLIGO detectors.

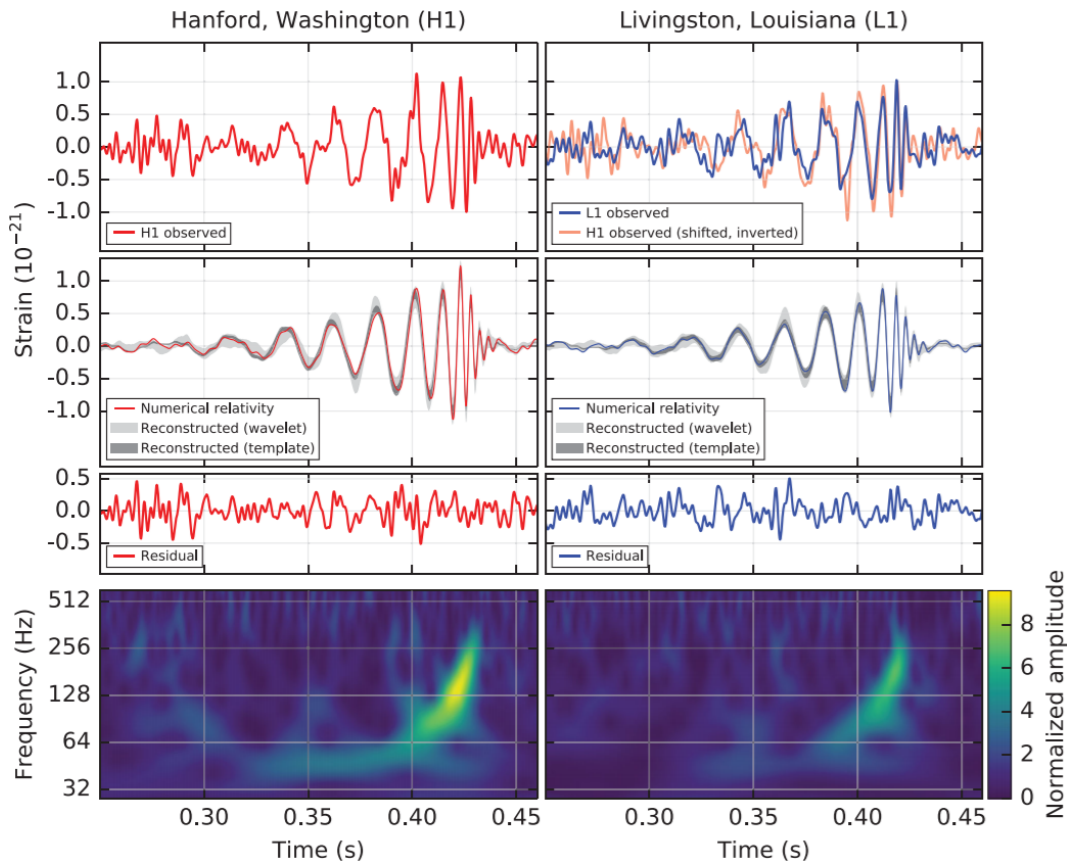


Figure 1.12.: The gravitational wave event GW150914 as observed by the LIGO Hanford (H1, left column panels) and Livingston (L1, right column panels) detectors. Times are shown relative to 14th September 2015 at 09:50:45 UTC. *First row*: Strain. *Second row*: Gravitational wave strain projected onto each detector in the 35-350 Hz band. *Third row*: Residuals after subtracting the filtered numerical relativity waveform from the filtered detector time series. *Fourth row*: A time frequency representation of the strain data, showing the signal frequency increasing over time. See [4] for more details about this plot and the GW150914 event.

1.7.2. Advanced Virgo

Advanced Virgo is the upgrade to initial Virgo and Virgo+ [102]. This upgrade is intended to increase the sensitivity of the Virgo detector by a factor of ~ 10 . This improvement will be achieved by increasing the mirror mass and the input power and implementing higher finesse arm cavities [103].

1.7.3. GEO-HF

As the GEO600 detector has 600 m arms and as this is shorter than the arm lengths of the LIGO and Virgo detectors, it is more difficult to implement upgrades to GEO that allow it to remain competitive in sensitivity [104]. Instead, the upgrades to GEO improved sensitivity in the high frequency (kHz) regime whilst also allowing for the interferometer to be tuned into lower frequencies to operate in “astrowatch mode” whenever the other detectors are offline.

The upgrades made to GEO, leading to this increased sensitivity at high frequencies, include methods for avoiding limitations imposed by the standard quantum limit and increased laser power [104].

1.7.4. KAGRA

KAGRA is a Japanese detector that, in its final form, will be based on the use of sapphire test masses and suspensions at cryogenic temperatures [105]. This detector is being built underground and the initial stage (iKAGRA), which has already been completed, will operate at room temperature, using fused silica test masses and suspensions [18]. Later

upgrades to the detector will allow it to be run at 20 K (bKAGRA) to reduce the effects of thermal noise [18]. An initial, basic Michelson version of bKAGRA will be operational in 2018, with improvements being implemented in the following years [17, 18].

The use of sapphire rather than fused silica for the KAGRA test masses and suspensions is designed to take advantage of sapphire's more favourable thermal noise performance at low temperatures (fused silica has a large, broad loss peak centred around 40 K) [106]. Much of the focus of this thesis is on hydroxide catalysis bonding of sapphire to allow the assembly of sapphire-based suspension systems intended for cryogenic operation.

1.8. Next generation detectors

The Advanced LIGO, Advanced Virgo and GEO-HF upgrades constitute the second generation of interferometric detectors. This second generation has been proven to have sufficient sensitivity to be able to detect gravitational waves from binary black hole coalescences. The first detection occurred shortly after the upgraded LIGO detectors were able to start taking data and a second detection occurred ~ 3 months later.

Following these detections it is imperative that further improvements to sensitivity be made in order to detect less energetic events and to allow precision astrophysical measurements to be carried out on the detected sources. Concepts concerning the third generation of detectors are in development in preparation for this.

There is the potential to increase the expected number of observations from ~ 40 per year for the Advanced LIGO detectors [90] up to on the order of millions per year for the next generation of detectors [90]. Further increases to sensitivity present new challenges, especially in the form of reductions to the contributions of thermal noise of the test masses

1. Gravitational Wave Detection

(and their coatings) and the suspension elements. One option which may allow this reduction in thermal noise is for third generation detectors to be operated at cryogenic temperatures [90, 89], however the move to cryogenic detectors will also present new challenges aside from the need to find suitable materials; the use of suitable systems for cooling the test masses, methods of heat extraction and an appropriate choice of laser are all important areas of concern [90].

Taking the KAGRA detector as an example and given its intended operating temperature of 20 K, the laser power will be limited by the amount of absorbed heat that can be extracted via the suspension fibres and the geometry of the fibres has been chosen with heat extraction in mind [107]. Cryocoolers will be used to bring the test masses down to 20 K [107]. The use of sapphire and silicon as materials for cryogenic gravitational wave detectors, and what this will mean for thermal noise contributions, is explored within this thesis.

1.8.1. The Einstein Telescope

One of the planned detectors is the Einstein Telescope (ET). This will feature three interferometers with 10 km arm lengths [90]. Two of these interferometers will be operated at cryogenic temperatures [90]. A design study for this detector system has been developed by teams including GEO600 and Virgo and this will be a new European detector [90]. It is likely that the test masses will be fabricated out of silicon and studies are underway to assess the suitability of silicon for this detector. Should silicon prove unsuitable, sapphire is a second option.

Silicon and sapphire bonding for suspension elements is currently under study and experiments in this area make up the focus of this thesis.

1.8.2. Space-based detectors

LISA, the Laser Interferometric Space Antenna, is a proposed space-based gravitational wave detector [69]. As a space-based detector it would not be subject to seismic noise and the effects of gravitational gradient noise would be much reduced. This allows sensitivity in frequency ranges impossible for Earth-based detectors. Additionally, the arm lengths are not limited by the Earth's curvature.

The exact configuration of the LISA mission is under review and will be informed by the results of the LISA pathfinder mission which was launched in late 2015 [108, 109]. LISA Pathfinder is a proof-of-concept mission dedicated to demonstrating the measurement of the position of test masses in free-fall at a level that would be required for a space-based interferometric gravitational wave detector such as LISA [108]. The LISA Pathfinder mission was announced as successful in June 2016, with a sensitivity two orders of magnitude better than requirements for LISA Pathfinder; this level of performance is consistent with that which would be required for the full LISA mission [108].

LISA has been chosen by ESA as an L3 mission and is due for launch in ~ 2034 [110].

1.9. Conclusions

In the previous 60 years the sensitivity of gravitational wave detectors has been improved by 6 orders of magnitude. A global network of interferometric detectors has been developed, built and upgraded. Rigorous and extended science runs have been carried out, allowing upper limits to be set on the strength of gravitational waves from a variety of sources. The first detections have been achieved and it is likely that this will now usher in a new era of observational astrophysics, allowing the discovery of new phenomena within

1. Gravitational Wave Detection

the Universe - phenomena unlikely to be discovered any other way.

While upgrades to detectors have already led to the first detections, further upgrades will be necessary. In particular, the effect of various noise sources must be reduced or avoided. In order for significant improvements to be made thermal noise must be further limited. This is the main focus of the work presented in this thesis.

2. Thermal Noise

2.1. Introduction

Thermal noise is a limiting factor in the sensitivity of interferometric gravitational wave detectors and arises from Brownian motion and temperature fluctuations within the test masses and suspension elements. It limits the performance of any Michelson-type interferometric gravitational wave detector. For example, in the case of the Advanced LIGO detectors, thermal noise limits the design sensitivity between ~ 10 -100 Hz [111]. Thermal noise is generally associated with the test mass substrates, coatings and suspensions, and these are carefully designed to minimise thermal noise as far as possible.

The sources of thermal noise can be divided into two major categories. The first of these is often termed “Brownian noise” and is caused by internal friction in a material (see sections 2.1.1 and 2.1.2 and the references therein). The second is thermoelastic noise and results from the effect of statistical temperature fluctuations in a material causing heat flow (and energy loss [106]).

2.1.1. Brownian motion

Brownian motion is random motion, originally observed by Robert Brown, in the form of pollen and dust particles moving in water [112]. Later, Einstein demonstrated that this motion was due to stochastic fluctuations in the rate at which impacts between the pollen particles and the water molecules occurred, i.e. the motion was due to the fluid surrounding the pollen, and not due to the pollen itself [81].

In a larger body the thermal motion of the atoms or molecules becomes correlated and thermal physics indicates that for a resonant system the thermal energy is $1/2k_B T$ per degree of freedom [21], where k_B is the Boltzmann constant and T is the temperature. The frequency spectrum of the thermal motion is dependent on the mechanical loss of the system and can be obtained by application of the fluctuation dissipation theorem [21].

2.1.2. The fluctuation dissipation theorem

The relationship between energy imparted and energy dissipated within a system was initially considered by Einstein was later developed further by Callen *et al* into the Fluctuation Dissipation Theorem [113, 114, 21]. This theorem describes the relationship between the excitation of a system (i.e. fluctuation) and the frictional mechanisms by which the excitation is damped (i.e. dissipation).

For a linear system, the equation of motion in the frequency domain can be written in terms of an external force, $F_{\text{ext}}(f)$, necessary to cause the system to move with a sinusoidal velocity of amplitude $v(f)$:

$$F_{\text{ext}}(f) = Z(f)v(f) \tag{2.1}$$

2. Thermal Noise

where the function $Z(f)$ is the mechanical impedance of the system. The reciprocal of the impedance is the admittance; $Y(f) \equiv 1/Z(f)$. The Fluctuation-Dissipation Theorem states that the power spectral density, $F_{\text{therm}}^2(f)$, of the fluctuating force is given by [21]:

$$F_{\text{therm}}^2 = 4k_B T \Re(Z(f)) \quad (2.2)$$

where $\Re(Z)$ is the real (i.e. dissipative) part of the impedance and the power spectrum, x_{therm}^2 , of the system's fluctuating motion can be given as:

$$x_{\text{therm}}^2(f) = \frac{k_B}{\pi^2 f^2} T \Re[Y(f)] \quad (2.3)$$

Taking a gas damped pendulum of resonant angular frequency ω_0 as an example, the equation of motion of the system, neglecting the fluctuating force, can be written as:

$$F_{\text{ext}} = m\ddot{x} + b\dot{x} + kx \quad (2.4)$$

where F_{ext} is a force applied to the system, k represents the spring constant of the pendulum ($m\omega_0^2$), b is the damping coefficient and x , \dot{x} and \ddot{x} are the position, velocity and acceleration respectively.

The external force, F_{ext} , needed for a given velocity, \dot{x} , can be determined by expressing all of the forces in the frequency domain and writing each in terms of velocity,

$$\dot{x} = i\omega x \quad \text{and} \quad \ddot{x} = i\omega \dot{x} \quad (2.5)$$

2. Thermal Noise

The impedance, $Z \equiv F_{\text{ext}}/\dot{x}$, can then be given by

$$Z \equiv b + i\omega m - \frac{ik}{\omega} \quad (2.6)$$

Using equation 2.6, the admittance of the system, $Y(f) \equiv Z^{-1}(f)$, becomes:

$$Y(f) = \frac{1}{b + i\omega m - \frac{ik}{\omega}} \quad (2.7)$$

By multiplying both the numerator and the denominator by $b - i\omega m + \frac{ik}{\omega}$, in order to rationalise the denominator, equation 2.7 becomes

$$Y(f) = \frac{b - i\omega m + \frac{ik}{\omega}}{b^2 + (\omega m - \frac{k}{\omega})^2} \quad (2.8)$$

This allows the real part of the admittance to be determined. Equation 2.3 then becomes,

$$x_{\text{therm}}^2(f) = \frac{k_B T b}{\omega^2 (b^2 + (\omega m - \frac{k}{\omega})^2)} \quad (2.9)$$

By noting that $k = \omega_0^2 m$,

$$x_{\text{therm}}^2(f) = \frac{k_B T}{\omega^2} \frac{b}{b^2 + (\omega m - \frac{\omega_0^2 m}{\omega})^2} = \frac{k_B T}{\omega^2} \frac{b}{b^2 + (\frac{\omega^2 m - \omega_0^2 m}{\omega})^2} \quad (2.10)$$

2. Thermal Noise

Finally, this simplifies to give,

$$x_{\text{therm}}^2(f) = \frac{k_B T b}{\omega^2 b^2 + (\omega^2 - \omega_0^2)^2 m^2} \quad (2.11)$$

providing an expression for the thermal noise power spectral density of an oscillator of resonant frequency ω_0 , in terms of its mass and damping coefficient.

2.2. Sources of dissipation

Sources of dissipation are categorised into two types: external sources of dissipation and internal sources of dissipation.

2.2.1. External sources of dissipation

There are a number of external sources of noise which could contribute to the thermal noise of a gravitational wave suspension system. These include,

- Gas damping: Residual gas molecules collide with suspension elements leading to a viscous damping effect [115]
- Frictional loss: Friction occurs at the contact points of suspension elements and test masses (also known as “stick-slip” losses) [116]
- Recoil damping: Energy is dissipated from the suspension elements into the support structure [115]

2. Thermal Noise

In order to minimise thermal noise these, and any other potential sources of noise, should be minimised as far as possible in the frequency range of interest.

2.2.2. Internal sources of dissipation

Once external sources of dissipation are minimised, the damping and thermal noise associated with the internal friction of the materials of choice for the test masses and their support fibres can be considered.

Internal damping exists in all anelastic materials. Ideal elastic materials obey Hooke's law (equation 2.12), which defines the relationship between force, F_{spr} , and a small displacement, x ; the amount by which a spring extends from its initial length.

$$F_{\text{spr}} = kx \quad (2.12)$$

A generalisation of Hooke's law gives the relationship between stress, σ , and strain, ϵ , such that $\sigma = \epsilon Y$, where Y is the Young's modulus. Since the strain is not created instantly in real, anelastic materials and such materials will continue to stretch after a stress is removed, it is clear that the strain must lag the stress. Through this process energy is dissipated.

Consider a periodic stress, σ , is given by,

$$\sigma = \sigma_0 e^{i\omega t} \quad (2.13)$$

2. Thermal Noise

Where σ_0 is amplitude of the stress and ω is the angular frequency of the oscillation which is applied to the anelastic material. As a result of this periodic stress, a periodic strain, ϵ , will arise such that,

$$\epsilon = \epsilon_0 e^{i(\omega t - \phi)} \quad (2.14)$$

Where $\epsilon_0 = \frac{\sigma_0}{Y}$ and ϕ is the loss angle, the angle by which the strain lags the stress. The loss angle is related to the anelastic material's internal friction. It is a measure of the energy dissipated in each cycle of oscillation.

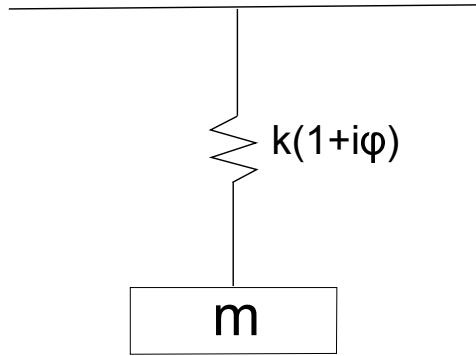


Figure 2.1.: A schematic diagram of a mechanical oscillator with a complex spring constant, $k(1 + i\phi)$.

Considering a modified version of Hooke's law with a complex spring constant (see figure 2.1) the time delay between the applied periodic stress and the resultant periodic strain can be found. Equation 2.12 becomes,

$$F_{\text{spr}} = k(1 + i\phi(f))x \quad (2.15)$$

Since, from equation 2.4, $F_{\text{ext}} = m\ddot{x} + b\dot{x} + kx$, this can then be rearranged to give $F_{\text{ext}} = m\ddot{x} + k(x + \frac{b}{k}\dot{x})$. Then, since from equation 2.5, $\dot{x} = i\omega x$, this can be substituted in to give an equation of the form, $F_{\text{ext}} = m\ddot{x} + k(x + \frac{ib}{k}\omega x)$, which then simplifies to,

2. Thermal Noise

$$F_{\text{ext}} = m\ddot{x} + k\left(1 + \frac{i\omega b}{k}\right)x \quad (2.16)$$

Hence, comparing equation 2.15 and equation 2.16 it can be seen that,

$$\phi \equiv \frac{\omega b}{k} = \frac{\omega b}{m\omega_0^2} \quad (2.17)$$

Here, $\phi(\omega)$ represents the degree of anelasticity of the spring and hence the damping present due to the internal friction of the spring material.

When considering a suspended mirror system such as those in interferometric gravitational wave detectors, the suspended mirrors can be modeled as harmonic oscillators with internal damping. The equation of motion for such a system can be written as,

$$m\ddot{x} = -k(1 + i\phi(f))x + F_{\text{ext}} \quad (2.18)$$

Using equation 2.5 leads to,

$$F_{\text{ext}} = i\omega m\dot{x} + \frac{k}{i\omega}(1 + i\phi(f))\dot{x} \quad (2.19)$$

Since the impedance, $Z \equiv \frac{F_{\text{ext}}}{\dot{x}}$, this is given by,

$$Z = \frac{k - \omega^2 m + ik\phi(f)}{i\omega} \quad (2.20)$$

2. Thermal Noise

Then, since the admittance, Y , is given by, $Y = 1/Z_{\text{ext}}$ this can be given as,

$$Y = \frac{i\omega}{k - \omega^2 m + ik\phi(f)} \quad (2.21)$$

By rationalising the denominator, equation 2.21 can be re-written as,

$$Y = \frac{\omega k \phi(f) + i(\omega k - \omega^3 m)}{(k - m\omega^2)^2 + k^2 \phi^2(f)} \quad (2.22)$$

Then, the real part of equation 2.22 is given by,

$$\mathbb{R}[Y] = \frac{\omega k \phi(f)}{(k - m\omega^2)^2 + k^2 \phi^2(f)} \quad (2.23)$$

From equation 2.9 and $k = \omega_0^2 m$ it can be seen that,

$$x_{\text{therm}}^2(f) = \frac{4k_B T \omega_0^2 \phi(f)}{m\omega[\phi^2(f)\omega_0^4 + (\omega_0^2 - \omega^2)^2]} \quad (2.24)$$

2.3. Thermal noise associated with a single resonant mode

In any mechanical system there will exist several resonant modes which may be excited. In terms of the mirror suspension system for a gravitational wave detector this will include the pendulum modes of the suspension (which occur at low frequencies, below

2. Thermal Noise

the detection band of the interferometer), the violin modes of the suspension fibres (which tend to lie within the detection band) and the internal modes of the test mass mirror (which lie above the detection band). For the pendulum and internal mirror modes, the off-resonance thermal noise may limit the sensitivity of the detector.

If a low loss suspension material is selected for the test masses and suspension elements then the mechanical loss of the system can be reduced. Thermal noise from the violin modes of the suspension can be effectively confined into a narrow frequency range centred on the resonant frequencies. This then leads to narrower and higher thermal noise peaks at the violin mode frequencies and overall lower off-resonance thermal noise. These sharp noise peaks can then be filtered from the interferometer signal without significantly reducing the detector's useful bandwidth.

Equation 2.24 can be simplified by considering in turn the thermal noise contribution in each of the three frequency ranges of interest: below the resonance peak, at the resonance peak and above the resonance peak.

Far below the resonance, $\omega \ll \omega_0$ and hence equation 2.24 can be approximated to,

$$x_{\text{therm}}^2(f) \approx \frac{4k_B T \omega_0^2 \phi(f)}{m\omega[\phi^2(f)\omega_0^4 + \omega_0^4]} = \frac{4k_B T \phi(f)}{m\omega\omega_0^2[\phi^2(f) + 1]} \quad (2.25)$$

Above the resonance, $\omega \gg \omega_0$ and hence equation 2.24 can be approximated to,

$$x_{\text{therm}}^2(f) \approx \frac{4k_B T \omega_0^2 \phi(f)}{m\omega^5} \quad (2.26)$$

Within the detection band, $\omega \approx \omega_0$ and equation 2.24 can be approximated to,

2. Thermal Noise

$$x_{\text{therm}}^2 \approx \frac{4k_B T \omega_0^2 \phi(f)}{m \omega_0 [\phi^2(f) \omega_0^4]} = \frac{4k_B T}{m \omega_0^3 \phi(f)} \quad (2.27)$$

Further, if a low loss material is chosen then $\phi(f) \ll 1$, from equation 2.25, the thermal noise in the detection band of the internal modes can then be approximated to,

$$x_{\text{therm}}^2(f) \approx \frac{4k_B T \phi(f)}{m \omega \omega_0^2} \quad (2.28)$$

Additionally, the contribution from the violin modes of the suspension fibres can be approximated to [117],

$$x_{\text{therm}}^2(f) \approx \frac{4k_B T}{m_{\text{fibre}} \omega_0^3 \phi(f_0)} \quad (2.29)$$

From equation 2.26 and 2.28 it is clear that the thermal noise power spectral density due to resonance far from the detection band is directly proportional to the mechanical loss, $\phi(\omega)$. As a result, the off-resonance thermal noise for the system can be reduced for such modes if a low loss material is chosen for the mirror and suspension elements.

However, from equation 2.29 it can be seen that when a resonant mode is within the detector band, the power spectral density of thermal noise close in frequency to the resonance is inversely proportional to the mechanical loss.

2.3.1. The loss factor

The loss factor, ϕ , of a system is a dimensionless quantity measuring the dissipation of mechanical energy of an oscillator at a resonant frequency f_0 . It is also known as the loss angle as it is defined as the angle by which strain lags stress in an anelastic material. It represents the fraction of the total energy that is dissipated per cycle of oscillation. The loss factor is given by [118],

$$\phi(f) = \frac{E_{\text{dissipated}}}{2\pi E_{\text{stored}}} \quad (2.30)$$

At a resonant frequency ($f = f_0$) the mechanical loss angle is defined by $\phi = (1/Q(f_0))$ where Q is the quality factor. At frequencies away from resonant peaks, x_{therm}^2 is proportional to $\phi(f)$.

The integral over all frequencies of the displacement power spectrum is independent of the amount of energy dissipated (or the mechanical loss). If the mechanical loss is reduced in the test masses and suspensions, the thermal noise displacement spectral density away from the resonant peaks will also be reduced. However, this also results in an increase in the thermal noise spectral density at the resonant peaks.

2.4. Thermal noise in a multi-resonance system

In an interferometric gravitational wave detector, the total thermal displacement of the multiple resonant modes of the system will be detected as motion in the front face of the mirror. Due to the presence of areas of high loss (such as coatings) the true mechanical dissipation of a real mirror is spatially inhomogeneous and as such the total thermal noise cannot be calculated by simply summing the individual modes [119].

If a pressure with the same spatial profile as the sensing beam intensity is applied to the front face of the mirror substrate, the power spectral density of the thermal noise per cycle, S_x , can be described as [120, 119, 21],

$$S_x(f) = \frac{2k_B T W_{\text{diss}}}{\pi^2 f^2 F_0^2} \quad (2.31)$$

where $W_{\text{diss}} = 2\pi f \phi E_{\text{strain}}$ is the dissipated power when an oscillatory force with peak magnitude F_0 acts on the front face of the test mass mirror and E_{strain} is the energy of elastic deformation when the test mass is maximally contracted or extended due to that force [120].

If the loss is homogenous and the radius of the laser beam is much smaller than the radius of the test mass, the test mass can be modeled as being half-infinite. In this case the power spectral density of the Brownian thermal noise associated with the test mass substrate can be described as [120, 121, 119],

$$S_x(f) = \frac{2k_B T (1 - \sigma^2)}{\pi^{3/2} f Y r_0} \phi_{\text{substrate}}(f, T) \quad (2.32)$$

2. Thermal Noise

where $\phi_{\text{substrate}}(f)$ is the mechanical loss of the test mass, Y is the Young's modulus of the test mass material, σ is the Poisson's ratio, r_0 is the radius of the laser beam when the electric field has fallen to $1/e$ of the maximum beam amplitude [120].

2.4.1. The Arrhenius equation

Internal friction is influenced by the arrangement of molecules within a material. The time taken for an equilibrium strain to develop in response to a stress applied to the material is dependent on internal properties which are functions of stress. These properties include the density of point defects, dislocations, impurities and crystal grain boundaries. For a new state of stress to be adjusted to (so that a new equilibrium state may be reached) energy barriers of level ΔE must first be overcome. This results in an exponential relaxation to the new equilibrium value, with a characteristic time, τ , which, for a two-level system, tends to obey the Arrhenius equation [106, 122]):

$$\tau = \tau_0 e^{\Delta E/k_b T} \quad (2.33)$$

Here, τ_0 is the characteristic time between attempts at passing the energy barrier, ΔE . This characteristic time is useful in understanding the frequency dependence of damping, as will be discussed in the following section.

2.4.2. Debye theory

If a spring has one significant relaxation process with energy barrier ΔE , its dynamics can be represented as an undamped spring with a spring constant k_1 in parallel with

2. Thermal Noise

a Maxwell unit (a series combination of an undamped spring k_2 and a pure velocity damping dashpot, α). See figure 2.2 for a diagram of such a system.

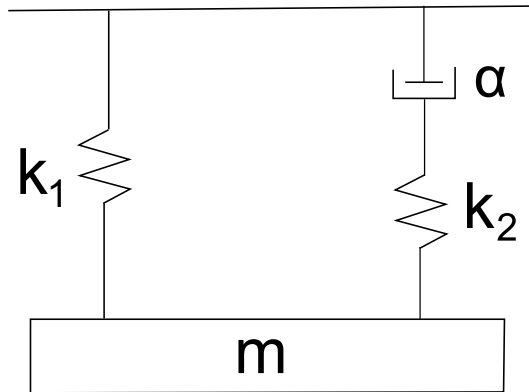


Figure 2.2.: A diagram of a typical anelastic solid with an ideal spring connecting in parallel with a Maxwell unit.

For such a model, the loss angle, ϕ with a characteristic frequency dependence is given by equation 2.34 [123].

$$\phi \approx \Delta \frac{\omega\tau}{1 + \omega^2\tau^2} \quad (2.34)$$

Where, $\Delta \equiv k_2/k_1$ is the “relaxation strength”, and $\tau = \alpha/k_2$ is the “relaxation time”. The Debye peak is the peak in the dissipation at frequency $\omega_{\text{peak}} = \tau^{-1}$.

Internal friction is generally independent of frequency [21, 124, 125, 126]. This is understood to be consistent with the Debye Peak having a characteristic frequency because a material may have several Debye peaks at frequencies separated by a few orders of magnitude; at frequencies away from these peaks the combined effects of the tails of the peaks is effectively constant with frequency.

2.5. Thermal noise in a gravitational wave detector

2.5.1. Coating thermal noise

Equation 2.31 demonstrates that when a laser is incident on the front surface of a test mass mirror, the level of thermal noise is related to the power dissipated in the test mass when an oscillating pressure is applied to its surface. The amount of power dissipated is proportional to both the elastic energy associated with the deformations caused by this pressure and to the mechanical loss [119, 127].

Most of this deformation will occur at, or close to, the footprint of the laser incident on the test mass. Hence, any dissipation source within this region will contribute more to the total thermal noise read out by the laser beam than an identical source would if it were situated further away.

In the case of a fused silica system of test masses and suspensions, such as those used in the Advanced LIGO detectors, the multilayer dielectric coatings on the surfaces of the test masses have dissipation of approximately 2×10^{-4} [128, 129, 130, 129]. This is in contrast to the fused silica substrate itself, which has a dissipation of approximately $\sim 1 \times 10^{-9}$ [131]. Hence the thermal noise arising due to the effect of the coatings will be the dominant effect when compared to the thermal noise due to the substrates.

Suspension thermal noise

The violin and pendulum modes of the suspensions both contribute to the thermal noise of the detector (see section 2.4 for more details). These sources arise from the pendulum suspension of the mirror used in interferometric detector designs, as shown in figure 2.3.

2. Thermal Noise

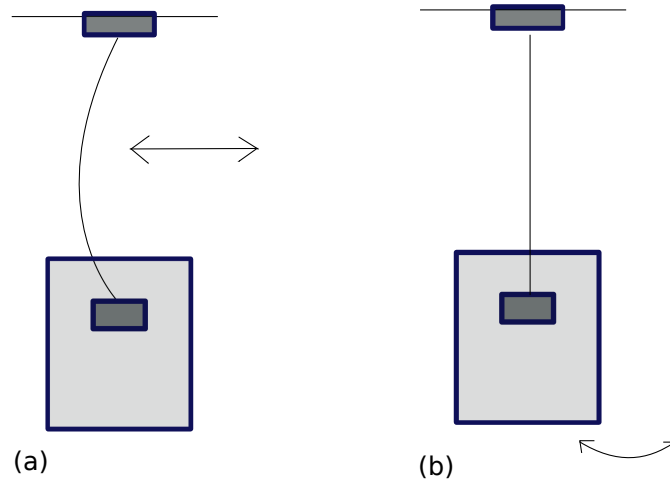


Figure 2.3.: Simplified diagram of (a) the fundamental violin mode and (b) the pendulum mode of a suspended test mass.

The loss factor of the pendulum is lower than that of the material used in the suspension fibres. The majority of a pendulum’s energy is stored as gravitational potential energy through the Earth’s gravitational field, which is lossless, and only a small fraction of the total energy stored in the flexing of the suspension fibres can be dissipated. This is known as the “dilution” effect. Equation 2.35 describes the mechanical loss for a pendulum,

$$\phi_{\text{pendulum}} = \phi_{\text{fibre}} \frac{E_{\text{flex}}}{E_{\text{grav}}} \quad (2.35)$$

The loss associated with the violin mode is likewise reduced from the intrinsic loss of the material by a dilution factor. The loss of the suspension fibre may be assumed to be spatially homogeneous and the rocking mode of the pendulum can be assumed to be constrained, hence the loss of the first violin mode is twice that of the pendulum mode [132, 133]. The thermal displacement of the violin mode couples to the thermal displacement of the test mass with a suppression factor of the ratio of the mass of the pendulum and fibre; $\frac{m}{m_{\text{fibre}}}$ [132].

Section 2.3 contains details of the thermal noise contributions of the pendulum and violin modes in equations 2.28 and 2.29, respectively. The attachment points or “ears” which

2. Thermal Noise

provide the interface between the test masses and the suspension fibres constitute a further contributor to the total thermal noise of the system. These “ears” are attached to the sides of the test masses via hydroxide catalysis bonding. Depending on the suspension design the fibres may be either welded to the ears (as in Advanced LIGO [9]) or the ears may have slots so that the fibres may slot into them and be held in place by “nail-heads” (such as in the KAGRA suspensions [18]).

2.5.2. Bond loss

The method for attaching suspension fibres to the test masses must be low loss in order to avoid degrading the pendulum mode loss factors [134]. Hydroxide catalysis bonding has been demonstrated to be a low loss and high strength technique for joining suspension elements in fused silica [135, 136], and silicon [137] suspensions.

Investigations have been made into the the mechanical loss of hydroxide-catalysis bonds between both silica and sapphire and these bonds have now been used in the GEO600 detector (see section 1.6.3), the advanced LIGO detectors (see section 1.7.1) and the advanced Virgo detector (see section 1.7.2). In all of these, fused silica “ears” are bonded onto the side of the test masses to provide an interface for the fibres to be welded to. The bonds are far enough away from the mirror face that their contribution to the thermal noise of the system has been calculated to be very small.

The hydroxide catalysis bonding technique is now being investigated and developed further for use in advanced cryogenic gravitational wave detector suspension systems such as KAGRA (see section 1.7.4) and the planned Einstein Telescope (see section 1.8.1).

2.5.3. Conclusion

Thermal noise is an important limiting factor to the sensitivity of gravitational wave detectors. The fluctuation-dissipation theorem may be used to inform the design and construction of gravitational wave detector suspension systems in such a way that the effect of mechanical losses, and thermal noise, will be minimised. Since any interface in the suspension will be associated with a certain amount of additional mechanical loss, it is advantageous to minimise the area of these interfaces for a given interface thickness.

One possible method of reducing thermal noise within future gravitational wave detectors is to operate them at cryogenic temperatures. However, to date the material of choice for the mirrors of gravitational wave detectors has been fused silica and this has a large, broad loss peak at ~ 40 K [106]. As such it is necessary to understand the loss behaviour of other materials; both sapphire and silicon are of particular interest as alternatives to fused silica due to their more desirable properties at cryogenic temperature.

The properties of hydroxide catalysis bonds between these materials were thus investigated with the goal of minimising the overall mechanical loss and thermal noise of suspensions. In particular the strength of bonds between sapphire pieces and between silicon pieces is studied as a greater strength would mean that a smaller bond area could be used and a smaller bond area means less bond material to contribute to the overall thermal noise of the system. Additionally, the mechanical loss of hydroxide catalysis bonds between thin sapphire discs is studied directly. The results of these experiments will help to inform future detector design. These investigations are described in the following chapters of this thesis.

3. Hydroxide catalysis bonding of sapphire

3.1. Introduction

In this chapter the process of hydroxide catalysis bonding of sapphire is discussed. In the experiments described in this chapter, several different chemical bonding solutions were used to create bonds between sapphire samples and the strengths of these bonds were measured. The strengths of bonds were of particular interest for consideration of the design and fabrication of the KAGRA test mass suspensions.

Hydroxide catalysis bonding, sometimes called silicate bonding or hydroxy-catalysis bonding, is a precision optical technique originally developed and patented at Stanford University by Gwo for use in the Gravity Probe B telescope [138, 139, 140, 141]. The technique was originally used to join fused silica pieces in this telescope and was later implemented in the construction of quasi-monolithic fused silica suspensions in laser interferometric gravitational wave detectors [135, 99, 98, 142, 143, 91]. Additionally it was used in joining the fused silica optics to the Zerodur optical bench for the LISA Pathfinder mission [109, 48], the proof-of-concept mission for the planned space-based detector, LISA [144, 145, 146]. It was selected for the latter purpose due to the high strength of the bonds as well as

3. Hydroxide catalysis bonding of sapphire

for the ability to precisely align parts during bonding and for the thin bonds that are produced [138, 145, 147].

It allows precision bonding of oxide-based or oxidisable optical components, creating optically clear bonds with strengths that can be similar to the bulk material [138, 145]. This is generally achieved at room temperature by applying an aqueous solution containing hydroxide ions (often sodium silicate [sodium hydroxide and silicon dioxide] or potassium hydroxide) to the two bonding surfaces and by placing the surfaces sufficiently close to each other to allow a chemical bond to form between them (see section 3.2).

Typically the substrates to be bonded are those which can form a silicate-like network, such as fused silica, or those which can be chemically linked to a silicate-like network. The nature of the technique means that the bonds take a short amount of time to start to form, on the order of approximately 30 seconds at room temperature when bonding glasses and fused silica [138, 148], which allows enough time for bond alignment to be adjusted, should that be necessary. The bonds created are strong, stable and very thin.

3.1.1. Use of hydroxide catalysis bonding in fused silica based suspensions

The first time hydroxide catalysis bonding was used in a gravitational wave detector was in the construction of the final stages of the GEO600 suspension systems [135]. The technique was used to join fused silica attachment pieces (“ears”) to the sides of the test masses, which provide weld points for the fused silica fibres which support the masses.

Previously, test masses were suspended in steel wire loops, for example in the earlier prototype interferometers of the LIGO detectors, which saw 10.7 kg fused silica test masses suspended in this way [149, 77, 150]. However, fused silica fibres have approximately $10^4 \times$

3. Hydroxide catalysis bonding of sapphire

lower intrinsic mechanical loss than steel wires [151] and any losses due to “stick and slip” friction between the wire loop and the test mass are removed as the fibres are welded to the ears which are in turn chemically joined to the test masses [116, 151]. The bond material has been shown to have a higher intrinsic mechanical loss than fused silica but the effect of the loss of the bond material on the overall thermal noise of a bonded system can be minimised because the bonds formed can be extremely thin (<100 nm) [147].

Following the success of this technique when used in the GEO600 suspensions, hydroxide catalysis bonding was adapted for use in the upgrades to the suspensions of the LIGO and Virgo detectors. In the case of LISA Pathfinder the ability to withstand thermal cycling and extreme forces associated with launch were additional advantageous characteristics of the bonds [140, 145]. A further advantage for many detectors, both ground-based and space-based, is that the bonds are vacuum compatible [140, 145].

While the suspension details of the designs for Advanced LIGO and Advanced Virgo do differ, both feature quasi-monolithic suspension systems with a final stage comprising fused silica test masses (Advanced LIGO has 40 kg test masses [9] while Advanced Virgo’s test masses are 42 kg [103]), suspended by four fused silica fibres, each with a minimum diameter of $400\text{ }\mu\text{m}$ [99, 100, 143, 152]. In aLIGO, as in GEO600, the fibres are welded onto small fused silica ears attached to the sides of the test masses with hydroxide catalysis bonds. While the suspension details of the designs for Advanced LIGO and Advanced Virgo do differ, both feature quasi-monolithic suspension systems with a final stage comprising fused silica test masses (Advanced LIGO has 40 kg test masses [9] while Advanced Virgo’s test masses are 42 kg [103]), suspended by four fused silica fibres, each with a minimum diameter of $400\text{ }\mu\text{m}$ [99, 100, 143, 152]. In Advanced LIGO, as in GEO600, the fibres are welded onto small fused silica ears attached to the sides of the test masses with hydroxide catalysis bonds.

3. Hydroxide catalysis bonding of sapphire

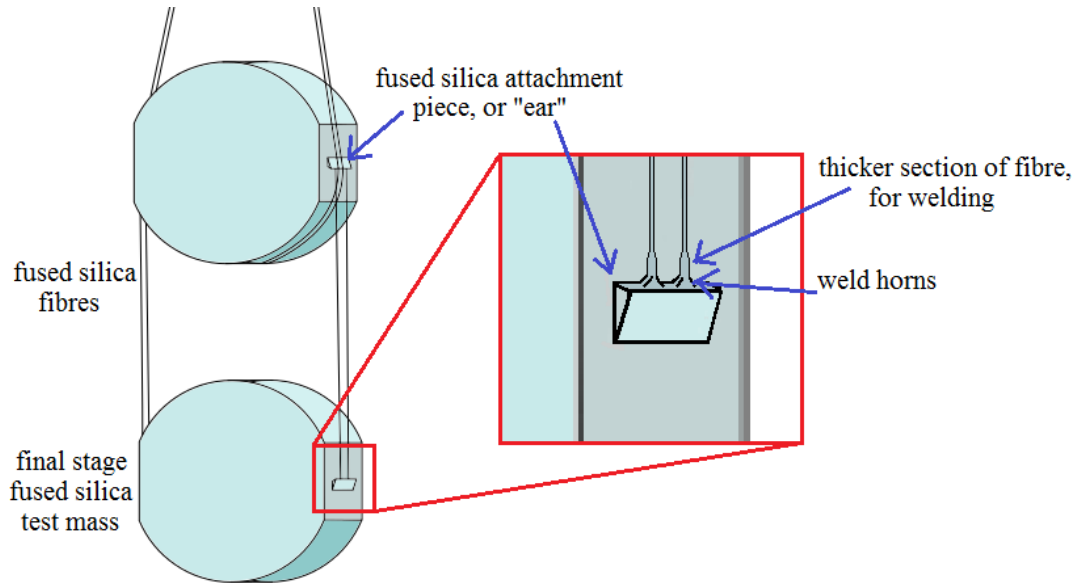


Figure 3.1.: Simplified schematic diagram of a suspended fused silica test mass such as those used in Advanced LIGO.

The aLIGO weld horns are sections that stick out from the main prism and the ends have a similar cross-sectional area to the expanded ends of the suspension fibres (see figure 3.1). The ears are first attached by hydroxide catalysis bonds to the test masses, then the fibres are welded to the horns using a CO_2 laser [98]. This keeps the welding area away from the test mass which could otherwise be damaged by the procedure. Here, the importance of the strength of the hydroxide catalysis bonds is clear, as they support the test mass in the suspension.

3.2. The hydroxide catalysis bonding procedure

In the suspension systems for the test masses of interferometric gravitational wave detectors, hydroxide catalysis bonds are chosen to join attachment pieces to test masses due to the relatively low contribution the bonds have to the overall thermal noise in the suspensions [147]. In order to minimise the noise contribution from hydroxide catalysis bonds the volume of bonding material should be minimised. To achieve this, hydroxide catalysis bonds are typically formed between surfaces with peak-to-valley flatnesses of

3. Hydroxide catalysis bonding of sapphire

$\lambda/10$ or less, where $\lambda = 633$ nm. Typical bond thickness is of the order of 60 nm - similar to the peak-to-valley flatness of the surfaces to be bonded [147].

Alkaline bonding solutions, most commonly aqueous potassium hydroxide solution or sodium silicate solution, are used to create the bonds [138]. This solution is placed on at least one of the two intended bonding surfaces and the two surfaces are brought into contact to allow the bond to form. In this way only a very small quantity of bonding solution is required for bonds to be successful, typically $\sim 0.4 \mu\text{l}$ per cm^2 of intended bonding surface [138] - much of this volume is made up of water which evaporates or is absorbed into the bulk material being bonded as the bonds cure, which leads to the very thin bond layers. Provided that the surfaces are sufficiently conformal, clean and hydrophilic the bonding solution will readily spread across the bonding area and a series of chemical reactions between the solution and the surfaces will take place. This will lead to a strong, rigid, transparent network of molecular chains forming between the two surfaces, as discussed below.

The time taken for a bond to form is dependent upon temperature and the pH of the solution, with bonding time increasing with decreasing temperature and with increasing hydroxide concentration [153]. In the experiments described in this chapter, the bonding procedure was carried out at room temperature (~ 293 K), bonds were cured for a minimum of four weeks at room temperature and the bonding solutions used were prepared such that their initial pH was 12 ± 0.1 as this pH has been found to be successful in forming bonds between fused silica, silicon, silicon carbide and Zerodur glass pieces in the past [135, 137, 115, 154, 155].

3.2.1. Surface preparation

For successful bonds to be formed, the surfaces to be bonded must be clean and hydrophilic [141]. This state is usually achieved by cleaning the surfaces manually in a clean room environment.

A standardised cleaning procedure, similar to one developed for use in joining the components of the Advanced LIGO suspensions [156], was used to prepare surfaces of all samples studied here before the bonds were formed in order to ensure comparability to previous hydroxide catalysis bonding studies. This procedure is as follows [156, 157]:

1. Rinse the surface with de-ionised water
2. Apply a paste of cerium oxide and de-ionised water to the surface with an Anticon Gold StandardWeight¹ clean room wipe, use this to rub the surface for ~ 30 seconds
3. Rinse with de-ionised water to remove the paste
4. Apply a paste of sodium bicarbonate and de-ionised water to the surface with a new clean room wipe, use this to rub the surface for ~ 30 seconds to remove any remaining cerium oxide
5. Rinse with de-ionised water to remove any remaining sodium bicarbonate
6. Repeat the sodium bicarbonate clean and rinse
7. Rinse the surface in spectroscopic grade $\geq 99.9\%$ methanol

¹<http://www.contecinc.com/>

3. Hydroxide catalysis bonding of sapphire

8. Immediately before bonding, wipe the surface with a new clean room wipe soaked in spectroscopic grade $\geq 99.9\%$ methanol

This process differs from the Advanced LIGO cleaning procedure only in that for Advanced LIGO steps 2 and 3 are repeated. These repeated steps are neglected because they have not been found to make a noticeable improvement to the cleanliness and hydrophilicity of the surfaces. As such, this process is considered sufficient when forming bonds for strength testing, although more thorough procedures may be demanded when forming bonds for real test mass suspensions. When the cleaning procedure is complete the surfaces are free from residues, organics and particulates and are highly hydrophilic [158].

3.2.2. Considerations in preparation of bonding solution

All bonding solutions are prepared in a clean room environment at room temperature and with de-ionised water such that they have a pH of 12 ± 0.1 . In the past when bonding solutions with this pH have been used to join other materials (e.g. fused silica, silicon, silicon carbide, Zerodur, etc [135, 137, 115, 154, 155]) bonds have been formed successfully; using the same pH when joining sapphire pieces allows for comparison between such bonds. The solutions are mixed via manual shaking for approximately 1 minute to ensure that the chemicals are properly dissolved before pH testing is carried out using a Metler Toledo SevenMulti bench top pH meter. The solutions are then centrifuged for ~ 30 seconds to separate out any remaining particulates. Finally, the upper third of the liquid from the centrifuged solution is passed through a UniPrep medical filter² with a $0.2 \mu\text{m}$ pore size, to remove any smaller particulates that may remain. For more detailed information on the preparations of the specific solutions used for bonding experiments detailed in this chapter, see section 3.4.3.

²<http://www.sigmaaldrich.com/labware/labware-products.html?TablePage=111298830>

3.2.3. Bond formation

Cleaned samples are kept in individual clean room wipes until they are bonded. To avoid the potential for re-contamination the time between cleaning and bonding should be short [156] and during these experiments never exceeded 3 hours. Immediately before bonding the surface of the sample is inspected under a high intensity “goose neck” light - this light allows any specks of dust, particulate contaminants or scratches to be clearly visible. If any contaminants are seen the surface is wiped again with a methanol soaked clean room cloth. Should this not remove the contaminant the sample is re-cleaned, following the procedure described in section 3.2.1.

When the surfaces are pristine a pipette is used to accurately measure out the quantity of solution needed to form the bond. A new pipette tip is used for each bond. The solution is taken from near the surface of the solution within the UniPrep filter and care is taken to avoid allowing the pipette tip to touch anything apart from the solution, at any time, to avoid potential contamination. The bonding solution is dispensed onto the surface of one sample and the second sample is gently placed on top of the first.

No weights are used in this process but a jig may be used to aid sample alignment. This procedure is carried out in a clean room flow cabinet to avoid the risk of new particulate contaminants coming into contact with the bonding surfaces. The chemical reaction begins, as described in the following three sections, and the bonds are left to cure.

3.2.4. Hydration and etching

An aqueous solution containing hydroxide ions, such as sodium silicate solution, is applied to the clean bonding surface. This surface has been made extremely hydrophilic by the cleaning procedure and so the OH^- ions in the solution are attracted to fill any small

3. Hydroxide catalysis bonding of sapphire

gaps or pits in the bonding surface. Any contaminants remaining on the surface at this stage will impede the hydration process - otherwise the solution will smoothly spread across it. When the surface is hydrated the remaining OH^- ions will attach to ions on the sample surface and will form weak bonds with them. In the case of fused silica these bonds will be formed with silicon ions; in the case of sapphire these bonds may be formed with alumina ions [159] (see section 3.2.7).

These additional bonds weaken the existing Si-O or Al-O bonds at the substrate surface, allowing ions to be liberated from the substrate. This process is known as etching. The result is silicate (or aluminate) molecules in suspension in the bonding solution [159]. As this process continues the concentration of OH^- ions is steadily depleted. See figure 3.2 for a diagram showing this process with fused silica substrates with sodium silicate solution. The process for bonding sapphire with sodium silicate solution is similar, but in this case an aluminosilicate network will form [159].

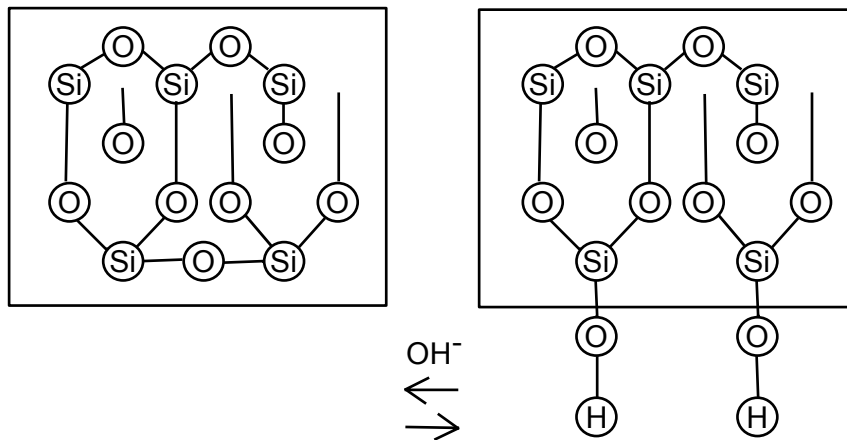
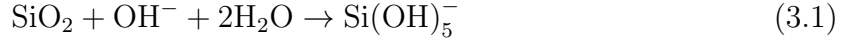


Figure 3.2.: Structure of fused silica (left). When fused silica is exposed to water and hydroxide ions it becomes hydrated and Si-O-H chains are formed (right).

3. Hydroxide catalysis bonding of sapphire

This process can be summarised with equation 3.1 [145],



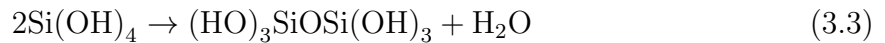
and a similar process occurs in the case of hydration and etching of sapphire [159] (see section 3.2.7 for more details).

3.2.5. Polymerisation

The decreasing concentration of OH^- ions in the bonding solution corresponds to a decrease in pH of the solution. When the pH drops below ~ 11 the suspended silicate ions begin to dissociate to form $\text{Si}(\text{OH})_4$, as shown in equation 3.2 [145]



The $\text{Si}(\text{OH})_4$ molecules then combine and polymerise, forming siloxane chains and water as in equation 3.3 [160, 145]



In the case of sapphire bonding the pH must be between 11 and 12 for similar, polymer-like chains to form [159, 161]. In both cases, water molecules are left behind as a by-product. See figure 3.3 for a diagram showing the process occurring when sodium silicate bonding solution is used to join fused silica surfaces.

3. Hydroxide catalysis bonding of sapphire

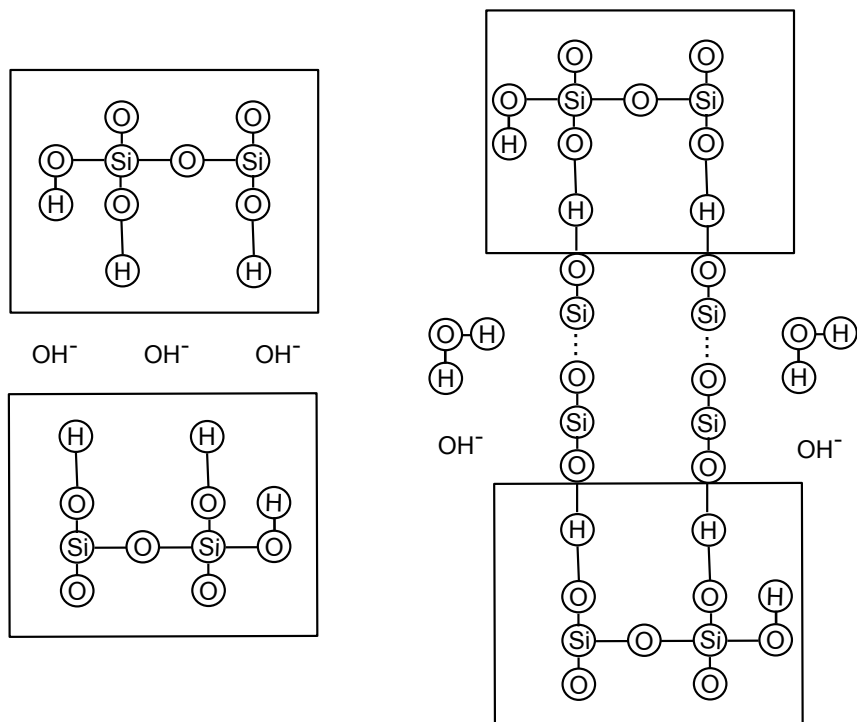


Figure 3.3.: The formation of the hydroxide catalysis bond. On the left, hydrated fused silica is in the presence of OH^- ions in an aqueous solution. OH^- ions are liberated from the sample surfaces, these then combine to form water molecules and a siloxane chain connects the surfaces, as on the right.

3.2.6. Dehydration

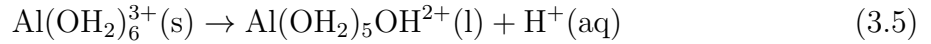
Over time the remaining water migrates to the edge of the bonding area and evaporates. In some substrate materials it may also be absorbed into the bulk material. The bond then strengthens over time as this water is removed. It has been found that, when the bonds are formed between fused silica substrates, the bonds reach their maximum strength after ~ 4 weeks of curing at room temperature [145].

3.2.7. Bond formation with sapphire substrates

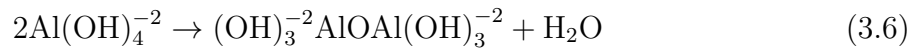
The chemical process involved in the hydroxide catalysis bonding of sapphire are similar to those involved in bonding fused silica, as described above, however there are a few differences. Here, the OH^- ions in the solution can react with the alumina surface in several ways, for example,



or³,



The following dimerisation process can then take place with the $\text{Al}(\text{OH})_4^-$ and $\text{Al}(\text{OH}_2)_5\text{OH}^{2+}$ ions, as shown in equations 3.6 and 3.7.

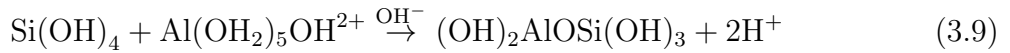


If the bonding solution chosen contains silicate ions, these will form a silicate-like network during dehydration and the liberated alumina ions will chemically react with the

³The interaction of the OH^- with alumina may only form $\text{Al}(\text{OH}_2)_5\text{OH}^{2+}$ if the molarity of the bonding solution is less than 1.5 and the pH is over 13 [162]

3. Hydroxide catalysis bonding of sapphire

silicate-like network in the solution, leading to the formation of a three-dimensional aluminosilicate network, in which some of the Si atoms of the silicate structure will be replaced with Al atoms, as given in equations 3.8 and 3.9.



Without the silicate ions, an aluminate network will form, although this process would be expected to occur more slowly.

3.3. A comparison of other bonding techniques

3.3.1. Indium bonding

Indium is also often used to bond non-metallic solids such as fused silica and metallic oxides such as sapphire [163]. As with hydroxide catalysis bonding it is necessary that the surfaces to be bonded are thoroughly cleaned before bonding is carried out and adhesion can be improved through the application of heat and pressure [164]. One challenge associated with indium bonding is that the indium readily oxidises which prevents good bond formation. However, this oxidation can be avoided either by carrying out bonding in an argon environment, through the use of an ultrasonic soldering iron, which inhibits oxide growth [165], or by treating the indium with hydrochloric acid prior to bonding [166].

3. Hydroxide catalysis bonding of sapphire

For joints which require the transmission of heat it may be advantageous to use indium as a bonding material. Work has been carried out to determine whether such bonds would be suitable for use in the KAGRA suspensions [166]. At KAGRA's eventual intended operating temperature of 20 K [167], indium bonds with a thickness of $\sim 10\ \mu\text{m}$ have been found to have a mechanical loss of 2×10^{-3} [166]. This should enable attainment of the desired level of thermal noise for KAGRA [167]. Additionally, it was found that it should be possible to extract sufficient heat through each indium joint such that it will be possible to keep the KAGRA suspensions at 20 K [166]. A further advantage is the possibility of separating the surfaces joined by indium bonds by applying heat to melt the indium. This could prove useful should the suspension need to be repaired or upgraded [168].

However, the low melting point of indium also represents a possible drawback to its use [169]. During the assembly of the detector it is likely that the suspensions will be thermally cycled several times and that the vacuum chambers may need to be baked out. This process may temporarily soften the indium and could lead to a misalignment or failure of the joined pieces. As such, it is important that in any detector design that utilises indium bonds, those bonds should be under compression [166].

3.3.2. Adhesives

A wide range of commercial adhesives are available. These are typically categorised as either reactive (for example epoxies and cyanoacrilates) or non-reactive adhesives (for example polyvinyl acetate [PVAc] and rubber cements), depending on whether or not a chemical reaction takes place as the adhesive hardens [170]. Chemical bonds may take the form of ionic, covalent or hydrogen bonds. In bonds which don't involve a chemical reaction the adhesion may be due to electrostatic or Van de Waals forces, or by moisture-aided diffusion of the adhesive into small pores in the substrate surface, followed by hardening as the moisture evaporates [170].

3. Hydroxide catalysis bonding of sapphire

The major advantages of such adhesives are usually associated with low cost and the ability to join a wide variety of substances (depending on the adhesive used). However, many adhesives lose stability when they are outside relatively narrow temperature ranges (epoxy, example, usually has an operating range of -30°C - 100°C) [171]. The majority of adhesive bonds of these kinds are also not compatible with vacuum conditions [172]. While adhesives designed for use in vacuum do exist, it is challenging to create very thin bonds using such adhesives - typically joints using these adhesives cannot be made thinner than a few microns and are often several millimeters thick [173, 174, 175]. Since this may result in more energy being stored in the bonds, thicker bonds may have a significant negative impact on the thermal noise performance of a suspension [147].

At present, there is no adhesive known to this author that is suitable for joining the components of test mass suspensions for gravitational wave detectors. Only hydroxide catalysis bonding can be used to produce bonds that are suitably thin, strong, transparent and vacuum compatible at a wide range of temperatures, with the additional advantage of the option for precision alignment due to the time taken for the bonds to begin to form and cure.

3.4. Hydroxide catalysis bonding for sapphire and silicon in cryogenic suspension systems

Future detectors including KAGRA [107], ET [68] and possible further upgrades to Advanced LIGO [90, 176] will be operated at cryogenic temperatures to further improve detector sensitivity by reducing thermal-mechanical loss and hence thermal noise. This low temperature operation will necessitate a change in material for the test masses and their suspensions as fused silica has a large, broad mechanical loss peak centred around $\sim 40\text{ K}$ making it an unfavourable choice of material for low temperature operation [106].

3. Hydroxide catalysis bonding of sapphire

Materials of particular interest for cryogenic use are sapphire [107] and silicon [177]. Both have more favourable properties than fused silica in terms of their thermo-mechanical losses in the cryogenic regime, making them interesting candidate materials for the test masses and suspensions of cryogenically-run detectors.

The KAGRA detector will also utilise hydroxide catalysis bonding in its suspension design. However, there will be several key differences when compared to room temperature detector suspensions. The material of choice for the KAGRA detector is sapphire [107] which has the immediate advantage over silicon of being optically transparent at 1064 nm [178], the wavelength of Nd:YAG lasers which are commonly used to illuminate gravitational wave detectors [179]. The fibres will be used not only to suspend the test masses, but also to extract heat from them, which will be necessary since the intended operating temperature of the detector is 20 K [167]. Hence, in order to extract sufficient heat via the suspension fibres, these fibres must have a greater diameter than the fused silica fibres used in Advanced LIGO [180].

Additionally, it is not currently possible to join single crystal sapphire fibres by heating them while maintaining the single crystal structure, so the fibres cannot be welded to weld horns on the attachment pieces, as was done for the advanced LIGO fused silica suspensions. Consequently, a new design of suspension fibres has been developed to allow the fibres to be connected to the test masses. Here, the fibres have “nailhead” ends (see figure 3.4), allowing them to slot into notches in the attachment pieces instead of being welded to them directly.

This nailhead design was chosen so that the suspension pieces can be disassembled for upgrades, or in the case of damage to the test masses or suspension elements. This may mean additional interface losses, as the nailhead itself, as well as part of the fibre will be in contact with the attachment pieces and there will be some friction between the surfaces here. However, it is hoped that when the detector is operated at cryogenic

3. Hydroxide catalysis bonding of sapphire

temperatures, the reduction in thermal noise will compensate for this. Each fibre will have a length of 300 mm and a diameter of 1.6 mm, while the nailheads are cubes with length 20 mm [180, 181]. The attachment pieces will be bonded with hydroxide catalysis bonding to flats on the sides of the KAGRA test masses.

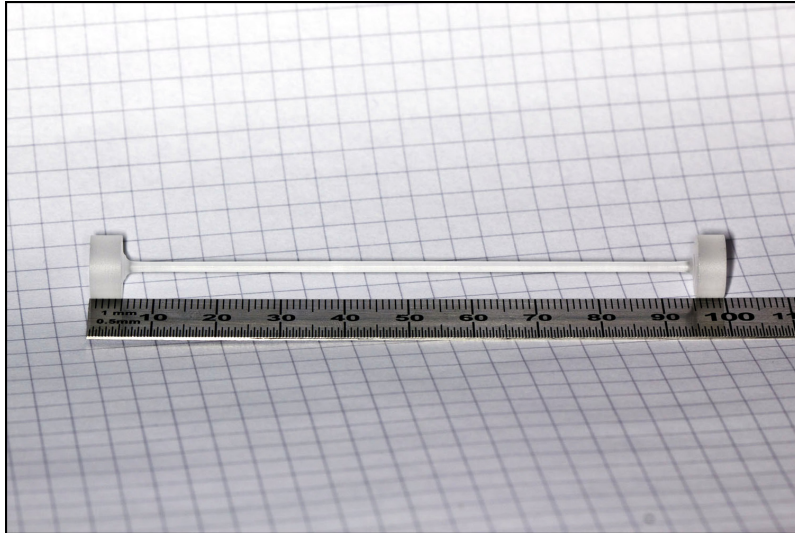


Figure 3.4.: Photograph of an example of an early-design for the sapphire fibres including cylindrical nailhead attachments, similar to those intended for use in the KAGRA suspensions which now have cuboid nailheads.

Likewise, the planned Einstein Telescope (ET) detector will also operate at cryogenic temperatures with silicon suspension systems (sapphire is a back-up option) [68]. Any further upgrades to Advanced LIGO and Advanced Virgo may involve the use of either material [90, 176]. As such it is important to thoroughly understand the characteristics of hydroxide catalysis bonds formed between pieces of these materials, to properly inform suspension design and to optimise bond strength and mechanical loss.

3.4.1. Sapphire samples for hydroxide catalysis bonding experiments

For the first set of experiments described here, a set of 116 sapphire samples with dimensions $5 \times 10 \times 20$ mm were procured from Crystran⁴. These were cut such that the m-plane of the sapphire crystal was parallel to the bonding surface as shown in figure

⁴<http://www.crystran.co.uk/>

3. Hydroxide catalysis bonding of sapphire

3.5. The edges of the intended bonding surfaces featured small chamfers, with widths on the order of 0.2 mm and all faces were polished with the exception of the face directly opposite the intended bonding face, which had a ground finish, see figure 3.6.

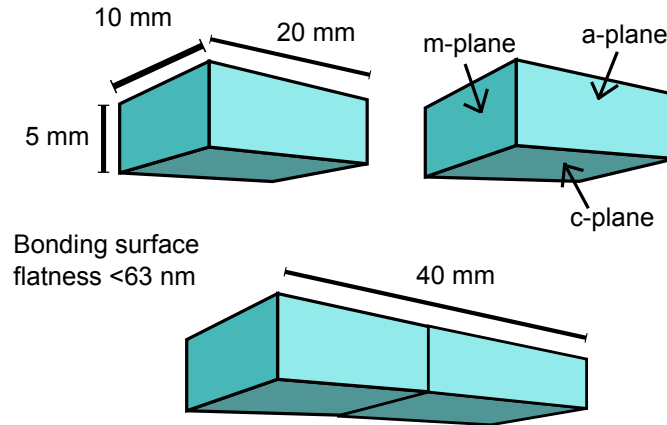


Figure 3.5.: Schematic diagram showing the dimensions and axes of Crystran sapphire blocks for hydroxide catalysis bonding experiments.



Figure 3.6.: Photograph of an example of a pair of bonded sapphire samples with dimensions as shown in figure 3.5. Note the ground 5×10 mm face to distinguish face intended for bonding.

The parts are produced to a specified flatness of $\lambda/10$ (63.3 nm) and an Ra roughness of 20 nm (Ra roughness is an arithmetic average deviation from the mean) as this has been shown to give successful bonds [145].

All samples are marked with identification numbers, to allow bonds to be characterised and tracked throughout the experiment. The flatness of the sample surfaces are measured with an interferometer (ZYGO GPI XP/D) and the roughness of the samples surfaces is measured with an optical surface profiler (Veeco: Wyko NT1100) at $2.5\times$ magnification, before cleaning and bonding is carried out as described in section 3.2.1.

3.4.2. Analysis of surface suitability of sapphire samples intended for hydroxide catalysis bonding experiments

Before bonding, a randomly selected subset of 20 of the 116 samples were measured to ensure that they had been produced to the intended dimensions. This was carried out using a micrometer and the 20 samples measured were found, on average, to have widths of 5.00 ± 0.005 mm and heights of 10 ± 0.005 mm. Additionally, the chamfers of the same subset of samples were measured using a table top SEM and the average chamfer width was found to be 0.16 mm. These chamfers are taken into account when calculating the strength of the bonds.

Almost all the samples in this set were found to have flatnesses of $\lambda/10$ or better. The few samples which were less flat were not deemed to have large enough features that they would be expected to adversely effect the success of bonds formed or the strength of those bonds. However, since all samples were labeled with identification numbers they could be carefully tracked, so that the flatness of any sample could be determined at a later date, should any unexpected effects occur. The average flatness measured was 50.6 nm, the smallest value of flatness measured was 30.6 nm and the largest value of flatness measured was 87.3 nm. The standard deviation between the flatnesses measured was 10.2 nm. A histogram showing the distribution of flatnesses is given in figure 3.7. An example of a typical flatness surface profile is shown in figure 3.8.

Likewise, all sample surface roughnesses were noted and associated with sample identification numbers. No sample surface had a roughness profile that might be expected to be associated with unsuccessful or weak bonds. The mean Ra roughness measured was 9.2 nm, the smallest value of Ra roughness measured was 6.8 nm and the maximum value of Ra roughness was 18.5 nm. The standard deviation of the measured Ra roughness was 2.0 nm. A histogram showing the distribution of Ra roughnesses is given in figure 3.9. An example of a typical roughness surface profile is shown in figure 3.10.

3. Hydroxide catalysis bonding of sapphire

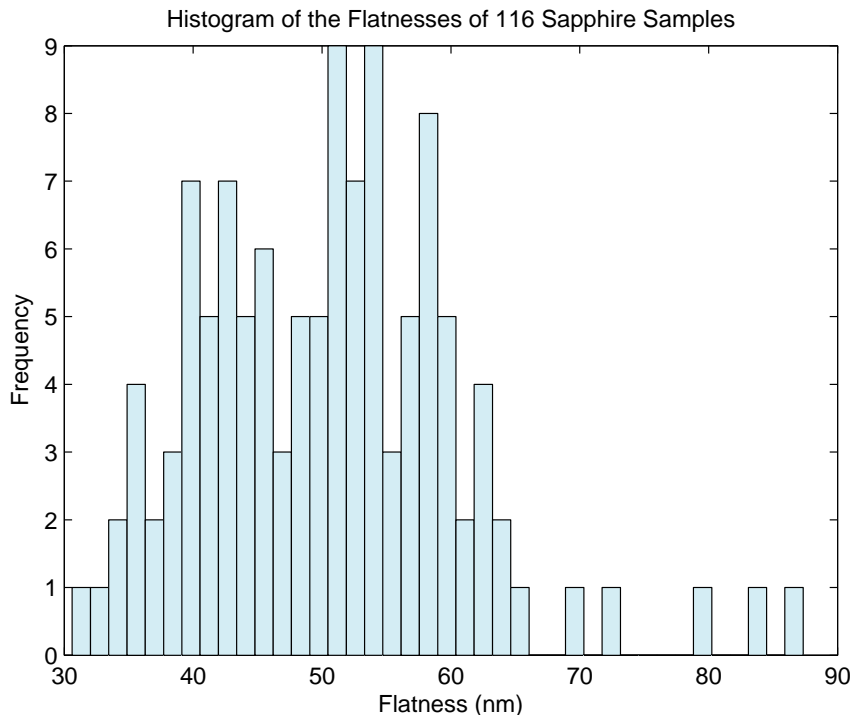


Figure 3.7.: A histogram of the measured peak-to-peak flatnesses of the 116 sapphire samples intended for hydroxide catalysis bonding experiments, as measured using an interferometer (ZYGO GPI XP/D).

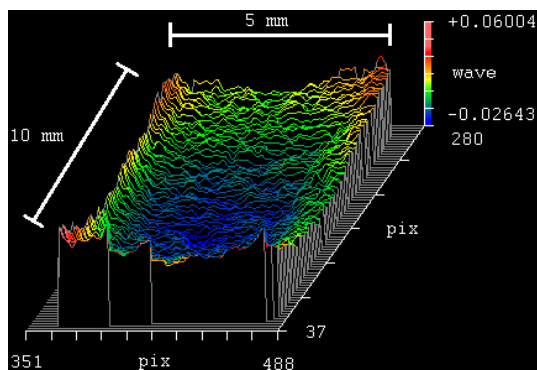


Figure 3.8.: A surface profile of a sapphire sample showing the flatness of the surface. The whole bonding surface of a 5 mm×10 mm sample is shown here.

3. Hydroxide catalysis bonding of sapphire

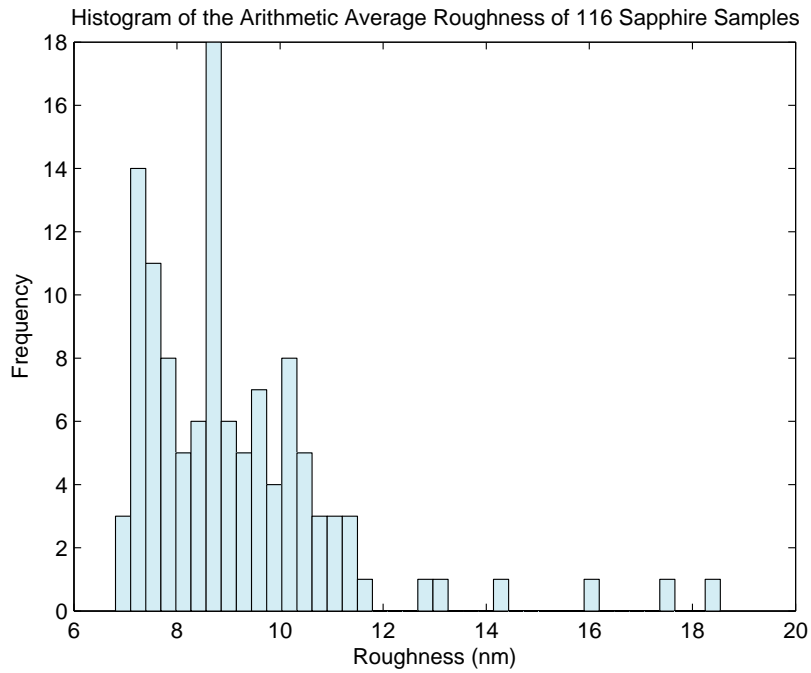


Figure 3.9.: A histogram of the measured Ra roughnesses of the 116 sapphire samples intended for hydroxide catalysis bonding experiments, as measured using an optical surface profiler (Veeco Wyko NT1100).

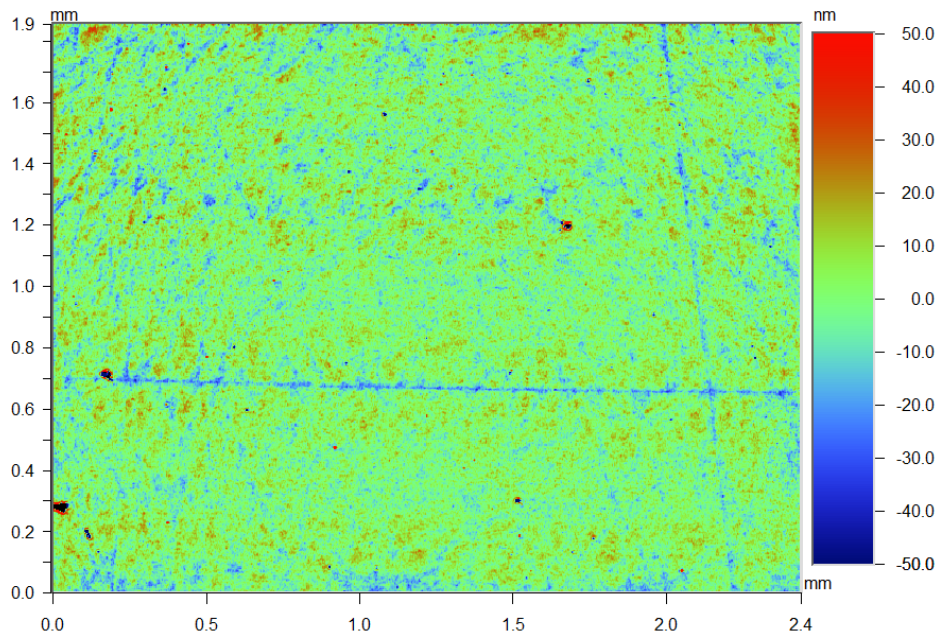


Figure 3.10.: An example of a surface profile, at $2.5\times$ magnification, of a sapphire sample showing the Ra roughness of the surface.

3.4.3. Preparation of solutions for bonding sapphire

Here the choice of bonding solution is considered. The solutions for bonding sapphire surfaces used in these experiments were aqueous solutions of sodium aluminate (NaAlO_2), sodium hydroxide (NaOH), sodium silicate (Na_2SiO_3) and potassium hydroxide (KOH), each prepared such that an initial pH of 12 ± 0.1 was created. The pH of each solution was measured after the solutions were prepared using a Mettler Toledo SevenMulti bench top meter⁵. Sodium aluminate was chosen with the aim of closely matching the refractive index of the bond to that of the sapphire samples (although this is not directly of interest for gravitational wave detector suspensions it may be of interest for potential optical applications). Sodium hydroxide was chosen with the goal of producing very thin bonds., thus minimising any optical reflections from the bond layer. Sodium silicate was chosen to allow comparison of the results obtained at Glasgow with prior studies of bond properties using this type of bonding solution to joint fused silica samples. Potassium hydroxide was chosen to allow comparison to results found by Dari *et al* [182] and Suzuki *et al* [183] when bonding sapphire.

In previous experiments involving the bonding of sapphire using a KOH bonding solution, some relatively low values of strength were found (e.g. 1.5 MPa [182], 6.53 MPa [183]); however, while Dari *et al* used KOH with an initial pH of 14.4, the initial pH of the KOH solution used by Suzuki *et al* is not clear. Additionally, Dari *et al* made a combination of bonds between randomly oriented sapphire samples and bonds between c-plane sapphire samples and measured the tensile strength of the bonds. Suzuki *et al* measured shear strengths of c-to-c plane bonds between sapphire pieces. Both used cylindrical samples rather than cuboids. No alternative bonding solutions were investigated in either study. Here, KOH and three other solutions are considered for comparison.

⁵<http://uk.mt.com>

3. Hydroxide catalysis bonding of sapphire

The pH of each solution was measured after the solutions were prepared using a Mettler Toledo SevenMulti bench top meter⁶. The sodium aluminate solution was prepared with 0.04 g of sodium aluminate powder with 12.5 ml of de-ionized water. The sodium hydroxide solution was a commercially available 0.01 M solution in de-ionized water. The sodium silicate solution was formed by diluting a commercially available solution (14% NaOH and 27% SiO₂) with de-ionized water at a volumetric ratio of 1:6, as used in previous studies [145]. The potassium hydroxide solution was prepared from using pellets dissolved in de-ionized water to give a volumetric ratio of 1:190 KOH:H₂O.

Each of the bonding solutions were mixed, via manual shaking for ~60 seconds, were then centrifuged to remove any large particles for ~30 seconds and finally were passed through a UniPrep medical filter with a 0.2 μm pore size to remove any smaller remaining particles in the solutions.

Using 98 of the available 116 cuboids this allowed 49 bonded samples to be created, with the remaining samples being reserved for future experiments. In the experiments described in this chapter, 10 cuboids were bonded with sodium aluminate solution, 10 with sodium hydroxide solution, 10 with potassium hydroxide solution and 19 with sodium silicate solution (9 of which were intended for strength testing at cryogenic temperatures). These bonds were allowed to cure at room temperature for a minimum of four weeks.

3.5. Bond inspection

During the bonding process, when the second sample is placed in contact with the first it briefly floats on the layer of bonding solution before the bond starts to form. This is the bond settling time. In these sapphire-bonding experiments, when bonding with the sodium aluminate, sodium hydroxide and potassium hydroxide solutions, this process

⁶<http://uk.mt.com>

3. Hydroxide catalysis bonding of sapphire

took ~ 30 seconds. With sodium silicate solution the process was faster, with the bonds settling within $\sim 5-10$ seconds.

Initially the bond layer appeared highly visually reflective and the bonds became transparent over the course of ~ 8 hours - this was true of all bonding solutions. This is in contrast to bonding fused silica, rather than sapphire, where the bonds become transparent almost immediately. It may be that the initial stages of the bonding process take longer when bonding sapphire than when bonding fused silica, perhaps because sapphire is more difficult to etch.

In some cases when bonding with sodium silicate solution the bonds were incomplete, leaving behind bubbles where the bonding solution had failed to spread across regions of the sample surface. Where these bubbles made up more than 10% of the surface the bonds were rejected as if this occurred when bonding pieces for a detector the pieces would be separated and cleaned and the bonds would be remade. Hence, strength data from such bonds is not included in the results presented in section 3.7.

In several cases when bonding with sodium aluminate, sodium hydroxide and potassium hydroxide the bond surface failed to become transparent and upon further inspection it was discovered that no bond had formed, this appeared to be a binary process, with either a perfect bond forming or no bond forming at all - in all of these cases the samples were cleaned again, as described in section 3.2.1, and the bonding procedure was repeated as previously with successful bonds being formed on the second attempt.

3.6. Tensile strength testing

The bond tensile strengths were measured using a four-point bending test (ASTM C 1161-2C [184]), as shown in figure 3.11. This is a standard test for determining tensile strengths of brittle materials such as ceramics and glass [185]. The bonded samples were placed in the holder and a force, F , was applied through a loading arm, using a Zwick-Roell static 200 kN machine with a 25 kN load cell, until the bond broke. The supports below the sample were placed a distance $L = 34 \pm 0.1$ mm apart and the force was applied equally through two line contacts on top of the sample a distance $l = 20 \pm 0.1$ mm apart, both of these distances were centred on the bond. This method allows the force to be evenly applied from above whilst the sample is supported from below. The tensile strength of the bond was then obtained from the maximum force using equation 3.10 below [186]:

$$\sigma_{\max} = \frac{3(L-l)F}{2bd^2} \quad (3.10)$$

where b is the sample thickness and d is the sample width (in this case 5.00 ± 0.005 mm and 10.00 ± 0.005 mm, respectively) - less the dimensions of the chamfers (the chamfers were approximately 0.16 mm, see section 3.4.1). This leads to values of b and d of 4.84 mm and 9.84 mm respectively, and thus a corresponding increase in the strength values than would be expected had the chamfers not been taken into account.

All bonds were broken at room temperature with the exception of a set of 9 of the 19 sodium silicate bonds which were broken at 77 K using the same set up as described above. To achieve this breaking temperature the samples and the sample holder were all immersed in a Teflon container filled with liquid nitrogen (see figure 3.12). The samples broken in liquid nitrogen were first placed in this container with tongs and when the production of vapour from the liquid nitrogen rapidly boiling had subsided thermal

3. Hydroxide catalysis bonding of sapphire

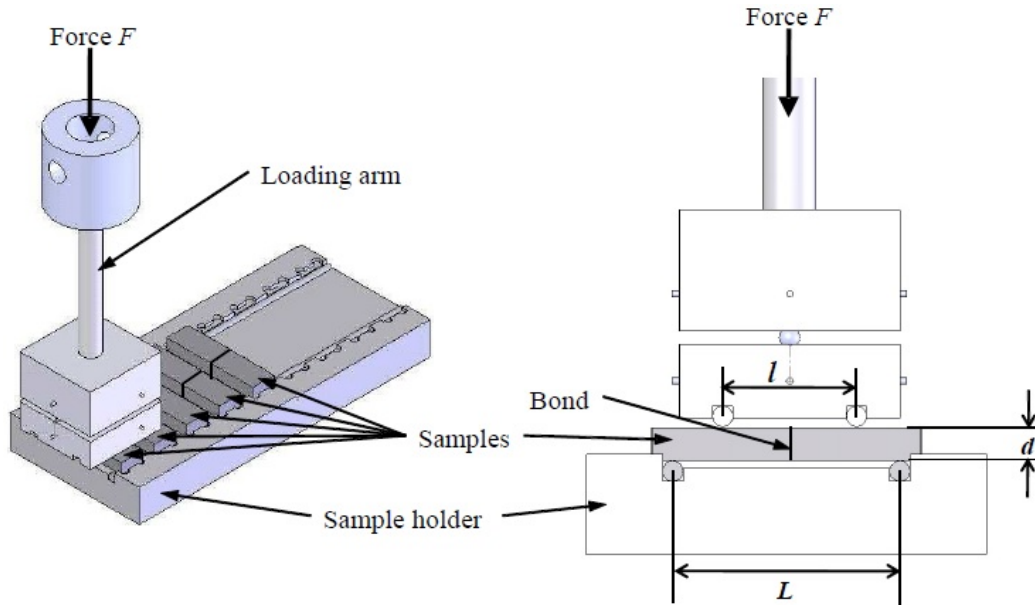


Figure 3.11.: 3D and detail CAD images of the bending strength set-up. The sample holder was placed in a Teflon bath, which was filled with liquid nitrogen for the cryogenic measurements [158].

equilibrium was assumed - this took ~ 90 seconds. The liquid nitrogen was re-filled between each bond strength test to compensate for the reduction in nitrogen volume due to it boiling.

3.7. Results

Sodium aluminate, sodium hydroxide and potassium hydroxide solutions here found to produce similar bond strengths, with mean strengths of 14, 12 and 16 MPa, respectively. The sodium silicate bonds broken at room temperature had a mean strength of 74 MPa whilst sodium silicate bonds broken at 77 K had a mean strength of 73 MPa. See table 3.1 for details of the mean, minimum and maximum tensile strengths recorded for bonds made with each chemical when broken at room temperature or 77 K. The results from this section have been published in the journal *Classical and Quantum Gravity* [187].

3. Hydroxide catalysis bonding of sapphire

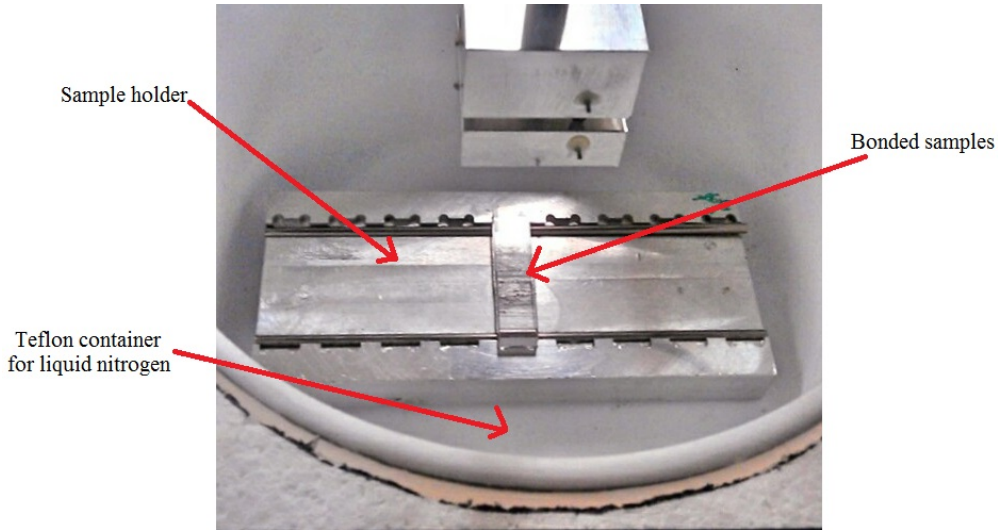


Figure 3.12.: Photograph showing the liquid nitrogen bath in which the samples and breaking equipment were cooled for cryogenic strength tests. The bath was filled with liquid nitrogen and the samples were completely submerged, here the liquid nitrogen is not shown for the sake of clarity.

Table 3.1.: Table of breaking strengths for hydroxide catalysis bonds between sapphire samples produced with a variety of bonding solutions, all with pH 12. The mean, minimum and maximum tensile strengths recorded are shown.

Chemical	Breaking temperature (K)	Strength (MPa)			σ	$\frac{\sigma}{\sqrt{N}}$
		Mean	Minimum	Maximum		
Sodium aluminate	293	14	7	17	3.3	1.1
Sodium hydroxide	293	12	7	16	2.4	0.8
Potassium hydroxide	293	16	7	58	15.0	4.7
Sodium silicate	293	74	53	91	18.3	5.8
Sodium silicate	77	73	38	89	22.5	7.5

Figure 3.13 shows the bond strength results that were obtained at room temperature. It can be seen that sodium silicate solution consistently produced stronger bonds than any of the other solutions. The strength of these sodium silicate bonds was found to be undiminished at cryogenic temperatures.

As can be seen from figure 3.13, the spread of strength results produced with sodium silicate solution bonds was greater than that produced with the other bonding solutions. However, even the weakest bonds measured would be significantly stronger than would be required in a typical suspension, with a significant safety margin. For example, the

3. Hydroxide catalysis bonding of sapphire

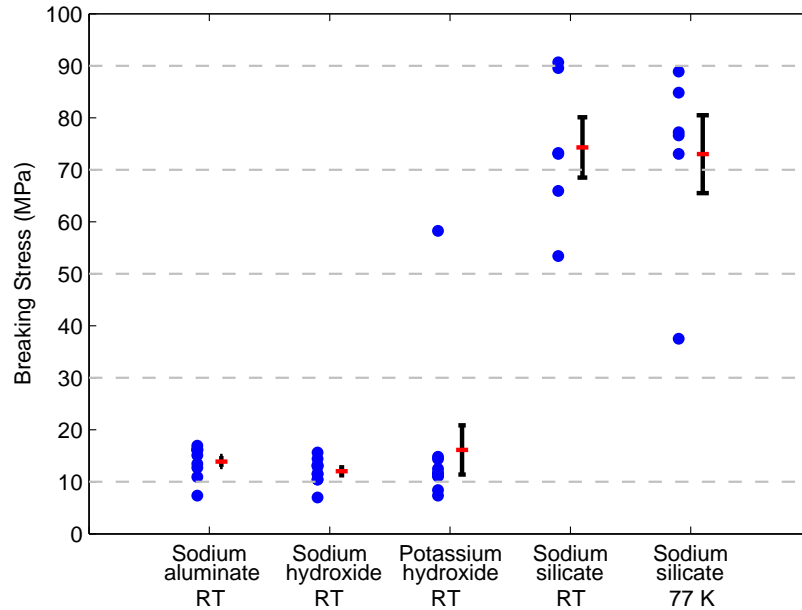


Figure 3.13.: Tensile strengths of bonds produced using various bonding solutions. The strengths are the blue points, the mean strength found for each set of samples is represented by the red bar. The error bars here indicate the standard error on the mean. Both the error bars and the mean indicators are offset from the main data set to the left, for clarity.

aLIGO and GEO suspensions required bond strengths of 0.16 MPa [147], and the KAGRA suspensions require bond strengths to be not less than 1 MPa [167], these values are chosen to be strong enough to support the test masses of these detectors with a significant safety factor (aLIGO has 40 kg fused silica test masses and KAGRA 23 kg sapphire test masses, with the KAGRA design factoring in a greater margin of safety for the support of the test masses). Although, due to the small number of samples, it is not possible to state with confidence an expected failure rate for, for example, how many bonds would fail out of 1000, it is encouraging to see that the strengths produced meet these requirements.

In almost every case the bonded samples broke cleanly across the bond. There was very little difference in the fracture morphology between samples in these experiments - only in three cases, all with sodium silicate solution, was the bulk sapphire damaged in breaking (see figures 3.14 and 3.15 for a comparison between clean breaks across the bonds and those breaks which resulted in damage to the bulk sapphire). This may have been due to

3. Hydroxide catalysis bonding of sapphire

small flaws in the bulk sapphire or to micro scratches in the non-bonding surfaces; such a defect would be the weakest point and may cause a break before the bond itself fails. The bonds that broke this way do not seem to have been particularly strong or particularly weak when compared to similar bonds.



Figure 3.14.: Bond broken cleanly with no damage to the sapphire samples.



Figure 3.15.: Broken bond with damage to the bulk sapphire, damage caused by strength testing shown circled in red.

3.7.1. False breaks

On two occasions “false breaks” were recorded. In the case of the room temperature sodium silicate set, one bond was too strong to be broken with the load cell. A strength of 91 MPa was recorded before it became impossible to increase the load further; this test was repeated using a load cell rated for higher loads and a strength of 75 MPa was then recorded. For later tests the load cell rated for higher loads was consistently used.

In the case of the sodium silicate set tested at 77 K, one bond appeared to break (i.e. the machine detected a break and stopped). When it was removed from the liquid nitrogen bath it was clear that the bond was still intact (it is possible that some small particle was in the way and when this was crushed the abrupt change in stress led to the machine recording the false break). The strength recorded during this first attempt at breaking

3. Hydroxide catalysis bonding of sapphire

the bond was 42 MPa. The temperature of the sample was allowed to return to room temperature, before being re-submerged in the liquid nitrogen bath for a second breaking attempt. The second attempt was successful and the strength recorded was 99 MPa.

The data recorded from these two false breaks are not included in the plot or error bars shown in figure 3.13.

3.8. Discussion and summary

Bend strength tests were carried out on hydroxide-catalysis bonds formed between sapphire samples with bonds produced using four different bonding solutions: sodium aluminate, sodium hydroxide, potassium hydroxide and sodium silicate. It was found that the type of solution used had considerable influence on the tensile strength of the bond produced and that sodium silicate solution produced the strongest bonds. The strengths recorded for sodium silicate bonds appeared undiminished when bonds were broken at cryogenic temperatures.

Sodium aluminate, sodium hydroxide and potassium hydroxide solutions were found to produce similar bond strengths, with mean strengths of 14, 12 and 16 MPa, respectively. The sodium silicate bonds broken at room temperature had a mean strength of 74 MPa whilst sodium silicate bonds broken at 77 K had a mean strength of 73 MPa. Table 3.1 contains details of the mean, minimum and maximum tensile strengths recorded for bonds made with each chemical when broken at room temperature or 77 K. These strength results demonstrate the suitability of hydroxide catalysis bonding as a technique for use in sapphire suspensions, as the bonds are strong enough to support a typical test mass [147], with a safety margin of more than 10.

3. Hydroxide catalysis bonding of sapphire

In a small number of cases, damage was done to the bulk sapphire during the strength testing procedure, however the level of damage does not seem to be related to the strength of the bond. Potentially, other fracture mechanisms start to play a role when the bonds are strong enough. All such bonds were produced with sodium silicate solution.

It is not immediately clear why the bonds formed using sodium silicate solution are so much stronger than those formed with other solutions. However, it is likely that this is due either to the silicate material in the solution contributing to the bond formation, or to the solution etching the sapphire surfaces more successfully. When compared to bonds formed using sodium silicate solution between fused silica samples, those formed with sapphire samples are much stronger. Since, in the case of fused silica the bulk of the sample is often damaged by the strength testing procedure, whereas the bulk of the sapphire is not, it is possible that this is the cause of the higher measured strengths in sapphire. Rather than the samples failing when sapphire pieces are bonded and strength tested, the bond itself fails. It is possible, due to the higher strength of sapphire, that these experiments are a more accurate measurement of the true strengths of hydroxide catalysis bonds.

While sodium silicate solution produced the strongest bonds, other solutions may still be suitable for bonding as all bonding solutions tested produced bonds that would be strong enough for use in a typical suspension [147]. The spread of strength results produced with sodium silicate solution bonds was greater than that associated with bonds formed with other solutions, as can be seen from figure 3.13.

In previous studies concerning the bonding of pieces of fused silica with sodium silicate solution, an average breaking strengths of 18 MPa was recorded [157]. Studies that used sodium silicate solution to bond pieces of silicon, an average breaking strength of 36 MPa [158] was recorded. In both cases, the reason for the lower strength is probably the lower stiffness or lower strength (or both) of the substrate material.

3. Hydroxide catalysis bonding of sapphire

Comparable tests carried out by Dari *et al* [182] and Suzuki *et al* [183] found a mean value of strength of 1.5 MPa and 6.5 MPa, respectively. The difference in strength may be due to the choice of bonding solution (the strengths found by Suzuki *et al* when using KOH bonding solution are similar to some of the strengths measured in the experiments described above when using the same solution), although it may also be that alternative sets of strength testing apparatus led to unexpected additional forces being applied to the samples, which are not applied in the case of the four-point bending test, causing the bonds to break at lower strengths than they otherwise might [159].

In summary, using the bonding procedure and strength testing procedure detailed in the preceding sections, it is clear that while any of the chemicals can be used to create reliable and strong bonds, sodium silicate solution gives the best results in terms of bond strength. This is true of bonds at room temperature and at liquid nitrogen temperatures. In the following chapters all bonds formed between sapphire samples were produced with sodium silicate solution for this reason.

4. Further experiments involving the strength of sapphire hydroxide catalysis bonds

4.1. Introduction

Following the findings detailed in Chapter 3, sodium silicate solution was chosen for use for further investigations into bonds between sapphire samples, given that it was used to produce the bonds with the greatest tensile strengths, of the solutions tested. Four experiments are detailed here, aimed at investigating;

1. the effect of bonding pieces of sapphire where the crystalline planes do not match across the bond
2. the effect of thermal cycling on bond strength
3. the possibility of re-bonding pieces that have previously been bonded and separated
4. the effect of different bond curing times on bond strength.

4. Further experiments involving the strength of sapphire hydroxide catalysis bonds

Together, the results from this set of experiments help to inform the suspension design for sapphire-based gravitational wave detectors.

4.1.1. Crystalline axes of sapphire

The crystalline structure of sapphire is considered here in terms of whether it may influence the strength of hydroxide catalysis bonds formed between sapphire samples with different crystal orientations.

Sapphire has a hexagonal crystal structure [178]. For the purposes of developing gravitational wave detector suspensions, there are three crystal planes that are of interest: a (1120), m (1010) and c (0001) (see figure 4.1) [178]. The thermal and mechanical properties of sapphire vary depending on the crystal cut and this may have an effect on strengths (and other properties such as thermal conductivity) of bond material formed between sapphire surfaces of different crystal orientation. Additionally, it may be more difficult to form bonds with some crystal planes than with others if, for example, the bonding solution is less effective at etching a given plane (certainly this is the case for some chemical etchants of sapphire [188]).

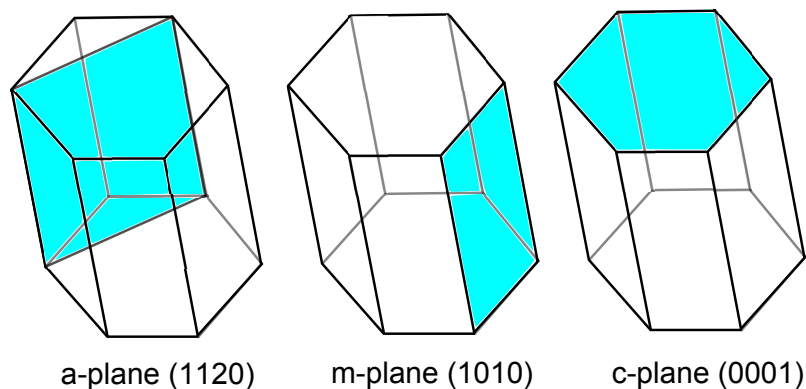


Figure 4.1.: A diagram of three of the crystal axes of sapphire. The planes highlighted in blue (a, m and c) are those of interest for fabrication of sapphire-based suspensions for gravitational wave detectors.

4. *Further experiments involving the strength of sapphire hydroxide catalysis bonds*

As such, it is important to understand the behaviour of bonds formed between sapphire pieces of various crystal orientations, both when those orientations match across the bond and when they do not.

4.1.2. Sapphire test mass suspensions in KAGRA

The sapphire suspensions for KAGRA [180, 189] will take a slightly different form to the suspensions for aLIGO [99] because single crystal sapphire cannot easily be joined through heating in such a way that the crystal structure is unchanged. As such, joining the pieces of sapphire suspensions in this way is not an option the way that welding fused silica suspensions is. This means there will be no “weld horns” (see section 3.1.1) on the attachment pieces between test mass and suspension fibres. Hence, some other solution is required to connect these parts. The current solution is to use attachment pieces with notches, allowing the use of fibres with “nail heads” to slot into these and thus suspend the test mass (see figure 4.2 [180]). In this design, hydroxide catalysis bonds would be formed between the attachment pieces and the sides of the test masses.

For this design the face of the test masses will be parallel to the c -plane of the sapphire crystal (i.e. the c -axis of the crystal is the cylindrical axis of the test mass) and the length of the sapphire fibres will be orthogonal to their c -planes (i.e. the c -axis of the fibre crystals is the cylindrical axis of the fibres) [167]. This implies that, at some point, sapphire pieces must be bonded such that the crystalline planes do not match. This will likely mean a c - a -plane interface, or a c - m -plane interface. Hence, the properties of bonds between sapphire pieces of different crystalline orientation are of particular interest for the KAGRA suspensions.

4. Further experiments involving the strength of sapphire hydroxide catalysis bonds

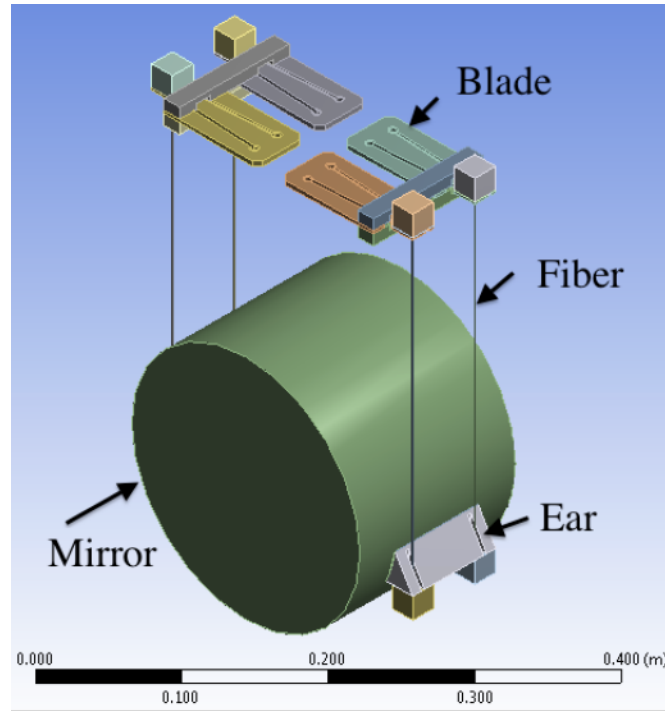


Figure 4.2.: A simplified diagram of the KAGRA sapphire test masses suspensions with attachment pieces for sapphire fibres with nail heads to slot into [180]. Hydroxide catalysis bonds join the ears and mirror at a flat section (not shown).

4.1.3. Strength testing

In this chapter two different measurements of bond strength are considered; bond tensile strength and bond shear strength. All the tensile strengths measured in this chapter were measured at room temperature while the shear strength tests were carried out at ~ 10 K. In general, the shear strength is expected to be less than the tensile strength, and A A Griffith concluded that, with respect to its capacity to cause failure, tensile stress represents a more important influence than compressive stress [190, 191]. However while this is true for ductile materials, it may not always be the case for brittle materials such as sapphire, and there will certainly be some dependence on crystal axis, as the results in this chapter suggest. This provides a potential cause of differences between the measured tensile and shear strengths in this thesis and should be considered when comparing shear strength results to tensile strength results. All of the shear strength measurements were carried out at liquid helium temperature. Measuring tensile strength and shear strength requires two different sets of apparatus.

Strength testing: Tensile strength

Bond tensile strength for this set of experiments was tested in the same way as in section 3.6, using the 4-point bend test. In the experiments described in this chapter, tensile strength was measured exclusively at room temperature to allow comparison with the room temperature strength measurements described in the previous chapter. In some cases, samples had a different geometry to those used in Chapter 3; in all cases, the geometry of the samples used is detailed in the relevant sections.

Strength testing: Torsional strength

Since the suspensions that will utilise these bonds will operate at cryogenic temperatures, the torsional strength tests were carried out at $\sim 4\text{K}$. The torsional strength tests described here took place at the High Energy Accelerator Research Organisation in Tokyo, Japan (this facility is also known as KEK). A custom built system was used which had previously been used to carry out room temperature measurements of shear strength [183]. This set up was designed to test the torsional strength of one bond at a time with the option of inserting the apparatus directly into a liquid helium dewar, hence allowing the bonds to be tested at cryogenic temperatures. However, it is also possible to use the apparatus in air, should room temperature measurements be desired. See figure 4.3 for a diagram and a photograph of this apparatus.

To measure the bond shear strength, a torque is applied to the top of the apparatus, rotating a long metal bar and the upper sample, with respect to the lower part of the apparatus and the lower sample. The maximum torque applied before the bond between the samples breaks is measured with a torque meter (Sugisaki-keiki co. DI-9 IP5RG).

4. Further experiments involving the strength of sapphire hydroxide catalysis bonds

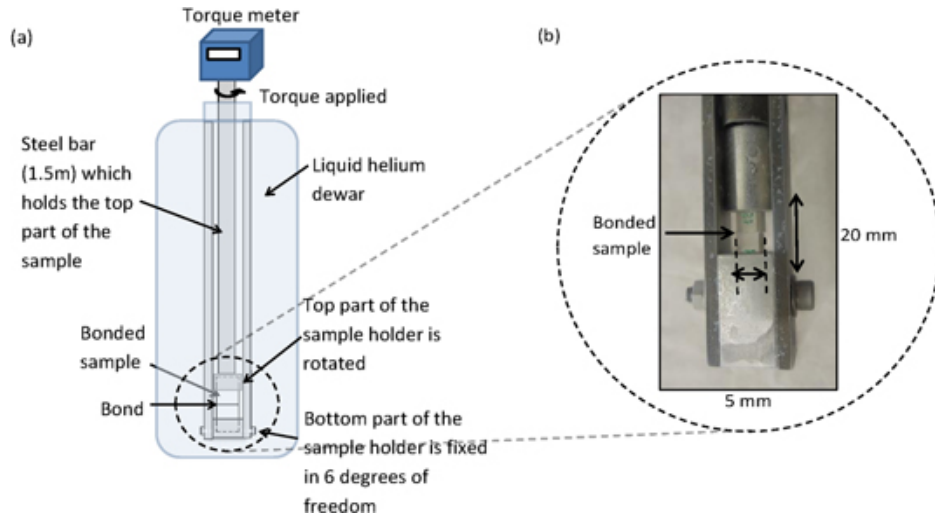


Figure 4.3.: Apparatus used to measure torsional shear strengths of hydroxide catalysis bonded sapphire samples at liquid helium temperatures. a) a schematic diagram of the apparatus, b) a photograph of an example of a pair of bonded samples ready for strength testing.

The design features an outer tube with a stop at the bottom in which the bottom half of the sample fits. The top half of the sample fits into the inner rod which has a close fit with the outer tube and to which a torque load is applied. Thus any sample misalignment is minimised which allows, as far as possible, only the effect of the shear forces acting on the bond to be measured. However, due to the close fit some frictional forces are associated with the strength testing procedure as it is necessary for the stationary and rotating parts to move past each other. To measure the effect of these frictional forces, the procedure is carried out several times with no sample in the apparatus to measure the torque necessary to overcome the frictional force. The torque required to break the bond can then be found from,

$$T = T_{\text{applied}} - T_0 \quad (4.1)$$

Where T is the torque required to break a bond, T_{applied} is the torque actually applied to rotate the pieces of the apparatus with a pair of bonded samples inserted into it, and T_0 is the torque needed to overcome the frictional forces associated with the rotation.

4. Further experiments involving the strength of sapphire hydroxide catalysis bonds

The shear stress of the bond at breaking point, τ , can then be found from this torque measurement and is dependent on the cross sectional area of the bond. In the experiments described in this chapter, there are two possible bond cross sectional areas; 5×5 mm and 5×10 mm. The shear stress across the bond layer is not uniform and is concentrated at the edges with a minimum in the bond centre (see figure 4.4).

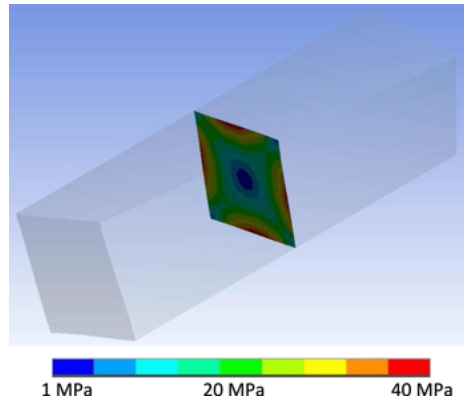


Figure 4.4.: Results of a finite element analysis model built by Haughian et al [192], demonstrating that the stress across the bond is not uniformly distributed.

The maximum shear stress can be calculated using Prandtl's membrane analogy (see equation 4.2) and was confirmed with Roark's formulas for stress and strain [193, 190].

$$\tau_{\max} = \frac{T}{\alpha ab^2} \quad (4.2)$$

where α is a constant related to the ratio of the length, a , to the width, b , of the cross sectional area, for example, in the case of a bond layer where $a = b$, $\alpha = 0.208$ [193, 190] and where $a = 2b$, $\alpha = 0.246$.

4.2. Influence of crystalline orientation on bond strength

To study the effect of the orientation of the sample crystalline axes on bond strength a set of 150 sapphire samples with dimensions $5 \times 5 \times 10$ mm were procured by collaborators in Japan from MolTech¹ for a series of bonding experiments. Of these, 50 samples were cut such that the a-plane of the sapphire crystal was parallel to the 5×5 mm bonding surface, 50 were cut such that the c-plane was parallel to the bonding surface and 50 were cut such that the m-plane was parallel to the bonding surface. The samples did not have chamfers. The 5×10 mm faces were produced with a ground finish while the 5×10 mm face not intended for bonding was polished to an optically clear finish and there was a superior polish on the intended bonding surface (a flatness of <60 nm was intended for the bonding faces). See figures 4.5 and 4.6 for diagrams of the samples' dimensions and a photograph of an example of one the samples, respectively.

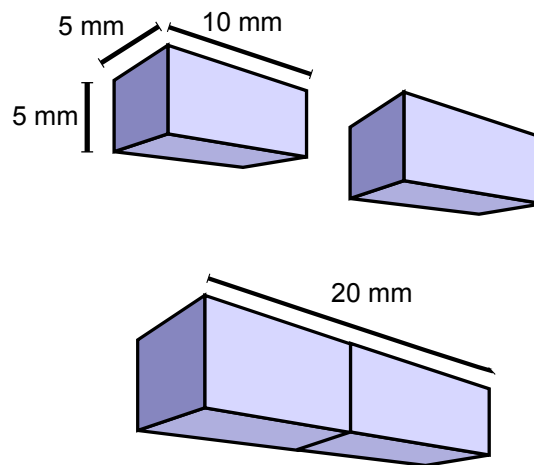


Figure 4.5.: Diagram of the dimensions of the sapphire samples for hydroxide catalysis bonding experiments with different crystal axis orientation.

As in the previous set of experiments detailed in Chapter 3, the samples were inspected for their suitability for bonding. Their dimensions were measured with calipers, the bond surface flatness of each sample was measured with a ZYGO GPI XP/D interferometer and the roughness of each sample was measured with a Wyko NT1100 Optical surface profiler from Veeco. Significant differences were found in the quality of the flatness polish

¹<http://www.mt-berlin.com/>

4. Further experiments involving the strength of sapphire hydroxide catalysis bonds

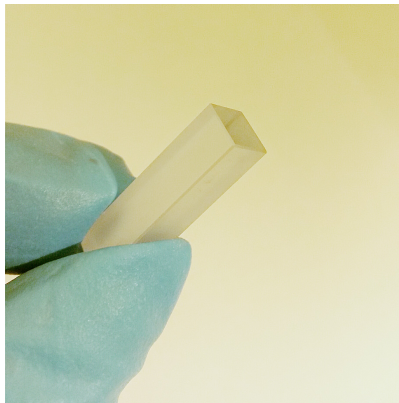


Figure 4.6.: Photograph of an example of one of the sapphire samples for hydroxide catalysis bonding experiments with different crystal axis orientation. This sample has a polished bonding surface parallel to the c-plane of the sapphire crystal.

between the different crystal cuts. Additionally, these samples were less flat than those ordered from Crystran for other experiments (see section 3.4.1 for a description of these samples). The samples for which the intended bonding face was parallel to the c-plane had a mean flatness of 101 nm (with a standard deviation of 69 nm and a standard error of 10 nm). The samples for which the intended bonding surface was parallel to the a-plane had a mean flatness of 260 nm (with a standard deviation of 104 nm and a standard error of 15 nm). The samples for which the intended bonding surface was parallel to the m-plane had a mean flatness of 241 nm (with a standard deviation of 121 nm and a standard error of 17 nm).

As in previous experiments, each sample was labeled with an identification number and for each sample the measured dimensions and flatness were recorded so that they could easily be recovered at a later date. The samples with the flattest bonding surfaces were chosen for use in experiments investigating the effect of bonding samples with different crystal orientations. Of these, the c-plane samples had a mean flatness of 86 nm (with a standard deviation of 20 nm and a standard error of 3 nm), the a-plane samples had a mean flatness of 122 nm (with a standard deviation of 24 nm and a standard error of 8 nm) and the m-plane samples had a mean flatness of 91 nm (with a standard deviation of 29 nm and a standard error of 10 nm). See figures 4.7–4.9 for histograms showing the flatnesses of all of the samples measured for these experiments.

4. Further experiments involving the strength of sapphire hydroxide catalysis bonds

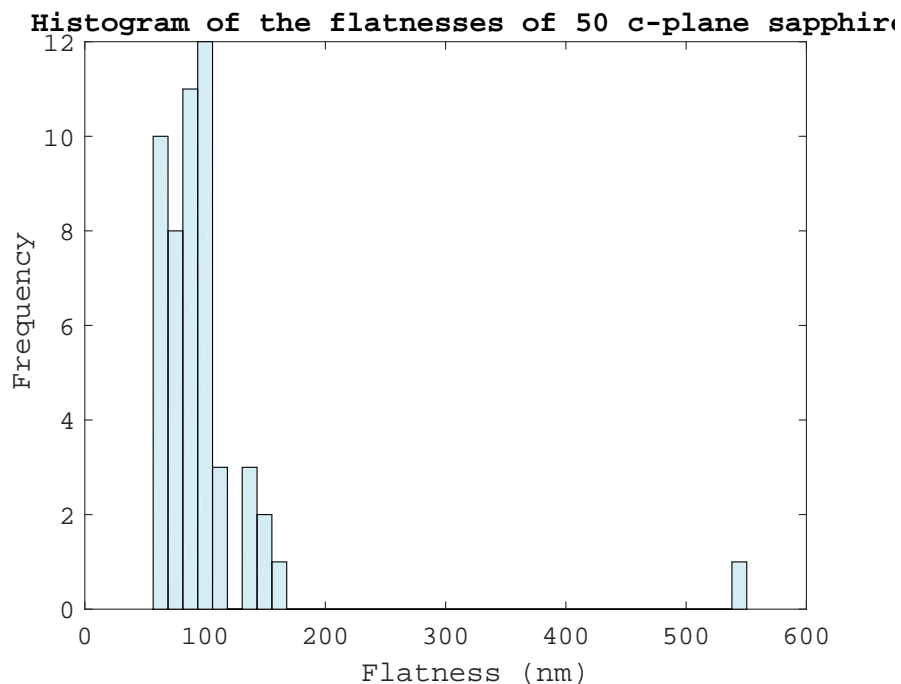


Figure 4.7.: Histogram showing the spread in flatnesses of the 50 c-plane sapphire samples.

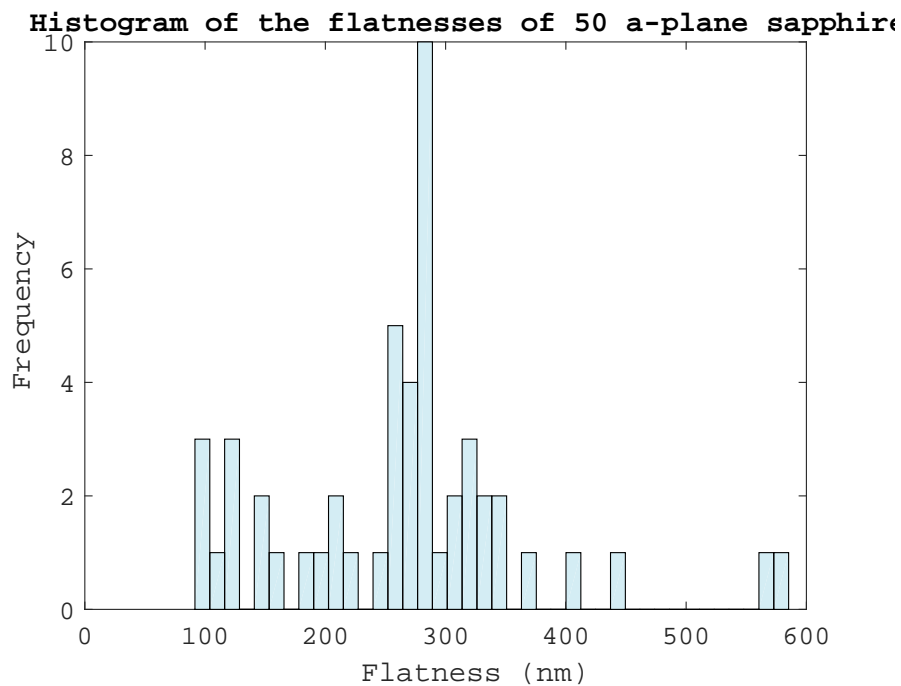


Figure 4.8.: Histogram showing the spread in flatnesses of the 50 a-plane sapphire samples.

4. Further experiments involving the strength of sapphire hydroxide catalysis bonds

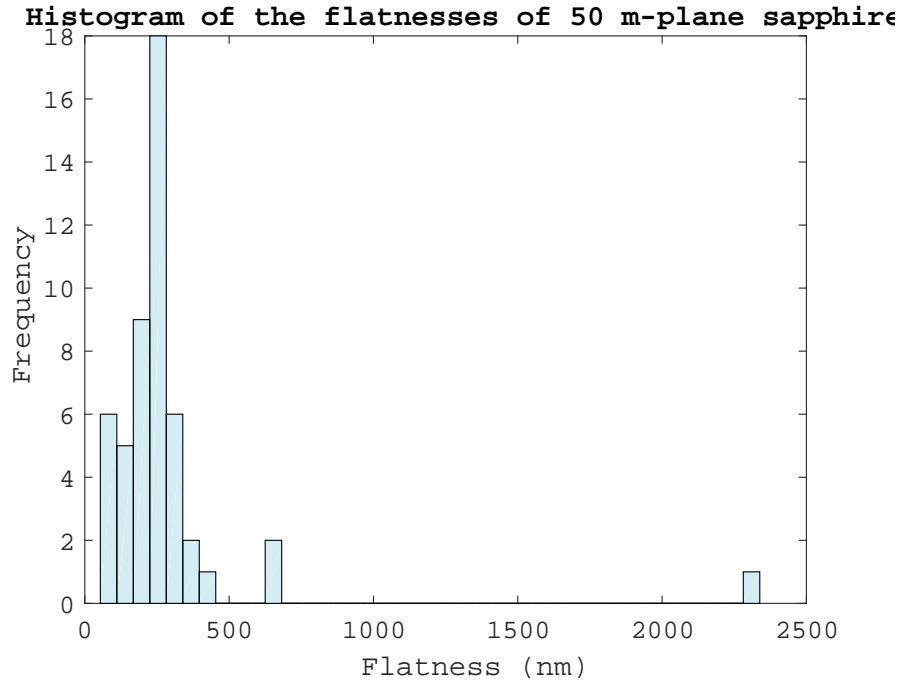


Figure 4.9.: Histogram showing the spread in flatnesses of the 50 m-plane sapphire samples.

Additionally, a subset of the samples' bonding surfaces were measured for roughness - ten of each type were measured. The c-plane samples had a mean Ra roughness of 4.2 nm, compared to 15.9 nm for the a-plane samples and 5.4 nm for the m-plane samples.

A total of 27 bonds were produced; 9 a-plane to c-plane bonds, 9 m-plane to c-plane bonds and 9 c-plane to c-plane bonds. These combinations were deemed to be of the most immediate interest for the KAGRA suspensions. The bonds were produced at room temperature in a clean room environment in Glasgow and were allowed to cure at room temperature for one week before being transported to Tokyo. In Tokyo they were allowed to cure at room temperature for a further 4 weeks before the bond strengths were tested. As in previous experiments, some samples contained bubbles and other unbonded regions within the intended bond surface.

Since any imperfect bonds would not be used in the construction of a real detector, these bonds were excluded from the strength results presented in section 4.2.2. In the end, this resulted in strength measurements for 5 a-plane to c-plane, 8 m-plane to c-plane and

4. Further experiments involving the strength of sapphire hydroxide catalysis bonds

7 c-plane to c-plane bonds. The procedures for producing the bonds were the same as those described previously in Chapter 3 (see sections 3.2.1, 3.2.3 and 3.4.3).

4.2.1. Shear strength measurements

The shear strength testing apparatus (see section 4.1.3) was first tested five times without the bonded samples to find a value for the torque required to overcome the frictional forces associated with moving the apparatus parts. This value, T_0 , found in this case to be 0.058 ± 0.0005 Nm, which would correspond to a shear strength of 1.2 MPa - this is small compared to the values measured for shear strength of the bonds, as shown in section 4.2.2, where a mean strength of 66 MPa was found.

Each pair of bonded samples was secured in the strength testing apparatus (see section 4.1.3), which was then inserted into a liquid helium dewar, allowing the liquid helium to wet and cool the samples. The apparatus was inserted into the helium slowly to avoid thermally shocking the bonds or the sapphire substrate. The samples were fully submerged within ~ 2 -3 minutes. This process causes some liquid helium to boil off, since the samples were previously at room temperature. When this boiling off of helium had visibly ceased (the boiling motion reduces drastically with time) it was considered that thermal equilibrium between the samples and the helium had been achieved.

4.2.2. Results

The measured shear strengths of the bonds at ~ 4 K are shown in figure 4.10. It can be seen that the bonds between a-plane to c-plane bonded sapphire pieces have similar measured shear strengths to the bonds between m-plane to c-plane bonded sapphire pieces (see figure 4.10 and table 4.1). However, the spread of results for both data sets is quite

4. Further experiments involving the strength of sapphire hydroxide catalysis bonds

wide. In both of these data sets every bond produced would have sufficient strength for use in a typical gravitational wave detector suspension [147], including in the KAGRA suspensions for which a strength of 1 MPa is sufficient [180].

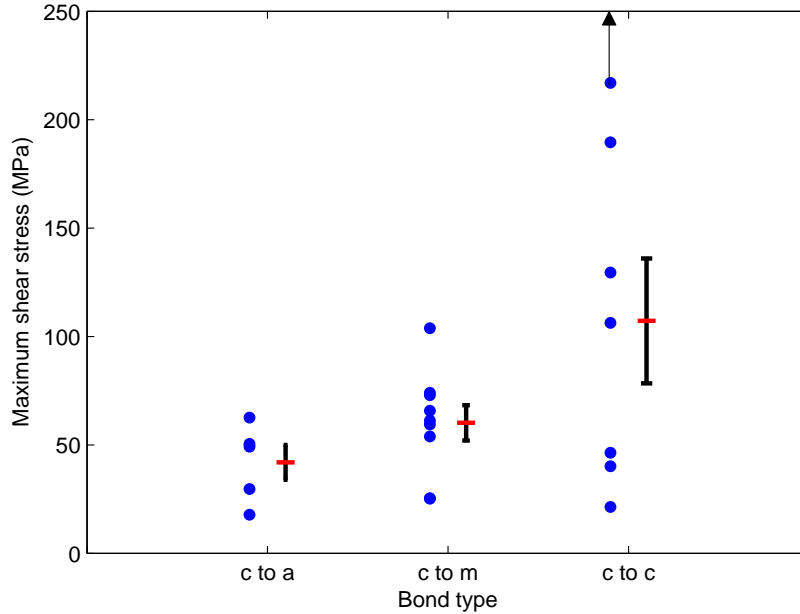


Figure 4.10.: Shear strength results obtained for bonded sapphire samples at liquid helium temperature. The results from three sets of bonds between sapphire samples with different crystal orientations are shown. Strengths were measured at ~ 4 K. An arrow shows a bond which overloaded the torque meter and could not be broken - this measurement has been removed from the results and from calculations of the mean, standard deviation and standard error.

Table 4.1.: Table of breaking torsional strengths for hydroxide catalysis bonds between sapphire samples with different crystal orientations are shown. All strengths reported here were measured at ~ 4 K.

Axes bonded	Strength (MPa)			σ	$\frac{\sigma}{\sqrt{N}}$
	Mean	Minimum	Maximum		
a-plane to c-plane	42	18	63	14	5
m-plane to c-plane	60	25	104	24	8
c-plane to c-plane	89	21	190	65	26

The bonds between the c-plane to c-plane sapphire samples had a higher average shear strength at ~ 4 K but also exhibit a wider range of strengths than the bonds between mis-matched crystalline axes. Of particular interest is the data point in figure 4.10 indicated with an arrow. This is the strength recorded for a bond that could not be broken with the strength testing. The maximum torque that can be measured using this

4. Further experiments involving the strength of sapphire hydroxide catalysis bonds

kind of torque meter is 5.7 Nm which, after subtracting the frictional effect (see section 4.2.1) corresponds to a shear strength of 217 MPa, so this bond must have at least that strength. In the results shown in table 4.1, this result has been removed from calculations of the mean, standard deviation and standard error and is only included in the plot in figure 4.10 for completeness.

Care should be taken when interpreting these results and comparing them to those shown in Chapter 3 and the other sections of this chapter. These are the only strength results for which sapphire samples of different crystalline axes were bonded and they are the only results for which those bonds were broken at liquid helium temperatures. Additionally, they are the only shear strength results and the bond geometry is not the same as that used for other experiments (a bond area of 5×5 mm is used here, compared to 5×10 mm elsewhere). What the results do suggest is, that for shear strengths of bonds at cryogenic temperatures, a-plane to c-plane bonds have similar strengths to a-plane to m-plane bonds, while c-plane to c-plane bonds appear to be stronger. While the cross axis bonds were, on average, less strong than the m-plane to m-plane bonds discussed in Chapter 3 it is unclear whether this is because of the different crystal planes, the different type of strength measured, the temperature, the sample geometry, or something else.

4.2.3. Conclusions

Bonds between sapphire samples with different crystal orientations show very promising strengths. With the information available here, should a suspension require bonds to be formed between sapphire pieces of different crystalline orientation, either c-plane to a-plane or c-plane to m-plane bonds are suitable choices, even with a significant safety factor [147] including for instruments such as KAGRA, which has a design which requires strengths of not less than 1 MPa [180]. The advantage of such a great safety factor is that if it were found that the mechanical loss of the bond layer were too high to allow the

4. Further experiments involving the strength of sapphire hydroxide catalysis bonds

detector suspensions to meet the thermal noise budget, the size of the bond area could be adjusted such that the bond's contribution to the thermal noise could be reduced.

The distribution of bond shear strengths exhibited by bonds produced between two sapphire c-planes is interesting; this is where both the strongest and weakest bonds were produced. It is currently unclear what the cause of this strength distribution is. A lack of available samples prevented a repeated set of tests to improve the statistics but investigating this further would be of interest.

4.3. Thermal cycling experiments

It is likely that in any detector intended for cryogenic operation the suspensions will be thermally cycled several times during its installation and operation. Thermal cycling will result in successive expansions and contractions of the suspension parts, and the bond material and sapphire can be assumed to have different thermal expansion coefficients. It is therefore important to understand whether such thermal cycling will have an impact on bond strength, especially since it might be expected that repeated stresses caused by different rates of expansion could have a detrimental effect.

4.3.1. Bonds for thermal cycling experiments

A set of 16 of the sapphire samples described in section 3.4.1 were used to make 8 bonds between the samples' m-planes for these experiments (see figure 3.5 for a diagram showing these samples). The bonds were made with sodium silicate solution at room temperature and in a clean room environment. The procedures for preparing bonding solution, cleaning the sample surfaces and forming the bonds were the same as those

4. Further experiments involving the strength of sapphire hydroxide catalysis bonds

described previously in Chapter 3 (see sections 3.2.1, 3.2.3 and 3.4.3). The bonds were cured for four weeks at room temperature. As in previous experiments the quality of the bonds were visually inspected and any bubbles or unbonded regions across the intended bonding surface were noted. In this set of experiments no bonds had any bubbles or unbonded regions which took up >10% of the intended bonding surface.

When the bonded samples were in the cryostat, their temperatures were lowered to ~ 10 K and were then allowed to increase naturally back to room temperature. They were slowly cycled this way three times; each cycle was carried out over a time period of one week. The bonded samples were then removed from the cryostat and the bond quality was visually inspected a second time. In this set of experiments the quality of the bonds was not noted to change after thermal cycling.

4.3.2. Strength testing

As with experiments detailed in the previous section and in Chapter 3, the tensile strengths of the bonds were measured using the 4-point bend test (see section 3.6). These tests were carried out at room temperature.

4.3.3. Results

In figure 4.11, the tensile strengths of the thermally cycled bonds are shown along with sodium silicate bonds from Chapter 3, to allow comparison with bonds which were not thermally cycled. The mean tensile strength of the bonds broken after three thermal cycles was 36 MPa, compared to a mean tensile strength of 74 MPa for bonds which were not cycled. A summary of the mean, minimum and maximum measured strengths for thermally cycled bonds, compared to un-cycled bonds, is presented in table 4.2.

4. Further experiments involving the strength of sapphire hydroxide catalysis bonds

Table 4.2.: Table of breaking strengths for sodium silicate hydroxide catalysis bonds between sapphire samples, comparing strengths of bonds which were thermally cycled to those which were not.

Thermal cycles	Breaking temperature (K)	Strength (MPa)			σ	$\frac{\sigma}{\sqrt{N}}$
		Mean	Minimum	Maximum		
3	293	36	27	49	14	6
0	293	74	53	91	8	3

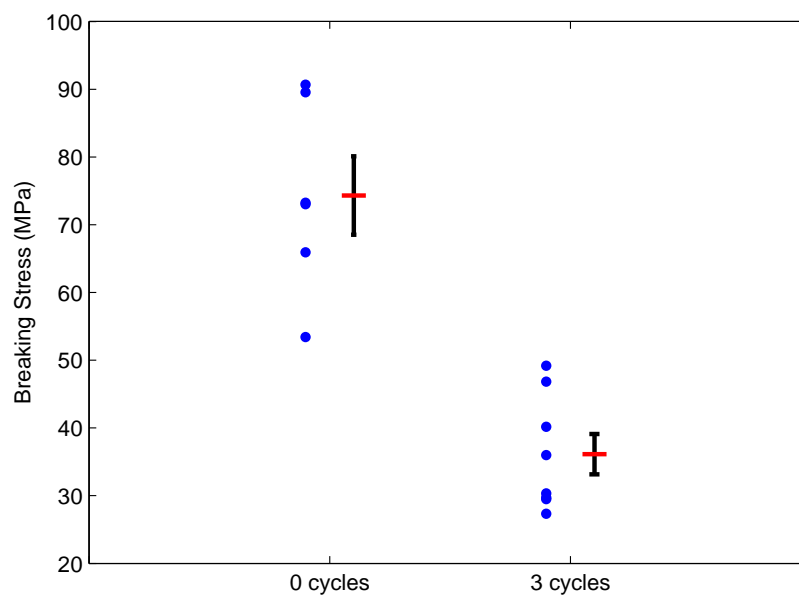


Figure 4.11.: Temperature effects on tensile strength of hydroxide catalysis bonded sapphire. Bonds were formed between m-planes of the sapphire pieces. Blue points show the strengths of individual bonds, red lines show the mean of a set of bonds and the error bars are one standard error on the mean.

4.3.4. Conclusions

Thermal cycling of the bonds does, in this case, appear to have led to a reduction in the average bond tensile strength measured, compared to previous sets of bonds which were not thermally cycled. Only three cycles were carried out and it is not understood whether this effect would continue to reduce the strength with further cycles, or not. However, it should be noted that even 27MPa is strong enough for such bonds to be used in typical suspensions [147] including a KAGRA suspension which has the requirement that any hydroxide catalysis bond between sapphire pieces must have a minimum strength of 1 MPa [180]. With just three thermal cycles, any trends associated with the number of thermal cycles carried out and the final bond strength are unclear. On the other hand, since typical detectors are likely to go through many more than three cycles (the initial LIGO detector had 6 data taking runs and aLIGO will have at least 5, for example) this result strongly suggests the need for further research.

It should also be noted that the standard error on the mean of the strength of thermally cycled bonds is lower than that of the bonds which did not undergo thermal cycling and that there is overlap between the strengths measured in the two data sets. More research is needed both to improve the statistics on this measurement and to consider the effect of further thermal cycles (perhaps to 10 or 20 cycles) to discover whether the strength will continue to be reduced as more cycles are carried out.

4.4. Repair of damaged bonds

It was noted that in the majority of cases (>85%) the bonds between the Crystran sapphire samples, used for experiments described in sections 3.4.1 and 4.3, broke cleanly with no damage to the bulk of the sapphire samples themselves (see figure 4.12 for

4. Further experiments involving the strength of sapphire hydroxide catalysis bonds

photographs comparing samples where the bond broke cleanly and those where the bulk of the sapphire was damaged). This is not usually the case when bonding and strength testing bonds produced with other materials, for example, fused silica or silicon, where chips and cracks in the bulk of the samples are common [157, 186]. One possible reason for this is that the bulk strength of sapphire is considerably higher than the bulk strength of fused silica (sapphire has a bulk modulus of ~ 250 GPa at room temperature [178] where fused silica has a bulk modulus of ~ 69 GPa [194]).

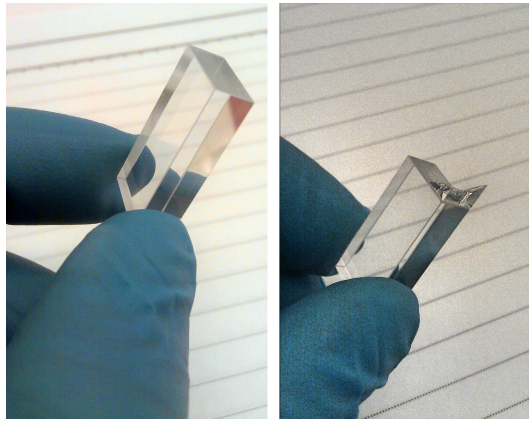


Figure 4.12.: Photographs comparing a sample not damaged by the strength testing procedure (left) to a sample which was damaged (right).

Since the surfaces of the samples were not obviously visibly damaged this was considered interesting from the perspective of potential repairs. If a surface which has previously been used for bonding can be successfully re-bonded this may be very useful. It would allow for bonds to be remade if they were found to be visually imperfect or if they were damaged at a later date. All of the bonds described in this section were produced using sapphire samples that had previously been bonded in the experiments described in sections 3.4.1 and 4.3. Sodium silicate solution was used to produce all bonds, as in previous sections of this chapter, since it was the solution which was used to produce bonds with the greatest strengths of the solutions studied in the previous chapter.

4.4.1. Re-bonding procedures

Those samples which were used in Chapter 3 and survived the four-point-bending test without chips or cracks appearing in their surfaces were further studied to determine whether they would be suitable for re-bonding experiments. Their surface flatnesses and roughnesses were remeasured and compared to those measured before bonding. It was found that the surface flatness measurements still gave values which would ordinarily be considered acceptable for bonding.

Therefore, 20 samples previously bonded with sodium aluminate, 6 samples previously bonded with potassium hydroxide and 16 samples previously bonded with sodium silicate (as described in Chapter 3) were then cleaned according to the standard cleaning procedure described in section 3.2.1.

A smaller subset of 16 samples (of which 12 were previously bonded with sodium silicate solution and 4 were previously bonded with potassium hydroxide) were first submerged for ten minutes in buffered hydrofluoric acid (HF). HF etches sodium silicate, but does not readily etch sapphire [195] so soaking the samples in this solution was intended to remove any lingering residue of the bonding material which might otherwise prevent bonds from forming properly [196, 195]. Following the HF clean the samples were also cleaned according to the standard cleaning procedure.

The samples were then bonded with sodium silicate solution at room temperature and the bonds were allowed to cure at room temperature for between 4 and 5 weeks (as according to section 3.2.3). After this curing time the bonds were broken using the 4-point bend test to determine the bond tensile strength. Unlike the other bonds described in this chapter and in Chapter 3, any change in bond quality over repeated rounds of bonding and strength testing is of interest. Therefore, poorer quality bonds (i.e. those in which 10% or more of the bond surface contains bubbles or unbonded regions) are included in

4. Further experiments involving the strength of sapphire hydroxide catalysis bonds

the strength testing results. These are indicated by circled points in the results presented in section 4.4.3.

Of the samples tested after having been bonded twice, 8 samples bonded using sodium aluminate in the first round, 3 samples bonded with sodium silicate in the first round and 3 samples bonded with potassium hydroxide in the first round were suitable for re-bonding a third time after strength testing separated them. They were all cleaned using cerium oxide, bicarbonate of soda and methanol using the standard cleaning procedure (HF was not used). They were then bonded using sodium silicate solution at room temperature. The bonds were cured at room temperature for 5 weeks before strength testing for the third time.

4.4.2. Investigating changes in surface conditions

It was expected that, by monitoring the conditions of the sample surfaces in terms of flatness and roughness, some light might be shed on any changes in strength of bonds between subsequent rounds of bonding and separating samples. For this reason, the conditions surfaces of a subset of all the samples bonded were studied at each stage. This had the added advantage that any samples with damaged surfaces, for example, those which developed chips or cracks as a result of the strength testing process, could be rejected from future rounds of bonding. It would potentially also highlight any differences due to the different chemical effects of the initial bonding solutions used.

The surface flatnesses tended to not exhibit obvious differences between each round of bonding in terms of the peak-to-peak flatness values and the overall flatness profile also changed very little, with only minor possible changes near the edges of the bonding surface (see figure 4.13 for an example of this). These minor changes may have been the result of bonding material residue left behind on the sample surfaces.

4. Further experiments involving the strength of sapphire hydroxide catalysis bonds

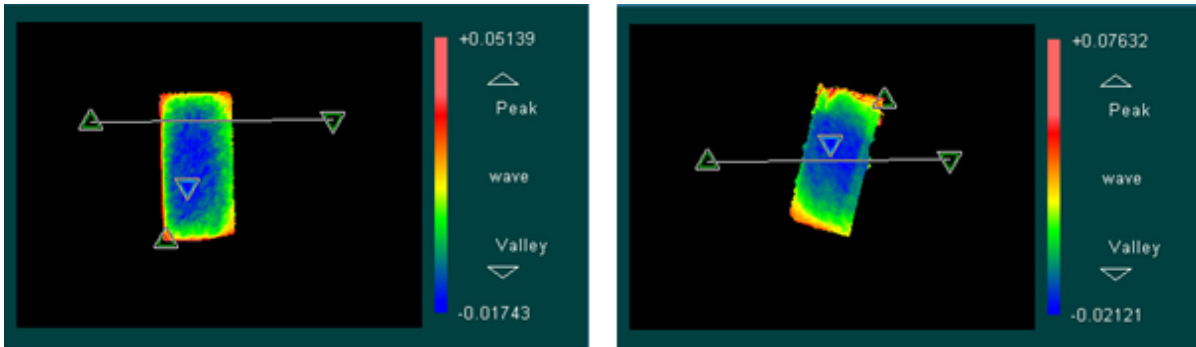


Figure 4.13.: Surface flatness images taken with a Zygo GPI XP/D interferometer showing the global flatness of a sapphire sample bonding surface. Left: a pristine sample, Right: the same sample after bonding and breaking three times.

The roughness measurements show a little more detail. Measurements were taken at 2.5x magnification (measuring a 1.9 x 2.4 mm area) using a Wyko NT1100 Optical surface profiler from Veeco. All of the profile images were plotted as surface plots over a 40 nm height range in order to allow a direct comparison between different surfaces between the rounds of bonding. An example of two such images can be seen in figure 4.14. Very little effect on roughness numbers was observed. It was noted that in some cases features (such as spikes or pits) developed on the surfaces as successive rounds of bonding were carried out. The roughness profiles were categorised as those which had no features, those which had clear features, and those which had minor features (see table 4.3).

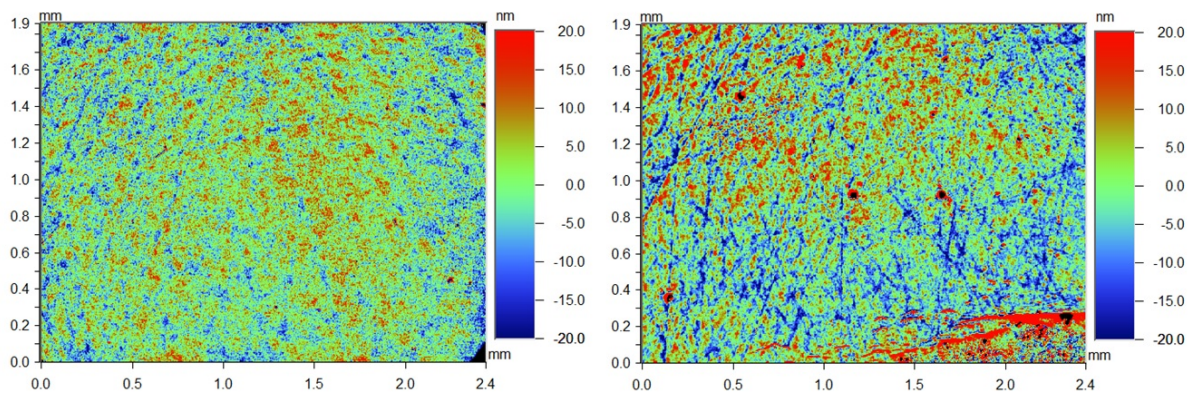


Figure 4.14.: Left: Example of a roughness profile of the surface of a typical pristine sample showing no features on the surface. Right: Roughness profile of the same sample after having been bonded twice with sodium silicate solution, showing marks, spikes and other features.

4. Further experiments involving the strength of sapphire hydroxide catalysis bonds

Table 4.3.: Summary of the analysis of roughness surface profile images

1st bond with		Cleaning	Number of images	Images without features	Images with possible features	Images with features
Pristine	N/A	Standard	78	66 (85%)	0 (0%)	12 (15%)
Bonded once	NaAlO ₂	Standard	None	N/A	N/A	N/A
	NaOH	Standard	None	N/A	N/A	N/A
	Na ₂ SiO ₃	Standard	25	6 (24%)	4 (16%)	15 (60%)
	KOH	Standard	19	11 (58%)	2 (11%)	6 (31%)
Bonded twice	NaAlO ₂	Standard	20	16 (80%)	2 (10%)	2 (10%)
	NaOH	Standard	15	12 (80%)	3 (20%)	0 (0%)
	Na ₂ SiO ₃	Standard	30	15 (50%)	3 (10%)	12 (40%)
		HF	11	6 (55%)	0 (0%)	5 (45%)
		Standard	3	3 (100%)	0 (0%)	0 (0%)
		HF	3	3 (100%)	0 (0%)	0 (0%)
Bonded 3 times	NaAlO ₂	Standard	10	6 (60%)	2 (20%)	2 (20%)
	Na ₂ SiO ₃	Standard	None	N/A	N/A	N/A
	KOH	Standard	None	N/A	N/A	N/A

4. Further experiments involving the strength of sapphire hydroxide catalysis bonds

Table 4.3 shows the results of counts of roughness images with or without features. The table is not complete due to missing data in certain areas. From this table it can be observed that 15% of images show features on the surfaces of pristine samples (i.e. the samples before they had ever been bonded). Of the samples which had been bonded once with sodium silicate solution a larger number of samples showed features (60%). In comparison, a slightly lower, but still raised number of samples (31%) showed features after bonding once with potassium hydroxide.

The number of roughness surface profile images showing features after having been bonded twice was then reduced again with 0% showing features for potassium hydroxide (although there were very few samples available here), 10% showing features for sodium aluminate and 20% showing possible features for sodium hydroxide. This is similar to the number of roughness surface profile images showing features for the pristine samples. The number of roughness surface profiles showing features for samples bonded twice with sodium silicate is 40% which, while raised, is lower than the number observed after the just one round of bonding.

This method of analysing changes to the surfaces is likely to be limited by the number of samples under study and as a result of this is hard to draw any statistically significant conclusions. However, it is clear that the surface quality of samples bonded with sodium silicate solution are affected more than when any of the other bonding solutions are used - while the exact mechanism is unclear, it is possible that sodium silicate solution more successfully etches the bonding surfaces than the other solutions do, this would explain both the greater strength of sodium silicate bonds, and the difficulty in producing new, high quality bonds between samples that have been bonded with sodium silicate solution in the past. It is not clear whether the use of HF to clean the samples has any effect.

4.4.3. Results and observations

The measured tensile strength of the bonds, as a function of the number of times a pair of samples have been bonded, is shown for the three different initial bonding solutions in figures 4.15-4.17. Note that, in figure 4.15, the temperatures shown indicate the temperature at which the bonds were broken in the first round of bonding and strength testing - all subsequent rounds of strength testing were carried out at room temperature. The same information is also given in tables 4.4–4.6 for clarity.

Table 4.4.: Table of breaking strengths for hydroxide catalysis bonds between sapphire samples produced with pristine samples and various bonding solutions, broken either at room temperature or at 77 K.

Number of bonds	Chemical used	Temp of strength test (K)	Strength (MPa)			σ	$\frac{\sigma}{\sqrt{N}}$
			Mean	Minimum	Maximum		
10	Sodium silicate	293	74	53	91	18.3	5.8
9	Sodium silicate	77	73	38	89	22.5	7.5
10	Potassium hydroxide	293	16	7	58	15.0	4.7
10	Sodium aluminate	293	14	7	17	3.3	1.1

For the samples bonded with sodium silicate solution (figure 4.15) during the first round the measured tensile strength of the bonds goes down significantly (from ~ 65 MPa to ~ 30 MPa) where a large number of samples also had an imperfect bond. In contrast to this, for the samples bonded with sodium aluminate and potassium hydroxide during the first round the average measured tensile strength of the bonds increases significantly (from ~ 12 - 15 MPa to ~ 40 - 50 MPa) when bonding again with sodium silicate solution during the second round and all of the bonds except for one had high bond quality.

4. Further experiments involving the strength of sapphire hydroxide catalysis bonds

Table 4.5.: Table of breaking strengths for hydroxide catalysis bonds between sapphire samples produced with samples that had been bonded once before. The second bonds were all produced using sodium silicate solution and either with or without a HF clean to prepare the surfaces before re-bonding. All of the strengths summarised here were measured at room temperature.

Number of bonds	Initial chemical	Second chemical	HF?	Strength (MPa)			σ	$\frac{\sigma}{\sqrt{N}}$
				Mean	Minimum	Maximum		
6	Sodium silicate (293 K)	Sodium silicate	No	22	2	58	20.6	8.4
2	Sodium silicate (77 K)	Sodium silicate	No	10	5	16	7.7	5.5
6	Sodium silicate (77 K)	Sodium silicate	Yes	37	14	54	16.7	6.8
3	Potassium hydroxide (293 K)	Sodium silicate	No	41	39	44	2.6	1.5
2	Potassium hydroxide (293 K)	Sodium silicate	Yes	25	13	36	16.3	11.5
9	Sodium aluminate (293 K)	Sodium silicate	No	42	34	49	5.6	1.9

4. Further experiments involving the strength of sapphire hydroxide catalysis bonds

Table 4.6.: Table of breaking strengths for hydroxide catalysis bonds between sapphire samples produced with samples that had been bonded twice before. The third bonds were all produced using sodium silicate solution and without a HF clean to prepare the surfaces before re-bonding. All of the strengths summarised here were measured at room temperature.

Number of bonds	Initial chemical	Second chemical	Strength (MPa)			σ	$\frac{\sigma}{\sqrt{N}}$
			Mean	Minimum	Maximum		
3	Sodium silicate (293 K)	Sodium silicate no HF	35	30	42	6.8	4.0
0	Sodium silicate (77 K)	Sodium silicate HF	Na	Na	Na	Na	Na
0	Sodium silicate (77 K)	Sodium silicate HF	Na	Na	Na	Na	Na
3	Potassium hydroxide (293 K)	Sodium silicate no HF	44	33	53	10.4	6
0	Potassium hydroxide (293 K)	Sodium silicate HF	Na	Na	Na	Na	Na
8	Sodium aluminate (293 K)	Sodium silicate no HF	13	0	37	11.7	4.12

4. Further experiments involving the strength of sapphire hydroxide catalysis bonds

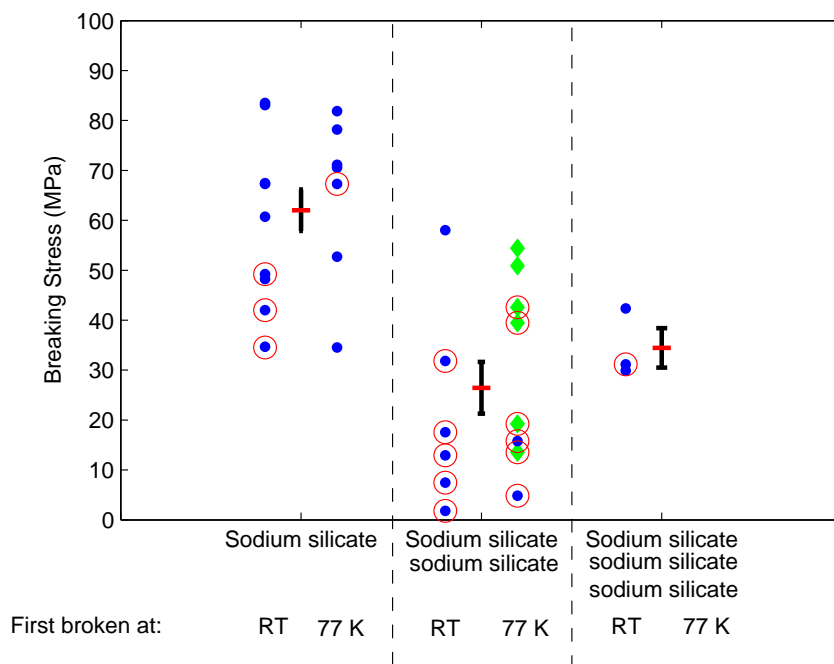


Figure 4.15.: Measured tensile strengths for samples bonded repeated using sodium silicate solution. The measured strengths are the blue and green points, with green points indicating that the samples were cleaned with HF before re-bonding, the mean strength for each data set is indicated by the red bar, error bars indicate the standard error on the mean. The circled points indicate imperfect bonds (<90% bonded).

4. Further experiments involving the strength of sapphire hydroxide catalysis bonds

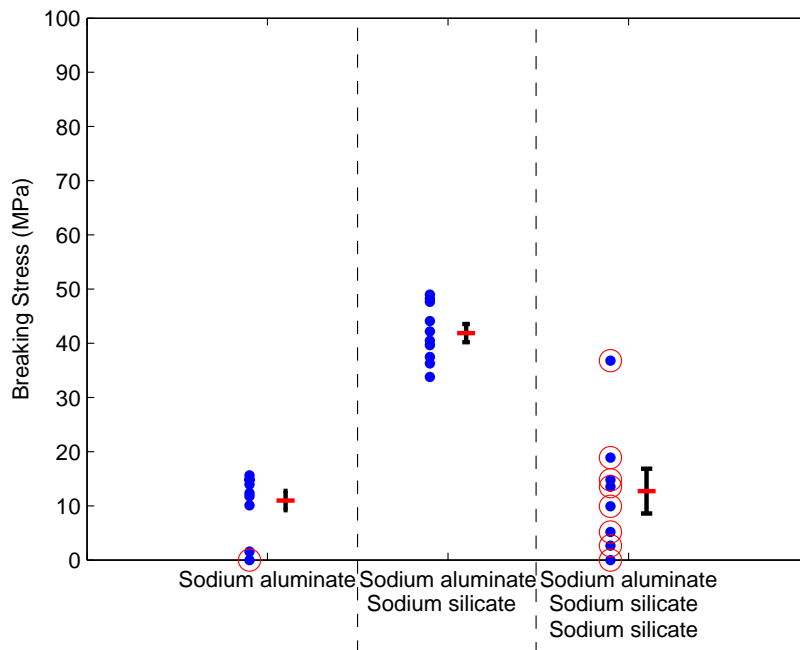


Figure 4.16.: Measured tensile strengths for samples bonded using sodium aluminate solution in the first round and using sodium silicate solution for the subsequent two rounds. The measured tensile strengths are the blue points, the mean strength for each data set is indicated by the red bar, error bars indicate the standard error on the mean. The circled points indicate imperfect bonds (<90% bonded).

The sodium silicate samples bonded a second time with sodium silicate solution gave a larger standard deviation in strengths measured (22 MPa), similarly to that in the first round of bonding (19 MPa). For these samples the standard deviations of samples tested at room temperature and 77 K is 19 MPa for both for the 1st time bonded and 21 MPa for both after the 2nd time they were bonded, showing very little variation in the spread of data. Additionally, the strength ranges found for both are over a very similar strength range - this is true both for those sets of bonds made with samples which had undergone HF cleaning and those which had not. Based on these tensile strength results it is unclear whether cleaning with HF has any significant effect on subsequent bond strength or quality.

The data for the sodium aluminate and potassium hydroxide samples re-bonded with sodium silicate solution remain clustered together closely (standard deviations of 6.5 and 14 MPa), similar to the first bonding round (5 and 15 MPa).

4. Further experiments involving the strength of sapphire hydroxide catalysis bonds

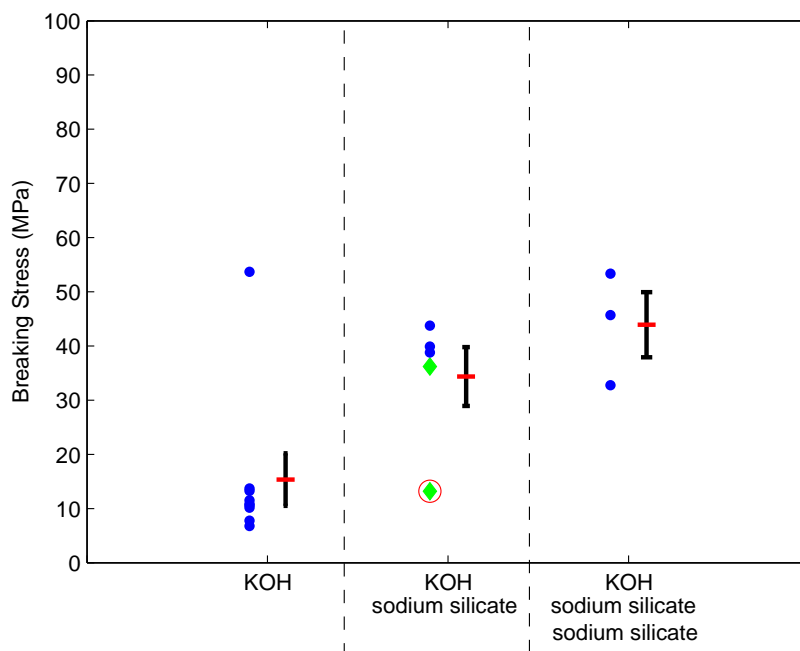


Figure 4.17.: Measured tensile strengths for samples bonded using potassium hydroxide solution in the first round and using sodium silicate solution for the following round. The measured breaking stresses are the blue and green points, with green points indicating that the samples were cleaned with HF before re-bonding, the mean strength for each data set is indicated by the red bar, error bars indicate the standard error on the mean. The circled points indicate imperfect bonds (<90% bonded).

4. Further experiments involving the strength of sapphire hydroxide catalysis bonds

Of the samples bonded with sodium silicate in the first two rounds (figure 4.15) only 3 of 14 samples tested in the second round were suitable for re-use in the third round, meaning that relatively more samples are damaged after two rounds of sodium silicate than samples that were bonded with any other bonding solution followed by sodium silicate. It should also be noted that none of the samples etched with HF in the second round were fit for re-use a third time (like those bonded with potassium hydroxide). Finally, the bonds made between the samples in the third round of bonding were tested again and were all measured to have high tensile strengths (between 35 and 50 MPa). These strengths are not correlated to the strengths or bond quality of the exact same samples in the second round.

Ten of the samples which were initially bonded with sodium aluminate solution were re-bonded with sodium silicate solution and eight of these were re-bonded a third time, again with sodium silicate solution. With these samples there was significant variation in bond quality between the second and third rounds of bonding, with all of the bonds in the third round being of poor quality when they were visually assessed. As mentioned in the previous section, it is possible that sodium silicate solution is more successful in etching the sapphire surfaces than the other solutions, leading both to high strengths of initial bonds and to less successful subsequent bonds due to the chemical changes that have already taken place at the sample surface.

4.4.4. Conclusions

It is clear that re-bonding surfaces which have previously been bonded using the hydroxide catalysis bonding technique is possible. Secondary bonds between samples originally bonded with sodium silicate solution are less strong and less reliable than the original bonds. However, if surfaces were previously bonded with other solutions (sodium aluminate or potassium hydroxide) and then bonded with sodium silicate solutions this

4. Further experiments involving the strength of sapphire hydroxide catalysis bonds

reduction in strength and reliability is not observed, instead the second round of bonds are often stronger and more reliable than the first.

The reason for this could be that, based on roughness measurements, surfaces bonded with sodium silicate solution in the first round are more affected than when using other solutions. This suggests that the etching action was more effective and that could explain the higher strength in the first round, but potentially also made the surface less suitable for a second round of bonding. The etching action of sodium aluminate and potassium hydroxide was potentially not as intense but did leave a good surface for bonding again (with sodium silicate).

The strength reducing significantly in the third round for those samples bonded with sodium aluminate followed by sodium silicate twice seems consistent with those samples having been bonded with sodium silicate twice in the sense that the sodium silicate has affected the surface after this bonding round, making it harder to make high strength good quality bonds. This does not explain why the strength and quality of the 3 bonds made with potassium hydroxide and sodium silicate twice thereafter and the 3 bonds made with sodium silicate three times has remained high. More tests would be required to test the statistical significance of these results.

It would be interesting to study the effects of re-bonding with other solutions. If, for example, strong bonds can be repeatedly produced between the same surfaces when using potassium hydroxide, then this would present a strong argument for bonding with potassium hydroxide as it would provide an option for repairs. Based on the results found in this section, if the need for repairs is anticipated then it may be advisable to make any initial bonds with either potassium hydroxide or sodium aluminate and, should bonds need to be re-made, to make subsequent ones with sodium silicate.

4.5. Bond curing time

To understand how bond curing time may influence bond strength, a set of 132 sapphire samples with dimensions $5 \times 5 \times 20$ mm were procured for a series of bonding experiments with sodium silicate solution. The 5×20 mm faces were produced with a ground finish while the 5×5 mm face not intended for bonding was polished to an optically clear finish and there was a superior polish on the intended bonding surface. Each sample had a fiducial mark to indicate crystal orientation (in this case bonds were formed between c-plane samples). See figure 4.18 for a diagram of the samples' dimensions.

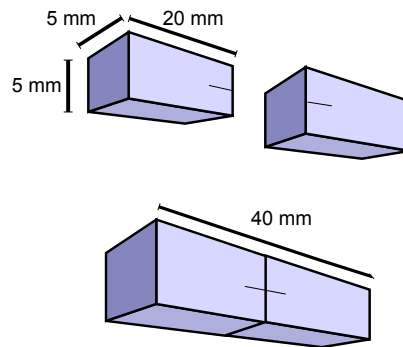


Figure 4.18.: Diagram of the dimensions of the sapphire samples for hydroxide catalysis bonding experiments investigating bond curing time, note fiducial mark to indicate crystal orientation. Bonds were formed between c-plane samples.

As in the previous set of experiments, all the samples were inspected for their suitability for bonding. Their dimensions were measured with a micrometer, the bond surface flatness of each sample was measured with an interferometer (ZYGO GPI XP/D) and the mean flatness of the bonding surfaces was found to be 40 nm. The surfaces of a subset of 20 randomly selected samples were measured using an Optical Surface Profiler (Veeco Wyco NT1100) and were found to have a mean Ra roughness of 6.5 nm. Each sample was labeled with an identification number and for each sample the measured dimensions and flatness were recorded so that they could easily be recovered at a later date.

Bonds were made at room temperature and cured for 2, 4, 8 or 12 weeks. For this set of measurements, 10 bonds were made and cured for 2 weeks, 10 were made and cured

4. Further experiments involving the strength of sapphire hydroxide catalysis bonds

for 4 weeks, 10 were made and cured for 8 weeks and 10 were made and cured for 12 weeks. During the curing period bonds were kept at room temperature ($\sim 20^\circ\text{C}$). For the first week of curing the bonded samples were held in place in the jigs used during bonding to aid alignment. Following this they were individually wrapped in Anticon Gold StandardWeight clean room wipes and stored safely in sample boxes until the curing times were complete. At a later date an additional 10 bonds were made and cured for 2 weeks and an additional 10 were made and cured for 4 weeks. These were treated in exactly the same way as the first set and were made to improve statistics.

An additional variable was considered for bonds cured for two weeks. In previous work the curing time of bonds has been reduced by curing at an elevated temperature (known as accelerated curing), usually $\sim 40^\circ\text{C}$ [155]. A set of 10 bonds was made and cured for one week at room temperature and then for one week at 40°C .

After the curing period the strengths of the bonds were tested at room temperature using a 4-point bending test as detailed in previous sections (see section 3.6 and figure 3.11).

4.5.1. Results

The strengths obtained for the bonds described above are shown in figure 4.19 in which sets of bonds produced on different days are shown separately and figure 4.20 in which the results from multiple sets are combined. A summary of the mean, minimum and maximum tensile strengths measured for the different curing times is given in table 4.7 - this does not include the data for the bonds which were heat treated.

It is clear that the average strengths of bonds is relatively high after two weeks, however longer curing times appear to give more consistent strengths (see figures 4.19-4.20 and table 4.7). Whilst bonds that have been cured for four weeks are strong, they are not as

4. Further experiments involving the strength of sapphire hydroxide catalysis bonds

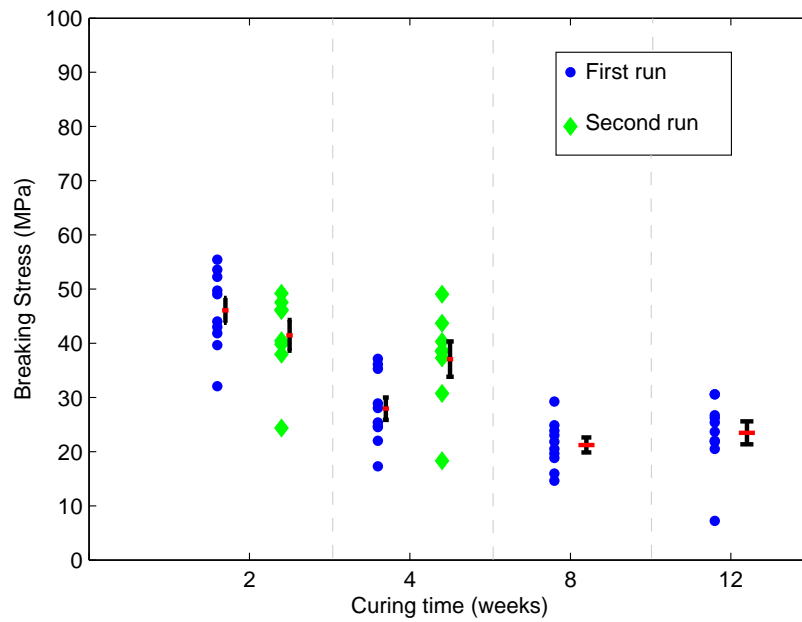


Figure 4.19.: Tensile strengths of sapphire-sapphire bonds with a range of curing times. The error bars shown here are the standard error of the mean. The first set of strength results is shown in blue and where further bonds were made the strengths of these are shown in green.

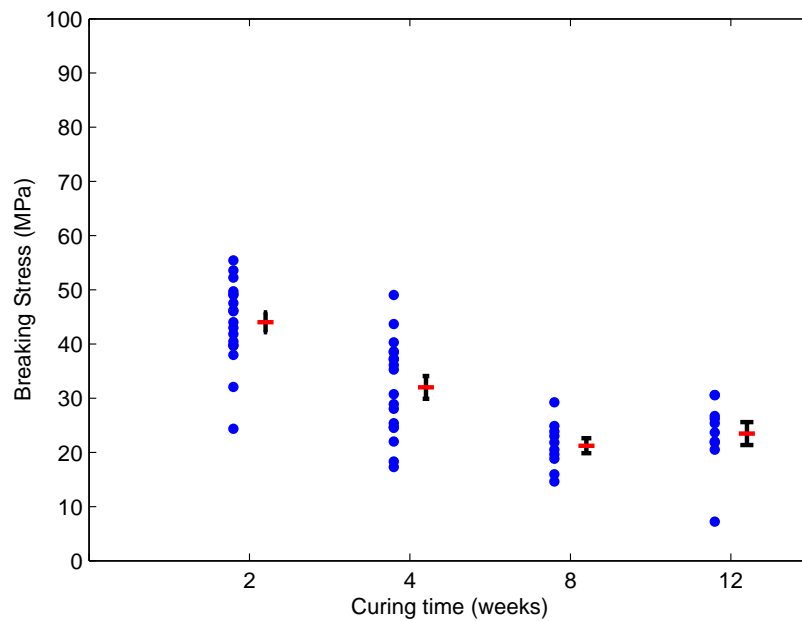


Figure 4.20.: Tensile strengths of sapphire-sapphire bonds with a range of curing times. The error bars shown here are the standard error of the mean.

4. Further experiments involving the strength of sapphire hydroxide catalysis bonds

Table 4.7.: Table of breaking strengths for hydroxide catalysis bonds between sapphire samples produced with strength testing carried out after 2, 4, 8 and 12 weeks of curing at room temperature. The mean, minimum and maximum tensile strengths recorded are shown. All strengths were measured at room temperature

Curing time	Strength (MPa)			σ	$\frac{\sigma}{\sqrt{N}}$
	Mean	Minimum	Maximum		
2 weeks, 1 st run	46	32	55	7	2
2 weeks, 2 nd run	42	24	49	8	3
2 weeks, all data	44	24	55	8	2
4 weeks, 1 st run	28	17	37	7	2
4 weeks, 2 nd	37	18	49	9	3
4 weeks, all data	32	17	49	9	2
8 weeks	21	15	29	4	1
12 weeks	24	7	31	7	2

strong as those bonds which were cured for two weeks and this trend appears to continue with increased curing times, possibly plateauing after 8 weeks. Additional tests after a greater range of curing times (for example for fewer than 14 days and for more than 12 weeks) would give a clearer understanding of how long the bonds take to reliably reach their long-term strength.

In the case of bonds formed between fused silica samples a different trend of strength results is seen, with strengths steadily increasing up to a four week curing time with little change in strength after that point [135, 145]. Hence, this result is not as expected; the difference may be due to the difference in surface chemistry between the two materials.

In figure 4.21 the strengths of bonds which went through an accelerated cure at 40°C are shown compared to the strength of bonds which were cured for two weeks without this heat treatment. The mean tensile strength measured for bonds which were heat treated and cured for a total of two weeks was 33 MPa (with a minimum strength of 26 MPa and a maximum strength of 44 MPa). The bonds which were not heat treated but were cured for a total of two weeks at room temperature only had a mean tensile strength of 44 MPa (with a minimum strength of 24 MPa and a maximum strength of 55 MPa). As can be seen from figure 4.21, the range of strengths is greater for those bonds which

4. Further experiments involving the strength of sapphire hydroxide catalysis bonds

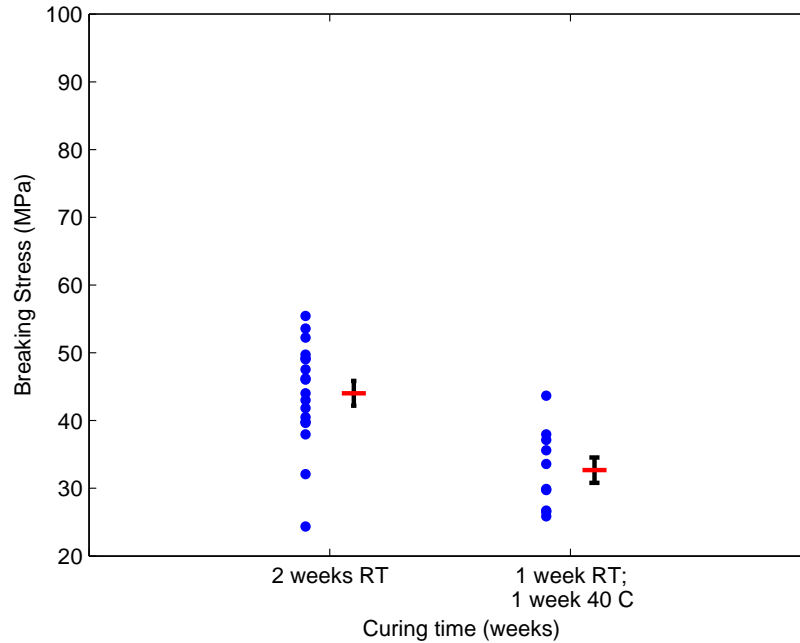


Figure 4.21.: Tensile strengths of sapphire-sapphire bonds for two different curing regimes. The error bars shown here are the standard error of the mean.

did not undergo a heat treatment than it is for those which did, however, fewer bonds were heat treated. The strengths are not within error of the 2 week room temperature cures, however, they are within error of the strengths of bonds that were cured for four weeks at room temperature. Hence it appears that heat treatments do indeed accelerate the curing process, although between the first two weeks and the second two weeks the average strength drops.

More strength results at a greater range of curing times is needed to establish a trend. However, these initial results suggest that, after a small decline in strength between the second and eighth week of curing, the strength of bonds may be starting to plateau by the twelfth week. Strength results after one, three, six and 24 weeks would help to understand any existing trends that aren't immediately clear here.

4.5.2. Conclusion

Sapphire bonds are strong after only two weeks of curing, with average strengths of 44 MPa, but results suggest that average strength may drop after this to around 23 MPa. The minimum strengths measured were 7 MPa, still a factor of 7 above the likely strength requirement for KAGRA (at 1 MPa) [167]. Further tests will be needed to understand how the bonds develop chemically over time so tests with curing times less than 2 weeks, and longer than 14 weeks, could shed light on this. It would also be of interest to carry out further experiments to discover whether the apparent drop in strength at longer curing times (8 and 12 weeks) is statistically significant.

Applying a heat treatment of one week of curing at 40 °C (which might be expected to have the effect of accelerated curing) also appears to cause a drop in average strength with respect to samples cured for 2 weeks at RT (consistent with that of a 4 week curing times at RT).

As mentioned earlier, when hydroxide catalysis bonds are made between fused silica samples these approach their maximum strength after four weeks. This is in contrast to the results shown here for bonds between sapphire samples. The difference may be due to how water leaves the bonds during the curing process; fused silica can absorb water more readily than crystalline sapphire so to leave a sapphire-sapphire bond water would need to migrate to the edge of the bond. It is possible that as this occurs the polymer-like chains that form the bonds are damaged.

4.6. Discussion and summary

The effects of several parameters on the strength of hydroxide catalysis bonds between sapphire samples with sodium silicate solution have been investigated. These included the crystalline orientation of the sapphire pieces being bonded, the effects of thermal cycling, whether or not the surfaces have been previously bonded and how long the bonds have cured for.

In terms of crystalline orientation, the strongest bonds were produced between samples where the crystalline orientation matches across the bond interface; bonds between two c-plane interfaces had an average torsional strength of 89 MPa and, as seen in the previous chapter, m-to-m bonds can also be very strong. Where bonds were formed between different crystal planes the average strengths measured were a little lower; 42 MPa for c-to-a bonds and 60 MPa for c-to-m bonds. However, if the bonds are intended for use in a typical gravitation wave detector suspension, then all configurations will produce bonds which are strong enough [147].

Since any gravitational wave detector suspension intended for cryogenic operation is likely to undergo multiple thermal cycles during its installation, it is interesting to note that a small number of thermal cycles can be associated with a decrease in bond strength. However, it is possible that this decrease in strength occurs after just one cycle and further cycles have little impact. Conversely, it is possible that each cycle reduces the bond strength further. More experiments are needed to determine these details. It is clear that after three thermal cycles between room temperature and liquid helium temperatures all of the bonds measured were strong enough for use in a typical cryogenic suspension, such as KAGRA [147, 180].

Options for suspension repair scenarios were explored since sapphire pieces usually survive post-bonding separation with no damage to the bulk substrate. After the initial bond

4. Further experiments involving the strength of sapphire hydroxide catalysis bonds

formed with sodium silicate solution, subsequent bonds with the same solution are less strong and less reliable and attempts to reclaim the surface with HF before bonding had little success. However, if a different solution (sodium aluminate or potassium hydroxide) was used to make the first round of bonds then strong, reliable bonds can be made with sodium silicate solution in the second round of bonding. If the need to re-make bonds is anticipated it may be wise to use one of these solutions in the first instance and sodium silicate in the second. Samples should not be bonded a third time.

The evolution of bond strength of hydroxide catalysis bonds formed between sapphire was studied. It is clear that after two weeks of curing at room temperature very strong bonds are produced (see sections 3.7, 4.2.2 and 4.3.3), but that the strength may drop to a lower level after this. The reason for this is not well understood as the chemical reaction is different for sapphire, when compared to bonding fused silica, for example, so this needs more investigation. Heat treatment during short bonding times does appear to accelerate the bond curing process. This difference in how bond strength changes over time when compared to fused silica bonds could be due to how water leaves the bond as it cures.

Although a variety of parameters may influence bond strength it is consistently found that hydroxide catalysis bonds made between sapphire with sodium silicate solution are very strong, and certainly strong enough for use in a sapphire-based gravitational wave detector suspension.

5. Loss measurements of hydroxide catalysis bonds between sapphire discs: Theory and modeling

5.1. Introduction

As discussed in Chapter 2, one source of thermal noise in gravitational wave detectors is internal friction in the hydroxide catalysis bonds which join the suspension pieces to the test masses. This contribution to the total thermal noise is an important one which can limit the sensitivity of gravitational wave detectors. Thus a measurement of the mechanical loss of hydroxide catalysis bonds formed between sapphire pieces is helpful to inform the design of any suspension that will use these materials. Since it is likely that any sapphire-based suspension system will operate at cryogenic temperatures it is important to have measurements of relevant mechanical losses at cryogenic temperatures as well as at room temperature.

5. Loss measurements of hydroxide catalysis bonds between sapphire discs: Theory and modeling

The mechanical loss of a system can be calculated using equation 5.1 [197, 118],

$$\phi(\omega_0) = \frac{E_{\text{dissipated}}}{2\pi E_{\text{stored}}} \quad (5.1)$$

Where $\phi(\omega_0)$ is the mechanical loss at angular resonant frequency ω_0 , $E_{\text{dissipated}}$ is the energy dissipated with each cycle of oscillation and E_{stored} is the total energy stored in the oscillating system. Note that $\phi(\omega_0)$ can also be considered as a phase lag between some oscillating perturbing force and the response of the material to that force, as described in Chapter 2, section 2.3.1.

This mechanical loss can be measured by observing the free decay of the amplitude of motion of an excited resonant mode (the “ringdown”) of angular frequency ω_0 with an initial amplitude of A_0 at time $t=0$. The time dependence of the amplitude decay $A(t)$ is given by equation 5.2 [198],

$$A(t) = A_0 e^{-\frac{\omega_0 t}{2/\phi(\omega_0)}} \quad (5.2)$$

If a resonant mode is excited and the amplitude of its motion is allowed to freely decay, the natural log of the amplitude of this motion may be plotted as a function of time. A straight line can then be fitted to the resulting curve and the gradient of this straight line, may be used to find the mechanical loss of the system, as following equation 5.3,

$$\phi(\omega_0) = \frac{2(\text{gradient})}{\omega_0} \quad (5.3)$$

5. Loss measurements of hydroxide catalysis bonds between sapphire discs: Theory and modeling

Early experiments found the value of mechanical loss of hydroxide catalysis bonds between fused silica pieces to be between 0.18 and 0.54 at room temperature [199]. This was later refined to between 0.51×10^{-1} and 1.5×10^{-1} for a bond with a thickness of 61 ± 4 nm [147]. This difference may be due to slightly different experimental techniques, in particular the geometries that were bonded and the method of bond formation.

The experiments described in these chapters concern mechanical loss measurements of hydroxide catalysis bonds between sapphire pieces.

In the past, the mechanical losses of hydroxide catalysis bonds between various substrates have been measured using large bonded cylinders [200]. If, alternatively, thin discs are used as the substrates in these experiments, the bond layer makes up a larger volume of the bonded system, potentially allowing this geometry to give a more sensitive probe of the bond mechanical loss (as described in section 5.4). Additionally, larger bonded cylinders tend to have resonant frequencies on the order of several tens of kilohertz, whereas the resonant frequencies of bonded thin discs can be lower, often just a few kilohertz. This lower frequency range is more relevant when considering the sensitive frequency bands of gravitational wave detectors. Finally, larger samples are more expensive than smaller ones. If it is possible to use smaller samples this will be advantageous for future experiments, as it will be possible to investigate more variables without such a limiting factor being placed on the research by cost. For these reasons, the sample geometry chosen for these experiments was thin sapphire discs (see section 5.3).

Some work has also been carried out using bonded cantilevers [117]. However, significant difficulties in creating high quality bonds between thin cantilevers were encountered with large air bubbles regularly forming in the bond layer. This makes reliable measurements of the bond losses challenging and as such the use of slightly thicker discs was deemed to be preferable as their thicker profile makes them easier to bond.

5.2. Mechanical loss of hydroxide catalysis bonds

The hydroxide catalysis bond layer formed between any two suitably flat and clean sapphire discs is likely to be thin. In the past bonds have been measured to have a thickness of ~ 60 nm [147] and in general the bond thickness has been found to be consistent with the peak to valley flatness of the samples bonded [147, 157, 199]. Compared to the disc thickness the bond thickness is therefore very small and it is likely that the contribution of the mechanical loss of the bond, to the overall mechanical loss of the bonded system under study, will also be small.

The mechanical loss of a hydroxide catalysis bond can be obtained by measuring experimentally the loss of a bonded sample, ϕ_{bonded} , the loss of a “blank” sample, i.e. one with the same dimensions as the bonded system but with no bond, ϕ_{blank} and by finding the amount of energy stored in a blank sample divided by the total energy stored in the system, $\frac{E_{\text{blank}}}{E_{\text{total}}}$, and the amount of energy stored in the bond divided by the total energy stored in the system, $\frac{E_{\text{bond}}}{E_{\text{total}}}$, through equation 5.4 [147],

$$\phi_{\text{bonded}}(\omega_0) \approx \frac{E_{\text{blank}}}{E_{\text{total}}} \phi_{\text{blank}}(\omega_0) + \frac{E_{\text{bond}}}{E_{\text{total}}} \phi_{\text{bond}}(\omega_0) \quad (5.4)$$

Since the substrate can be assumed to be far larger than the bond, $E_{\text{total}} \approx E_{\text{blank}}$. Hence, $\frac{E_{\text{blank}}}{E_{\text{total}}} \approx 1$. Equation 5.4 can then be rearranged to give the mechanical loss of the bond, ϕ_{bond} , as shown in equation 5.5,

$$\phi_{\text{bond}}(\omega_0) \approx \frac{\phi_{\text{bonded}}(\omega_0) - \phi_{\text{blank}}(\omega_0)}{\frac{E_{\text{bond}}}{E_{\text{total}}}} \quad (5.5)$$

5. Loss measurements of hydroxide catalysis bonds between sapphire discs: Theory and modeling

The energy ratio, $\frac{E_{\text{bond}}}{E_{\text{total}}}$, and frequency of each resonant mode is found using finite element analysis with the ANSYS¹ Workbench software package (see section 5.4) [147].

5.3. Sapphire discs for bond loss experiments

Six sapphire discs were acquired from Guild Optical Associates² with the aim of measuring the mechanical loss of a hydroxide catalysis bond formed between sapphire samples. The crystal orientation of the discs is such that the c-axis is perpendicular to the flat surface of each disc. The dimensions of the discs were specified as 1.5 mm, 1.0 mm and 0.5 mm in thickness (two discs of each thickness were acquired) and 50.8 mm in diameter when ordered, these were later measured directly and found to be accurate to within ± 0.02 mm (the discs which should have been 0.5 mm thick were 0.48 mm and 0.49 mm thick and the discs which should have been 1.0 mm were 1.01 mm and 1.02 mm thick). The 1.0 and 0.5 mm thick discs were intended for bonding while the 1.5 mm thick discs were intended as “blanks” and would be used for comparison to the bonded discs. The faces of the discs were polished by Guild Optical Associates the surface flatnesses were measured using the Zygo interferometer before bonding. They were found to have flatnesses between 300 nm and 1300 nm (see figure 5.1 for an example of a surface flatness profile). The edges were polished such that they were visibly clear.

¹<http://www.ansys.com>

²<http://www.guildoptics.com/>

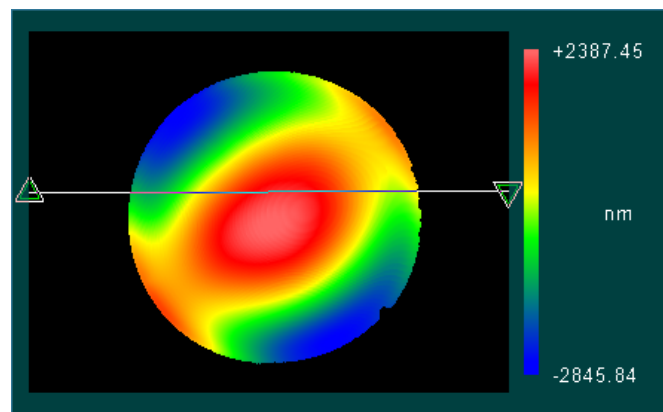


Figure 5.1.: The surface flatness profile of a sapphire disc. This is one of the two 0.5 mm thick discs, it had a rms flatness of ~ 1500 nm.

5.4. Finite element modeling of bonded sapphire discs and cylinders

5.4.1. Introduction

Finite element analysis (FEA) is a technique for analysing a model of a material or object in order to understand how stresses can affect that model. It can be used to find various stresses and strains within a model as well as its resonant modes, among other things, depending on the properties of interest. In this technique a model is divided into many small elements, connected by nodes. Then, partial differential equations that describe the model's behaviour, at the location of each of the node, can be solved. In this way, solutions can be found to describe the system, even where analytic solutions prove challenging or impossible.

When considering the resonant modes of a system such as a disc, a modal analysis must be carried out. This allows the natural mode shapes and frequencies of a freely vibrating object to be found. It is also possible to run models of constrained objects and to compare how the mode shapes and frequencies change when an object is constrained when compared to those of a free object.

5. Loss measurements of hydroxide catalysis bonds between sapphire discs: Theory and modeling

Before measuring the mechanical loss, finite element analysis models were built, corresponding to each individual sapphire disc and to the system of two bonded sapphire discs. These models were built using the ANSYS Workbench software package and were constructed to allow modal analysis of the sapphire samples so that the resonant mode shapes and the mode frequencies of each system could be studied as well as the energy stored in the discs and the bond layer respectively.

The shapes of the resonant modes is of particular importance, as these determine the distribution of movement across the face of the discs. Hence, optimal detection of the motion using the interferometric set up can be arranged. In order for the movement induced by a resonant mode to be detected, there must be motion of the disc along the direction of the sensing beam. The mode shape also indicates whether the mode will be damped by the support fibres (as discussed in section 6.2). An example of the mode shape of one resonant mode of a pair of bonded sapphire discs is shown in figure 5.2.

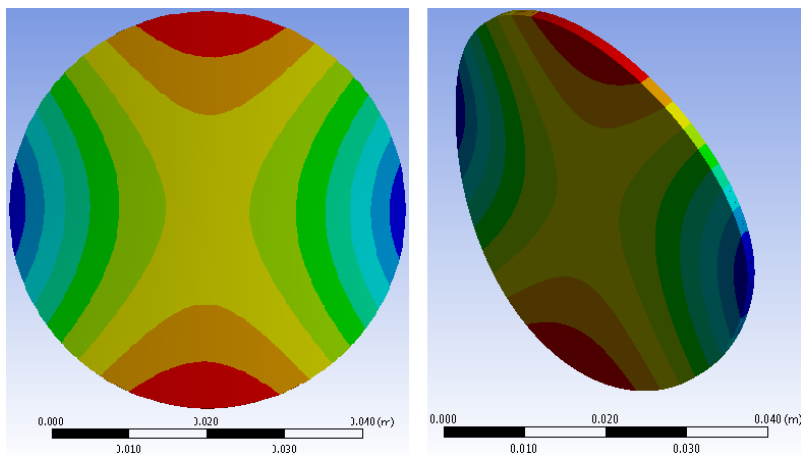


Figure 5.2.: Resonant mode at ~ 860 Hz for a sapphire disc 50.8 mm in diameter with a thickness of 1.5 mm. The amplitude of motion is indicated by colour where blue indicates less motion while red indicates more motion.

The strain energy ratio, $\frac{E_{\text{bond}}}{E_{\text{total}}}$, indicates whether or not the bond contribution to mechanical loss will be measurable. This is affected by several factors including the position and thickness of the bond between the two discs, the thickness of the two discs, and the ratio between those two thicknesses, and the Young's moduli of both the discs and the bond. Initially, two sets of models were designed to better understand these effects; one

5. Loss measurements of hydroxide catalysis bonds between sapphire discs: Theory and modeling

in which the position of the bond between the two discs was varied and one in which the thickness of the discs was varied.

These models were made in order to investigate where the bond should be such that a high fraction of the energy stored in the bonded system will be stored within the bond layer - this makes it easier to calculate the bond losses. Hence the question of whether the bond should be positioned in the centre, rather than off-centre, in the system, was considered. Additionally, models were created to demonstrate that the use of thinner discs rather than thicker cylinders is advantageous when measuring the bond losses.

The energy stored in each part of each model was determined for the resonant modes of interest, such that the fraction of the total energy stored in the bond could be found. When bond loss is of interest a high ratio between the energy stored in the bond and that stored in the substrate is desirable as this allows for the most accurate probe of the bond loss.

The analysis works by dividing a model of a solid object into a finite number of smaller sections or elements by “meshing” the object. The behaviour of each of these small elements can then be calculated. In general, models with dense meshes and thousands of elements provide the most accurate and reliable results, however the finer the mesh the greater the computing time is required to solve the model. A compromise is usually sought where the mesh is fine enough to give a sufficiently accurate result without the necessity for prohibitively long computation times. This can be achieved through a trial and error method, starting with a small number of large elements and gradually increasing the number of elements (and correspondingly decreasing their size) until the point where an increase in the number of elements used does not lead to a change in the results of the model. This “convergence” process must be carried out for each model that is used. An example of a convergence plot is shown in figure 5.3.

5. Loss measurements of hydroxide catalysis bonds between sapphire discs: Theory and modeling

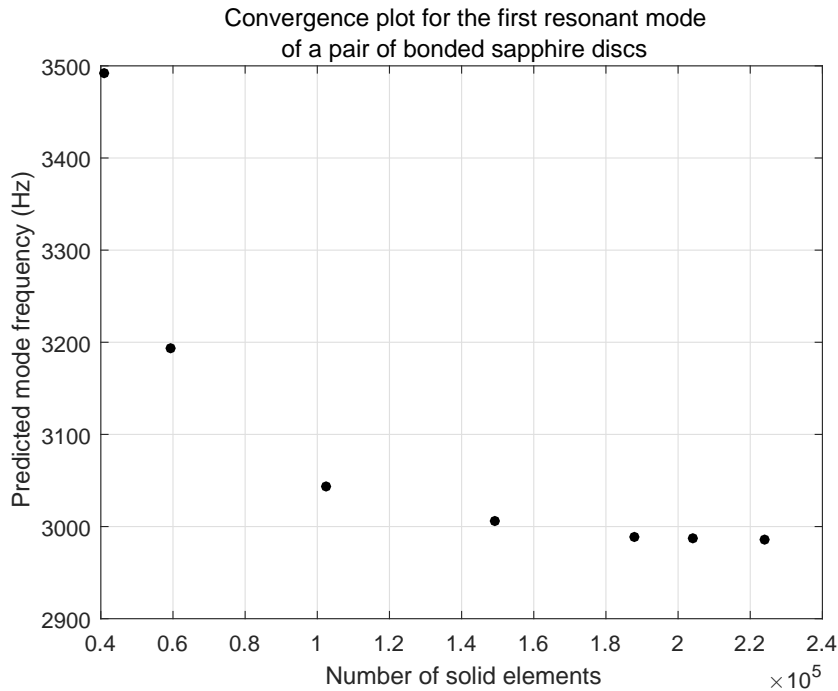


Figure 5.3.: An example of how the FEA modeling converges on a value as the number of elements is increased. In this instance the predicted resonant frequency for the first resonant mode of a pair of bonded sapphire discs is shown.

In particular, areas of interest such as interfaces or, in the case of these calculations, the bond, should be densely meshed and should therefore contain a high number of elements. In the models described in this chapter, the bond layer typically contained ~ 146000 elements³. With the meshes used in these models, the results found were similar to those found using analytic calculations, however, these results are likely to be more accurate when compared to a real system, as FEA models can be used take into account a bond layer and certain options for clamping the discs, which is challenging to do analytically (see section 6.6 for analytic calculations and more details).

In the past, models of this kind of have been carried out without restricting the degrees of freedom in which the system can move [157, 98], and in many cases these “unclamped” models do provide sufficient accuracy. However, since the FEA models detailed in this chapter were intended for comparison between a system in which the discs are supported

³The same mesh density was used for the models presented in Appendix B which includes details of a model where the discs and the bond layer were assumed to have the same Young’s modulus; here the strain energy ratios are the same for each of the resonant modes, as would be expected since, this is the same as a solid sapphire disc.

5. Loss measurements of hydroxide catalysis bonds between sapphire discs: Theory and modeling

(see section 6.2) it is possible that some of the resonant modes under investigation may be damped and impossible to excite due to the suspension wires that support the disc. Because of this the clamping of the models was given some consideration and initially points on the edge of the disc were clamped such that they were free to move in any direction except for the z-direction (See figure 5.4) unless otherwise stated.

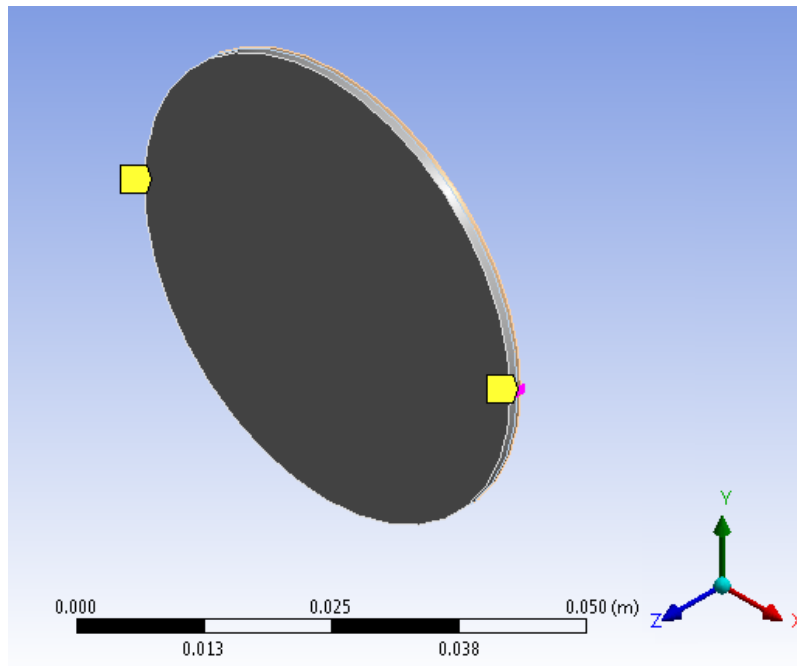


Figure 5.4.: An FEA model of two bonded sapphire discs, one with thickness 0.5 mm, one with thickness 1.0 mm, both with diameter 50.8 mm. The discs are clamped such that the points, indicated by the arrows, are unable to move in the z-direction.

However, the disc is only slightly constrained by the fibres, not truly clamped and hence unclamped models were also considered as a final check. Initial room temperature measurements of the mechanical loss of a blank, 0.5 mm thick sapphire disc indicated that the resonant modes were excited at frequencies closest to those predicted by FEA models in which the discs were clamped as described above, as opposed to models in which they were not clamped (see section 6.8 for details of the modes measured). However, results from both clamped and unclamped models are presented in later sections and are used to extract the bond loss, since the true answer is likely to lie somewhere between the two sets of results.

5.4.2. Elastic constants of sapphire

Before any finite element model of a crystalline solid can be built it is necessary to understand the elastic constants of the material of interest. These properties govern the distortion of the material. Since single crystal sapphire is anisotropic, the Young's modulus of sapphire in any direction is dependent on the relative crystalline orientation. A stiffness matrix is therefore required to fully describe the elastic modulus of sapphire. Since sapphire has a hexagonal crystal structure, its stiffness, $|\mathbf{c}|$, is described by the following matrix [201, 202],

$$|\mathbf{c}| = \begin{vmatrix} c_{11} & c_{12} & c_{13} & c_{14} & 0 & 0 \\ c_{12} & c_{11} & c_{13} & -c_{14} & 0 & 0 \\ c_{13} & c_{13} & c_{33} & 0 & 0 & 0 \\ c_{14} & -c_{14} & 0 & c_{44} & 0 & 0 \\ 0 & 0 & 0 & 0 & c_{44} & c_{14} \\ 0 & 0 & 0 & 0 & c_{14} & \frac{1}{2}(c_{11} - c_{12}) \end{vmatrix}$$

By convention, the Young's modulus is defined relative to the c-axis of the sapphire crystal. For the c-axis of a sapphire crystal the stiffness matrix is as follows,

$$|\mathbf{c}| = \begin{vmatrix} 4.889 & 1.568 & 1.115 & -0.231 & 0 & 0 \\ 1.568 & 4.889 & 1.115 & 0.231 & 0 & 0 \\ 1.115 & 1.115 & 4.931 & 0 & 0 & 0 \\ -0.231 & 0.231 & 0 & 1.451 & 0 & 0 \\ 0 & 0 & 0 & 0 & 1.451 & -0.231 \\ 0 & 0 & 0 & 0 & -0.231 & 1.660 \end{vmatrix} \times 10^{11} \text{ kg/ms}^2$$

Since the sapphire discs intended for use in mechanical loss measurements are aligned such that the c-axis of the crystal is along the optical axis of the disc, the stiffness matrix,

$|c|$ can be used directly in the finite element models. For sapphire pieces with different orientations some matrix transformations would first be required in order to produce accurate models [202]. In the finite element models described in this chapter the above stiffness matrix was used in the modal analysis of sapphire and the Young's modulus of the bond material was assumed to be 7.9 GPa, a value which has been measured in the past for hydroxide catalysis bonds [199]. Since the bond material can be assumed to be isotropic, no stiffness matrix is necessary to describe its behaviour.

5.4.3. Resonant mode shapes and frequencies

One of the initial goals of the FEA analysis was to restrict the frequency ranges over which resonant modes are expected for the system of bonded discs. This saves time when working with real bonded sapphire discs because it means there is no need to search over broad frequency bands when trying to excite these resonant modes. Additionally, the shapes of the modes are important as some of these are more likely than others to be damped by the supporting tungsten fibres.

Using a model of two bonded sapphire discs with diameter 50.8 mm and thicknesses 0.5 mm and 1.5 mm respectively, a set of expected modes were found. These modes are the ones that would be expected if the discs were clamped as described above. Table 5.1 lists the resonant frequencies expected for the first 20 modes.

As can be seen from the first twenty mode frequencies listed in table 5.1, some resonant modes are relatively close together in frequency, for example, the two resonant modes occurring at 21241 Hz and 21886 Hz. These tend to be "split modes" with mode shapes that are very similar but rotated with respect to each other. In some instances it is possible to measure both split modes (see section 6.8 for an example of this). However, due to the rotation of the mode it is more common that one of the two is damped due

5. Loss measurements of hydroxide catalysis bonds between sapphire discs: Theory and modeling

Table 5.1.: The frequencies of the first twenty resonant modes of a system of bonded sapphire discs, as predicted by FEA analysis, in Hz. These discs are 50.8 mm in diameter and have thicknesses of 0.5 mm and 1.0 mm, respectively. The bond layer is 300 nm thick.

860	19391
1841	21241
4828	21886
6088	24461
7471	28008
10814	28831
12543	29247
14587	30972
17098	34105
18551	35956

to the friction between the disc edge and the suspension fibres and in this case only one mode will be measurable.

The shapes of the first five modes listed in table 5.1 are displayed in figure 5.5.

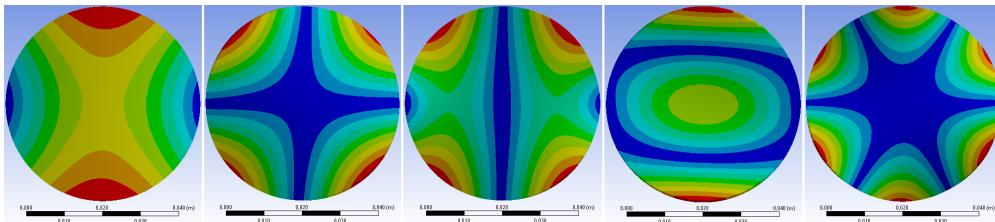


Figure 5.5.: The mode shapes of the first five resonant modes for a bonded pair of clamped sapphire discs, as predicted by FEA analysis. The resonant frequencies of these modes are (from left to right): 859.9 Hz, 1840.8 Hz, 4828.2 Hz, 6088.3 Hz and 7470.5 Hz. Red indicates areas where more motion would be expected, blue indicates less motion.

From figure 5.5, it is clear to see the potential for some modes to be damped. In this figure, red indicates areas that will exhibit a great deal of motion when the resonant mode is excited while blue areas indicate less motion. So, for example, if the first mode at 859.9 Hz is excited and the suspension fibres touch the blue areas the mode should be relatively easy to excite, but if the disc is rotated 90° the fibres will contact the red areas and will damp the motion. This information is helpful as it suggests that, should it be difficult to excite any resonant mode, this problem may be solved by rotating and re-suspending the disc.

5.4.4. The effect of disc thickness on strain energy ratio

Prior experiments to study the loss of hydroxide catalysis bonds between sapphire used bonded cylinder samples with a geometry as shown in figure 5.6 [147, 200] rather than the thinner disc samples studied here and described above. This set of FEA calculations investigate how the energy ratio, $\frac{E_{\text{bond}}}{E_{\text{total}}}$, varies as the substrate thickness is reduced whilst the bond thickness is held constant in order to evaluate the potential benefit of using thin discs. This was initially done for a symmetric system in which the bond is placed centrally between two discs of equal thickness. Following this, the effect on $\frac{E_{\text{bond}}}{E_{\text{total}}}$ as the bond is offset from the line of symmetry was studied.

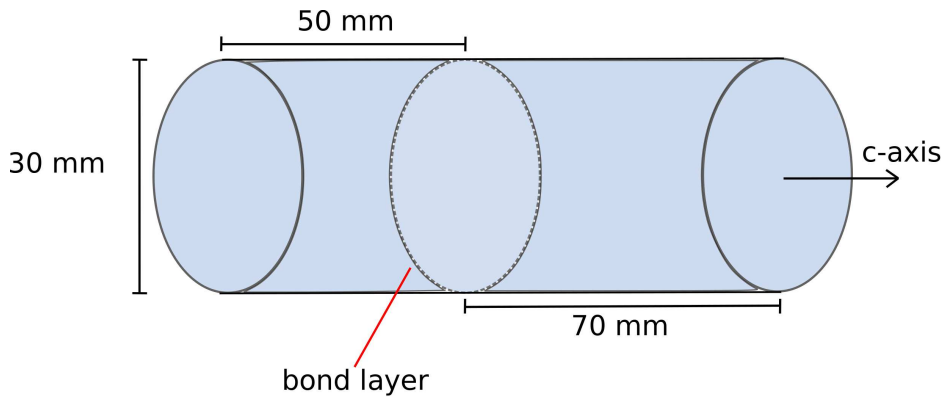


Figure 5.6.: A diagram indicating the geometry of bonded cylinders used for loss measurements in previous experiments [147, 200]. The bond layer is expected to have a similar thickness to the flatness of the bonded surfaces, usually ~ 60 nm.

Models were built with discs of thickness varying between a combined thickness of 1.5 mm, up to a thickness of 100 mm (i.e. cylinders rather than discs). In all cases the diameter of the discs (or cylinders) was 50.8 mm. The results from these models were compared to similar FEA models and experimentation by Haughian *et al* which were used in first experiments investigating the mechanical loss of bonds between sapphire substrates [200]. Models in which the bond was centrally placed were built alongside models in which one disc or cylinder had double the width of the other.

5. Loss measurements of hydroxide catalysis bonds between sapphire discs: Theory and modeling

Figures 5.7 and 5.8 show how the strain energy ratio, $\frac{E_{\text{bond}}}{E_{\text{total}}}$, changes as the geometry of the sapphire discs or cylinders changes, with figure 5.7 showing this for the situation where the two sapphire pieces have equal thicknesses and figure 5.8 showing this where the one sapphire piece is twice the thickness of the other.

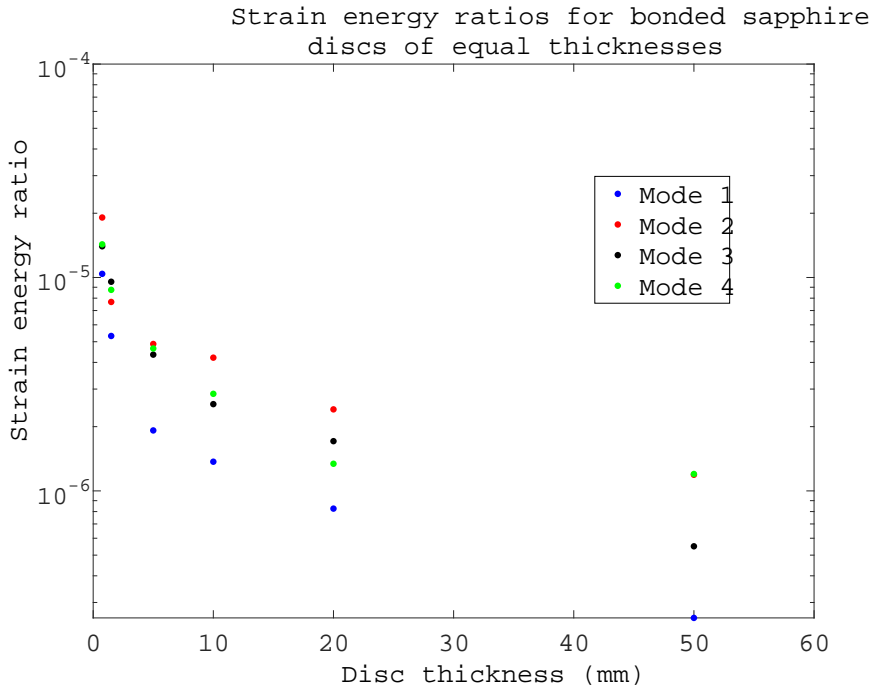


Figure 5.7.: Strain energy ratio as the total length of a pair of bonded discs or cylinders increases. Here the two discs have equal thicknesses and the bond layer has a thickness of 300 nm. Discs and cylinders have a diameter of 50.8 mm.

As can be seen from both figure 5.7 and figure 5.8, the ratio of strain energy that is stored in the bond compared to that stored in the whole system decreases with increasing disc thickness. This is expected, as when thinner discs are used, the bond makes up a greater portion of the total volume of the system and hence more energy can be stored in it. This suggests that the effect of a bond should be more obvious when samples with smaller thicknesses are bonded.

Additionally, where bonds are placed away from the centre, i.e. when one disc or cylinder is thicker than the other, this results in a higher strain energy ratio than when the bond is directly in the centre of two discs of equal thickness. Hence, the results shown in figures 5.7 and 5.8 suggest that the use of a pair of bonded thin discs with unequal thicknesses

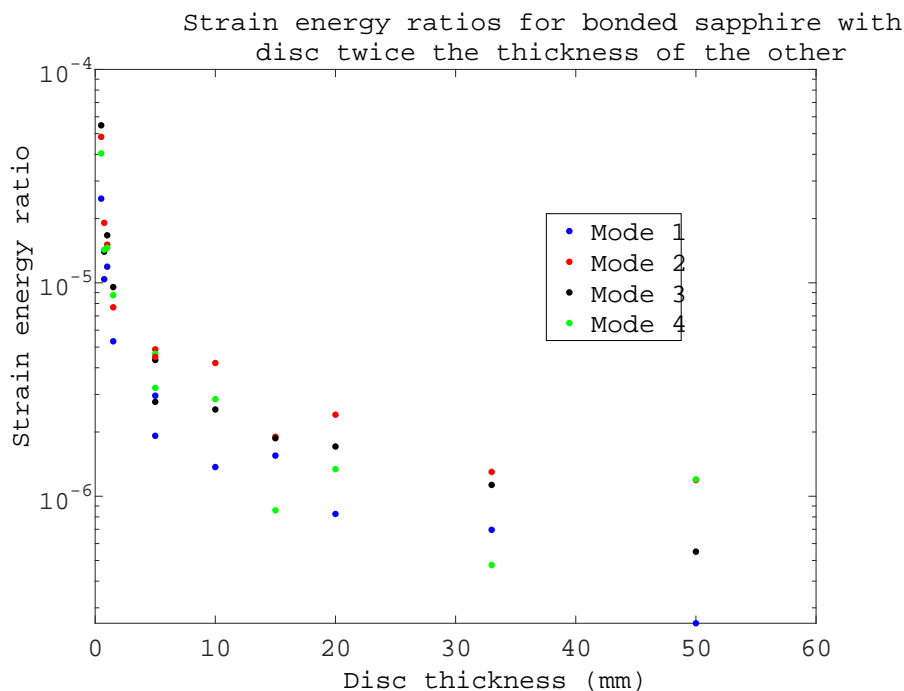


Figure 5.8.: Changing strain energy ratio as the total length of a pair of bonded discs or cylinders increases. Here the thicker disc in each case has twice the thickness of the thinner disc and the bond layer has a thickness of 300 nm. Discs and cylinders have a diameter of 50.8 mm.

will allow a better probe of the value of bond mechanical loss than the use of a pair of bonded cylinders would.

5.4.5. The effect of bond position on strain energy ratio

A series of FEA models of two bonded sapphire discs were built. In each case, the two discs both had a diameter of 50.8 mm and a combined thickness of 1.5 mm. The bond layer between the discs was 60 nm, a thickness for bonds that has been measured in the past [199] and had a Young's modulus of 7.9 GPa⁴. The models were designed to compare the strain energy ratio for a system where the bond was centrally placed (i.e. the two discs had equal thickness) to that where it was placed off-centre (i.e. one disc was thicker than the other).

⁴In later experiments and calculations, due to the less flat profiles of the discs bonded, a bond thickness of 300 nm was used. Where this is done it is highlighted.

5. Loss measurements of hydroxide catalysis bonds between sapphire discs: Theory and modeling

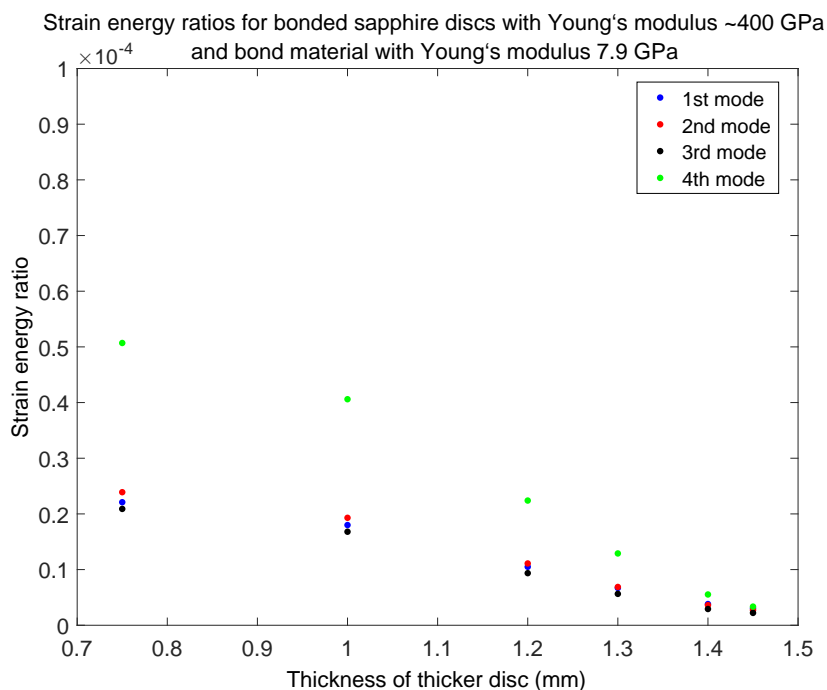


Figure 5.9.: Strain energy ratio as the position of the bond between bonded sapphire discs is changed.

Figure 5.9 shows the effect on strain energy ratio of changing the position of the bond between the two sapphire discs. Note that the general trend shows that as the position of the bond moves further from the centre the strain energy ratio decreases approximately linearly. This is in contrast to the situation when fused silica discs are bonded using the hydroxide catalysis bonding technique, in which previous models have shown the energy ratio increasing as the bond is placed further from the centre of the system (see figure B.5 in section B.1 of appendix B).

Note also that this trend is slightly different to those shown in figures 5.7 and 5.8 because a different variable is being considered. Here, in contrast to those results shown in the previous section, the total volume of sapphire and bond material is the same in each model, only the position of the bond layer is changed. Previously, the total volume of the system was changed, but the position of the bond layer was the same; for the results shown in figure 5.7 it was in the centre, and in figure 5.8, the thicker disc was always twice the thickness of the thinner disc. Since bond position is studied here, rather than total volume, it is unsurprising to see a slightly different trend.

5.4.6. Summary of FEA modeling calculations

Based on the results above, the effect of the bond on the mechanical loss of a bonded system is enhanced by using thinner discs. When bonding discs rather than cylinders, a greater fraction of the total volume is made up by the bond material, this means that a greater fraction of the total energy can be stored in the bond layer. As a result, measuring the effect of a real bond between two sapphire discs should be easier than measuring the effect of a similar bond between two thicker sapphire cylinders, as is demonstrated by the results shown in figure 5.7.

Further, as when the bond layer is further from the centre of the bonded pair of discs, i.e. when the two discs are of unequal thickness and thus the bonded pair are asymmetric, the strain energy ratio, $\frac{E_{\text{bond}}}{E_{\text{total}}}$, increases, as shown in figure 5.9. Hence, bonding pair of discs asymmetrically would be expected to give a better probe of bond loss.

The results from these models will be used in the following chapter in several ways; they suggest frequency ranges over which resonant modes might be expected and they indicate whether a resonant mode might be expected to be damped by the tungsten support fibres. Additionally, these results are used in conjunction with the data recorded during the mechanical loss measurements detailed in the following chapter in order to extract values for the bond loss.

6. Loss measurements of hydroxide catalysis bonds between sapphire discs: Experiment

6.1. Introduction

As described in Chapter 5, FEA was used to gain initial information about a system of two bonded sapphire discs in terms of mode frequencies and shapes, and also in terms of the energy stored in each part of the system. This was to allow interpretation of the experimental results. From the FEA it was clear that thin discs would be an advantageous choice of geometry over thicker cylinders as this means that the bond layer takes up a greater proportion of the total volume and hence, extracting the bond loss should be more straightforward. However, some experimental measurements of a bonded system of discs are also necessary in order for a value for bond loss to be calculated. These experiments are described in this chapter.

6.2. Nodal suspension of bonded sapphire discs

Previous work on measuring the loss of bonds featured the use of larger suspended cylinders [157] and clamped cantilevers [117]. As mentioned before, it was found that bonding thin cantilevers is challenging as the flexible cantilevers tend to trap bubbles while the bonds are curing, resulting in large unbonded regions [117, 203]. The use of more rigid bonded cylinders was more successful, however, as mentioned earlier when using large cylinders the bond represents only a small fraction of the sample volume, potentially making the measurements less sensitive to the actual bond loss.

Prior work on the mechanical losses of disc samples have been carried out with a “nodal support” system which suspends the discs with support contacts at, or close to, the nodes of the disc resonant modes. These nodes are points of minimum motion for sets of resonant modes of a sample. The resonant modes are excited and the amplitude of their oscillation is monitored over time [204, 205, 206, 207]. One example of this technique was developed by Numata *et al* [204, 205] and was further developed for use with thin discs by Cumming [206]. The disc nodal support system was initially used for measuring low loss coatings on thin silica discs [206]. This technique was developed further for measuring the loss of bonds between thin sapphire discs as described here.

In this instance, the disc is suspended with 50 μm diameter tungsten fibres, such that minimal contact is made between the edges of the disc and the fibres that support it. The tungsten is wiped clean with methanol before it is used to support the discs. Tungsten fibres are known to be suitable for suspending samples for loss measurements [136]. This design is intended to minimise frictional loss at the support contact points (see figure 6.1 for a diagram of the experimental arrangement).

When the mechanical loss is measured, the resonant modes of the discs are excited using an electrostatic drive plate positioned behind the back surface of the disc. The motion

6. Loss measurements of hydroxide catalysis bonds between sapphire discs: Experiment

of the front surface is monitored using an interferometer. The measurements described in this chapter were carried out using a commercial SIOS interferometer¹.

6.3. Experimental procedure

Each resonant mode is excited in turn by applying a signal at the expected resonant mode frequency via the electrostatic drive plate - the frequency range over which the experimental modes are expected is found through the FEA modeling described in the previous chapter. When the amplitude of the motion of the disc is significantly above the background noise, and ideally is as great as possible, the signal to the drive plate is stopped and the amplitude of motion is allowed to decrease naturally. This amplitude is monitored over time. Hence the “ringdown time,” the time it takes for the amplitude to decrease by this amount. The gradient of the ringdown curve over time is used to give a value of the mechanical loss of the system, as according to equation 5.3.

The flattest 0.5 mm thick disc, as measured using a Zygo interferometer (see section 5.3), was suspended in the nodal suspension for loss measurements first. This first measurement was designed to ensure that if any major flaws existed in the sapphire that were not immediately visible, and if these flaws had any effect on the loss, this effect would not be mistakenly attributed to the bond loss. Secondly, the flattest 1.5 mm disc was measured, this was for comparison with the bonded discs later.

Next, the flattest 0.5 mm thick and the flattest 1.0 mm thick disc were bonded and the bonds were cured for four weeks at room temperature. Finally, the mechanical loss of this bonded system was also measured. These measurements were carried out both at room temperature and at cryogenic temperatures.

¹<http://www.sios-de.com>

6. Loss measurements of hydroxide catalysis bonds between sapphire discs: Experiment

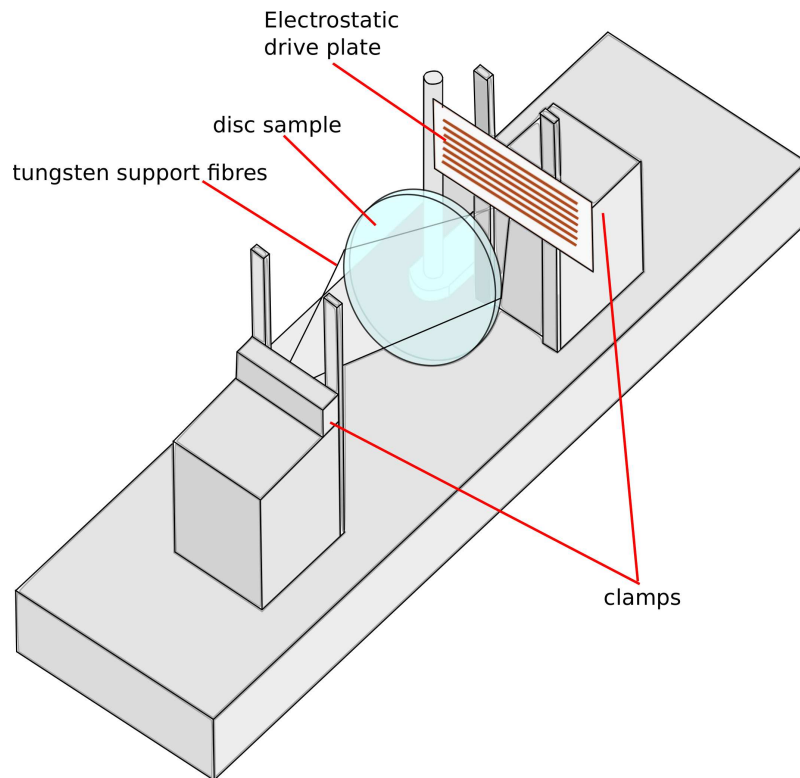


Figure 6.1.: A schematic diagram of the nodal support clamp for measuring the mechanical loss of discs (not to scale).

6.4. Cooling procedure

The nodal suspension and the disc were cooled in a cryostat (IR Labs HDL-14). This model of cryostat has a space for a cooled experiment and two windows (see figure 6.2). When the nodal suspension supporting the disc is fixed to the base plate of the experiment space, the cryostat is closed. The cryostat must then be inverted in order allow evacuation and cooling. The initial evacuation utilises a roughing pump and a combined turbo pump and vacuum gauge (Varian: Turbo-V 301-AG²) is used to monitor the internal pressure. The pressure is reduced to $\sim 1 \times 10^{-5}$ mbar, where it stabilises, i.e. it does not change over the course of several hours. It is important that the pressure is stable when loss measurements are taken as fluctuations in pressure can affect the results. This procedure takes approximately 3 hours.

²www.vacuum-pumps.us/Varian

6. Loss measurements of hydroxide catalysis bonds between sapphire discs: Experiment

When the cryostat is evacuated the cryogen spaces can be filled. The cryostat has two spaces - one for liquid nitrogen and one for liquid helium (see figure 6.2). However, if liquid helium were directly placed into the helium space when the space was at room temperature a great deal of helium would be needed to reduce the temperature sufficiently. Since helium is far more expensive than nitrogen, nitrogen is used in both cryogen spaces initially. After approximately one day, the temperature of the full system stabilises at ~ 77 K (i.e. the temperature of the experiment space remains at 77 K for ~ 2 hours), then remaining nitrogen can be pumped out of the helium space.

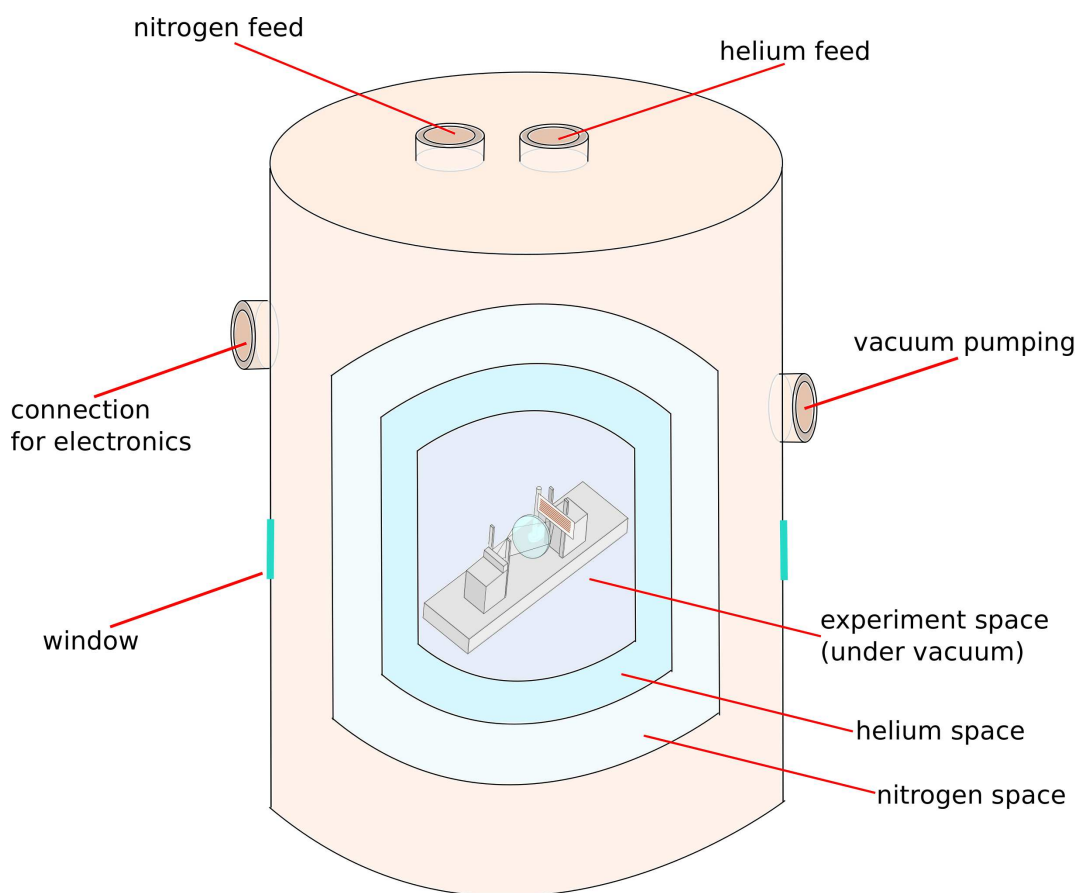


Figure 6.2.: Diagram of the cryostat for the experimental set up (not to scale).

To ensure that no nitrogen is left behind in the helium space, a heater on the base plate is used to raise the temperature to ~ 90 K - this precaution is taken to avoid the production of nitrogen ice, which can cause a dangerous blockage in the cryostat. Finally, the helium space is filled with liquid helium. The temperature of both cryogen spaces, as well as the experiment space, are all monitored to ensure that no cryogen runs out. Cryogens

6. Loss measurements of hydroxide catalysis bonds between sapphire discs: Experiment

will steadily boil off over time and when this happens they must be topped up. The reduction in temperature also leads to a reduction in pressure down to $\sim 1 \times 10^{-7}$ mbar. When the temperature and the pressure of the experiment have stabilised, i.e. when the temperature of the clamp has been the same to within 1 K for one hour and the pressure has been the same for several hours, measurements can be carried out.

6.5. Temperature calibrations

The temperature of the disc itself is of interest during the mechanical loss experiments. However, if a temperature sensor is attached to a disc it is likely that any excited resonant modes would be strongly damped by the presence of the sensor and hence that any measurement of mechanical loss would be much higher than the intrinsic loss value of the system. Thus, in order to know the temperature of the disc during mechanical loss measurements, a method of determining the temperature of the disc in the absence of a sensor is necessary.

To do this, temperature sensors are attached to the nitrogen tank, the base-plate (directly in contact with helium when liquid helium is being used), one of the clamps and the disc. The procedures for cooling the cryostat are carried out as normal (see section 6.4). When the temperature of the disc and clamp reduce and plateau, contact gas is used to reduce the temperature further (see section 6.5.1). The time, contact gas pressure and temperature from all four temperature sensors were all monitored and recorded throughout these “temperature calibrations”.

In this way, during mechanical loss experiments when a temperature sensor cannot be mounted directly on the disc, the approximate temperature of the disc can be found based on the temperatures given by the sensors mounted on the nitrogen tank, base plate

6. Loss measurements of hydroxide catalysis bonds between sapphire discs: Experiment

and on each of the clamps (the sensor that would have been on the disc is moved to the second clamp in this configuration), as well as the length of time for which the sensors have recorded a given temperature and the current contact gas pressure if any contact gas is used. This allows the temperature of the disc to be known with an accuracy of up to ± 2 K, as calculated from several temperature calibration runs, when temperature sensors are no longer attached.

An example of the monitored temperatures from the four sensors, for one of the temperature calibration runs is shown in figure 6.3.

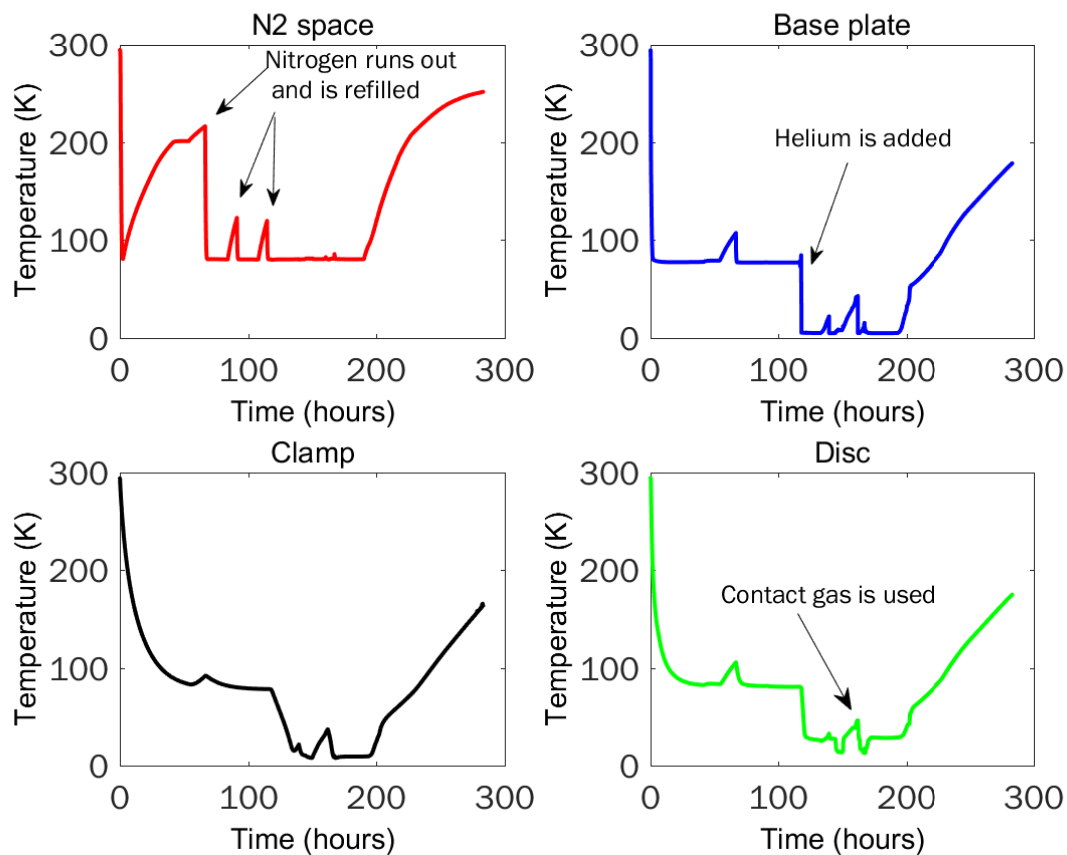


Figure 6.3.: Data from an example of a temperature calibration run to find the temperature of a disc from the temperature of other parts of the cryostat and the clamp. The disc used in this calibration run was a sapphire disc, 1.5 mm thick with a radius of 50.8 mm.

In figure 6.3 several features can be seen. The first is a sharp drop in temperature as the cryostat is cooled with liquid nitrogen. As the liquid nitrogen boils off the temperature

6. Loss measurements of hydroxide catalysis bonds between sapphire discs: Experiment

of the cryostat rises until the nitrogen is refilled - this can be seen within the first ten hours in the N₂ space, which is closest to the ambient temperature of the room. It is only when the N₂ space is almost empty of nitrogen that the other temperature sensors begin to report a temperature increase, after around 60 hours.

Following this, a second sharp drop in temperature can be seen in the plot for the base plate and more gradual decreases in temperature can be seen for the clamp and disc - this corresponds to emptying the liquid nitrogen from the helium space and filling it with liquid helium, in this instance the helium space was filled with liquid helium after approximately 120 hours. It should be noted that the disc cools faster than the clamp, this effect was reproducible and is discussed in more detail in section 6.5.2. Subsequent temperature spikes indicate that either one or both of the cryogens is depleted and the following drops in temperature indicate that these cryogens have been replenished.

Slightly before 200 hours, contact gas is introduced into the experiment space to further decrease the temperature of the clamp and disc. Finally, the contact gas is removed and the whole system is allowed to return naturally to room temperature. Heaters are not used during this period, although heaters are mounted within the cryostat and are used during the cooling procedure to remove residual liquid nitrogen from the liquid helium space before it is filled with helium (see section 6.4).

In total, four temperature calibration runs were carried out; two using a blank sapphire disc of thickness 1.5 mm and diameter 50.8 mm, one using a blank sapphire disc of thickness 0.5 mm and diameter 50.8 mm and one using a bonded pair of sapphire discs with combined thickness of 1.5 mm and diameter 50.8 mm. Although the thinnest disc cooled slightly more quickly than the thickest disc the differences were not significant. The behaviour of the bonded and blank discs was also very similar during temperature calibrations. For more temperature calibration curves, see Appendix A.

6. Loss measurements of hydroxide catalysis bonds between sapphire discs: Experiment

Early measurements with a temperature sensor mounted on the disc³ and with helium in the helium space showed that the disc temperature plateaued at ~ 47 K, however, later measurements found an average plateau temperature of ~ 19 K. The disc temperature at this stage was recorded without contact gas having been introduced into the system. However, as mentioned earlier, the temperature may be further reduced through the use of contact gas if required.

6.5.1. Contact gas

The tungsten support fibres will not conduct enough heat to allow the disc to fall to the desired temperature of < 20 K due to their small cross-sectional area (see section 6.5.2). Instead, contact gas is used to bring the disc down to the lowest temperatures.

The use of contact gas involves injecting small amounts of room temperature helium into the vacuum space of the cryostat. As the helium atoms move around the cryostat they contact the base plate, walls and clamp, losing heat energy to each of these. They also contact the disc, and if they have first contacted the base plate, for example, they will gain heat energy from the disc as it will be at a higher temperature. In this way the disc can be cooled further.

However, using contact gas causes the liquid helium in the cryostat to boil off at an increased rate. Additionally, for safe use of an electrostatic drive plate the pressure inside the vacuum chamber of the cryostat should be kept low to avoid electrical breakdown. So, there is a limit on how much contact gas can be used. When the contact gas has cooled the disc, its mechanical loss can be measured. The procedure of injecting and removing contact gas was also carried out during temperature calibrations (see figure 6.3).

³The temperature sensors were commercially supplied by Lakeshore Cryotronics Inc (<http://www.lakeshore.com/>), and were specifically designed for use at low temperatures

6. Loss measurements of hydroxide catalysis bonds between sapphire discs: Experiment

Using different contact gas pressures leads to the clamp and disc to settle at different temperatures. It can take of the order of an hour for the temperature to stabilise after a change in contact gas pressure. As such, the number of temperature steps for which data can be acquired is time limited. In general, four temperature steps between 12 K and 30 K were taken during these experiments, with more data taken at additional temperatures which did not require the use of contact gas.

Changes in pressure led to very rapid changes in temperature when at these low pressures and temperatures. As a result, where contact gas was used to cool the disc, the cryostat pressure was not allowed to return back to the original pressure of $\sim 1 \times 10^{-7}$ mbar before the loss measurements were carried out. As a result of this, the loss measurements carried out at the lowest temperatures (below ~ 20 K) were carried out at pressures of up to 5×10^{-4} mbar. The following calculation was carried out to ensure that gas damping did not have a significant effect on the losses measured [115]. The gas damping, or residual gas loss, for a system is given by equation 6.1 [115],

$$\phi_{\text{gas}} = \frac{AP}{m_{\text{disc}}\omega} \sqrt{\frac{M_{\text{He}}}{RT}} \quad (6.1)$$

Where, A is the surface area of the disc, P is the pressure, m_{disc} is the mass of the disc, ω is the angular frequency of the resonant mode, M_{He} is the molecular mass of helium, R is the ideal gas constant and T is the temperature. Gas loss increases for high pressures and frequencies and for low temperatures so, at the highest pressure of 5×10^{-4} mbar (0.05 Pa), the lowest recorded temperature of 13 K and a frequency of ~ 14.5 kHz, $\phi_{\text{gas}} = 1.4 \times 10^{-9}$. This low value suggests that it is highly unlikely that the resonant modes of the discs were damped by residual gas in the system.

Further, where contact gas is not used, the loss due to residual gas is even lower. Assuming the lowest temperature where contact gas was not used of ~ 27 K and a pressure here of

6. Loss measurements of hydroxide catalysis bonds between sapphire discs: Experiment

$\sim 1 \times 10^{-7}$ mbar (1×10^{-5} Pa) the gas loss is $\phi_{\text{gas}} = 1.9 \times 10^{-13}$ for the same resonant mode. It is clear that, for these experiments, the effect of residual gas is negligible.

6.5.2. Cooling Rates of the disc and clamp

From figure 6.3 it can be seen that the disc initially cools at a more rapid rate than the clamp. This unexpected effect led to the first temperature calibration attempt being ended early, as it was suspected that a temperature sensor was malfunctioning or else misplaced. However, with careful inspection of the temperature sensors and experimental set up this was found to not be the case. Repeating the temperature calibrations always gave the same effect, even when the sensors used to record the temperature of the clamp and disc were swapped. Analytical calculations of the heat flow in the system were carried out in order to better understand this.

The disc is suspended by two tungsten fibres which, since each one meets the disc at only one point, can be modeled as four tungsten fibres, each with a diameter of 50×10^{-6} m and a length of 6 cm (see figure 6.1 for a diagram). Hence the heat conducted through a tungsten fibre as a function of time is given by equation 6.2 as follows,

$$\frac{dQ}{dt} = \frac{\kappa A \Delta T}{l} \quad (6.2)$$

Where κ is the thermal conductivity of tungsten ($173 \text{ W}/(\text{mK})$ [208]), A is the cross-sectional area of the tungsten wire, T is the temperature and l is the length of the tungsten wire. For a temperature range of room temperature (293 K) to 77 K this gives a value of heat flow of 2.8×10^{-4} W per wire, or 1.1×10^{-3} W in total.

6. Loss measurements of hydroxide catalysis bonds between sapphire discs: Experiment

In terms of radiation of heat from the surface of the discs,

$$\frac{dQ}{dt} = \sigma A(T_1^4 - T_2^4)\epsilon \quad (6.3)$$

Where σ is the Stefan-Boltzmann constant ($5.67 \times 10^{-8} \text{ Wm}^{-2}\text{K}^{-4}$ [209]), A is the surface area of the discs (in the case of these discs this is $4.3 \times 10^{-3} \text{ m}^2$), $T_1 = 293 \text{ K}$, $T_2 = 77 \text{ K}$ and ϵ is the emissivity of sapphire (0.567 [210]). This gives a value for the radiation of heat from the surface of the sapphire disc of 1.01 W.

The cryostat has two windows, each with a radius of 1 cm and the radius of the cryostat itself is 14.25 cm. Hence the solid angle from each window is given by equation 6.4,

$$\Omega = \frac{2\pi r^2}{4\pi R^2} = \frac{r^2}{2R^2} = \frac{(1 \times 10^{-2})^2}{2(14.25 \times 10^{-2})^2} = 0.0025 \quad (6.4)$$

Then, the heat radiation onto the windows of the cryostat is given by equation 6.5,

$$\frac{dQ}{dt} = \epsilon\sigma AT_{\text{window}}^4\Omega \quad (6.5)$$

and the heat radiation onto the disc is given by equation 6.6,

$$\frac{dQ}{dt} = \epsilon\sigma AT_{\text{disc}}^4\Omega \quad (6.6)$$

6. Loss measurements of hydroxide catalysis bonds between sapphire discs: Experiment

Hence, the system will reach an equilibrium when $\epsilon\sigma AT_{\text{window}}^4\Omega = \epsilon\sigma AT_{\text{disc}}^4\Omega$, i.e. the equilibrium temperature of the disc can be given as,

$$T_{\text{disc}} = T_{\text{window}}\sqrt[4]{\Omega} \quad (6.7)$$

Since the window is in contact with the nitrogen shield, T_{window} it was initially assumed that its temperature would be 77 K. This gives an equilibrium temperature of 17.2 K for the disc. To check this, one temperature calibration was carried out in which a temperature sensor was mounted on the inside of a window and the actual temperature was found to be 119 K, presumably because the outer part of the window is at room temperature. This higher temperature for the window leads to a predicted disc temperature of 26.6 K, between the minimum and maximum temperatures found without contact gas of ~ 16 K and ~ 47 K. Presumably, the external temperature of the room plays a part in this variation, as does the length of time for which the discs are allowed to cool.

6.6. Analytical calculations

The resonant modes of a disc are given by [211],

$$f = \frac{\lambda^2}{2a^2\sqrt{\frac{\rho}{D}}\pi} \quad (6.8)$$

where, f is the frequency, a is the radius of the disc, ρ is the density, D is the flexural rigidity, defined as,

6. Loss measurements of hydroxide catalysis bonds between sapphire discs: Experiment

$$D = \frac{Yt^2}{12(1 - \nu)} \quad (6.9)$$

Y is the Young's modulus, t is the thickness of the disc, ν is the Poisson's ratio and λ is dependent on the mode and is given by Bessel functions. For the first seven modes of an unsupported disc, $\lambda^2=5.513, 8.892, 12.75, 20.41, 35.28, 38.34$ and 53.16 . Hence, for a sapphire disc with radius 25.4 mm, thickness 1.5 mm, density 4000 kg/m³, Young's modulus 400 GPa and Poisson's ratio 0.25 the first seven resonant frequencies would be, 2356 Hz, 3799 Hz, 5448 Hz, 8721 Hz, 15074 Hz, 16382 Hz and 22714 Hz.

The FEA calculations in the previous chapter (section 5.4.3) found a slightly lower set of frequencies, however, if the first mode found using these calculations is compared to the second mode found using FEA, and the second mode found here is compared to the third mode using FEA, then on average the frequencies predicted are within 12% of each other. The discrepancies are likely due to the fact that the FEA calculations involved discs "clamped" at two positions at the edge of the disc, which could also explain the appearance of additional modes such as the first one found via FEA that is not found with these calculations. Additionally, the FEA models included the bond layer between the two discs. A system such as this is challenging to find analytic solutions for.

The modes measured for the bonded pair of sapphire discs were ~ 6 kHz and ~ 14.5 kHz, which agrees with these calculations to within 91% and 96%, respectively. The FEA calculations agreed with the modes found to within 99% for both modes.

Finding the thermoelastic loss for a disc is not straightforward, however, if the disc is approximated to a square plate with a side of length 50.8 mm and a thickness of 1.5 mm (i.e. with similar dimensions to that of discs used), the thermoelastic loss at a given frequency can be found according to equation 6.10,

6. Loss measurements of hydroxide catalysis bonds between sapphire discs: Experiment

$$\phi = \Delta \frac{\omega\tau}{1 + \omega^2\tau^2} \quad (6.10)$$

Where Δ is the relaxation strength and is given by equation 6.11, ω is the angular resonant frequency, τ is the relaxation time and is given by equation 6.12 [212]

$$\Delta = \frac{YT\alpha^2}{\rho C} \quad (6.11)$$

$$\tau = \frac{\rho C t^2}{\pi^2 \kappa} \quad (6.12)$$

Y is the Young's modulus, T is the temperature, α is the linear coefficient of expansion, ρ is the density, C is the specific heat capacity, t is the thickness and κ is the thermal conductivity. Since α , C and κ all also vary with temperature this should be taken into account and in the calculations carried out in this chapter the temperature variations for these properties are taken from Touloukian [213]. By using this set of equations, the thermoelastic loss for each resonant mode can be found across the desired temperature range, as shown in the plot in figure 6.4.

For equations 6.10–6.12 and from the plot in figure 6.4 it is clear to see that for a square sapphire plate, thermoelastic loss changes little with temperature above 100 K, but below 100 K a decrease in temperature corresponds to a decrease in thermoelastic loss. It is partly thanks to this effect that sapphire is a good choice of material for cryogenic suspension systems.

However, while this effect will be seen to some extent regardless of the geometry of the piece of sapphire under study, it would be naive to expect a sapphire disc to behave in

6. Loss measurements of hydroxide catalysis bonds between sapphire discs: Experiment

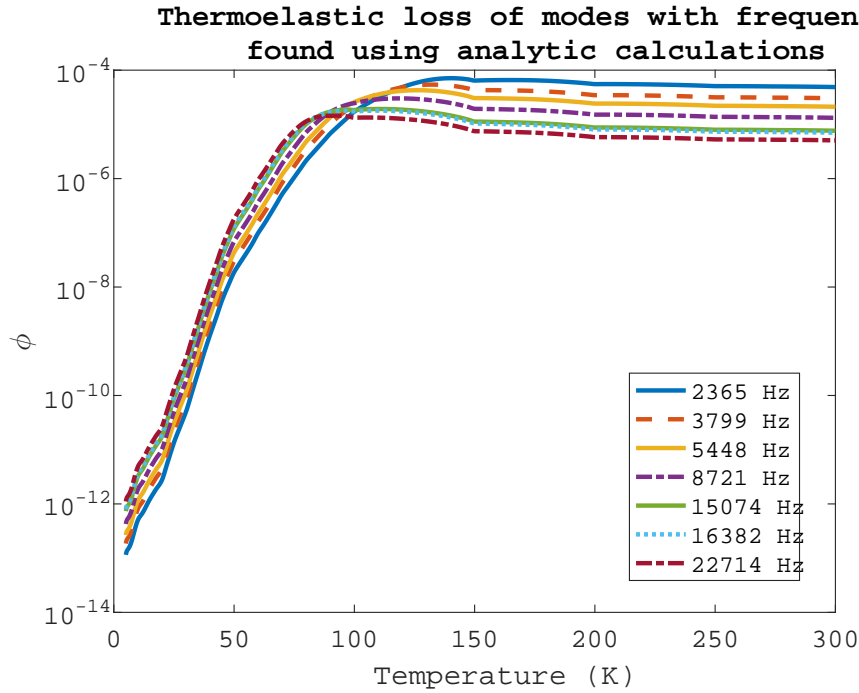


Figure 6.4.: Calculated thermoelastic loss for a square sapphire plate with a square cross section of length 50.8 mm and with thickness 1.5 mm.

exactly the same way as a square sapphire plate. Although these calculations give some initial indication of the behaviour that might be expected, they are insufficient without finite element analysis [206] and experimentation with real samples.

It is assumed that the thermoelastic loss for a bonded disc will be very similar to that for a blank disc with the same geometry. From the previous chapter, in section 5.2 it can be seen from equation 5.5 that the thermoelastic losses will therefore cancel, removing this factor from the analysis and allowing a value of the loss of the bond layer to be found.

6.7. Loss measurements of sapphire discs

6.7.1. Disc preparation

It was decided that, when the samples were bonded, the flattest 1.0 mm thick disc would be bonded to the flattest 0.5 mm thick disc (as measured using a Zygo interferometer, see section 5.3). The less flat discs would also be bonded together.

Before being suspended for mechanical loss measurements, the discs were cleaned with methanol-soaked clean room wipes. They were then suspended and the clamps suspending them were securely fixed within the cryostat. When the cryostat had been closed, a red laser diode was used to check that the discs had not fallen out of their suspension before any mechanical loss measurements were attempted. This was done by shining the laser diode at the disc and finding the reflected laser spot from the disc's surface. In an instance where the disc had fallen out of the suspension, no reflected spot would be visible and the disc can be re-suspended before the experiment space is evacuated.

6.7.2. Loss of unbonded sapphire discs

Initial loss measurements of two unbonded discs were carried out at room temperature under vacuum in the cryostat. The mechanical losses of the 0.5 mm disc and the 1.5 mm disc were measured. Initially all of the discs were intended for measurement, however time constraints led to the measurements of only these two (and later a bonded pair). It was considered that, assuming no unusually high loss values were found for two of the discs, the mechanical loss of the bond was likely to be so much higher than the mechanical loss of the discs that any flaws in the discs, leading to higher than expected mechanical losses would likely have a negligible effect.

6. Loss measurements of hydroxide catalysis bonds between sapphire discs: Experiment

Subsequently, the 0.5 mm thick disc and the 1.5 mm thick disc were consecutively re-suspended in the cryostat. For each disc, new measurements were taken at room temperature and then the temperature was cooled, first to liquid nitrogen and then to liquid helium temperatures. To reach the minimum temperature, contact gas was used. Measurements were taken at all temperature points where possible. However, in some temperature regimes certain modes become difficult or impossible to find.

6.7.3. Hydroxide catalysis bonding of sapphire discs

The discs were cleaned under UV lights in an ozone environment for 30 minutes. This procedure was recommended by Gwo [214] and was chosen over the standard cleaning procedure described in Chapter 3, section 3.2.1; since the discs are much thinner than the cuboids used in experiments described in previous chapters, manual cleaning was considered to have greater potential for leading to damage. The discs were wiped with a methanol soaked Anticon Gold StandardWeight clean-room wipe immediately prior to bonding. The bonding solution was produced as according to Chapter 3, section 3.4.3.

Bonds were formed and cured at room temperature before the discs were used for the mechanical loss experiments. Both bonds contained a small number of bubbles. The pair of samples with the smallest un-bonded area was selected for use in the bond loss experiments (this was also the pair of discs which were measured to have the flattest surfaces). See figure 6.5 for photographs showing the bonded discs.

6.7.4. Loss measurements of bonded sapphire discs

Initial loss measurements of the bonded pair of discs were carried out at room temperature. The bonded samples with the “better” bond (i.e. the one with the fewer bubbles)

6. Loss measurements of hydroxide catalysis bonds between sapphire discs: Experiment

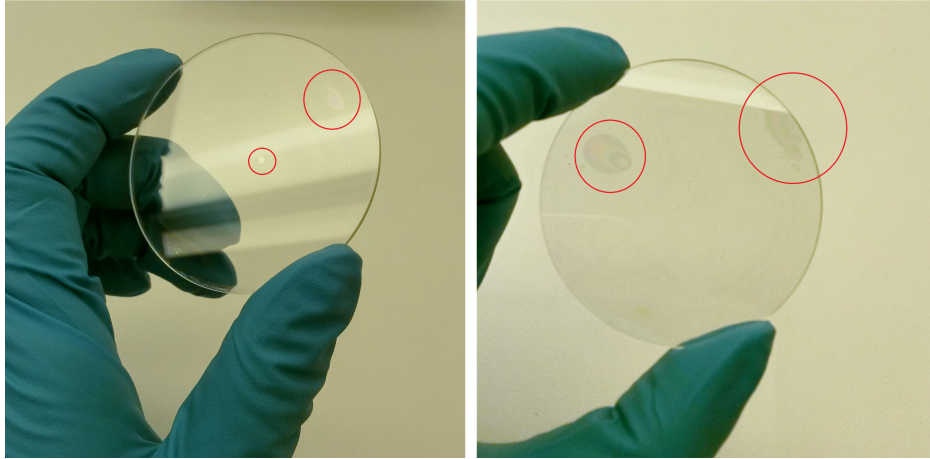


Figure 6.5.: Left: A more complete bond layer with fewer bubbles in the intended bond region, Right: a less complete bond layer. The bonded samples on the left were chosen for bond loss experiments. Bubbles are circled in red.

was suspended in the cryostat so that it could be cooled. FEA models were used to inform the frequency ranges over which resonant modes were likely to be found. The mode shapes from these models were used to inform whether or not the resonant modes could be damped by the supporting wires once excited. However, due to initial difficulties in finding the resonant modes, the second pair of bonded discs was suspended in a second, room temperature vacuum tank in order to double the opportunities to find a mode.

A resonant mode at ~ 6 kHz was detected using the disc in the room temperature set up and the precise frequency of this mode was used to refine the frequency search range to find the same mode in the disc in the cryostat. This led to the detection of a “split mode” at ~ 6 kHz for the disc in the cryostat (see section 5.4.3). These modes were only measurable below room temperature as the ringdown time above room temperature was so short.

Later a second resonant mode was detected at ~ 14.5 kHz for the disc in the cryostat but this mode was never detected or measured for the disc in the room temperature set up and was measurable over a smaller temperature range than the ~ 6 kHz mode. When the resonant modes were found they were excited using the electrostatic drive plate and the “ringdowns” were measured to find the mechanical loss.

6. Loss measurements of hydroxide catalysis bonds between sapphire discs: Experiment

New measurements were taken at room temperature to confirm that the resonant modes could still be found and then the discs were cooled, first to liquid nitrogen and then to liquid helium temperatures. To reach the minimum temperature, contact gas was used. Measurements were taken at all temperature points where carrying out measurements was possible.

6.8. Results

The first disc that was measured was one of the two 0.5 mm thick discs. The mechanical losses measured are shown in figure 6.6. Here 7 resonant modes were found, excited and measured between ~ 20 K and ~ 300 K. These modes appeared at ~ 2.1 kHz, ~ 2.3 kHz, ~ 3.6 kHz, ~ 4.9 kHz, ~ 7.9 kHz, ~ 13 kHz and ~ 15 kHz (the frequencies are temperature dependent) - these resonant frequencies agree with those found using FEA analysis. The mechanical loss can clearly be seen to decrease as the temperature decreases, as would be expected for sapphire, and this loss varies between $\sim 4 \times 10^{-7}$ and $\sim 8 \times 10^{-4}$.

Figure 6.7 shows the mechanical loss measurements for the blank, unbonded sapphire disc with thickness of 1.5 mm and diameter 50.8 mm. Here four modes were measured between room temperature and ~ 15 K. These modes appeared at 6.3 kHz, 14.5 kHz, 25.3 kHz and 40.4 kHz. As can clearly be seen, the mechanical loss is reduced at lower temperatures. However, the modes were not all measurable for the full temperature range, as is reflected by the gap in the data between 150 K and 280 K. In particular, it was only possible to measure the 40.4 kHz mode at room temperature, while the other modes were measurable over a greater range of temperatures.

Figure 6.8 shows the mechanical loss measurements for the bonded pair of sapphire discs. One disc had a thickness of 1.0 mm and the other had a thickness of 0.5 mm. Both had a

6. Loss measurements of hydroxide catalysis bonds between sapphire discs: Experiment

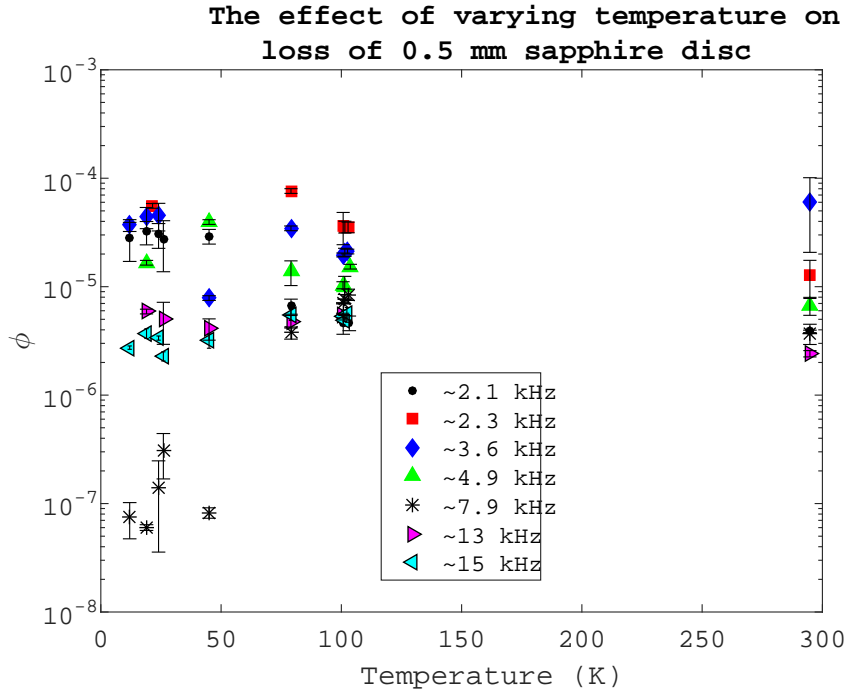


Figure 6.6.: Mechanical loss measurements for a sapphire disc with thickness 0.5 mm and diameter 50.8 mm. The different coloured points represent the measured losses associated with each of the different resonant modes. The loss for each mode was measured three times at each temperature step and the average of those three measurements is shown here. The error bars indicate the standard deviation on the three measurements.

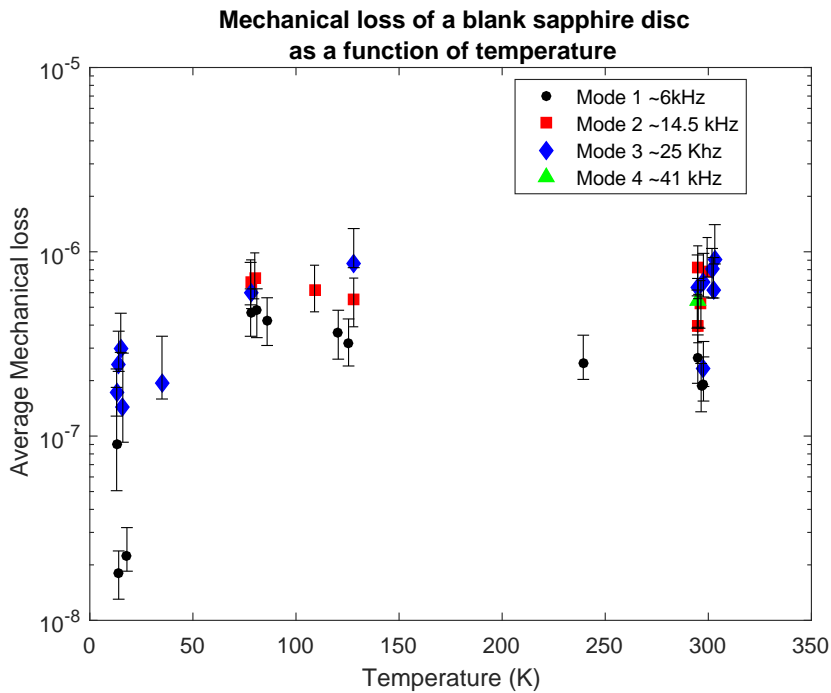


Figure 6.7.: Mechanical loss measurements for a sapphire disc with thickness 1.5 mm and diameter 50.8 mm. The error bars here indicate the standard deviation of the bond losses measured at each temperature step.

6. Loss measurements of hydroxide catalysis bonds between sapphire discs: Experiment

diameter of 50.8 mm. Here three modes are measured between ~ 260 K and 13 K - two of these modes were a pair of split modes around ~ 6 kHz, the third mode was at ~ 14.5 kHz. As with the unbonded disc, over certain temperature ranges it was not possible to measure the mechanical loss and this is reflected in the gaps in the data. In particular, measuring any mode at room temperature was challenging and lead to unreliable data which is excluded from this plot. For each temperature step, each mode was excited three times and three ringdowns of the mode were recorded. In each case here, average recorded loss from the three measurements, is shown.

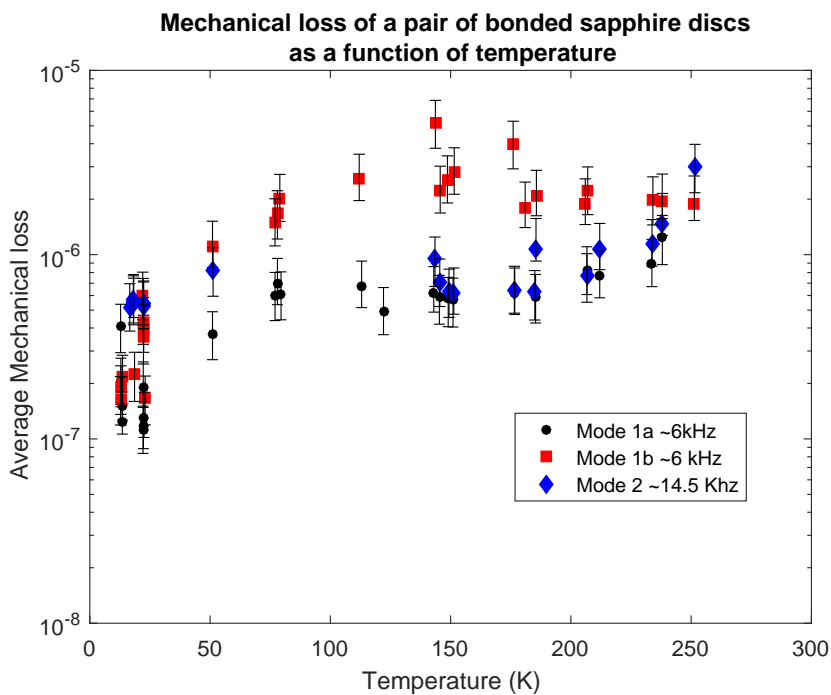


Figure 6.8.: Mechanical loss measurements for a pair of bonded sapphire discs with a combined thickness of 1.5 mm and diameter 50.8 mm. The error bars here indicate the standard deviation of the bond losses measured at each temperature step.

In figure 6.9 the data from figures 6.7 and 6.8 are combined.

It should be noted that the measured losses shown in figures 6.7 and 6.8 are significantly lower than the thermoelastic loss calculated for a sapphire cantilever in section 6.6. This indicates that the use of a cantilever to model a disc has some limitations, however, it is also clear that for both the cantilever approximation and the measured losses for the discs, the values start to decrease with temperature below ~ 100 K.

6. Loss measurements of hydroxide catalysis bonds between sapphire discs: Experiment

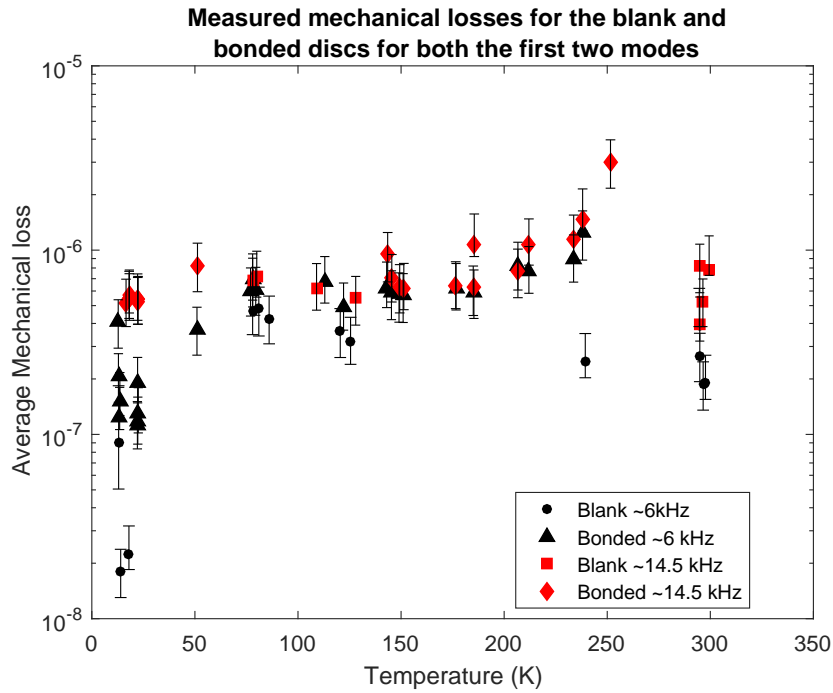


Figure 6.9.: Mechanical loss measurements for a pair of bonded sapphire discs with a combined thickness of 1.5 mm and diameter 50.8 mm, compared with the data for a blank sapphire disc with the same dimensions. The error bars here indicate the standard deviation of the bond losses measured at each temperature step.

Since not all modes were measured at all temperatures, the mechanical loss is interpolated across temperature ranges where there was enough data to do so. Data is particularly sparse between ~ 150 K and ~ 190 K and as such care should be taken when interpreting the results in this temperature range. In particular, there is very little data available in this temperature range for the 14.5 kHz mode.

Interpolating from the available data and using the results from the FEA models of strain energy, the loss of the bond can be extracted. The FEA models used assume a bond thickness of 300 nm and bond Young's modulus of 7.9 GPa. The resulting bond loss information is shown in figure 6.10 which indicates that as temperature decreases so does bond loss. The lowest value of loss for the 6 kHz mode was found at ~ 13 K and was 1.2×10^{-3} , this increased to 1.1×10^{-2} at ~ 240 K. The lowest value of loss for the 14.5 kHz mode was 2.7×10^{-4} at ~ 80 K; at ~ 300 K this rose to 2.6×10^{-2} . It is possible that the 14.5 kHz mode is less lossy than the 6 kHz mode because of the mode shape - if the points

6. Loss measurements of hydroxide catalysis bonds between sapphire discs: Experiment

at which the disc was suspended moved less for the 14.5 kHz mode, less energy would be lost through friction between the disc and the suspension fibres, leading to the lower measured loss values.

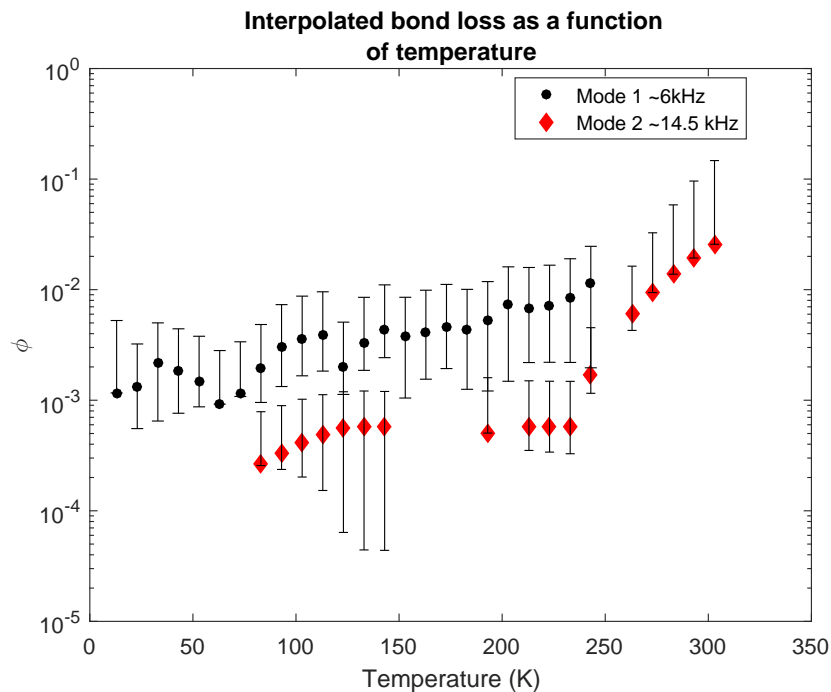


Figure 6.10.: Interpolated mechanical loss of a hydroxide catalysis bond with thickness 300 nm, between two clamped, bonded sapphire discs with a combined thickness of 1.5 mm and diameter 50.8 mm. Error bars indicate the standard deviation on the mean.

Two sets of FEA models were built for analysis of this data. It is challenging to accurately model the effect of “clamping” a disc using a nodal support as discussed in the previous sections. The tungsten fibres do not truly clamp the disc in that they do not ensure that the edges of the disc remain completely still; rather they support the disc which can still swing, rotate and bounce by a small amount within the support. Hence, a model in which the disc is clamped (as shown in figure 5.4) and one in which the disc is not clamped were both considered. The results in figure 6.10 were found with the results from the clamped model. The results presented in figure 6.11 were based on the results from an unclamped model. The true values for the bond loss are likely to lie somewhere between those in figures 6.10 and 6.11.

6. Loss measurements of hydroxide catalysis bonds between sapphire discs: Experiment

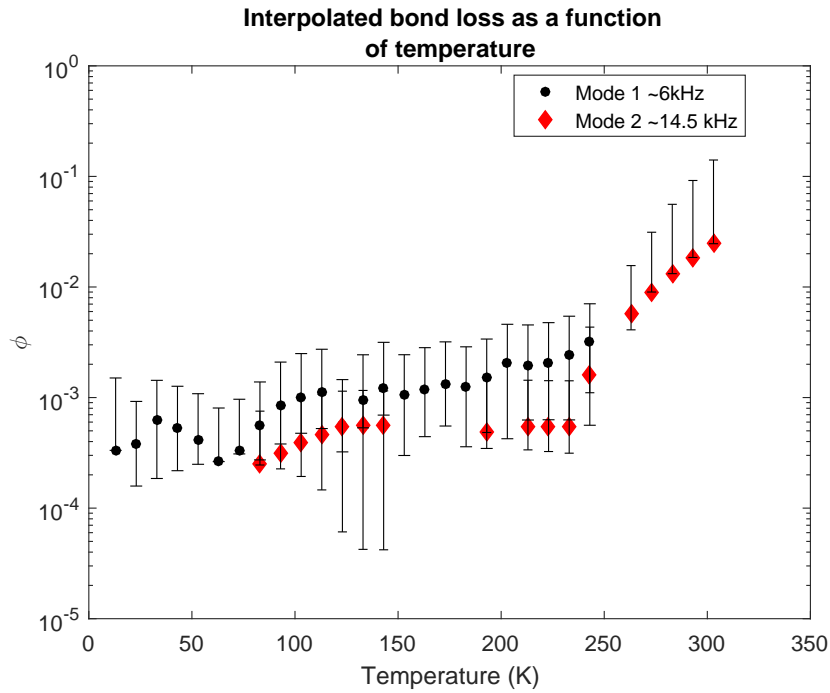


Figure 6.11.: Interpolated mechanical loss of a hydroxide catalysis bond with thickness 300 nm, between two unclamped, bonded sapphire discs with a combined thickness of 1.5 mm and diameter 50.8 mm. Error bars indicate the standard deviation on the mean.

The main difference between the results presented in figures 6.10 and 6.11 is that the latter features lower loss values. Additionally, the loss values for the two modes tend to be closer for these results. Here, a lower value for the bond loss for the 6 kHz mode at ~ 13 K of 3.3×10^{-4} and an upper value of 3.2×10^{-3} at ~ 243 K are found. For the 14.5 kHz mode, the lower bond loss value is 2.5×10^{-4} at ~ 80 K and the upper value is 2.46×10^{-2} at ~ 300 K. Figure 6.12 shows the difference between the results where the clamped and the unclamped models are used. The mean difference for the ~ 6 kHz mode is $\sim 3 \times 10^{-2}$ and the mean difference for the ~ 14.5 kHz mode is 2.1×10^{-4} but the differences are temperature dependent and have a greater effect as the temperature is increased.

Hence, if the differences between these two models are used to give an estimate of the uncertainty of the bond loss, the lower value for the bond loss for the 6 kHz mode at ~ 13 K is between $\sim 3.3 \times 10^{-4}$ and $\sim 4 \times 10^{-3}$ and the upper value, at ~ 243 K, is between $\sim 3.2 \times 10^{-3}$ and $\sim 1.2 \times 10^{-2}$. For the 14.5 kHz mode at ~ 80 K, the loss is between $\sim 2.4 \times 10^{-4}$ and $\sim 9.7 \times 10^{-4}$ and is between 2.46×10^{-2} and 4.27×10^{-2} at ~ 300 K.

6. Loss measurements of hydroxide catalysis bonds between sapphire discs: Experiment

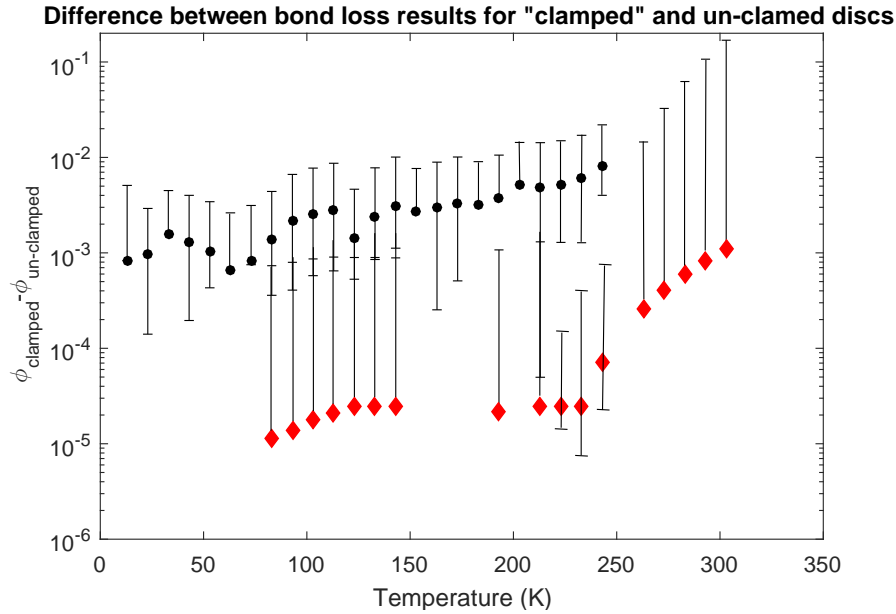


Figure 6.12.: Interpolated mechanical loss of a hydroxide catalysis bond with thickness 300 nm, between two unclamped, bonded sapphire discs with a combined thickness of 1.5 mm and diameter 50.8 mm. Error bars indicate the standard deviation on the mean.

This information can be used to find the strain for a particular detector design. Returning to the discussion of thermal noise in Chapter 2 (section 2.4), equation 2.31 (reproduced here for convenience) can be used to find the thermal noise [120].

$$S_x(f) = \frac{2k_B T W_{\text{diss}}}{f^2 \pi^2 F_0^2} \quad (6.13)$$

Where k_B is the Boltzmann constant, T is the temperature, f is the frequency, and $W_{\text{diss}} = 2\pi f \phi E_{\text{strain}}$ is the dissipated power when an oscillatory force with peak magnitude F_0 acts on the front face of the test mass mirror and E_{strain} is the energy of elastic deformation when the test mass is maximally contracted or extended due to that force [120]. The value for E_{strain} can be found through FEA modeling but for a given test mass design all other values are known with the exception of the loss factor of interest, ϕ , which has now been measured for the bond loss between sapphire pieces.

6. Loss measurements of hydroxide catalysis bonds between sapphire discs: Experiment

The strain in the interferometer arms is then given by [215, 216, 217],

$$\frac{2S_x(f)}{L_{\text{arm}}} \quad (6.14)$$

Where L_{arm} is the length of one of the interferometer arms. So, for example, for an interferometer with the design of the KAGRA detector with 3 km arm lengths, 21 kg sapphire test masses with diameter of 220 mm and thickness 150 mm, assuming a beam radius of 38 mm and a bond area of 30 mm × 80 mm with an operating temperature of 20 K [218], a strain energy of 5.8×10^{-19} J [217] with a bond loss, as measured in the experiments described above of $\sim 1.3 \times 10^{-3}$ (see figure 6.10), there is a strain of $\sim 3.7 \times 10^{-26}$ at 100 Hz. In the case of KAGRA, the design requirement is 2×10^{-25} and hence these results suggest that hydroxide catalysis bonds between sapphire pieces will meet the thermal noise requirements of such a detector.

6.9. Conclusions

Assuming a pair of sapphire discs with Young's modulus ~ 400 GPa, with one disc of thickness 1.01 mm and one 0.49 mm and with both having a diameter of 50.8 mm (the actual, measured dimensions of the discs with which these experiments were carried out) alongside a bond layer with a Young's modulus of 7.9 GPa and a thickness of 300 nm, strain energy ratios were calculated using FEA models. A bond thickness of 300 nm resulted in the resonant frequencies predicted being closest to those actually measured experimentally, and is similar to the flatnesses measured for the discs used.

Since, as mentioned earlier, it is not straightforward to accurately model how the tungsten support fibres restrict the motion of the disc two models were produced; one in which the

6. Loss measurements of hydroxide catalysis bonds between sapphire discs: Experiment

bonded discs were clamped and one in which they were not. The models in which the discs are clamped predict resonant modes closer in frequency to those that were actually measured experimentally however it is clear that the fibres do not truly clamp the disc. Certain resonant modes will be strongly damped by the fibres depending on the shapes of the modes and where the greatest points of motion are. When attempts were made to excite modes some of those predicted by the FEA analysis would not excite, it is likely that these are the modes that were strongly damped. Since the disc motion is somewhat, but not entirely, restricted by the fibres, bond loss values using results from both the clamped and unclamped FEA models are presented in the preceding section.

The mechanical loss of a hydroxide catalysis bond between two sapphire discs decreases with decreasing temperature. At room temperature bond losses of approximately 2.5×10^{-2} were found. At cryogenic temperatures this decreases down to as low as $\sim 2.5 \times 10^{-4}$. This is an initial measurement which is limited by the small number of modes that were measurable, the bubbles in the intended bonding area, the flatness of the discs, the potential variations in bond thickness across the plane of the discs, and so on. However, these results are similar to results found by Haughian *et al* [200] in which the mechanical loss of bonds between sapphire cylinders was found to be $\sim 3 \times 10^{-2}$ at room temperature and $\sim 3 \times 10^{-4}$ at 20 K. As an initial measurement this gives some indication of what behaviour might be expected of bonds in a gravitational wave suspension system that uses hydroxide catalysis bonds between sapphire components.

In the case of an interferometer with the current KAGRA design, these bonds are a factor of 5 better than is required by the thermal noise budget. While it is possible that this could be improved further should higher quality bonds be produced, it indicates that hydroxide catalysis bonding is a suitable technique for use in cryogenic interferometric gravitational wave detector suspensions.

7. Thermal cycling of silicon-silicon hydroxide catalysis bonds

7.1. Introduction

Silicon is a material of interest for future gravitational wave detector test mass suspension systems intended for cryogenic operation [90]. It has desirable thermo-mechanical properties, including low mechanical loss, at cryogenic temperatures [136, 219, 220, 221]. This is in contrast to fused silica, which has a broad mechanical loss peak centred around ~ 40 K [106]. In particular, the Einstein Telescope (ET) is likely to have silicon suspensions [90, 68]. Silicon may also be an interesting candidate material for future upgrades of existing detectors as these may also operate in the cryogenic regime.

For use in such a detector, investigations into hydroxide catalysis bonds between silicon surfaces are underway. The strength of the bonds at both room temperature and at liquid nitrogen temperatures, as well as the thickness of bonds, have already been studied to some extent [137, 182, 158, 186, 117]. Beveridge *et al* reported that sodium silicate bonds between silicon were measured to have an average thickness of ~ 47 nm and tensile strengths of ~ 36 MPa [158]. In previous experiments, van Veggel *et al* reported strengths of between 30 MPa to 50 MPa, and also noticed that bonds regularly had wedged cross

7. Thermal cycling of silicon-silicon hydroxide catalysis bonds

sections, with the bond thickness varying across the bond area [137]. Dari *et al* found strengths of ~ 9 MPa using KOH rather than sodium silicate solution and using a different strength testing apparatus [182].

Unlike sapphire and fused silica, untreated silicon cannot be directly bonded using the hydroxide catalysis bonding technique [139, 117]. Therefore, some additional steps are required to adapt the bonding procedure such that bond formation between silicon surfaces is possible. For successful bonds to be formed an SiO_2 oxide layer must first be deposited or grown on the silicon surface [117, 154]. The hydroxide can then react with this SiO_2 layer to form the bond [139]. Otherwise, bonding solutions may react with the silicon to form hydrogen bubbles which may lead to a foam forming within the bonding solution and bond layer.

Previous studies into the possible methods of growing or depositing an oxide layer on silicon were carried out by Beveridge *et al*; wet thermal oxides were tested and it was discovered that a minimum oxide thickness of 50 nm was needed for successful bond formation [158]. Further studies investigated a range of oxidation methods, including dry thermal oxide, ion beam sputtered and e-beam deposited. The dry thermal oxide technique consistently led to bonds with the greatest strengths [186]. Ion beam sputtered coatings were also associated with high quality bonds but the process must be outsourced and is more costly. For these reason, for the bonds described in this chapter, the silicon samples were oxidised before bonding using the dry thermal oxide technique.

As with sapphire suspensions, any silicon suspension intended for cryogenic operation is likely to undergo multiple thermal cycles during its installation. Hence it is important to understand the effect of thermal cycling on bond strength. The details of experiments into this effect is are discussed in this chapter.

7.2. Silicon samples for hydroxide catalysis bonding experiments

An undoped $\langle 111 \rangle$ Czochralski-grown silicon ingot with thickness 150 mm and diameter 150 mm was procured from Prolog¹ and from this 140 $\langle 111 \rangle$ silicon samples were cut and polished by Spanoptic². The samples were cuboids with dimensions $5 \times 10 \times 20$ mm (see figure 7.1). They had 0.2 mm chamfers on the intended bonding face, which was nominally polished to a peak-to-peak flatness of 60 nm, a degree of flatness used in past samples with which successful bonds have been produced [138, 154, 137]. The other faces were not polished and had a ground finish.

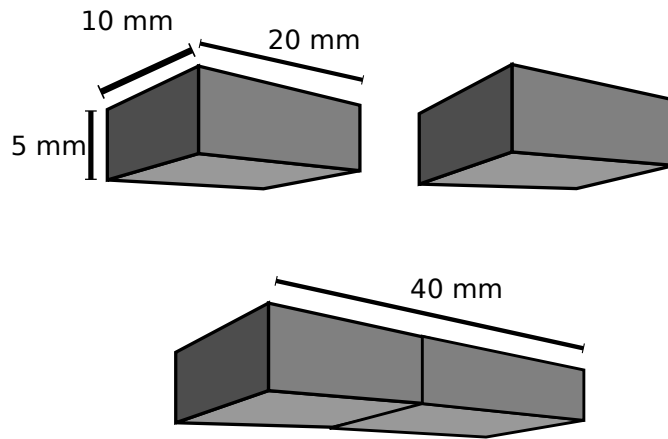


Figure 7.1.: Diagram of the $\langle 111 \rangle$ silicon samples used for experiments involving thermal cycling of hydroxide catalysis bonds between silicon. The 5×10 face of the samples are parallel to the $\langle 111 \rangle$ plane.

The samples' dimensions were measured with calipers, their bonding surface flatnesses were measured with a ZYGO GPI XP/D interferometer. The mean flatness of the intended bonding surface was 46 nm with a standard deviation of 11 nm (excluding four samples with unusually poor flatnesses of 185, 261, 285 and 445 nm). See figure 7.2 for an example of a flatness surface profile and 7.3 for a histogram showing the distribution of flatnesses of the samples.

¹<http://semicor.en.ec21.com>

²<http://www.spanoptic.com>

7. Thermal cycling of silicon-silicon hydroxide catalysis bonds

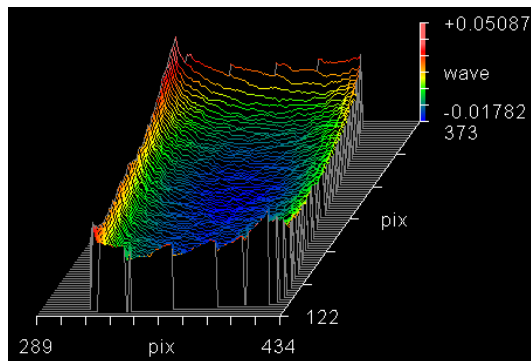


Figure 7.2.: An example of the flatness profile of the intended bonding surface of one of the silicon samples. The surface shown here is the 5×10 mm bonding surface of one of the samples.

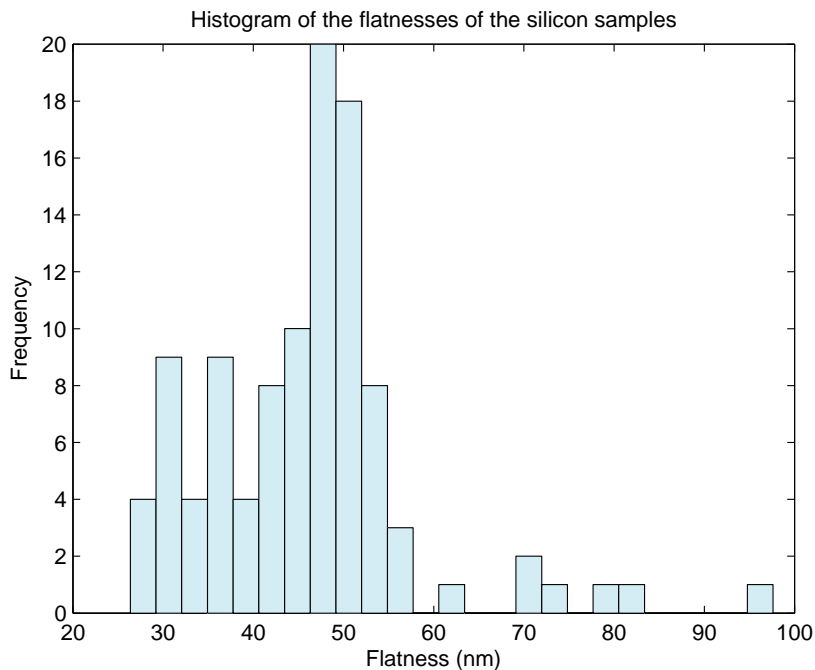


Figure 7.3.: Histogram showing the distribution of flatnesses of the intended bonding surface of the silicon samples. Four sample flatnesses are not represented here as they had unusually poor values (185, 261, 285 and 445 nm) and were not used.

7. Thermal cycling of silicon-silicon hydroxide catalysis bonds

The samples were also visually assessed to check for any chips or cracks - those samples which did have chips or cracks in the surface were not used for bonding experiments; a total of three samples were removed for this reason. The flatness information was recorded alongside information on the sample condition and was associated with a sample identification number which was scribed onto the sample surface, so that it could be referred to later, should any bonds have unusually high or low strength to the extent that this would merit further investigation of the samples used to make the bond.

7.3. Oxidation of silicon surfaces

Before any samples intended for bonding were oxidised, pieces of $\langle 111 \rangle$ silicon cantilever were used to characterise the oxidation rate of samples in a quartz tube furnace (Carbolite-Gero³). Oxidation rates of silicon have been found to be highly dependent on temperature and humidity and it should be expected that different ovens will give different oxidation rates [222]. The longer samples spend in the furnace, the thicker the oxide layer on the surfaces. In the first instance it was found that an oxide layer of 150 nm would grow in ~ 3 hours. Since it was found that an oxide layer at least 50 nm thick was required for successful bonds, this gave a safety factor of three.

Later, one of the furnace seals was changed and a second characterisation was carried out - it was found that an oxide layer of 150 nm would now grow in ~ 5 hours. It is likely that the change in seal altered the rate of air flow, however this was not directly measured. In all cases the oven was allowed to stabilise over one hour after having been set to heat to 1000 °C. See appendix C for more details on oven characterisation.

Before any samples or characterisation pieces were inserted into the oven for oxidation the temperature was set to 1000 °C and was allowed to heat for one hour in order to

³carbolite-gero.com

7. Thermal cycling of silicon-silicon hydroxide catalysis bonds

ensure that the temperature had fully stabilised. Oxidation was carried out at ambient pressure, however the air in the oven was not circulated through the tube.

Apart from the seal being changed and the oxidation time being correspondingly increased, there was at no point any other change to the procedure for growing the dry thermal oxide. The oxide thickness on each of the silicon cantilever pieces was measured using an ellipsometer (Sentech SE 400adv⁴).

The silicon samples described in this chapter were first cleaned in “piranha solution” - a 1:7 volumetric ratio of hydrogen peroxide and sulphuric acid - for ~10 minutes, to remove any surface contaminants. The samples were then rinsed, first in copious quantities of de-ionised water in order to remove any remaining piranha solution, and secondly in methanol to prevent water marks from forming. They were then placed onto a silica rack and were baked in the quartz tube furnace at 1000 °C in a dry air environment.

The samples were oxidised in batches of no more than 10 samples simultaneously. In total 16 batches of samples were oxidised; the first 8 batches were used to make the first round of bonds and the second 8 batches were oxidised to produce the second round of bonds. The oven seal was replaced between the oxidation of the 5th and 6th batches.

After oxidising the samples, the thickness of oxide was measured for each sample and this information was also associated with the samples' identification numbers. The average oxide thickness was 147 nm, with a standard deviation of 25 nm across the sample set. See figure 7.4 for a histogram showing the distribution of oxide thicknesses.

⁴<http://www.sentech.com/>

7. Thermal cycling of silicon-silicon hydroxide catalysis bonds

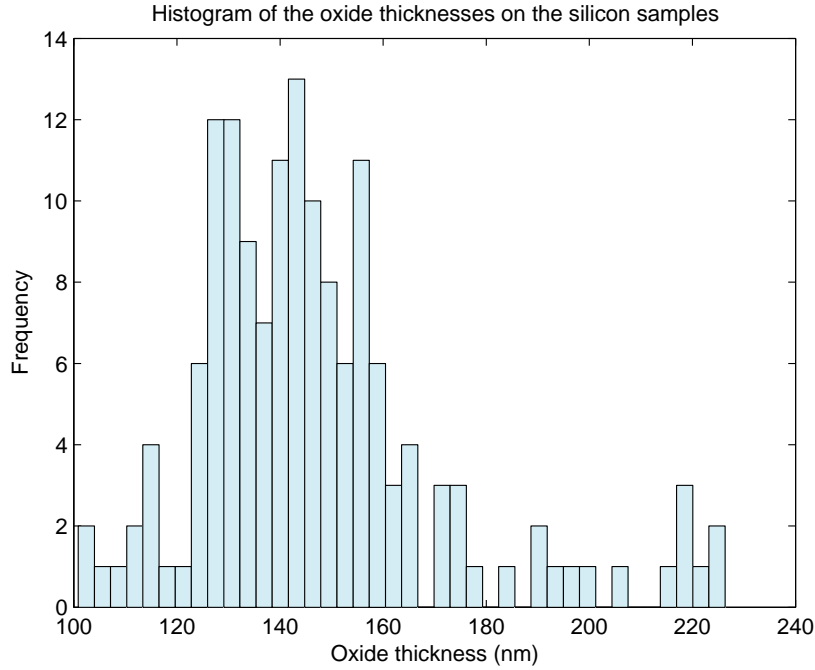


Figure 7.4.: Histogram showing the distribution of oxide layer thicknesses on silicon samples after oxidation

7.4. Bonding of silicon surfaces

The samples were cleaned according to the standard cleaning procedure, as used for cleaning sapphire samples for bonding (detailed in section 3.2.1). They were then bonded in a clean room environment, using sodium silicate solution at room temperature (see section 3.2.3 for full details of this procedure) and the bonds were allowed to cure at room temperature for four weeks. During the first week of curing they were held in aluminium alignment jigs. They were then wrapped in individual Anticon Gold StandardWeight clean-room wipes and stored in a sample box for the remaining three weeks.

For the first set of thermal cycling experiments, 40 bonds were produced (using a total of 80 silicon samples): 10 bonds to be thermally cycled 3 times, 10 to be thermally cycled 10 times, 10 to be thermally cycled 20 times and 10 which were not cycled and acted as a control set. The samples in the control set were treated in exactly the same way as the samples for thermal cycling and the bonding procedure used was exactly the same.

7. Thermal cycling of silicon-silicon hydroxide catalysis bonds

Later a further 29 bonds were produced (using a total of 58 silicon samples) to improve statistics; 7 to be thermally cycled 3 times, 8 to be thermally cycled 10 times, 7 to be thermally cycled 20 times and 7 in the control set.

Nothing about the procedure was changed between the first and second run of the experiment except some samples in the first set and all samples in the second set were oxidised after the oven seal was changed (see section 7.3 and appendix C) however the oxide thicknesses before and after the seal change are similar and no other differences were observed in the two sets.

The bonds for each group (control, 3 cycles, 10 cycles and 20 cycles) were randomly selected from the full set of bonds. This was to avoid any effects associated with the different batches of samples that were oxidised simultaneously.

7.5. Thermal cycling procedure

When the bonds had fully cured, they were transported to the University of Jena, Germany for thermal cycling between room temperature and ~ 4 K.

Each thermal cycle took ~ 2 hours; one hour to bring the bonded samples close to liquid helium temperature (~ 10 K) and one to return them to room temperature. This was achieved by mounting the samples in a holder with a temperature sensor and lowering this directly into a dewar of liquid helium. The samples were secured in the sample holder with Teflon tape (see figure 7.5). This was then closed by screwing a closed-ended aluminium tube over the entire holder.

7. Thermal cycling of silicon-silicon hydroxide catalysis bonds

A temperature sensor was mounted under the tape and directly underneath one of the samples, allowing the temperature to be monitored at all times during the cycling. The level of helium in the dewar was also monitored using this temperature sensor, as over time the helium would boil off. Monitoring the helium level to allowed adjustment of the rate at which the samples were moved such that in each cycle the samples spent the same length of time at liquid helium temperatures. The sample holder was then drawn out of the helium to the top of the dewar and was allowed to return to room temperature.

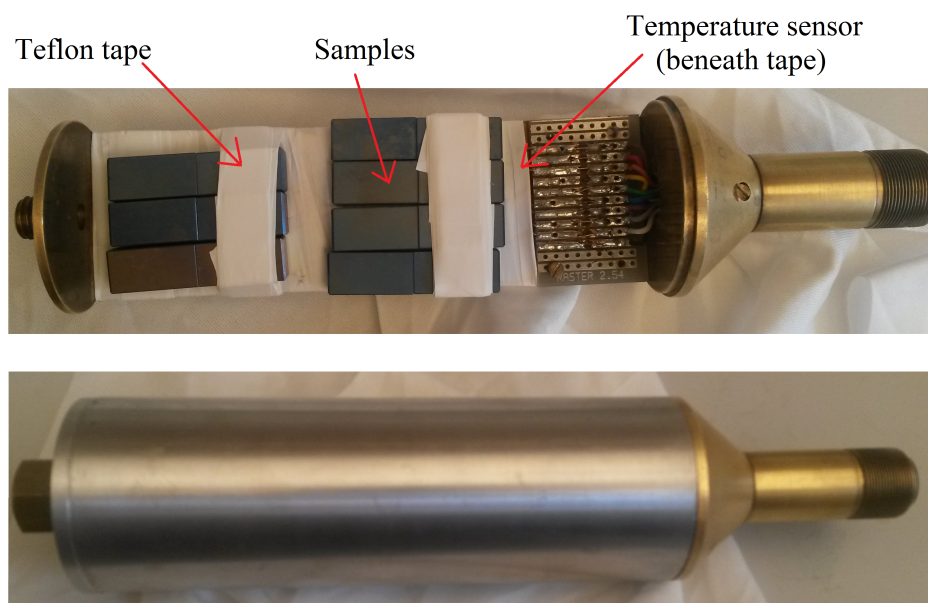


Figure 7.5.: Sample holder for thermally cycling bonds between silicon. A maximum of ten samples were cycled per set, with 7 mounted on one face and 3 mounted on the opposite face (not visible). The top image shows the samples as mounted into the holder and the bottom shows the holder closed

A wait period was added so that the sample holder spent some time stationary, both at the top of the dewar and while submerged in liquid helium. This was done in an attempt to ensure that the samples came to equilibrium at their maximum and minimum temperatures for each cycle. In fact, while the temperature of the samples reached an equilibrium at the bottom of the dewar during each cycle, the temperature at the top of the dewar had not fully stabilised at the top of the dewar before the next cycle began. See figure 7.6 for an example of how the temperature of the sample holder changed during the thermal cycles.

7. Thermal cycling of silicon-silicon hydroxide catalysis bonds

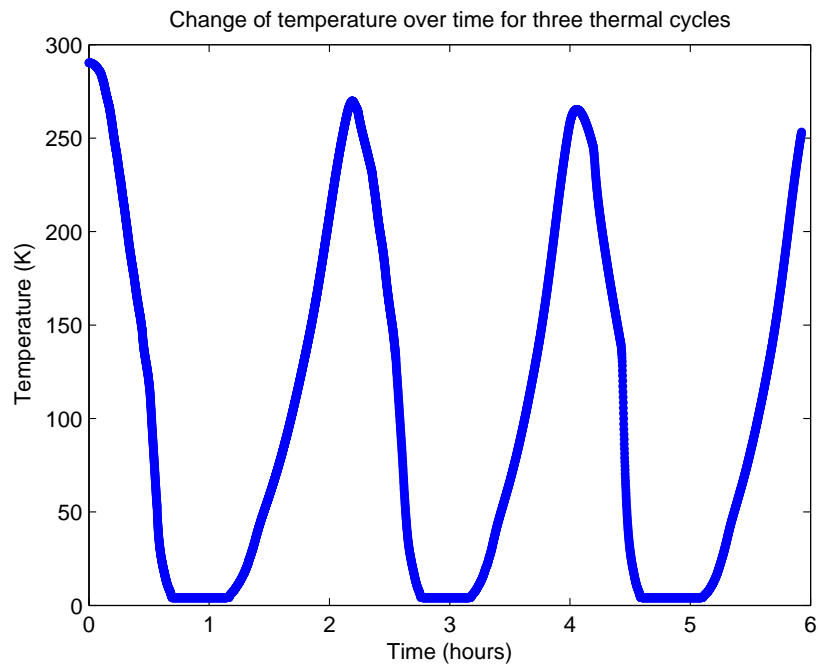


Figure 7.6.: An example of the change in temperature of a set of bonded silicon samples over time during three thermal cycles, as recorded via the temperature sensor in the sample holder with the samples.

7.5.1. Strength testing

After the thermal cycling process the bonded samples were re-packed in Anticon Gold StandardWeight clean room wipes, returned to the sample boxes and transported back to Glasgow for strength testing. This was carried out five weeks after the bonds were formed. The tensile strengths were obtained using the 4-point bending test at room temperature, in the same way as described in Chapter 3, section 3.6.

7.5.2. Breaking mechanisms

In contrast to bonding experiments with sapphire pieces, in which the tensile strength testing procedure rarely resulted in damage to the bulk substrate, silicon was often damaged by the strength testing procedure. Three breaking mechanisms were identified: “Bond failure,” in which the samples were separated cleanly across the bond. Typically

7. Thermal cycling of silicon-silicon hydroxide catalysis bonds

after breaking this would feature visible “bubbles” where the bonding solution had failed to spread across the full intended bonding surface; “oxide failure,” in which the oxide layer appeared to have failed - indicated by a sharp change of colour - and “diagonal break,” in which there was significant damage to the bulk silicon. These are the same breaking mechanisms as those identified by Beveridge *et al* in previous experiments in hydroxide catalysis bonding of silicon [186]. See figure 7.7 for photographs of these three types of breaks. For each bond the breaking mechanism was recorded, in case this mechanism might be associated with bonds of a greater or lesser strength; if a bond is incomplete and fails this is likely to have a negative impact on the strength measured, this has been seen in bonds formed between fused silica samples in the past [157].



Figure 7.7.: Photographs of silicon surfaces after being bonded, thermally cycled and the bonds having been broken. From left-to right, image a) shows a bond failure, probably because the bond was incomplete; the white arrow indicates marks on the surface formed by bubbles in the bond. Image b) shows a typical diagonal break, where the bulk material has failed. Image c) shows damage to the oxide layer, the white arrow indicates the sharp change in colour that shows where the oxide layer has failed.

In figure 7.7a, it appears that the bond was incomplete - evidence of bubbles is still visible. In figure 7.7b, the bulk of the sample is damaged - this is a typical diagonal break and is similar to that which is observed when high quality bonds with fused silica are broken. In figure 7.7c the oxide layer on the silicon seems to be damaged.

7.6. Results

7.6.1. Bond Strength

The measured tensile strength results are shown in figure 7.8 in which the strengths of the first set of bonds measured are shown in blue and the strengths of the second set of bonds are shown in green. Figure 7.9 shows the two sets are combined.

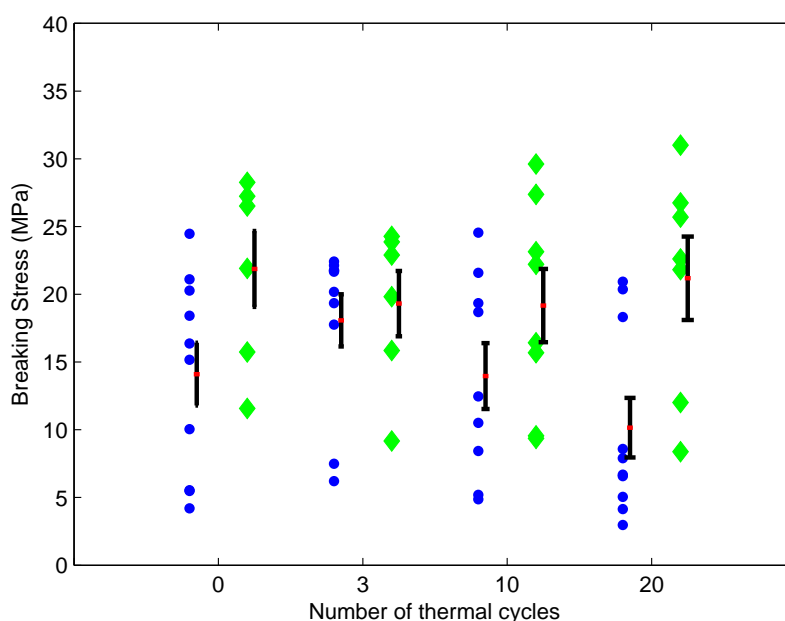


Figure 7.8.: Tensile strengths of silicon-silicon bonds after thermal cycling. The error bars shown here indicate the standard error on the mean. Blue points show the first round of bonds, green points show the second

The strengths obtained in the two rounds of the experiment were obtained in the same way and as such there is no reason to separate them. Hereafter when the strengths of bonds are discussed both sets of strengths are combined. The mean measured tensile strength of the control bonds was 17 MPa, the mean measured tensile strength of the bonds which were thermally cycled 3 times was 19 MPa, the mean measured tensile strengths of the bonds which were thermally cycled 10 times was 16 MPa and the mean measured tensile strengths of the bonds which were thermally cycled 20 times was 15 MPa. See table 7.1

7. Thermal cycling of silicon-silicon hydroxide catalysis bonds

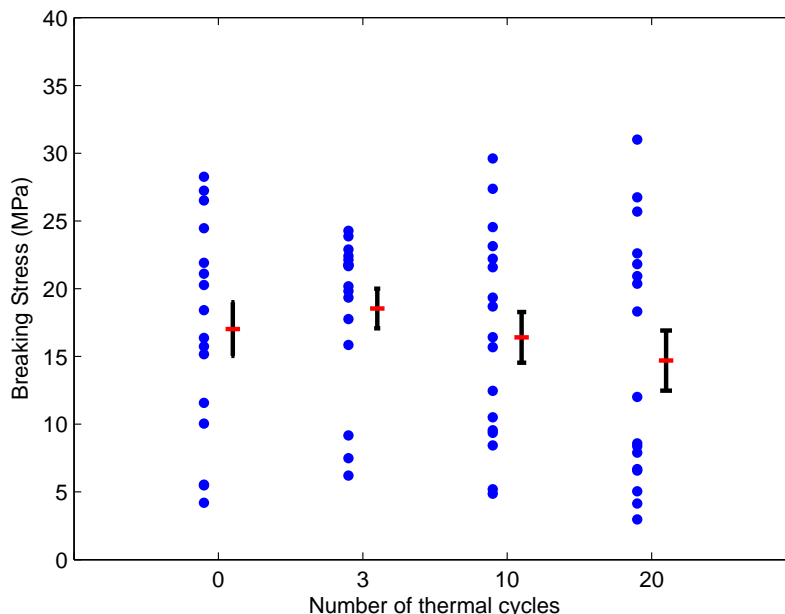


Figure 7.9.: Tensile strengths of silicon-silicon bonds after thermal cycling. The error bars shown here indicate the standard error on the mean. All measured strengths are included here

for a summary of the mean, minimum and maximum strengths measured (these values are combined values from both experimental data sets).

Table 7.1.: Table of breaking strengths for hydroxide catalysis bonds between silicon samples after 0, 3, 10 and 20 thermal cycles between room temperature and liquid helium temperatures. All strength tests were carried out at room temperature.

Number of cycles	Strength (MPa)			σ	$\frac{\sigma}{\sqrt{n}}$
	Mean	Minimum	Maximum		
0	17	4	28	7.9	1.9
3	19	6	24	5.9	1.5
10	16	5	30	7.7	1.9
20	15	3	32	9.1	2.2

7.6.2. The effect of breaking mechanism on bond strength

Figure 7.7 shows photographs of the samples' surfaces after breaking via the three different breaking mechanisms that were identified; "bond failure", "diagonal break" and "oxide failure". In this set of strength measurements a total of 16 bonds broke in this way via the "bond failure" mechanism. A total of 37 bonds broke via the "diagonal break"

7. Thermal cycling of silicon-silicon hydroxide catalysis bonds

mechanism, damaging the bulk silicon material, suggesting that the bond was at least as strong as the silicon itself in these cases. There were 14 cases where the oxide layer appeared to have failed. It is possible that in these cases the strength measured was therefore the strength of the oxide, rather than the strength of the bond.

As such it may be the case that the bonds which broke by the typical diagonal mechanism (in which the bulk of the sample is damaged, rather than the samples simple separating at the bond interface, see figure 7.7b) give the most reliable representation of the bond strengths. Figure 7.10 shows the measured tensile strengths of each silicon-silicon bond, with the different possible breaking mechanisms indicated. This image shows that the samples with bond failures tend to have lower strengths, which is consistent with what has been seen in the past [186, 157]. For contrast, figure 7.11 shows the strengths of thermally cycled bonds which broke via the diagonal breaking mechanism with measured strengths from other types of breaks omitted.

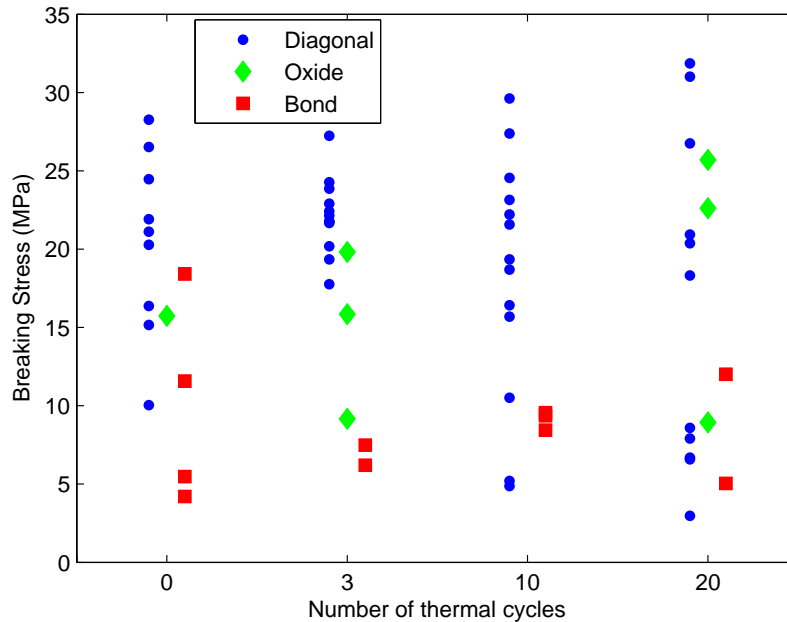


Figure 7.10.: Tensile strengths of silicon-silicon bonds after thermal cycling the three possible breaking mechanisms (“diagonal break”, “oxide failure” and “bond failure”) shown separately.

When considering exclusively those bonds which broke “diagonally” (i.e., those in which the strength testing procedure resulted in damage to the bulk silicon samples) the differ-

7. Thermal cycling of silicon-silicon hydroxide catalysis bonds

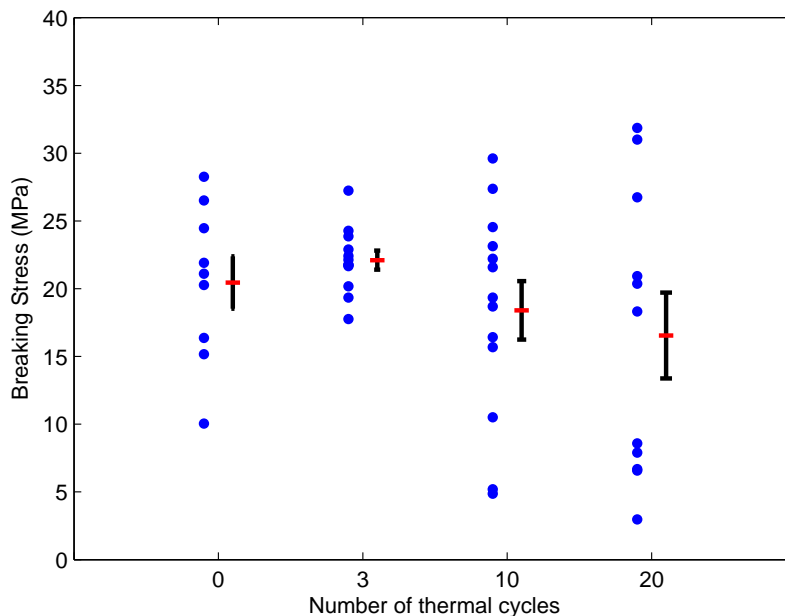


Figure 7.11.: Tensile strengths of silicon-silicon bonds after thermal cycling with poorer quality bonds (i.e. those where the oxide failed or those bonds which contained bubbles) excluded. The error bars shown here are the standard error on the mean.

ences between the strengths associated with different numbers of thermal cycles is smaller. Bonds which were not thermally cycled and broke via this mechanism had a mean strength of 21 MPa, those which were thermally cycled 3 times had a mean strength of 22 MPa, those which were thermally cycled 10 times had a mean strength of 18 MPa and those which were thermally cycled 20 times had a mean strength of 18 MPa. See table 7.2 for a table summarising the mean, minimum and maximum measured tensile strengths in each case.

Although the spread of measured strengths is greatest for bonds which were thermally cycled 20 times, the strengths are within error of bonds which were not thermally cycled and those which were thermally cycled 10 times. Hence, bond reliability appears to be reduced through multiple cycles but it is not clear that the average strength of the bonds is significantly reduced.

7. Thermal cycling of silicon-silicon hydroxide catalysis bonds

Table 7.2.: Table of breaking strengths for hydroxide catalysis bonds between silicon samples after 0, 3, 10 and 20 thermal cycles between room temperature and liquid helium temperatures. The values in this table include only those bonds which broke via the “diagonal” breaking mechanism. All strengths were measured at room temperature.

Number of cycles	Strength (MPa)			σ	$\frac{\sigma}{\sqrt{N}}$
	Mean	Minimum	Maximum		
0	21	10	28	5.8	1.9
3	22	18	27	2.4	0.7
10	18	5	30	7.7	2.2
20	17	3	32	10.5	3.1

7.6.3. Conclusions

Thermal cycling appears not to have a negative effect on the average strengths of bonds even up to 20 cycles, provided those cycles are carried out slowly and the bonds are not thermally shocked. However, there is a clear spread in the strengths obtained. It is possible that part of the cause of this may be poor bond quality. When bonding fused silica or sapphire it is easy to assess bond quality visually before breaking as the materials are optically transparent. When using these materials poor quality bonds (e.g. bonds that are incomplete or contain bubbles or other flaws) may be remade or removed from the results easily. As silicon is optically opaque it is not so straightforward to assess bond quality until after the bonds are broken.

Even when bonds which broke only via the “diagonal” breaking mechanism (i.e. those which may be assumed to be high quality) are considered, there is still a significant spread in measured strengths and the standard error on the mean is similar with or without those strengths associated with other breaking mechanisms. This spread is more pronounced for those bonds which underwent more thermal cycles. Thus thermal cycling may cause less reliable bond strength.

It should be noted however, that on average the strength results shown in figure 7.11 (those strengths associated with “diagonal” bond breaks), have superior strengths, on

7. Thermal cycling of silicon-silicon hydroxide catalysis bonds

average, than those shown in figure 7.9 (all strengths). It is possible that strength is less affected by thermal cycling when a high quality bond is formed.

These results highlight the importance of assessing bond quality. One option for doing so when bonding silicon may be the use of an infrared camera, as silicon is transparent at infrared wavelengths. If bubbles or imperfections are detected, the bonded surfaces should be separated and cleaned and the bonds should be remade. This, however, may not necessarily detect flawed oxides and as such a different method for detecting these is necessary. This is especially desirable since, as can be seen from figures 7.10 and 7.11, including those bonds which broke via oxide failure reduces the average strength measured and increases the spread of the results.

8. Conclusions

Great successes in gravitational wave detection have already been seen through the use of ground based interferometric detectors that utilise fused silica test masses and suspensions. The next steps in gravitational wave detection involve improving the sensitivity of the detectors even further. One way of doing this is to operate the detectors at cryogenic temperatures in order to reduce thermal noise. This will necessitate the use of a different material for the suspensions as fused silica exhibits a large, broad loss peak centred around 40 K. It is likely that the material of choice will be sapphire or silicon and indeed a sapphire based detector is already being built in Japan (KAGRA).

Within this thesis a selection of experiments investigating hydroxide catalysis bonds between sapphire pieces, and those between silicon pieces, have been described. These experiments mostly assessed the strength of bonds. This not only helps to ensure that the bonds will be sufficiently strong to support the test masses, but also informs suspension design; if bonds are stronger the bond area can be smaller which in turn has a positive impact on thermal noise performance.

It was found that hydroxide catalysis bonds between sapphire samples can be extremely strong both at room temperature and at cryogenic temperatures. Average tensile strengths of 74 MPa were recorded at room temperature when bonds were formed using sodium silicate solution. The same solution was used to produce bonds that were measured to have

8. Conclusions

strengths of 73 MPa at 77 K. The high strength of bonds produced using this chemical, when compared to other chemicals, led to its use in the experiments that followed.

The effects of bonding different crystalline planes of sapphire were then considered in terms of bond strength. In general, for the planes studied, it was found that matched-plane bonds had average strengths that were higher than mixed-plane bonds; 74 MPa for m-plane to m-plane bonds as had initially been found and 107 MPa for c-plane to c-plane bonds, compared to 42 MPa and 60 MPa for a-plane to c-plane and m-plane to c-plane bonds, respectively. It should be noted, though, that the c-plane to c-plane bonds also exhibited the greatest spread in strength results of any bonds tested. The cause of this is not immediately clear, although it may be due to rotational mis-match of the c-axis in these bonds. However, the design plans for the KAGRA detector meant that mixed-plane bonds were of significant interest. It is therefore encouraging that even the lowest strengths measured still meet the KAGRA design specification of having strengths of at least 1 MPa with a significant safety factor.

Since any gravitational wave detector intended for cryogenic operation is likely to undergo many thermal cycles during its lifetime, the effect of these cycles was of interest. The effect on strength of carrying out 3 thermal cycles was found to be associated with an apparent drop in strength. Uncycled bonds were measured to have an average strength of 74 MPa compared to bonds which were cycled three times and had an average strength of 36 MPa. However, this strength is still sufficient to support a test mass in a typical suspension design and it is not currently clear whether this decrease in strength would continue with subsequent cycles. More experiments are planned for the future but these are outwith the scope of this thesis.

The possibility of repairing damaged bonds, or re-bonding the same samples in a situation where the suspension design is changed, was then considered. It was found that re-bonding was possible and that the resulting bonds could be strong with average strengths

8. Conclusions

of the order of 40 MPa. However, while changes in bonding solution may lead to different average strengths as repeated rounds of bonding and separating samples are carried out, each round of re-bonding with sodium silicate solution was associated with a decrease in average strength. While re-bonding is possible, it is not advisable to continuously reuse the same sapphire pieces multiple times.

When hydroxide catalysis bonds are formed between fused silica samples and these bonds are cured at room temperature, the strength of the bonds increases for the first 4 weeks. After this period any change in strength has not been found to be significant. However, the chemistry of bond formation with sapphire samples is slightly different. It was found that the average strength of sapphire-sapphire bonds is actually slightly reduced after two weeks of curing, right up to twelve weeks of curing (average strengths of 44 MPa were measured after 2 weeks, compared to 24 MPa after twelve). It is possible that this is due to how water leaves the bond. Additionally, a heat treatment of 7 days at 40 K after curing for 7 days at room temperature was found to give strengths consistent with bonds that had been cured for four weeks at room temperature. Again, all strengths measured were still sufficiently strong for bonds used in typical suspension. The strengths of bonds cured for shorter (and longer) periods are of interest.

To understand the possible sensitivity of a future detector it is necessary to understand the thermal noise performance and the mechanical loss of the bond material will contribute to this. Sapphire discs were bonded and the mechanical losses of the bonded discs were measured between room temperature and close to liquid helium temperatures. The mechanical losses measured were compared to those of a blank disc (one which did not contain a bond layer) with the same geometry. Finite element analysis of models of the discs were used alongside this information to give a value for the mechanical loss of a bond. This was carried out between room temperature and liquid helium temperatures and the value was found to be between $\sim 1.2 \times 10^{-4}$ and $\sim 1.1 \times 10^{-3}$. These loss values lead to a thermal noise contribution for hydroxide catalysis bonds between sapphire, of

8. Conclusions

$\sim 3.7 \times 10^{-26}$ at 100 Hz for a suspension like those in the current KAGRA design. In the case of KAGRA, the design requirement is 2×10^{-25} and hence these results suggest that hydroxide catalysis bonds between sapphire pieces will meet the thermal noise requirements of such a detector.

Silicon is also of interest for possible future detectors and some research has already been carried out on the strength of hydroxide catalysis bonds formed between silicon pieces. However, the effect of thermal cycling on bond strength for silicon samples was investigated here for the first time. Strengths were measured after 3, 10 and 20 cycles between room temperature and ~ 10 K and were compared to strengths of bonds which were not cycled. It was found that the average strength does not alter significantly with increased numbers of thermal cycles. However, there is a wide spread in the strengths measured. It is possible that this is because silicon is not optically transparent and hence, unlike bonds made with fused silica or sapphire, it is challenging to visually assess bond quality. This highlights the need for some other method of assessment, possibly involving the use of an infrared camera.

The results of these experiments demonstrate the continued suitability of the hydroxide catalysis bonding technique in the fabrication of suspensions for future gravitational wave detectors intended for cryogenic operation. The use of silicon and sapphire test masses and suspension elements alongside hydroxide catalysis bonds is possible, the bonds are strong and, given suitable suspension designs, the bond loss should not be a limiting factor on detector sensitivity. To continue to improve the sensitivity of detectors, and thus allow the use of gravitational wave detectors to do astronomy, a move to cryogenic detectors is necessary. Hydroxide catalysis bonding will allow the suspensions of such detectors to be built with very similar designs to those used in the past.

Appendices

A. Temperature calibration runs for low temperature mechanical loss experiments with sapphire discs

Sapphire discs described in Chapter 6 were used for measuring the mechanical loss of hydroxide catalysis bonds between sapphire. Since mounting temperature sensors directly onto the sapphire discs would result in the resonant modes of the discs being heavily damped, some temperature calibrations were required.

To run temperature calibrations a temperature sensor was mounted on the back face of the sapphire disc of interest. This disc was then suspended using the nodal support suspension system, as described in Chapter 6. The cryostat was operated exactly as it would be if mechanical loss measurements were being carried out, with the exception that no resonant modes were excited or monitored. Rather, the cryostat was first evacuated, then cooled to liquid nitrogen temperatures, then to liquid helium temperatures. Finally, contact gas was used to further reduce the temperature in the experimental space within the cryostat and, when the temperature had stabilised, the cryogens were allowed to naturally boil off and the full system was allowed to return to room temperature.

A. Temperature calibration runs for low temperature mechanical loss experiments with sapphire discs

During this procedure, temperature sensors on the helium and nitrogen shields and temperature sensors on the sapphire discs and the clamping blocks were monitored. The temperatures were recorded throughout, alongside time and pressure data. This information allowed the approximate temperature of the disc to be deduced during the mechanical loss measurements, when no temperature sensor was mounted on its surface.

In total, four temperature calibrations were carried out; two temperature calibrations using a sapphire disc with a thickness of 1.5 mm and a diameter of 50.8 mm, one temperature calibration using a sapphire disc with a thickness of 0.5 mm and a diameter of 50.8 mm and one temperature calibration using a pair of bonded sapphire discs with a combined thickness of 1.5 mm and a thickness of 0.5 mm. More details about these discs are given in section 5.3 in Chapter 6.

The temperature data for these temperature calibrations is presented in figures A.1-A.4.

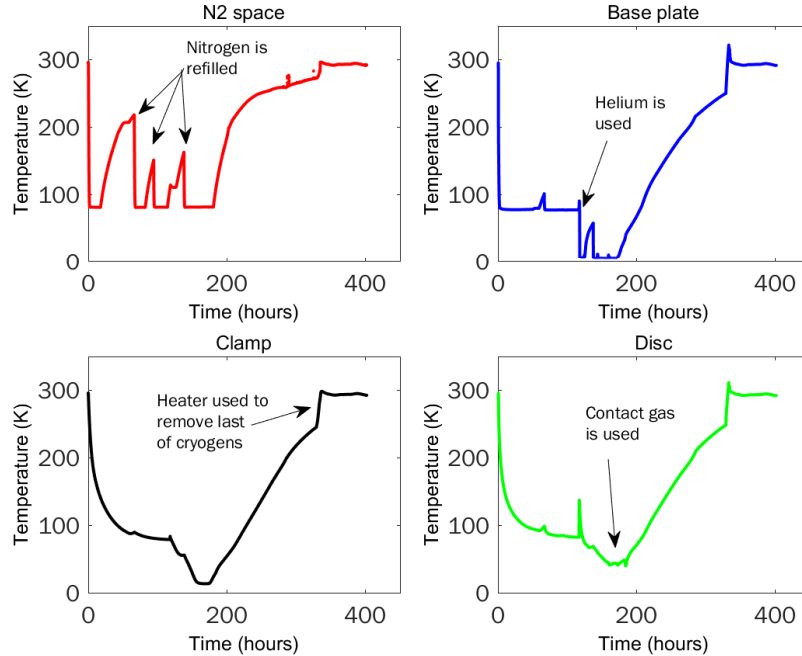


Figure A.1.: Data from the first of the temperature calibrations. The disc used in this calibration run was a sapphire disc, 1.5 mm thick with a radius of 50.8 mm.

A. Temperature calibration runs for low temperature mechanical loss experiments with sapphire discs

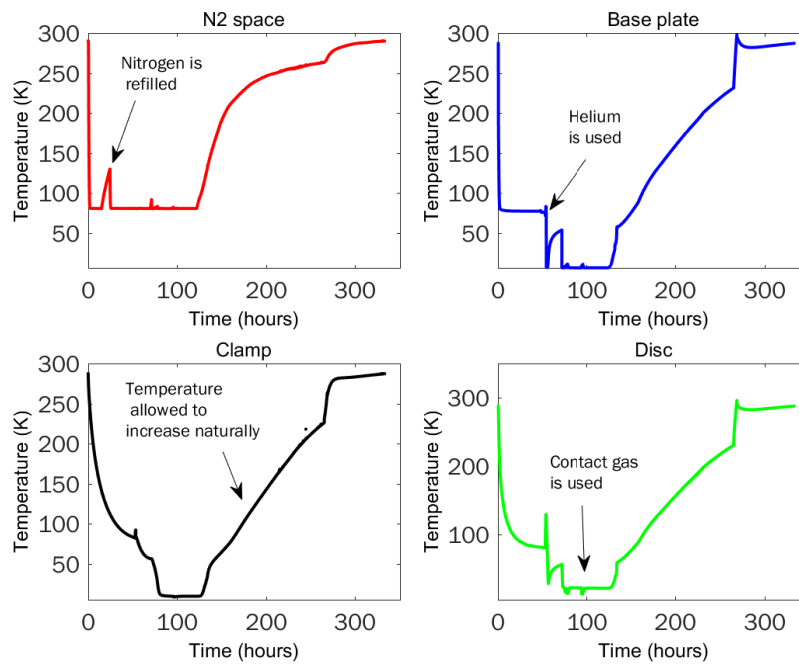


Figure A.2.: Data from the second of the temperature calibrations. The disc used in this calibration run was a sapphire disc, 1.5 mm thick with a radius of 50.8 mm.

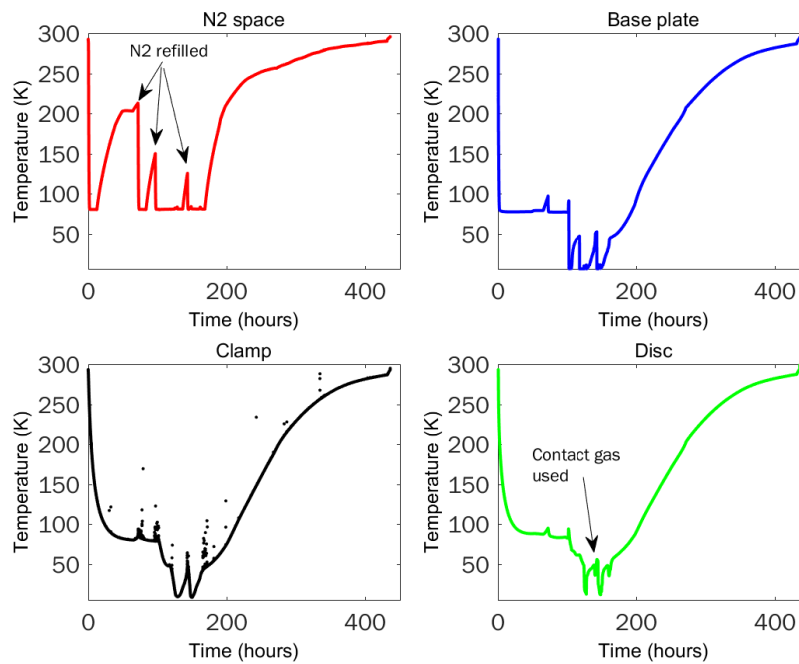


Figure A.3.: Data from the third of the temperature calibrations. The disc used in this calibration run was a sapphire disc, 0.5 mm thick with a radius of 50.8 mm.

A. *Temperature calibration runs for low temperature mechanical loss experiments with sapphire discs*

In figure A.4 one of the temperature sensors, that which would normally be mounted on the clamping block, was instead mounted on the cryostat window in order to discover how much heat was entering the experiment space via the windows.

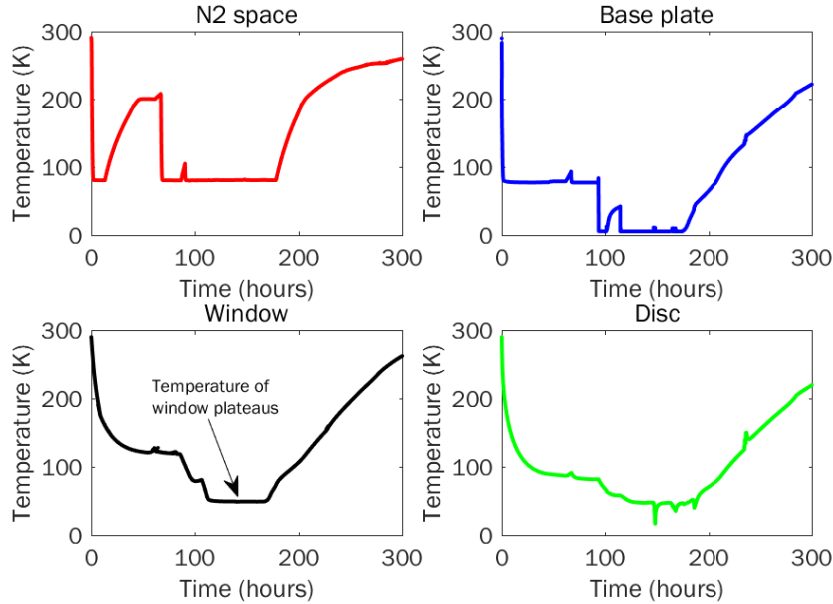


Figure A.4.: Data from the fourth of the temperature calibrations. The discs used in this calibration run was a pair of bonded sapphire discs with a combined thickness of, 1.5 mm and a radius of 50.8 mm.

The temperature sensor on the window indicated that the temperature of the window was slightly higher than that of the clamp. When the clamp would be expected to be at liquid nitrogen temperatures, the window was at ~ 119 K. This value was used in chapter 6, section 6.5.2 to help to understand the cooling rates of the different parts of the experimental set up.

The various spikes in the calibration curves indicate when a cryogen either ran out, or was pumped out of the cryostat. The subsequent drops in temperature indicate that the cryogen space was refilled. At the end of each temperature calibration the remaining cryogenes were allowed to boil off naturally and the cryostat returned to room temperature.

B. Additional FEA calculations

B.1. The effect of Young's modulus on strain energy ratio

In this experiment, FEA models were built in which the two sapphire discs both had a diameter of 50.8 mm and a combined total thickness of 1.5 mm, but the thickness of each disc was varied. The bond had a constant thickness of 60 nm and in this instance the Young's modulus of the bond was varied to find the effect of Young's modulus on strain energy ratios. So, where in the previous section the strain energy was considered as a function of the location of the bond in the samples, now different assumed bond Young's modulus values, (7.9, 27, 72, and 400 GPa), were considered.

A Young's modulus of 7.9 GPa is the measured value of hydroxide catalysis bonds between fused silica [199], 72 GPa is the Young's modulus of fused silica and 400 GPa is that of sapphire. Figures B.1–B.4 contain plots showing how the strain energy ratios alter with the ratio of Young's modulus between the sapphire substrate and the bond material.

As is clear to see from figures B.1–B.4, the ratio between the Young's modulus of the bond material and the Young's modulus of the substrate has a clear effect on how much energy is stored in bond compared to how much is stored in the substrate. This explains why

B. Additional FEA calculations

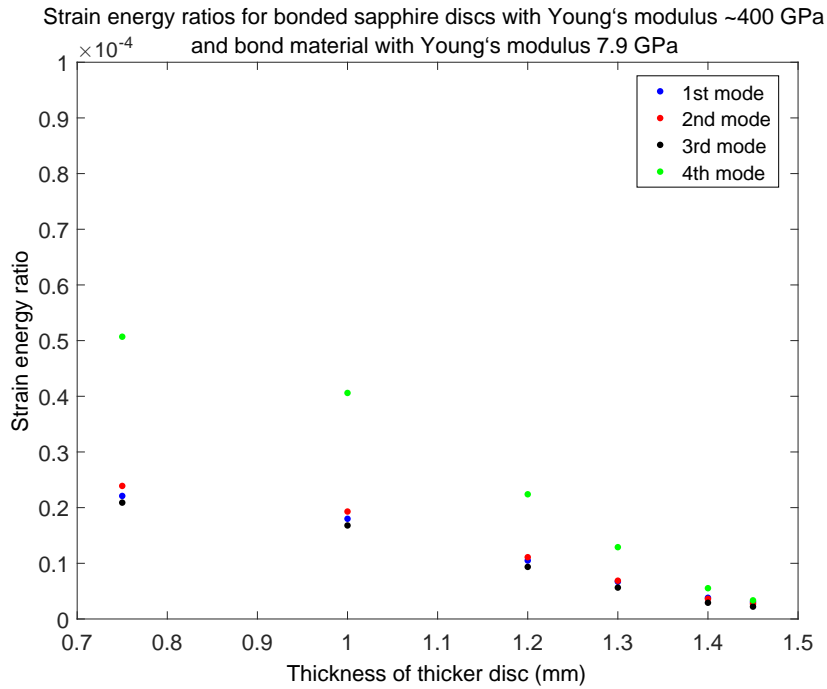


Figure B.1.: The results of FEA models into the effect on strain energy ratio of changing the position of the bond between bonded sapphire discs, where the Young's modulus of the bond is 7.9 GPa and the Young's modulus of the sapphire discs is ~ 400 GPa

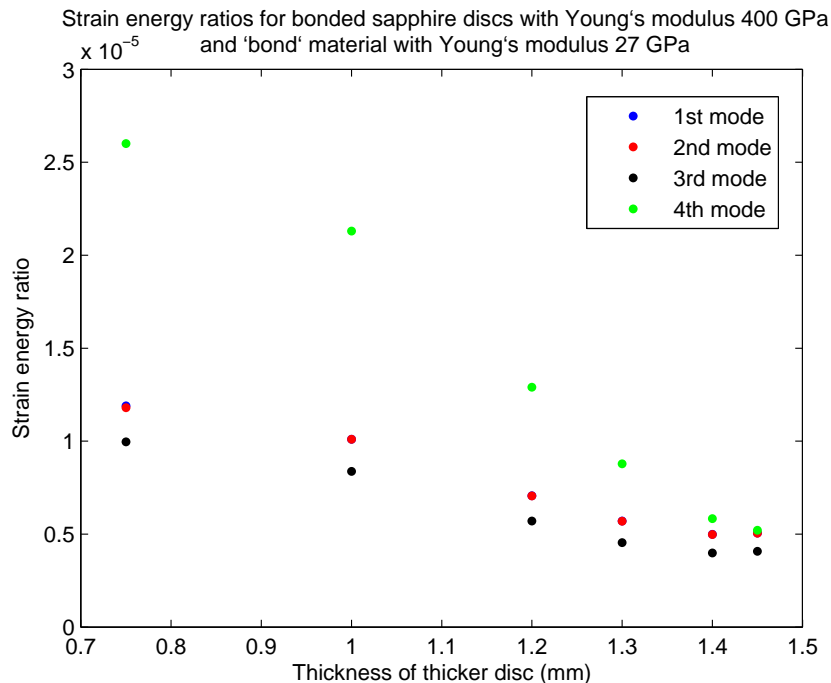


Figure B.2.: The results of FEA models into the effect on strain energy ratio of changing the position of the bond between bonded sapphire discs, where the Young's modulus of the bond is 25 GPa and the Young's modulus of the sapphire discs is ~ 400 GPa

B. Additional FEA calculations

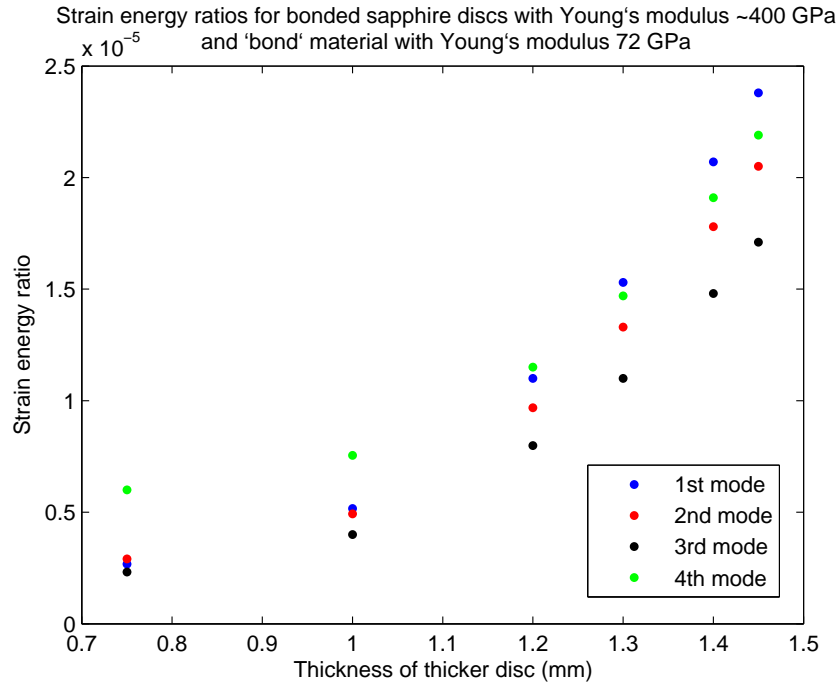


Figure B.3.: The results of FEA models into the effect on strain energy ratio of changing the position of the bond between bonded sapphire discs, where the Young's modulus of the bond is 72 GPa and the Young's modulus of the sapphire discs is ~ 400 GPa

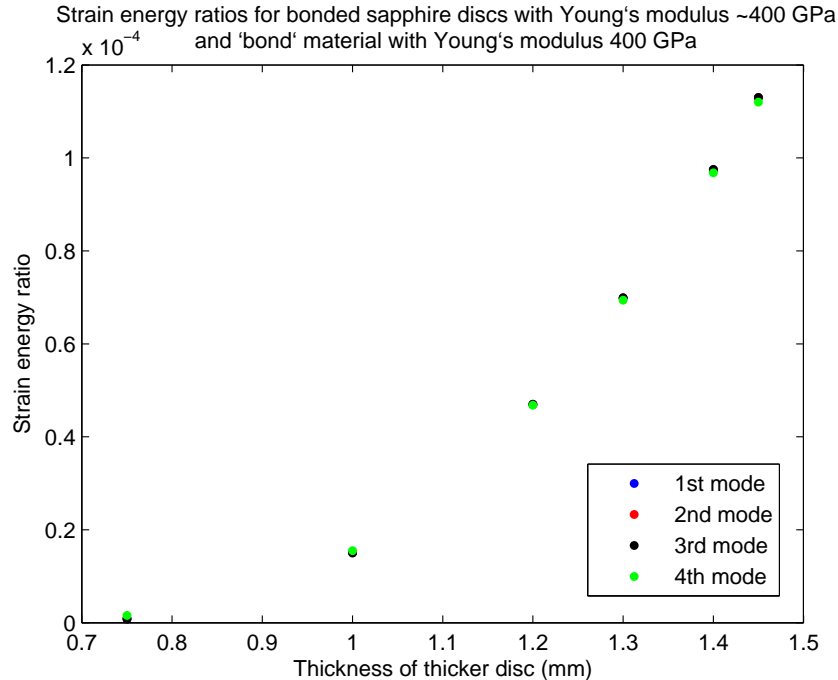


Figure B.4.: The results of FEA models into the effect on strain energy ratio of changing the position of the bond between bonded sapphire discs, where both the Young's modulus of the bond and the Young's modulus of the sapphire discs is ~ 400 GPa. Here, the points overlap, as would be expected as this is equivalent to a solid sapphire disc.

B. Additional FEA calculations

a different effect is seen when considering similar models using fused silica discs, rather than sapphire discs, in which moving the bond layer further from the centre corresponds to an increase in strain energy ratio.

As a check, models with fused silica discs were built to investigate this effect. Figure B.5 shows that as the ratio of Young's modulus of the bond changes with respect to the Young's modulus of the fused silica, this effect also begins to occur with silica discs.

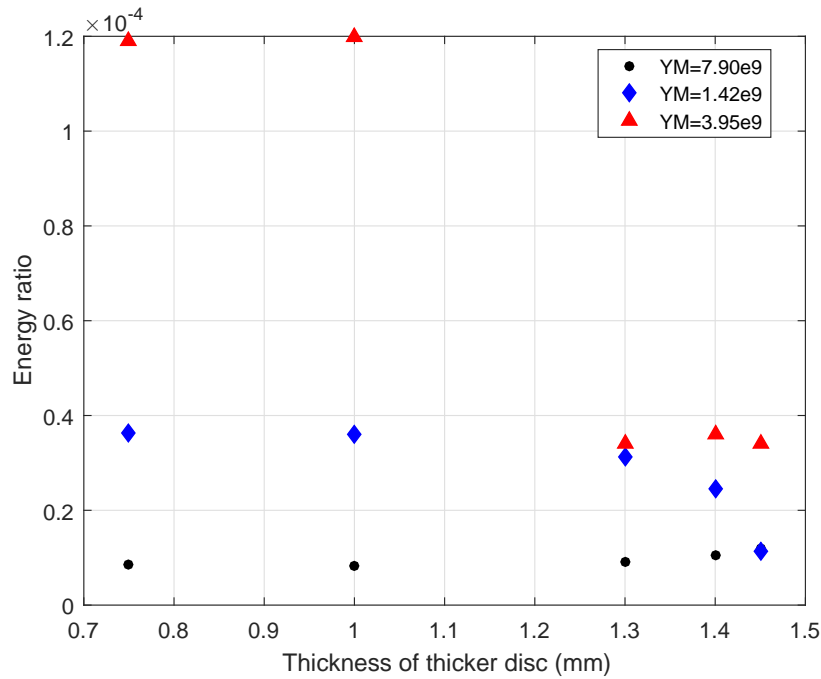


Figure B.5.: The results of FEA models into the effect on strain energy ratio of changing the position of the bond between bonded silica discs, where the Young's modulus of the bond material is also changed with respect to the Young's modulus of the fused silica. Here, only the first resonant mode is shown.

B.2. The effect of bond thickness on strain energy ratio

This final experiment involved varying the thickness of the bond layer in a series of FEA models. These involved sapphire discs with diameter 50.8 mm with one disc with a thickness of 1.0 mm and one with a thickness or 0.5 mm. The bond layer thickness was varied between 60 nm and 1 μ m. The results of these models can be seen in figure B.6,

B. Additional FEA calculations

in which two of the resonant modes predicted by the FEA analysis were considered; one at ~ 6 kHz and one at ~ 14 kHz (for bonds of different thicknesses the exact frequency of these modes changes somewhat).

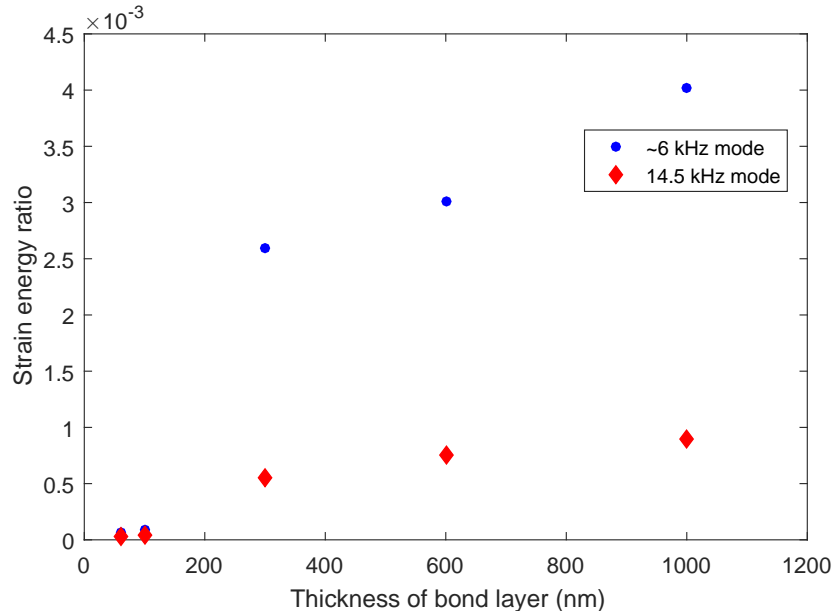


Figure B.6.: The results of FEA models into the effect on strain energy ratio of changing the thickness of the bond between bonded sapphire discs

From figure B.6 it can be seen that the portion of energy stored in the bond increases for increasing bond thickness, as would be expected. In the past, hydroxide catalysis bonds formed between fused silica samples have been measured to be ~ 60 nm thick [199], similar to the peak-to-peak flatness of the surfaces that were bonded. Since these discs were not as flat as that, it is likely that the bond layer is thicker. The FEA models that use a bond with a thickness of 300 nm predict resonant modes with frequencies most similar to those actual measured when the sapphire discs described in section 5.3 were bonded and their resonant modes were excited. The FEA models with other bond thicknesses predicted resonant modes at frequencies that match the actual frequencies of the discs less well. Additionally, the discs bonded were not as flat as typical samples and 300 nm is closer to the flatness measured for the discs. For these reasons, the FEA models which featured a bond with a thickness of 300 nm were used to calculate the mechanical loss of the bond, as described in section 6.8.

C. Oven characterisation for growing oxide layers on silicon samples

Before any samples intended for bonding were oxidised, pieces of $\langle 111 \rangle$ silicon cantilever were used to characterise oxidation rate of samples in the furnace. The longer samples spend in the furnace, the thicker the oxide layer on the surfaces. In the first instance it was found that an oxide layer of 150 nm would grow in ~ 3 hours. Since it was found that an oxide layer at least 50 nm thick was required for successful bonds, this gave a safety factor of three. Later, one of the furnace seals was changed and a second characterisation was carried out - it was found that an oxide layer of 150 nm would now grow in ~ 5 hours (it is possible that the older seal was allowing slightly more air to leak into the oven). In all cases the oven was allowed to stabilise over one hour after having been set to heat to 1000°C . See figures C.1 and C.2 for plots showing the thickness of oxide layer as a function of time, before and after the furnace seal was changed.

Apart from the seal being changed and the oxidation time being correspondingly increased, there was at no point any other change to the procedure for growing the dry thermal oxide. The oxide thickness on each of the silicon cantilever pieces was measured using an ellipsometer (Sentech SE 400adv¹).

¹<http://www.sentech.com/>

C. Oven characterisation for growing oxide layers on silicon samples

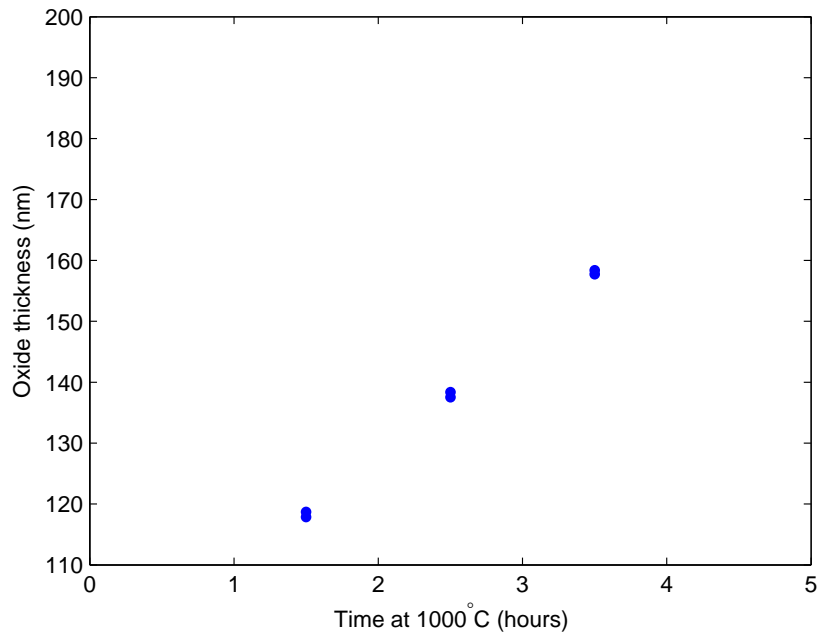


Figure C.1.: Thickness of oxide layer on $\langle 111 \rangle$ silicon pieces as a function of time spent in a quartz furnace at 1000°C, before the furnace seal was changed

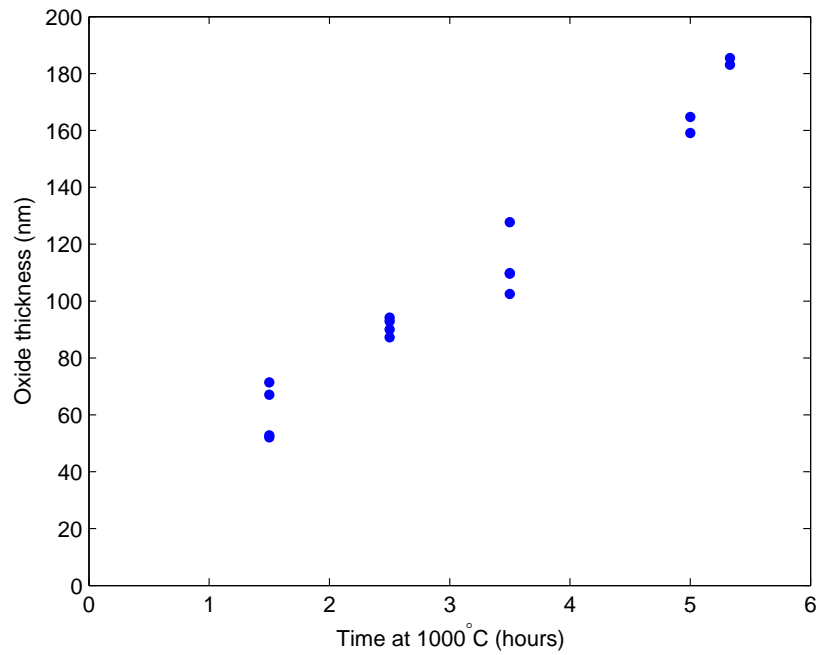


Figure C.2.: Thickness of oxide layer on $\langle 111 \rangle$ silicon pieces as a function of time spent in a quartz furnace at 1000°C, after the furnace seal was changed

Bibliography

- [1] A. Einstein, “Die grundlage der allgemeinen relativitätstheorie,” *Annalen der Physik*, vol. 354, no. 7, pp. 769–822, 1916.
- [2] A. Einstein, *Über Gravitationswellen*. Wiley Online Library, 1918.
- [3] J. Weber, “Detection and generation of gravitational waves,” *Physical Review*, vol. 117, no. 1, p. 306, 1960.
- [4] B. Abbott, R. Abbott, T. Abbott, M. Abernathy, F. Acernese, K. Ackley, C. Adams, T. Adams, P. Addesso, R. Adhikari, *et al.*, “Observation of gravitational waves from a binary black hole merger,” *Physical review letters*, vol. 116, no. 6, p. 061102, 2016.
- [5] J. Weber, “Evidence for discovery of gravitational radiation,” *Physical Review Letters*, vol. 22, pp. 1320–1324, 1969.
- [6] M. Cerdonio, M. Bonaldi, D. Carlesso, E. Cavallini, S. Caruso, A. Colombo, P. Falferi, G. Fontana, P. Fortini, R. Mezzena, *et al.*, “The ultracryogenic gravitational-wave detector AURIGA,” *Classical and Quantum Gravity*, vol. 14, no. 6, p. 1491, 1997.

Bibliography

- [7] P. Astone, M. Bassan, P. Bonifazi, P. Carelli, M. G. Castellano, G. Cavallari, E. Coccia, C. Cosmelli, V. Fafone, S. Frasca, *et al.*, “Long-term operation of the Rome “Explorer” cryogenic gravitational wave detector,” *Physical Review D*, vol. 47, no. 2, p. 362, 1993.
- [8] P. Aufmuth and K. Danzmann, “Gravitational wave detectors,” *New Journal of Physics*, vol. 7, no. 1, p. 202, 2005.
- [9] J. Aasi, B. Abbott, R. Abbott, T. Abbott, M. Abernathy, K. Ackley, C. Adams, T. Adams, P. Addesso, R. Adhikari, *et al.*, “Advanced LIGO,” *Classical and Quantum Gravity*, vol. 32, no. 7, p. 074001, 2015.
- [10] B. F. Schutz, “Networks of gravitational wave detectors and three figures of merit,” *Classical and Quantum Gravity*, vol. 28, no. 12, p. 125023, 2011.
- [11] S. Dwyer, L. S. Collaboration, *et al.*, “Advanced LIGO status,” in *Journal of Physics: Conference Series*, vol. 610, p. 012013, IOP Publishing, 2015.
- [12] J. Degallaix, T. Accadia, F. Acernese, M. Agathos, A. Allocca, P. Astone, G. Ballardin, F. Barone, M. Bejger, M. Beker, *et al.*, “Advanced Virgo status,” in *9th LISA Symposium*, vol. 467, p. 151, 2013.
- [13] B. Abbott, R. Abbott, T. Abbott, M. Abernathy, F. Acernese, K. Ackley, C. Adams, T. Adams, P. Addesso, R. Adhikari, *et al.*, “Astrophysical implications of the binary black hole merger GW150914,” *The Astrophysical Journal Letters*, vol. 818, no. 2, p. L22, 2016.
- [14] B. Abbott, R. Abbott, T. Abbott, M. Abernathy, F. Acernese, K. Ackley, C. Adams, T. Adams, P. Addesso, R. Adhikari, *et al.*, “GW151226: Observation of gravita-

Bibliography

- tional waves from a 22-solar-mass binary black hole coalescence,” *Physical Review Letters*, vol. 116, no. 24, p. 241103, 2016.
- [15] R. A. Hulse and J. H. Taylor, “Discovery of a pulsar in a binary system,” *The Astrophysical Journal*, vol. 195, pp. L51–L53, 1975.
- [16] J. M. Weisberg and J. H. Taylor, “Relativistic binary pulsar B1913+ 16: thirty years of observations and analysis,” *arXiv preprint astro-ph/0407149*, 2004.
- [17] R. Kumar, D. Chen, A. Hagiwara, T. Kajita, T. Miyamoto, T. Suzuki, Y. Sakakibara, H. Tanaka, K. Yamamoto, and T. Tomaru, “Status of the cryogenic payload system for the KAGRA detector,” in *Journal of Physics: Conference Series*, vol. 716, p. 012017, IOP Publishing, 2016.
- [18] R. Flaminio, K. collaboration, *et al.*, “The cryogenic challenge: status of the KAGRA project,” in *Journal of Physics: Conference Series*, vol. 716, p. 012034, IOP Publishing, 2016.
- [19] C. Unnikrishnan, “IndIGO and LIGO-India: scope and plans for gravitational wave research and precision metrology in India,” *International Journal of Modern Physics D*, vol. 22, no. 01, p. 1341010, 2013.
- [20] C. Cutler and K. S. Thorne, “An overview of gravitational-wave sources,” in *Proceeding of the 16th general relativity and gravitation conference (NT Bishop and SD Maharaj, eds.)*, pp. 72–111, 2002.
- [21] P. R. Saulson, *Fundamentals of Interferometric Gravitational Wave Detectors*. World Scientific, 1994.

Bibliography

- [22] B. F. Schutz, “Sources of gravitational waves,” in *NASA Conference Publication*, vol. 3046, 1989.
- [23] J. Miller, L. Barsotti, S. Vitale, P. Fritschel, M. Evans, and D. Sigg, “Prospects for doubling the range of Advanced LIGO,” *Physical Review D*, vol. 91, no. 6, p. 062005, 2015.
- [24] M. C. W. Sandford, “First International LISA Symposium,” *Classical Quantum Gravity*, vol. 14, p. 1397, 1997.
- [25] B. S. Sathyaprakash and B. F. Schutz, “Physics, astrophysics and cosmology with gravitational waves,” *Living Reviews in Relativity*, vol. 12, no. 2, p. 1, 2009.
- [26] M. Pitkin, S. Reid, and S. Rowan, “Gravitational wave detection by interferometry (ground and space),” *Living Reviews in Relativity*, vol. 14, no. 5, 2011.
- [27] S. Rowan, “Gravitational waves: A new astronomy,” *LIGO DCC G1601581-v1*, 2016.
- [28] B. F. Schutz, “Determining the hubble constant from gravitational wave observations,” *Nature*, 1986.
- [29] B. P. Abbott *et al.*, “Prospects for observing and localizing gravitational-wave transients with advanced ligo and advanced virgo,” *Living Rev. Relativity*, vol. 19, no. 1, 2016.
- [30] B. Abbott, R. Abbott, T. Abbott, M. Abernathy, F. Acernese, K. Ackley, C. Adams, T. Adams, P. Addesso, R. Adhikari, *et al.*, “The rate of binary black hole merg-

Bibliography

- ers inferred from Advanced LIGO observations surrounding GW150914,” *arXiv preprint arXiv:1602.03842*, 2016.
- [31] E. Chaisson and S. McMillan, *Astronomy today*. Prentice Hall Upper Saddle River, NJ, 2005.
- [32] M. Gilfanov and A. Bogdan, “An upper limit on the contribution of accreting white dwarfs to the typeIa supernova rate,” *Nature*, vol. 463, pp. 924–925, 2010.
- [33] C. D. Ott, “The gravitational-wave signature of core-collapse supernovae,” *Classical and Quantum Gravity*, vol. 26, no. 6, 2009.
- [34] D. G. Blair, *Advanced gravitational wave detectors*. Cambridge University Press, 2012.
- [35] A. Hewish, S. J. Bell, J. D. H. Pilkington, P. F. Scott, and R. A. Collins, “Observation of a rapidly pulsating radio source,” *Nature*, vol. 217, no. 5130, p. 709, 1968.
- [36] B. Abbott, R. Abbott, R. Adhikari, J. Agresti, P. Ajith, B. Allen, R. Amin, S. Anderson, W. Anderson, M. Arain, *et al.*, “Upper limits on gravitational wave emission from 78 radio pulsars,” *Physical Review D*, vol. 76, no. 4, p. 042001, 2007.
- [37] B. Zink, O. Korobkin, E. Schnetter, and N. Stergioulas, “Frequency band of the f-mode chandrasekhar-friedman-schutz instability,” *Physical Review D*, vol. 81, no. 8, p. 084055, 2010.
- [38] R. V. Wagoner, “Gravitational radiation from accreting neutron stars,” *Astrophysical Journal*, vol. 222, pp. 345–348, 1984.

Bibliography

- [39] J. Hough, H. Walther, and B. F. Schutz, “Proposal for a joint German-British interferometric gravitational wave detector,” *Max-Planck-Institut fur Quantenoptik Report*, no. 147, 1989.
- [40] B. P. Abbott, R. Abbott, and R. Adhikari, “LIGO: the Laser Interferometer Gravitational-wave Observatory,” *Reports on Progress in Physics*, vol. 72, no. 7, 2009.
- [41] M. Cerdonio, L. Franceschini, and G. Fontant, “Status of the AURIGA gravitational wave antenna and perspectives for the gravitational waves search with ultracryogenic resonant detectors,” *Gravitational Wave Experiments*, pp. 176–194, 1995.
- [42] P. Astone, M. Bassan, P. Bonifazi, P. Carelli, E. Coccia, C. Cosmelli, V. Fafone, S. Frasca, A. Marini, G. Mazzitelli, *et al.*, “The gravitational wave detector NAUTILUS operating at $t= 0.1$ k,” *Astroparticle Physics*, vol. 7, no. 3, pp. 231–243, 1997.
- [43] E. Mauceli, M. P. McHugh, W. O. Hamilton, W. W. Johnson, and A. Morse, “Search for periodic gravitational radiation with the ALLEGRO gravitational wave detector,” *arXiv preprint gr-qc/0007023*, 2000.
- [44] A. Abramovici, W. E. Althouse, and R. W. P. Drever, “LIGO - the Laser Interferometer Gravitational-wave Observatory,” *Science*, vol. 256, pp. 325–333, 1992.
- [45] C. Bradaschi, R. del Fabbro, and A. di Virgilio, “The Virgo Project: A wide band antenna for gravitational wave detection,” *Nuclear instruments and methods in physics research A*, vol. 289, pp. 518–525, 1990.

Bibliography

- [46] H. Luck and the GEO600 team, “The GEO600 project,” *Classical and quantum gravity*, vol. 14, pp. 1471–1476, 1997.
- [47] K. Tsubono, “TAMA project,” *Gravitational wave detection*, p. 183, 1997.
- [48] F. Antonucci, M. Armano, H. Audley, G. Auger, M. Benedetti, P. Binetruy, C. Boatella, J. Bogenstahl, D. Bortoluzzi, P. Bosetti, *et al.*, “LISA Pathfinder: mission and status,” *Classical and Quantum Gravity*, vol. 28, no. 9, p. 094001, 2011.
- [49] G. Hobbs, A. Archibald, and Z. Arzoumanian, “The international pulsar timing array project: using pulsars as a gravitational wave detector,” *Classical and Quantum Gravity*, vol. 27, no. 8, p. 084013, 2010.
- [50] C. Cheng, Q.-G. Huang, and S. Wang, “Constraint on the primordial gravitational waves from the joint analysis of bicep2 and planck hfi 353 ghz dust polarization data,” *Journal of Cosmology and Astroparticle Physics*, vol. 2014, no. 12, p. 044, 2014.
- [51] S. Detweiler, “Pulsar timing measurements and the search for gravitational waves,” *The Astrophysical Journal*, vol. 234, pp. 1100–1104, 1979.
- [52] G. H. Janssen, B. W. Stappers, and M. Kramer, “European pulsar timing array,” *40 Years of Pulsars: Millisecond Pulsars, Magnetars and More*, vol. 983, pp. 633–635, 2008.
- [53] M. A. McLaughlin, “The North American nanohertz observatory for gravitational waves,” *Classical and Quantum Gravity*, vol. 30, no. 22, p. 224008, 2013.

Bibliography

- [54] R. N. Manchester, “The Parkes pulsar timing array project,” *40 Years of Pulsars: Millisecond Pulsars, Magnetars and More*, vol. 983, pp. 584–592, 2008.
- [55] J. Weber, “Gravitational-wave-detector events,” *Physical Review Letters*, vol. 20, pp. 1307–1308, 1968.
- [56] J. Weber, “Anisotropy and polarisation in the gravitational-radiation experiments,” *Physical Review Letters*, vol. 22, p. 1320, 1969.
- [57] J. Weber, “Evidence for discovery of gravitational radiation,” *Physical Review Letters*, vol. 25, p. 180, 1970.
- [58] J. A. Tyson and R. P. Giffard, “Gravitational-wave astronomy,” *Annual Review of Astronomy and Astrophysics*, vol. 16, pp. 521–554, 1978.
- [59] M. P. McHugh, Z. Allen, and W. O. Hamilton, “The ALLEGRO gravitational wave detector,” *The Ninth Marcell Grossmann Meeting*, pp. 1904–1905, 2002.
- [60] P. Astone, M. Bassan, and P. Bonifazi, “The EXPLORER gravitational wave antenna: recent improvements and performances,” *Classical and Quantum Gravity*, vol. 19, pp. 1905–1910, 2002.
- [61] P. Astone, L. Baggio, and M. Bassan, “IGEC2: A 17-month search for gravitational wave bursts in 2005-2007,” *Physical Review Letters D*, vol. 82, no. 2, p. 022003, 2010.
- [62] S. M. Merkowitz and W. W. Johnson, “Spherical gravitational wave antennas and the truncated icosahedral arrangement,” *Physical Review Letters D*, vol. 51, pp. 2546–2558, 1995.

Bibliography

- [63] L. Gottardi, A. de Waard, and O. Usenko, “Sensitivity of the spherical gravitational wave detector miniGRAIL operating at 5 K,” *Physical Review Letters D*, vol. 76, no. 10, p. 102005, 2007.
- [64] O. D. Aguiar, L. A. Andrade, and J. J. Barroso, “The Brazilian gravitational wave detector Mario Schenberg: Status report,” *Classical and Quantum Gravity*, vol. 23, no. 239, 2006.
- [65] M. Cerdonio, L. Conti, and J. A. Lobo, “Wideband dual sphere detector of gravitational waves,” *Physical Review Letters*, vol. 87, no. 3, p. 031101, 2001.
- [66] S. Sing, L. A. D. Lorenzo, I. Pikovski, and K. C. Schwab, “Detecting continuous gravitational waves with superfluid He,” *arXiv*, no. 1606.04980, 2016.
- [67] R. L. Forward, “Wide band laser interferometer gravitational radiation experiment,” *Physics Review D*, vol. 17, pp. 379–390, 1978.
- [68] M. Punturo, M. Abernathy, F. Acernese, B. Allen, N. Andersson, K. Arun, F. Barone, B. Barr, M. Barsuglia, M. Beker, *et al.*, “The Einstein Telescope: A third-generation gravitational wave observatory,” *Classical and Quantum Gravity*, vol. 27, no. 19, p. 194002, 2010.
- [69] K. Danzmann and A. Rudiger, “LISA technology - concept, status, prospects,” *Classical and Quantum Gravity*, vol. 20, no. 1, 2003.
- [70] K. Danzmann, L. S. Team, *et al.*, “Lisa and ground-based detectors for gravitational waves: An overview,” in *Second International LISA Symposium on the Detection and Observation of Gravitational Waves in Space*, pp. 3–10, American Inst. of Physics, 1998.

Bibliography

- [71] R. Weiss, “MIT quarterly progress report,” (*Research Laboratory of Electronics*), vol. 105, no. 54, 1972.
- [72] D. Shoemaker, R. Schilling, and L. Schnupp, “Noise behaviour of the Garching 30-meter prototype gravitational wave detector,” *Physical Review Letters D*, vol. 38, no. 2, 1988.
- [73] E. Schmutzer, ed., *A gravity-wave detector using optical cavity sensing*, vol. 306, Cambridge Press, 1983.
- [74] B. J. Meers, “Recycling in laser-interferometric gravitational-wave detectors,” *Physical Review D*, vol. 38, no. 8, pp. 2317–2326, 1988.
- [75] J. R. Smith, L. S. Collaboration, *et al.*, “The path to the enhanced and advanced ligo gravitational-wave detectors,” *Classical and Quantum Gravity*, vol. 26, no. 11, p. 114013, 2009.
- [76] K. Strain and B. J. Meers, “Experimental demonstration of dual recycling for interferometric gravitational wave detectors,” *Physics Review Letters*, vol. 66, no. 11, pp. 1391–1394, 1991.
- [77] S. Rowan and J. Hough, “Gravitational wave detection by interferometry (ground and space),” *Living Rev. Relativity*, vol. 3, no. 3, pp. 1–41, 2000.
- [78] S. Hild, M. Abernathy, F. Acernese, P. Amaro-Seoane, N. Andersson, K. Arun, F. Barone, B. Barr, M. Barsuglia, M. Beker, *et al.*, “Sensitivity studies for third-generation gravitational wave observatories,” *Classical and Quantum Gravity*, vol. 28, no. 9, p. 094013, 2011.

Bibliography

- [79] J. Hough, S. Rowan, and B. Sathyaprakash, “The search for gravitational waves,” *Journal of Physics B: Atomic, Molecular and Optical Physics*, vol. 38, pp. S497–S519, 2005.
- [80] N. A. Robertson, G. Barton, and G. Cagnoli, “Advanced LIGO Suspension System Conceptual Design,” *LIGO-DCC T010103*, 2010.
- [81] A. Einstein, *Investigations on the Theory of the Brownian Movement*. Courier Corporation, 1956.
- [82] M. Evans, S. Ballmer, and M. Fejer, “Thermo-optic noise in coated mirrors for high-precision optical measurements,” *Physical Review D*, vol. 78, no. 10, 2008.
- [83] W. A. Edelstein, J. Hough, J. R. Pugh, and W. Martin, “Limits to the measurement of displacement in an interferometric gravitational radiation detector,” *Journal of Physics E: Scientific Instruments*, vol. 11, no. 7, p. 710, 1978.
- [84] B. Picinbono and C. Bendjaballah, “Photoelectron shot noise,” *Journal of Mathematical Physics*, vol. 11, no. 7, 1970.
- [85] R. Slusher, L. Hollberg, B. Yurke, J. Mertz, and J. Valley, “Observation of squeezed states generated by four-wave mixing in an optical cavity,” *Physical Review Letters*, vol. 55, no. 22, p. 2409, 1985.
- [86] C. M. Caves, “Quantum-mechanical noise in an interferometer,” *Physical Review D*, vol. 23, no. 8, p. 1693, 1981.
- [87] H. Vahlbruch, A. Khalaidovski, N. Lastzka, C. Gräf, K. Danzmann, and R. Schn-

Bibliography

- abel, “The geo 600 squeezed light source,” *Classical and Quantum Gravity*, vol. 27, no. 8, p. 084027, 2010.
- [88] V. Giovannetti, S. Lloyd, and L. Maccone, “Quantum-enhanced measurements: Beating the standard quantum limit,” *Science*, vol. 306, pp. 1330–1336, 2004.
- [89] K. Kuroda, M. Ohashi, and S. Miyoki, “Large-scale cryogenic gravitational wave telescope,” *International Journal of Modern Physics D*, vol. 8, pp. 557–579, 1999.
- [90] M. Punturo, M. Abernathy, and F. Acernese, “The third generation of gravitational wave observatories and their science reach,” *Classical and Quantum Gravity*, vol. 27, no. 8, p. 084007, 2010.
- [91] T. Accadia, F. Acernese, F. Antonucci, P. Astone, G. Ballardin, F. Barone, M. Barsuglia, A. Basti, T. S. Bauer, M. Bebronne, *et al.*, “Status of the Virgo project,” *Classical and Quantum Gravity*, vol. 28, no. 11, p. 114002, 2011.
- [92] H. Grote, L. S. Collaboration, *et al.*, “The GEO 600 status,” *Classical and Quantum Gravity*, vol. 27, no. 8, p. 084003, 2010.
- [93] E. Schreiber, “Fighting high-frequency noise at GEO 600: The use of squeezed states of light and a look beneath the shot noise,” *LIGO DCC G1501378-v1*, 2015.
- [94] S. Kawamura, “Ground-based interferometers and their science reach,” *Classical and Quantum Gravity*, vol. 27, no. 8, 2010.
- [95] J. Abadie, B. P. Abbott, R. Abbott, M. Abernathy, T. Accadia, F. Acernese, C. Adams, R. Adhikari, P. Ajith, B. Allen, G. Allen, and E. Amador, “Predictions

Bibliography

- for rates of compact binary coalescences observable by ground-based gravitational-wave detectors,” *Classical and Quantum Gravity*, vol. 27, 2010.
- [96] G. M. Harry and The LIGO Scientific Collaboration, “Advanced LIGO: The next generation of gravitational wave detectors,” *Classical and Quantum Gravity*, vol. 27, no. 8, p. 084006, 2010.
- [97] J. Aasi, J. Abadie, B. Abbott, R. Abbott, T. Abbott, M. Abernathy, T. Accadia, F. Acernese, C. Adams, T. Adams, *et al.*, “Prospects for localization of gravitational wave transients by the advanced LIGO and advanced Virgo observatories,” *Living Reviews in Relativity*, vol. 19, 2016.
- [98] A. Cumming, A. Bell, L. Barsotti, M. Barton, G. Cagnoli, D. Cook, L. Cunningham, M. Evans, G. Hammond, G. Harry, *et al.*, “Design and development of the advanced LIGO monolithic fused silica suspension,” *Classical and Quantum Gravity*, vol. 29, no. 3, p. 035003, 2012.
- [99] S. Aston, M. Barton, A. Bell, N. Beveridge, B. Bland, A. Brummitt, G. Cagnoli, C. Cantley, L. Carbone, A. Cumming, *et al.*, “Update on quadruple suspension design for Advanced LIGO,” *Classical and Quantum Gravity*, vol. 29, no. 23, p. 235004, 2012.
- [100] L. Carbone, S. Aston, R. Cutler, A. Freise, J. Greenhalgh, J. Heefner, D. Hoyland, N. Lockerbie, D. Lodhia, N. Robertson, *et al.*, “Sensors and actuators for the Advanced LIGO mirror suspensions,” *Classical and Quantum Gravity*, vol. 29, no. 11, p. 115005, 2012.
- [101] G. Cagnoli, H. Armandula, C. Cantley, D. Crooks, A. Cumming, E. Elliffe, M. Fejer, A. Gretarsson, G. Harry, A. Heptonstall, *et al.*, “Silica suspension and coating de-

Bibliography

- velopments for Advanced LIGO,” in *Journal of Physics: Conference Series*, vol. 32, p. 386, IOP Publishing, 2006.
- [102] R. Flaminio, A. Freise, A. Gennai, P. Hello, P. L. Penna, G. Losurdo, H. Lueck, N. Man, A. Masserot, B. Mours, *et al.*, “Advanced Virgo white paper,” *VIRNOT-DIR1390304*, 2005.
- [103] F. Acernese, M. Agathos, K. Agatsuma, D. Aisa, N. Allemandou, A. Allocca, J. Amarni, P. Astone, G. Balestri, G. Ballardini, *et al.*, “Advanced Virgo: a second-generation interferometric gravitational wave detector,” *Classical and Quantum Gravity*, vol. 32, no. 2, p. 024001, 2014.
- [104] B. Willke, P. Ajith, and B. Allen, “The GEO-HF Project,” *Classical and Quantum Gravity*, vol. 23, 2006.
- [105] T. Akutsu, K. collaboration, *et al.*, “Large-scale cryogenic gravitational-wave telescope in japan: Kagra,” in *Journal of Physics: Conference Series*, vol. 610, p. 012016, IOP Publishing, 2015.
- [106] V. B. Braginsky, V. P. Mitrofanov, V. I. Panov, and C. Eller, *Systems with small dissipation*. University of Chicago Press, 1985.
- [107] K. Somiya, “Detector configuration of KAGRA—the Japanese cryogenic gravitational-wave detector,” *Classical and Quantum Gravity*, vol. 29, no. 12, p. 124007, 2012.
- [108] M. Armano, H. Audley, G. Auger, J. Baird, M. Bassan, P. Binetruy, M. Born, D. Bortoluzzi, N. Brandt, M. Caleno, *et al.*, “Sub-femto-g free fall for space-based

Bibliography

- gravitational wave observatories: LISA Pathfinder results,” *Physical Review Letters*, vol. 116, no. 23, p. 231101, 2016.
- [109] P. McNamara, S. Vitale, and K. D. (on behalf of the LISA Pathfinder Science Working Team, “LISA Pathfinder,” *Classical and Quantum Gravity*, vol. 25, p. 114034 (8pp), 2008.
- [110] G. Ciani, A. Chilton, T. Olatunde, S. Apple, J. W. Conklin, and G. Mueller, “Lisa technologies in new light: exploring alternatives for charge management and optical bench construction,” *IAU General Assembly*, vol. 22, p. 57787, 2015.
- [111] S. J. Waldman, “The Advanced LIGO gravitational wave detector,” *arXiv:1103.2728*, 2011.
- [112] R. Brown, *A Brief Account of Microscopical Observations Made on the Particles Contained in the Pollen of Plants, and on the General Existence of Active Molecules in Organic and Inorganic Bodies*. Edinburgh New Philosophical Journal, 1828.
- [113] H. B. Callen and T. A. Welton, “Irreversibility and generalized noise,” *Physical Review*, vol. 83, no. 1, p. 34, 1951.
- [114] R. Green and C. H, “On the formalism of thermodynamic fluctuation theory,” *Physical Review*, vol. 83, no. 6, 1951.
- [115] S. Twyford, *Developments towards low loss suspensions for laser interferometric gravitational wave detectors*. PhD thesis, University of Glasgow, 1998.
- [116] T. J. Quinn, C. C. Speake, R. S. Davis, and W. Tew, “Stress-dependent damping in

Bibliography

- Cu Be torsion and flexure suspensions at stresses up to 1.1 GPa,” *Physics Letters A*, vol. 197, no. 3, pp. 197–208, 1995.
- [117] N. L. Beveridge, *Characterisation of silicon-silicon hydroxide catalysis bonds for future gravitational wave detectors*. PhD thesis, University of Glasgow, 2012.
- [118] A. P. French, *Vibrations and waves*. CRC press, 1971.
- [119] Y. Levin, “Internal thermal noise in the LIGO test masses: A direct approach,” *Physical Review D*, vol. 57, no. 2, p. 659, 1998.
- [120] G. Harry, T. P. Bodiya, and R. DeSalvo, *Optical coatings and thermal noise in precision measurement*. Cambridge University Press, 2012.
- [121] F. Bondu, P. Hello, and J.-Y. Vinet, “Thermal noise in mirrors of interferometric gravitational wave antennas,” *Physics Letters A*, vol. 246, no. 3, pp. 227–236, 1998.
- [122] I. Martin, H. Armandula, C. Comtet, M. Fejer, A. Gretarsson, G. Harry, J. Hough, J. M. Mackowski, I. MacLaren, C. Michel, *et al.*, “Measurements of a low-temperature mechanical dissipation peak in a single layer of ta2o5 doped with tio2,” *Classical and Quantum gravity*, vol. 25, no. 5, p. 055005, 2008.
- [123] C. M. Zener and S. Siegel, “Elasticity and anelasticity of materials.,” *The Journal of Physical Chemistry*, vol. 53, no. 9, pp. 1468–1468, 1949.
- [124] A. Kimball and D. Lovell, “Internal friction in solids,” *Physical Review*, vol. 30, no. 6, p. 948, 1927.
- [125] T. Quinn, C. Speake, and L. Brown, “Materials problems in the construction of

Bibliography

- long-period pendulums,” *Philosophical Magazine A*, vol. 65, no. 2, pp. 261–276, 1992.
- [126] Y. Huang and P. R. Saulson, “A method for measuring the dependence of internal friction on strain,” *Review of scientific instruments*, vol. 65, no. 6, pp. 2102–2106, 1994.
- [127] Y. T. Liu and K. S. Thorne, “Thermoelastic noise and homogeneous thermal noise in finite sized gravitational-wave test masses,” *Physical Review D*, vol. 62, no. 12, p. 122002, 2000.
- [128] G. M. Harry, A. M. Gretarsson, P. R. Saulson, S. E. Kittelberger, S. D. Penn, W. J. Startin, S. Rowan, M. M. Fejer, D. Crooks, G. Cagnoli, *et al.*, “Thermal noise in interferometric gravitational wave detectors due to dielectric optical coatings,” *Classical and Quantum Gravity*, vol. 19, no. 5, p. 897, 2002.
- [129] D. Crooks, P. Sneddon, G. Cagnoli, J. Hough, S. Rowan, M. Fejer, E. Gustafson, R. Route, N. Nakagawa, D. Coyne, *et al.*, “Excess mechanical loss associated with dielectric mirror coatings on test masses in interferometric gravitational wave detectors,” *Classical and Quantum Gravity*, vol. 19, no. 5, p. 883, 2002.
- [130] S. D. Penn, P. H. Sneddon, H. Armandula, J. C. Betzwieser, G. Cagnoli, J. Camp, D. Crooks, M. M. Fejer, A. M. Gretarsson, G. M. Harry, *et al.*, “Mechanical loss in tantala/silica dielectric mirror coatings,” *Classical and Quantum Gravity*, vol. 20, no. 13, p. 2917, 2003.
- [131] A. Ageev, B. C. Palmer, A. De Felice, S. D. Penn, and P. R. Saulson, “Very high quality factor measured in annealed fused silica,” *Classical and Quantum Gravity*, vol. 21, no. 16, p. 3887, 2004.

Bibliography

- [132] J. Logan, J. Hough, and N. Robertson, “Aspects of the thermal motion of a mass suspended as a pendulum by wires,” *Physics Letters A*, vol. 183, no. 2, pp. 145–152, 1993.
- [133] G. I. González and P. R. Saulson, “Brownian motion of a mass suspended by an anelastic wire,” *The Journal of the Acoustical Society of America*, vol. 96, no. 1, pp. 207–212, 1994.
- [134] S. Rowan, S. Twyford, R. Hutchins, J. Kovalik, J. Logan, A. McLaren, N. Robertson, and J. Hough, “Q factor measurements on prototype fused quartz pendulum suspensions for use in gravitational wave detectors,” *Physics Letters A*, vol. 233, no. 4, pp. 303–308, 1997.
- [135] S. Rowan, S. M. Twyford, J. Hough, D.-H. Gwo, and R. Route, “Mechanical losses associated with the technique of hydroxide-catalysis bonding of fused silica,” *Physics Letters A*, vol. 246, no. 6, pp. 471–478, 1998.
- [136] S. Rowan, G. Cagnoli, P. Sneddon, J. Hough, R. Route, E. Gustafson, M. Fejer, and V. Mitrofanov, “Investigation of mechanical loss factors of some candidate materials for the test masses of gravitational wave detectors,” *Physics Letters A*, vol. 265, no. 1, pp. 5–11, 2000.
- [137] A. Van Veggel, J. Scott, D. Skinner, B. Bezensek, W. Cunningham, J. Hough, I. Martin, P. Murray, S. Reid, and S. Rowan, “Strength testing and SEM imaging of hydroxide-catalysis bonds between silicon,” *Classical and Quantum Gravity*, vol. 26, no. 17, p. 175007, 2009.
- [138] D.-H. Gwo, “Ultraprecision bonding for cryogenic fused-silica optics,” in *SPIE’s*

Bibliography

International Symposium on Optical Science, Engineering, and Instrumentation, pp. 136–142, International Society for Optics and Photonics, 1998.

- [139] D.-H. Gwo, “Ultra precision and reliable bonding method,” Sept. 4 2001. US Patent 6,284,085.
- [140] D.-H. Gwo, S. Wang, K. A. Bower, D. E. Davidson, P. Ehrensberger, L. Huff, E. Romero, M. T. Sullivan, K. Triebes, and J. A. Lipa, “The Gravity Probe-B star-tracking telescope,” *Advances in space research*, vol. 32, no. 7, pp. 1401–1405, 2003.
- [141] D.-H. Gwo, “Hydroxide-catalyzed bonding,” Apr. 15 2003. US Patent 6,548,176.
- [142] C. Affeldt, K. Danzmann, K. Dooley, H. Grote, M. Hewitson, S. Hild, J. Hough, J. Leong, H. Lück, M. Prijatelj, *et al.*, “Advanced techniques in GEO 600,” *Classical and Quantum Gravity*, vol. 31, no. 22, p. 224002, 2014.
- [143] P. Amico, L. Bosi, L. Carbone, L. Gammaitoni, F. Marchesoni, M. Punturo, F. Travasso, and H. Vocca, “Monolithic fused silica suspension for the Virgo gravitational waves detector,” *Review of scientific instruments*, vol. 73, no. 9, pp. 3318–3323, 2002.
- [144] S. Vitale, “Space-borne gravitational wave observatories,” *General Relativity and Gravitation*, vol. 46, no. 5, pp. 1–19, 2014.
- [145] E. J. Elliffe, J. Bogenstahl, A. Deshpande, J. Hough, C. Killow, S. Reid, D. Robertson, S. Rowan, H. Ward, and G. Cagnoli, “Hydroxide-catalysis bonding for stable optical systems for space,” *Classical and Quantum Gravity*, vol. 22, no. 10, p. S257, 2005.

Bibliography

- [146] G. Heinzel, C. Braxmaier, M. Caldwell, K. Danzmann, F. Draaisma, A. Garcia, J. Hough, O. Jennrich, U. Johann, C. Killow, *et al.*, “Successful testing of the LISA Technology Package (LTP) interferometer engineering model,” *Classical and Quantum Gravity*, vol. 22, no. 10, p. S149, 2005.
- [147] L. Cunningham, P. G. Murray, A. Cummin, E. J. Elliff, G. D. Hammond, K. Haughian, J. Hough, M. Hendry, R. Jones, and I. M. others, “Re-evaluation of the mechanical loss factor of hydroxide-catalysis bonds and its significance for the next generation of gravitational wave detectors,” *Physics Letters A*, vol. 374, no. 39, pp. 3993–3998, 2010.
- [148] S. Reid, G. Cagnoli, D. R. M. Crooks, J. Hough, P. Murray, S. Rowan, M. M. Fejer, R. Route, and S. Zappe, “Mechanical dissipation in silicon flexures,” *Physics Letters A*, vol. 351, no. 4, pp. 205–211, 2006.
- [149] S. Kawamura and F. Raab, “Suspension design requirements,” *LIGO DCC T950011-14*, 1995.
- [150] N. Robertson, G. Cagnoli, D. Crooks, E. Elliffe, J. Faller, P. Fritschel, S. Gößler, A. Grant, A. Heptonstall, J. Hough, *et al.*, “Quadruple suspension design for advanced LIGO,” *Classical and Quantum Gravity*, vol. 19, no. 15, p. 4043, 2002.
- [151] P. Fritschel, “Second generation instruments for the laser interferometer gravitational wave observatory (LIGO),” in *Astronomical Telescopes and Instrumentation*, pp. 282–291, International Society for Optics and Photonics, 2003.
- [152] V. Collaboration, “Advanced Virgo technical design report,” *Technical design reports*, 2012.

Bibliography

- [153] S. Reid, G. Cagnoli, E. Elliffe, J. Faller, J. Hough, I. Martin, and S. Rowan, “Influence of temperature and hydroxide concentration on the settling time of hydroxy-catalysis bonds,” *Physics Letters A*, vol. 363, no. 5, pp. 341–345, 2007.
- [154] A. Van Veggel, D. Van Den Ende, J. Bogenstahl, S. Rowan, W. Cunningham, G. Gubbels, and H. Nijmeijer, “Hydroxide catalysis bonding of silicon carbide,” *Journal of the European Ceramic Society*, vol. 28, no. 1, pp. 303–310, 2008.
- [155] A. A. van Veggel and C. J. Killow, “Hydroxide catalysis bonding for astronomical instruments,” *Advanced Optical Technologies*, vol. 3, no. 3, pp. 293–307, 2014.
- [156] A. A. van Veggel, H. Armandula, N. Beveridge, W. Cunningham, R. Jones, and G. Moreno, “Preparation of an end or input test mass (ETM/ITM) (hydroxide catalysis bonding of ears),” tech. rep., California Institute of Technology, California, USA, 2013. LIGO-E1000278-v9.
- [157] K. A. Haughian, *Aspects of materials research for advanced and future generations of gravitational wave detectors*. PhD thesis, University of Glasgow, 2012.
- [158] N. L. Beveridge, A. A. van Veggel, M. Hendry, P. Murray, R. A. Montgomery, E. Jesse, J. Scott, R. B. Bezensek, W. Cunningham, J. Hough, *et al.*, “Low-temperature strength tests and SEM imaging of hydroxide catalysis bonds in silicon,” *Classical and Quantum Gravity*, vol. 28, no. 8, p. 085014, 2011.
- [159] E. J. Elliffe, *Aspects of thermal noise modeling in ground-based gravitational wave detectors and developments of hydroxide catalysis bonding for space-based gravitational wave detectors and other optical applications*. PhD thesis, University of Glasgow, 2005.

Bibliography

- [160] R. K. Iler, *The chemistry of silica: solubility, polymerization, colloid and surface properties, and biochemistry*. Wiley, 1st ed., 1979.
- [161] K. Mackenzie, I. Brown, P. Ranchod, and R. Meinhold, “Silicate bonding of inorganic materials,” *Journal of materials science*, vol. 26, no. 3, pp. 763–768, 1991.
- [162] K. F. Purcell and J. C. Kotz, *Inorganic Chemistry*. Holt-Saunders International Editions, 1997.
- [163] R. Straessle, Y. Pétremand, D. Briand, and N. F. de Rooij, “Evaluation of thin film indium bonding at wafer level,” *Procedia Engineering*, vol. 25, pp. 1493–1496, 2011.
- [164] M. Alexe and U. Gösele, *Wafer bonding: applications and technology*, vol. 75. Springer Science & Business Media, 2013.
- [165] E. W. Mortimer, “Ultrasonic soldering iron,” Dec. 3 1957. US Patent 2,815,430.
- [166] G. Hofmann, D. Chen, G. Bergmann, G. D. Hammond, M. Hanke, K. Haughian, D. Heinert, J. Hough, A. Khalaidovski, J. Komma, *et al.*, “Indium joints for cryogenic gravitational wave detectors,” *Classical and Quantum Gravity*, vol. 32, no. 24, p. 245013, 2015.
- [167] E. Hirose, T. Sekiguchi, R. Kumar, R. Takahashi, the KAGRA collaboration, *et al.*, “Update on the development of cryogenic sapphire mirrors and their seismic attenuation system for KAGRA,” *Classical and Quantum Gravity*, vol. 31, no. 22, pp. 224004–224018, 2014.
- [168] P. G. Murray, I. W. Martin, L. Cunningham, K. Craig, G. D. Hammond, G. Hof-

Bibliography

- mann, J. Hough, R. Nawrodt, D. Reifert, and S. Rowan, “Low-temperature mechanical dissipation of thermally evaporated indium film for use in interferometric gravitational wave detectors,” *Classical and Quantum Gravity*, vol. 32, no. 11, p. 115014, 2015.
- [169] R. Straessle, Y. Pétremand, D. Briand, M. Dadras, and N. de Rooij, “Low-temperature thin-film indium bonding for reliable wafer-level hermetic MEMS packaging,” *Journal of Micromechanics and Microengineering*, vol. 23, no. 7, p. 075007, 2013.
- [170] A. H. Landrock and S. Ebnesajjad, *Adhesives technology handbook*. William Andrew, 2008.
- [171] K. Richter and R. Steiger, “Thermal stability of wood-wood and wood-FRP bonding with polyurethane and epoxy adhesives,” *Advanced Engineering Materials*, vol. 7, no. 5, pp. 419–426, 2005.
- [172] K. Tamura, K. Nakada, N. Taneichi, P. Andry, J. Knickerbocker, and C. Rosenthal, “Novel adhesive development for CMOS-compatible thin wafer handling,” in *Electronic Components and Technology Conference (ECTC), 2010 Proceedings 60th*, pp. 1239–1244, IEEE, 2010.
- [173] E. Reedy and T. Guess, “Comparison of butt tensile strength data with interface corner stress intensity factor prediction,” *International Journal of Solids and Structures*, vol. 30, no. 21, pp. 2929–2936, 1993.
- [174] W. Bascom, R. Cottington, R. Jones, and P. Peyser, “The fracture of epoxy-and elastomer-modified epoxy polymers in bulk and as adhesives,” *Journal of Applied Polymer Science*, vol. 19, no. 9, pp. 2545–2562, 1975.

Bibliography

- [175] D. Hunston, A. Kinloch, and S. Wang, “Micromechanics of fracture in structural adhesive bonds,” *The Journal of Adhesion*, vol. 28, no. 2-3, pp. 103–114, 1989.
- [176] R. DeSalvo, “Path-finding towards a cryogenic interferometer for LIGO,” *Classical and Quantum Gravity*, vol. 19, no. 7, p. 2021, 2002.
- [177] S. Rowan, J. Hough, and D. R. M. Crooks, “Thermal noise and material issues for gravitational wave detectors,” *Physics Letters A*, vol. 347, no. 1, pp. 25–32, 2005.
- [178] E. R. Dobrovinskaya, L. A. Lytvynov, and V. Pishchik, “Properties of sapphire,” in *Sapphire*, pp. 55–176, Springer, 2009.
- [179] R. L. Savage, P. King, and S. Seel, “A highly stabilized 10-watt Nd: YAG laser for the Laser Interferometer Gravitational-Wave Observatory (LIGO),” *Laser Physics*, vol. 8, no. 3, pp. 679–685, 1998.
- [180] D. Chen, *Study of a cryogenic suspension system for the gravitational wave telescope KAGRA*. PhD thesis, University of Tokyo, 2014.
- [181] A. Khalaidovski, G. Hofmann, D. Chen, J. Komma, C. Schwarz, C. Tokoku, N. Kimura, T. Suzuki, A. O. Scheie, E. Majorana, *et al.*, “Evaluation of heat extraction through sapphire fibers for the GW observatory KAGRA,” *Classical and Quantum Gravity*, vol. 31, no. 10, p. 105004, 2014.
- [182] A. Dari, F. Travasso, H. Vocca, and L. Gammaitoni, “Breaking strength tests on silicon and sapphire bondings for gravitational wave detectors,” *Classical and Quantum Gravity*, vol. 27, no. 4, p. 045010, 2010.
- [183] T. Suzuki, T. Tomaru, N. Sato, T. Haruyama, T. Shintomi, A. Yamamoto,

Bibliography

- T. Uchiyama, S. Miyoki, M. Ohashi, K. Kuroda, *et al.*, “Application of sapphire bonding for suspension of cryogenic mirrors,” in *Journal of Physics: Conference Series*, vol. 32, p. 309, IOP Publishing, 2006.
- [184] “Standard test method for flexural strength of advanced ceramics at ambient temperature,” 2006. ASTM norm C 1161-2C.
- [185] G. D. Quinn and R. Morrell, “Design data for engineering ceramics: a review of the flexure test,” *Journal of the American Ceramic Society*, vol. 74, no. 9, pp. 2037–2066, 1991.
- [186] N.L. Beveridge, A. A. van Veggel, W. Cunningham, J. Hough, I. W. Martin, R. Nawrodt, S. Reid, and S. Rowan, “Dependence of cryogenic strength of hydroxide catalysis bonded silicon on type of surface oxide,” *Classical and Quantum Gravity*, vol. 30, no. 2, p. 025003, 2013.
- [187] R. Douglas, A. A. van Veggel, L. Cunningham, K. Haughian, J. Hough, and S. Rowan, “Cryogenic and room temperature strength of sapphire jointed by hydroxide catalysis bonding,” *Classical and Quantum Gravity*, vol. 31, no. 4, p. 045001, 2014.
- [188] N. Aota, H. Aida, Y. Kimura, Y. Kawamata, and M. Uneda, “Fabrication mechanism for patterned sapphire substrates by wet etching,” *ECS Journal of Solid State Science and Technology*, vol. 3, no. 5, pp. N69–N74, 2014.
- [189] E. Hirose, D. Bajuk, G. Billingsley, T. Kajita, B. Kestner, N. Mio, M. Ohashi, B. Reichman, H. Yamamoto, and L. Zhang, “Sapphire mirror for the KAGRA gravitational wave detector,” *Physical Review D*, vol. 89, no. 6, p. 062003, 2014.

Bibliography

- [190] A. Ugural and S. Fenster, *Advanced Strength and Applied Elasticity*. Upper Saddle River, NJ: Prentice Hall, 2003.
- [191] A. A. Griffith, “The phenomena of rupture and flow in solids,” *Philosophical transactions of the royal society of london. Series A, containing papers of a mathematical or physical character*, vol. 221, pp. 163–198, 1921.
- [192] K. Haughian, R. Douglas, A. A. van Veggel, J. Hough, A. Khalaidovski, S. Rowan, T. Suzuki, and K. Yamamoto, “The effect of crystal orientation on the cryogenic strength of hydroxide catalysis bonded sapphire,” *Classical and Quantum Gravity*, vol. 32, no. 7, p. 075013, 2015.
- [193] W. Young and R. Budynas, *Roark’s Formulas for Stress and Strain*, vol. 7. New York: McGraw-Hill, 2002.
- [194] W. C. Oliver and G. M. Pharr, “An improved technique for determining hardness and elastic modulus using load and displacement sensing indentation experiments,” *Journal of materials research*, vol. 7, no. 06, pp. 1564–1583, 1992.
- [195] K. R. Williams, K. Gupta, and M. Wasilik, “Etch rates for micromachining processing-part II,” *Journal of Microelectromechanical Systems*, vol. 12, no. 6, pp. 761–778, 2003.
- [196] K. R. Williams and R. S. Muller, “Etch rates for micromachining processing,” *Microelectromechanical Systems, Journal of*, vol. 5, no. 4, pp. 256–269, 1996.
- [197] A. Norwick and B. Berry, “Anelastic relaxation in crystalline solids,” *New York*, p. 20, 1972.

Bibliography

- [198] H. J. Pain, *The physics of vibrations and waves*. John Wiley, 2005.
- [199] P. Sneddon, S. Bull, G. Cagnoli, D. Crooks, E. Elliffe, J. Faller, M. Fejer, J. Hough, and S. Rowan, “The intrinsic mechanical loss factor of hydroxy-catalysis bonds for use in the mirror suspensions of gravitational wave detectors,” *Classical and Quantum Gravity*, vol. 20, no. 23, p. 5025, 2003.
- [200] K. Haughian, A. A. van Veggel, J. Hough, and S. Rowan, “Mechanical loss of hydroxide catalysis bonds between sapphire substrates (in preparation),” *Physical Review D*, In press.
- [201] B. A. Auld, *Acoustic fields and waves in solids*. Ripol Klassik, 1973.
- [202] P. G. Murray, *Measurement of the mechanical loss of test mass materials for advanced gravitational wave detectors*. PhD thesis, University of Glasgow, 2008.
- [203] E. C. Chalkley, *Investigations of the properties of materials for the optics and suspensions of future gravitational wave detectors*. PhD thesis, University of Glasgow, 2010.
- [204] K. Numata, S. Otsuka, M. Ando, and K. Tsubono, “Intrinsic losses in various kinds of fused silica,” *Classical and Quantum Gravity*, vol. 19, no. 7, p. 1697, 2002.
- [205] K. Numata, K. Yamamoto, H. Ishimoto, S. Otsuka, K. Kawabe, M. Ando, and K. Tsubono, “Systematic measurement of the intrinsic losses in various kinds of bulk fused silica,” *Physics Letters A*, vol. 327, no. 4, pp. 263–271, 2004.
- [206] A. V. Cumming, *Aspects of mirrors and suspensions for advanced gravitational wave detectors*. PhD thesis, University of Glasgow, 2008.

Bibliography

- [207] M. Granata, E. Saracco, N. Morgado, A. Cajgfinger, G. Cagnoli, J. Degallaix, V. Dolique, D. Forest, J. Franc, C. Michel, *et al.*, “Mechanical loss in state-of-the-art amorphous optical coatings,” *Physical Review D*, vol. 93, no. 1, p. 012007, 2016.
- [208] R. Powell, C. Y. Ho, and P. E. Liley, “Thermal conductivity of selected materials,” tech. rep., DTIC Document, 1966.
- [209] W. Blevin and W. Brown, “A precise measurement of the Stefan-Boltzmann constant,” *Metrologia*, vol. 7, no. 1, p. 15, 1971.
- [210] A. Wittenberg, “Total hemispherical emissivity of sapphire,” *JOSA*, vol. 55, no. 4, pp. 432–435, 1965.
- [211] A. W. Leissa, *Vibration of Plates*. NASA, 1969.
- [212] C. Zener, “Internal friction in solids. I. Theory of internal friction in reeds,” *Physical review*, vol. 52, no. 3, p. 230, 1937.
- [213] Y. S. Touloukian, “Thermophysical properties of matter-the TPRC data series. volume 2. thermal conductivity, nonmetallic solids,” tech. rep., DTIC Document, 1970.
- [214] J. Gwo, “Private communication.”
- [215] S. L. Larson, W. A. Hiscock, and R. W. Hellings, “Sensitivity curves for spaceborne gravitational wave interferometers,” *Physical Review D*, vol. 62, no. 6, p. 062001, 2000.

Bibliography

- [216] “GWINC.” <http://lhocds.ligo-wa.caltech.edu:8000/advligo/GWINC>. 2016.
- [217] A. A. van Veggel, “Private communication,” 2016.
- [218] K. Yamamoto, “Kagra design requirements,” *ET Meeting, Lyon*, 2014.
- [219] S. Rowan, R. L. Byer, M. M. Fejer, R. K. Route, G. Cagnoli, D. R. Crooks, J. Hough, P. H. Sneddon, and W. Winkler, “Test mass materials for a new generation of gravitational wave detectors,” in *Astronomical Telescopes and Instrumentation*, pp. 292–297, International Society for Optics and Photonics, 2003.
- [220] W. Winkler, K. Danzmann, A. Rüdiger, and R. Schilling, “Heating by optical absorption and the performance of interferometric gravitational-wave detectors,” *Physical Review A*, vol. 44, no. 11, p. 7022, 1991.
- [221] D. McGuigan, C. Lam, R. Gram, A. Hoffman, D. Douglass, and H. Gutche, “Measurements of the mechanical Q of single-crystal silicon at low temperatures,” *Journal of Low Temperature Physics*, vol. 30, no. 5, pp. 621–629, 1978.
- [222] B. E. Deal and A. Grove, “General relationship for the thermal oxidation of silicon,” *Journal of Applied Physics*, vol. 36, no. 12, pp. 3770–3778, 1965.